PART 1: SYNTHESIS OF CERAMIC POWDERS BY ELECTROSPRAY PYROLYSIS

PART 2: AN APPROACH TO INTERPLANETARY PARTICLE SAMPLING

Thesis by

Aaron John Rulison

In Partial Fulfillment of the Requirements

for the Degree of

Doctor of Philosophy

California Institute of Technology

Pasadena, California

1992

(Defended May 20, 1992)

Acknowledgement

I owe thanks to several people who made this research possible... to my advisor, Professor Richard Flagan, whose limitless supply of ideas and suggestions catalyzed my efforts... to Professor Thomas Ahrens, who enlightened me through countless conversations and interactions with his research group... to those with whom I worked on a daily basis in the laboratories: Xiaoming Li, Chak Chan, Brian Wong, Steve Rogak, Shih-Chen Wang, Melissa Richmond, and Martha Shaw... to Evelina Cui, who never failed to smile... to Carol Garland, who always managed to work me into her busy schedule... to Rayma Harrison and Gunilla Hastrup, who are the most willfully helpful people I know... to Joe Fontana, Rich Eastveldt, Hai Vu, and Marty Gould, whose skills were essential... to my parents, John and Tudie, who have supported me longer than anyone, and to my wife, Dan Chen, whose positive influence on my life exceeds any other.

Abstract

In Part 1, the application of electrospray atomization for the production of ceramic powders is described. A model of the Taylor cone was developed which predicts the droplet size, volumetric flow rate, and electrical current for atomization of electrolytic solutions as functions of the liquid's specific electrical conductivity, surface tension, absolute viscosity, and density, as well as the applied electrical potential and atomizer geometry. Experimental verification was obtained for atomization of sodium iodide in n-propyl alcohol. The knowledge gleaned from the sodium iodide experiments was used to apply electrospray atomization to the production of submicron, spheroidal, and yttria particles by atomization of yttrium nitrate in n-propyl alcohol and thermal decomposition of the resulting aerosol droplets. This process is named "electrospray pyrolysis." A means of increasing the ceramic powder production rate for industrial and more extensive laboratory use via arrays of Taylor cones was experimentally tested.

In Part 2, a method of sampling interplanetary dust particles (IDPs) is described. IDPs move at speeds ~10 km/s relative to an interplanetary probe. A gas-filled balloon stops the particles by drag and ablation after they penetrate the balloon's skin. A model for ablation and deceleration of particles in the continuum and transition regimes was developed and experimentally tested using 7 μm diameter glass spheres moving with an initial speed of 5 km/s through xenon gas at 0.1 and 0.2 atm. To analyze stopped IDPs by mass spectrometry, microscopy, etc., they must be deposited on a small sample substrate. To this end, a method of inward electrostatic precipitation was devised, modelled, and experimentally tested for ~1 μm carbon soot particles in a cylindrical chamber. By this method, ~10μm IDPs can be intercepted by a ~1 m

noble gas-filled balloon, and deposited on a $\sim$1 mm centrally located sample substrate for subsequent analysis.

Contents

Acknowledgement ii

Abstract iii

List of Figures viii

List of Tables xv

Introduction 1

1 Electrospray Atomization of Electrolytic Solutions 4

1.1 Introduction 7

1.2 Theory 13

1.3 The Boundary Layer 13

1.3.1 Acceleration of the Jet 21

1.3.2 Jet Break-up and Droplet Charging 23

1.4 Experiment 25

1.5 Results 30

1.6 Conclusions 39

2 Further Data on Volumetric Flow Rate and Current in Electrospray Atomization of Electrolytic Solutions 45

3 Evaporation of Charged Droplets 54

4 Synthesis of Lanthana-doped Yttria by Electrospray Pyrolysis 59

4.1 Introduction 60

4.2 Experiment 61

4.3 Results and Discussion 65

4.3.1 Undoped Yttria 65

4.3.2 Lanthana-doped Yttria 86
4.4 Conclusions 93

5 Scale-up of Electrospray Atomization using Linear Arrays of Taylor Cones 99
5.1 Introduction 99
5.2 Experiment 100
5.3 Results and Discussion 102
5.4 Conclusions 114

6 Ablation of Silicate Particles in High-speed Continuum and Transition Flow with Application to the Collection of Interplanetary Dust Particles 115
6.1 Introduction 116
6.2 Ablation and Deceleration 117
6.3 Experiment 129
6.4 Results 138
6.5 Conclusions 146

7 Inward Electrostatic Precipitation of Particles in Spherical and Cylindrical Chambers 148
7.1 Introduction 149
7.2 Theory 153
7.2.1 Particle Charging in a Gas 153
7.2.2 Particle Motion 155
7.2.3 Particle Loss to the Screens 163
7.3 Experiments 166
7.4 Conclusions 171

Appendix A: Pressure Difference Across a Conducting, Dielectric Liquid/Air Interface with an Applied Electric Field 175

Appendix B: Program Listing–EHDA1.F 176

Appendix C: Program Listing–EHDA2.F 187

Appendix D: Program Listing–DISRUPT.F 192

Appendix E: Program Listing–BIN1.F 208

Appendix F: Program Listing–BIN2.F **216**

Appendix G: Program Listing–DEV.F **221**

Bibliography **225**

List of Figures

1.1 Schematic drawing of the Taylor cone and liquid jet. 7

1.2 Coordinate systems. Spherical coordinates are used for the boundary layer analysis. Cylindrical coordinates are used for the jet flow analysis. 8

1.3 Photograph of a Taylor cone with jet. The solution was 2.4×10^{-5} g/ml of methylene blue ($C_{16}H_{18}ClN_3S{\cdot}3H_2O$) in 23% isopropyl alcohol/77% distilled water (by volume) (r_c=0.45 mm, V = +10.4 kV, h=15 mm). 10

1.4 Schematic of the electrospray atomizer. 26

1.5 Schematic of the overall experimental apparatus. 28

1.6 Volumetric flow rate of liquid versus specific electrical conductivity for three values of P. 32

1.7 Total electrical current versus specific electrical conductivity for three values of P. 33

1.8 Volume-mean dried particle size versus specific electrical conductivity for three values of P. 34

1.9 Volume-mean droplet size versus specific electrical conductivity for three values of P. 35

1.10 Specific charge versus specific electrical conductivity for three values of P. 36

1.11 Rayleigh charge limit fraction versus specific electrical conductivity for three values of P. 37

1.12 Electric field penetration factor (top), jet electric field factor (middle), and charging geometry factor (bottom) versus P. 40

1.13 Dried NaI particle size distribution measured by SEMS. Variable concentration. 41

1.14 Dried NaI particle size distribution measured by SEMS. Variable P. . 42

2.1 Schematic of the electrospray atomizer without a discharger in the drying chamber. 46

2.2 Volumetric flow rate of liquid versus specific electrical conductivity for three values of P for the atomizer without the discharger. 48
2.3 Total electrical current versus specific electrical conductivity for three values of P for the atomizer without the discharger. 49
2.4 Specific charge versus specific electrical conductivity for three values of P for the atomizer without the discharger. 50
2.5 Volumetric flow rate of liquid versus electrode radius for the atomizer without the discharger. 51
2.6 Total electrical current versus electrode radius for the atomizer without the discharger. 52
2.7 Predicted droplet size versus electrode radius for the atomizer without the discharger. 53

3.1 Size distributions of dried solute particles resulting from one initial droplet of 1 μm diameter for two initial solution concentrations. The width of the histogram bars in the $C_o = 0.1$ cases and $C_o = 0.01$ case are 0.05 and 0.015 nm, respectively. 58

4.1 Schematic of the electrospray atomizer. 63
4.2 Absolute viscosity of solutions of hydrated yttrium nitrate in n-propyl alcohol at 24°C. The number next to each point gives the hydration level. 67
4.3 Density and surface tension of solutions of hydrated yttrium nitrate in n-propyl alcohol at 24°C. The number next to each point gives the hydration level. 68
4.4 Specific electrical conductivity of solutions of yttrium nitrate hexahydrate in n-propyl alcohol at 25°C. The number next to each point gives the hydration level. 69
4.5 Volumetric flow rate of liquid versus concentration of hydrated yttrium nitrate in n-propyl alcohol. The number next to each point indicates the hydration level. 70
4.6 Computed profile of yttrium nitrate pentahydrate in n-propyl alcohol being accelerated according to the low Reynolds number approximation. 72
4.7 Volume-mean droplet size versus concentration of hydrated yttrium nitrate in n-propyl alcohol. The number next to each point gives the hydration level. 73

4.8 Mass throughput of yttrium oxide for solutions of hydrated yttrium nitrate in n-propyl alcohol. The number next to each point gives the hydration level. 74
4.9 Size distribution of yttrium oxide particles synthesized from yttrium nitrate pentahydrate in n-propyl alcohol, cured at 550°C for 5.7 seconds. Top: 44.2 g/l. Middle: 93.4 g/l. Bottom: 441 g/l. 76
4.10 Transmission electron micrographs of yttria particles synthesized from 44.2 g/l yttrium nitrate pentahydrate in n-propyl alcohol, cured at 550°C for 5.7 seconds. 77
4.11 Transmission electron micrographs of yttria particles synthesized from 441 g/l yttrium nitrate pentahydrate in n-propyl alcohol, cured at 550°C for 5.7 seconds. 78
4.12 Transmission electron micrographs of yttria particles synthesized from 93.4 g/l yttrium nitrate hexahydrate in n-propyl alcohol, cured at 550°C for 5.7 seconds. Top: bright field micrograph. Bottom: Dark field micrograph. 80
4.13 Transmission electron micrograph of yttria particles synthesized from 93.4 g/l yttrium nitrate hexahydrate in n-propyl alcohol, cured at 550°C for 5.7 seconds. 81
4.14 Schematic explanation of the dependence of particle structure on hydration level in yttrium and lanthanum nitrates. 83
4.15 Size distribution of yttrium oxide particles synthesized from 441 g/l yttrium nitrate pentahydrate in n-propyl alcohol, cured at 550°C for 5.7 seconds, high efficiency case. 85
4.16 Transmisson electron micrograph of an yttria particle synthesized from 441 g/l yttrium nitrate pentahydrate in n-propyl alcohol, cured at 550°C for 5.7 seconds, high efficiency case. 85
4.17 X-ray diffraction pattern for undoped yttria powder synthesized from 441 g/l yttrium nitrate pentahydrate in n-propyl alcohol electrosprayed at P=1.3, cured at 550°C for 5.7 seconds, high potential case. 87
4.18 Size distribution of lanthana-doped yttria particles synthesized from 445 g/l hydrated metal nitrates in n-propyl alcohol, cured at 656°C for 5.1 seconds (top) or 725°C for 4.7 seconds (bottom). 88
4.19 Transmission electron micrograph of lanthana-doped yttria particles synthesized from 445 g/l hydrated metal nitrates in n-propyl, cured at 656°C for 5.3 seconds. 90

4.20 X-ray diffraction pattern for lanthana-doped yttria powder synthesized from 445 g/l hydrated metal nitrates in n-propyl alcohol, cured at 656°C for 5.3 seconds. 92
4.21 Transmission electron micrograph of lanthana-doped yttria particles synthesized from 445 g/l hydrated metal nitrates in n-propyl alcohol, cured at 725°C for 4.7 seconds. 94
4.22 Transmission electron micrographs of lanthana-doped yttria particles synthesized from 445 g/l hydrated metal nitrates in n-propyl alcohol, cured at 725°C for 4.7 seconds. Top: Bright field image. Bottom: Dark field image. 95
4.23 X-ray diffraction patterns for lanthana-doped yttria powder synthesized from 445 g/l hydrated metal nitrates in n-propyl alcohol, cured at 725°C for 4.7 seconds. 96

5.1 Multiple electrode electrospray apparatus. 101
5.2 Onset potential of Taylor cones versus capillary radius to spacing ratio. 104
5.3 Average electrical current per cone versus capillary radious to spacing ratio. 106
5.4 Volumetric flow rate per cone versus capillary radius to spacing ratio. 107
5.5 Photographs of a Taylor cone established on a capillary electrode placed opposite a slotted flat plate electrode. $R/S \rightarrow 0$, $P = 1.39$. 108
5.6 Photographs of a linear array of Taylor cones established on capillary electrodes placed opposite a slotted flat plate electrode. $R/S = 0.16$, $P = 1.39$. 109
5.7 Photographs of a linear array of Taylor cones established on capillary electrodes placed opposite a slotted flat plate electrode. $R/S = 0.31$, $P = 1.39$. 110
5.8 Photograph of the right-hand side of a linear array of Taylor cones established on capillary electrodes placed opposite a slotted flat plate electrode. $R/S = 0.31$, $P = 1.39$. 111
5.9 Photographs of a linear array of Taylor cones established on capillary electrodes placed opposite a slotted flat plate electrode. $R/S = 1.6$, $P = 1.39$. 112
5.10 Photograph of the right-hand side of a linear array of Taylor cones established on capillary electrodes placed opposite a slotted flat plate electrode. $R/S = 1.6$, $P = 1.39$. 113

6.1 Drag coefficient C_D for a sphere as a function of Re_1 for various M_1. . 122
6.2 (a) Schematic diagram of the bow shock through which the gas must pass to reach the particle. (b) Approximation of the bow shock by a normal shock of the same Mach number. The fluid state upstream of the shock is denoted as 1. The fluid downstream of the shock is denoted as 2. 124
6.3 Nusselt number Nu_2 for a sphere versus Re_2 for various M_2 and for $\mathrm{Pr} = 2/3$ (monatomic gas). The minimum value of Re_2 needed to satisfy the condition that a bow shock forms ahead of the particle is indicated by the crosses. This corresponds to the condition that $\mathrm{Kn}_1 \leq 0.33$. In the $M_2 = 0.2$ case, the minimum Re_2 is less than 1. . 127
6.4 Scanning electron micrograph of the original (unablated) soda-lime glass spheres. The mean diameter is 7.1 μm. 129
6.5 Size distribution of original (unablated) soda-lime glass spheres. The size distribution represents the diameters of 503 spheres measured by hand from SEM micrographs. 130
6.6 Schematic of the capture chamber used in the ablation experiments. The particles and aluminum cup move downward. The cup travels through the central tube while the particles penetrate the plastic film and enter the xenon gas. The particles settle to the bottom of the chamber to be collected on a Teflon sheet. The sheet is then divided and mounted on electron micrograph stubs. 132
6.7 Schematic of the system used to adjust and maintain xenon gas pressure inside the capture chamber while the impact vacuum tank is evacuated. The gun is fired in the vertical position. The impact tank is evacuated to $\sim$ 1 Torr. 133
6.8 Typical scanning electron micrographs of particles which perforated the film but were not exposed to gas, so that no ablation could occur. The particles are undamaged, indicating that the reduction of diameter described below must be due to ablation. The small white square seen on the micrographs is an aiming aid for the EDS system. 135
6.9 Typical scanning electron micrographs of film perforations made by high-speed particles. The film is 13 μm thick. The debris seen on the film is from the gun blast, and is not related to the glass particles. . . 136

6.10 Scanning electron micrographs of soda-lime glass particles ablated in 0.1 atm (top) and 0.2 atm (bottom) Xe gas at 295 K. The initial speed was approximately 4500 m/s. The initial sizes (arrowed), calculated for these particles by the average ratios of final to initial radius for each pressure, are indicated for comparison. 137

6.11 Ablated radius R_f for xenon at 295 K versus pressure p_1 for various Q (MJ kg^{-1})(ρ_p =2420 kg m^{-3} and v_0 = 4500 m s^{-1}). The two experimental values of v_0 were of slightly different values (4540 m s^{-1} for p_1 = 0.1 atm and 4300 m s^{-1} for p_1 = 0.2 atm). The meteor theory curve is calculated assuming no variation of σ with gas pressure. There is agreement between the present model and the experiment results for $Q = 1.5 \pm 0.2$ MJ kg^{-1}. 140

6.12 Free-stream Knudsen number Kn_1 histories for particles ablating in various free-stream gas pressures (Pa) (Q =1.9 MJ kg^{-1}, $\rho_p = 10^{-3}$, v_0 = 10 km s^{-1}, and R_0 = 5 μm). 142

6.13 $\hat{R}_f$ versus $2R_0$ for various values of v_0 (km s^{-1})(Q = 1.9 MJ kg^{-1}, ρ_p = 1000 kg m^{-3}). The curves are terminated on the left-hand side where the condition that a bow shock forms ahead of the particle, i.e., $\mathrm{Kn}_1 \leq 0.33$, is violated. 143

6.14 $\hat{M}$ and $\hat{R}$ versus t for two pressures (Pa)(Q = 1.35 MJ kg^{-1}, ρ_p =2420 kg m^{-3}, v_0 = 4.5 km s^{-1}, and R_0 = 3.53 μm). 144

6.15 $\hat{R}_f$ versus ρ_p for various Q (MJ kg^{-1}) (v_0 =10 km s^{-1}, R_0 = 5 μm, and p_1 = 0.2 atm. 145

7.1 Concept drawing for the Dust and Ring Analyzer (DARA). 150

7.2 Geometry of the inward electrostatic precipitator. Particles dispersed throughout the chamber after being slowed by gas drag and ablation are collected by charging them and applying an electric field to force them toward the small planchet at the center. Solid lines indicate trajectories of IDPs in space. Dashed lines indicate trajectories during deceleration. Dotted lines indicate trajectories during electrostatic precipitation. . . 152

7.3 Dimensionless electric field strength versus dimensionless radial position for spheres with zero screens and three optimally positioned screens. The screens increase the field strength in the outer part of the chamber. 159

7.4 Dimensionless particle motion characteristics for a sphere with zero and three screens. The speed of the particle is more constant in the three screen case. 160
7.5 Collection time as a function of particle diameter and dielectric constant. Large particles with large dielectric constant are collected in the least amount of time ($\mu = 5 \times 10^{-5}$ kg m^{-1}s^{-1}, $E_\infty = 1.4 \times 10^4$ V/m, $R = 1$, V_T=20 kV, and $\hat{T}_T = 5.44$). 161
7.6 Field lines according to the finite element solution. One section of the periodic geometry that extends to infinity to the left and right is shown. 165
7.7 Schematic drawing of the cylindrical inward precipitator constructed for the experiments. 167
7.8 Overall experimental apparatus. The particle motion was recorded using a long range microscope and video cassette recorder. 168
7.9 Photograph of particles near the central collection rod (end view). The outline of the collection rod is drawn. Scattered light from the laser is seen at the surface of the rod. No charge or electric field exist. 169
7.10 Photographs showing a particularly slow particle (chosen for photographic clarity) near the collection rod (end view) (top) 0 s, (bottom) 0.17 s. The particle was moving toward the rod with an average speed of 4.5 mm/s. 170
7.11 Photographs showing a particularly slow particle (chosen for photographic clarity) near the screen (end view) (top) 0 s (bottom) 1.00 s. The particle was charged and moving toward the screen and collection rod to the left (not shown) with an average speed of 1.5 mm/s. 172

List of Tables

1.1 Terms in the boundary layer growth equation. 20
1.2 Specific electrical conductivity of NaI in n-propyl alcohol at 25°C. . . 25
1.3 Properties of sodium iodide in n-propyl alcohol 30
1.4 Dried Nai particle size distribution statistics. 39
1.5 Further dried NaI particle size distribution statistics. 43

2.1 Values of A_1, A_2, and A_3 for experimentally tested values of P. 46

4.1 Correlation between oxide particle structure and lanthanum content. . 89

7.1 Optimal screen positions for a spherical inward electrostatic precipitator. 158
7.2 Effect of dimensionless planchet size. 159
7.3 Optimal screen positions for a cylinder. 163

Introduction

Electrospray atomization uses electrical forces to overcome surface tension forces in liquids, resulting in the dispersion of that liquid into droplets. It is usually implemented by allowing a liquid to flow out of a ~1 mm diameter capillary and applying a high potential between the capillary and a flat plate counter-electrode placed several centimeters away. The resulting electrical forces on the liquid counterbalance the surface tension forces and the liquid forms a Taylor cone, named after the first researcher to explain it [1]. It is from the tip of the Taylor cone that liquid droplets or ions are emitted.

Part 1 of this thesis, **Synthesis of Ceramic Powders by Electrospray Pyrolysis**, is an investigation of electrospray atomization with application to synthesis of ceramic powders. Chapter 1 contains a description of the Taylor cone and a mathematical model for atomization of electrolytic solutions which predicts the droplet size, electrical current, and volumetric flow rate of liquid. The liquid properties affecting these quantities are the specific electrical conductivity, surface tension, absolute viscosity, and density. The important operating parameters are the applied electric field strength and atomizer geometry. Experiments using solutions of sodium iodide in n-propyl alcohol were performed to verify the accuracy of the model and to establish the range of attainable droplet sizes and volumetric flow rates. In Chapter 2, further data on atomizer performance over an extended range of liquid properties and operating conditions is reported and compared to the model results. Chapter 3 is a short, computational demonstration of the effect of Rayleigh charge disruptions on the size distribution of charged, evaporating aerosol droplets.

The knowledge gleaned in the first three chapters is used to apply electrospray

atomization to the synthesis of ceramic powders. This is described in Chapter 4. Solutions of hydrated yttrium nitrate in n-propyl alcohol were atomized and the resulting aerosol droplets were thermally decomposed to form yttrium oxide particles, which are difficult to make by other means. Conditions for achieving optimal particle shape, structure, and size distributions were discovered. Chapter 5 addresses the problem of increasing the ceramic powder production rate. A linear array of atomization sites was constructed and shown to be very compact, thus establishing a means of reaching useful production rates. Chapters 1 through 5 thus report a promising new method for the production of ceramic powders, named "electrospray pyrolysis."

The solar system contains large numbers of interplanetary dust particles (IDPs) which are in various orbits around the sun and planets. These range in size, composition, and origin. Data on IDPs is valuable because it provides insights into the development and current state of the solar system. For example, IDPs may have played a significant role in supplying the early Earth with organic material, possibly leading to the development of life.

Part 2 of this thesis, **An Approach to Interplanetary Particle Sampling**, addresses the problem of collecting IDPs for composition and orbit determination. Since IDPs move at speeds ~10 km/s relative to a spacecraft, the problem is essentially one of reducing the kinetic energy of the particle while leaving it as intact as possible. Chapter 6 describes the use of noble gas drag and ablation to stop particles. Modelling and experiments are described which elucidate the conditions leading to relatively undamaged particles. After the IDPs are stopped, they must be deposited on a collection substrate for subsequent analysis by mass spectrometry, microscopy,

etc. A means of charging and electrostatically moving a particle from an unknown location in a gas-filled chamber to a small, centralized collection substrate is described, modelled, and experimentally tested in Chapter 7. Chapters 6 and 7 thus present a means of sampling IDPs for compositional and orbit determination.

Appendix A gives a treatment of the pressure difference across a conducting, dielectric liquid/air interface with an applied electric field. Appendices B through G list computer programs used to implement the electrospray model and to process experimental particle size distribution data.

Chapter 1

Electrospray Atomization of Electrolytic Solutions

Abstract

We have explored droplet production by electrospray atomization of electrolytic solutions theoretically and experimentally. It is hypothesized that the spray results from the formation and breakup of a liquid jet at the tip of a Taylor cone. The jet is formed from liquid which is accelerated by the tangential electrical stress on the face of the cone. It breaks up along its axis into charged droplets due to a longitudinal instability. We have developed a model with three empirical constants to predict the mass flow rate, current, and droplet radius as functions of the liquid's specific electrical conductivity, surface tension, viscosity, and density, from balances on mass, momentum, and charge. Experiments using sodium iodide dissolved in n-propyl alcohol were performed to measure the volumetric flow rate, total electrical current, and aerosol size distribution as functions of the specific electrical conductivity, applied potential, and capillary radius. The results confirm the general predictions of the model.

Nomenclature

Refer to Figs. 1.1 and 1.2.

A	cross-sectional area (normal to the r-direction) inside the cone
A_b	cross-sectional area (normal to the r-direction) of the boundary layer flow
A_i	cross-sectional area (normal to the r-direction) of the inner flow
A_1	electric field penetration efficiency
A_2	jet electric field factor
A_3	geometric charging factor
b_i	terms in the boundary layer growth equation
c	solute concentration
D	ion diffusivity
e	elementary charge
E_r	tangential component of the electric field
E_p, E_z	perpendicular and tangential components of the electric field on the jet surface, respectively
E_ϕ	normal component of the electric field
ϵ	permittivity of the liquid
ϵ_0	permittivity of free space
f	ionic friction factor
F	charge per mole of ions
ϕ_b	boundary layer angle
ϕ_c	cone half-angle
ϕ_f	final boundary layer angle
Φ_i	terms in the boundary layer growth equation
g	electric field self-similarity function
g_r	r-component of the body force
h	electrode to counter-electrode spacing
I_cond	conduction current
I_sur	convection current
I_total	total current
k	Boltzmann constant
L	cone length scale
$\dot{m}$	boundary layer mass flow rate
μ	absolute viscosity
n_i	number of elementary charges per surface ion
p	hydrostatic pressure
P	overpotential ratio $= V/V_s$
P_m	boundary layer momentum flux
q_d	charge per drop

q_{limit}	Rayleigh charge limit
q_{steady}	steady state charge per drop
Q	volumetric flow rate of liquid
r, ϕ, θ	spherical coordinates
$\hat{r}$, $\hat{\phi}$, $\hat{\theta}$	unit vectors in spherical coordinates
r, θ, z	cylindrical coordinates
r_{c}	electrode radius
r_{cap}	value of r at the electrode edge
r_{jet}	jet radius
R	universal gas constant
Re	Reynolds number
ρ	liquid density
ρ_c	charge volume density
t	time
T	absolute temperature and surface tension
τ	z-component of the shear stress on the jet surface
τ_{ϕ_c}	r-component of the shear stress on the cone's surface
σ	specific electrical conductivity
u_{i}	r-component speed of the surface ions
u_r, u_ϕ, u_θ	r, ϕ, and θ components of the fluid velocity
u_z	z-component of the jet velocity
U	boundary layer speed scale
V	applied potential
V_{s}	minimum potential to establish the Taylor cone

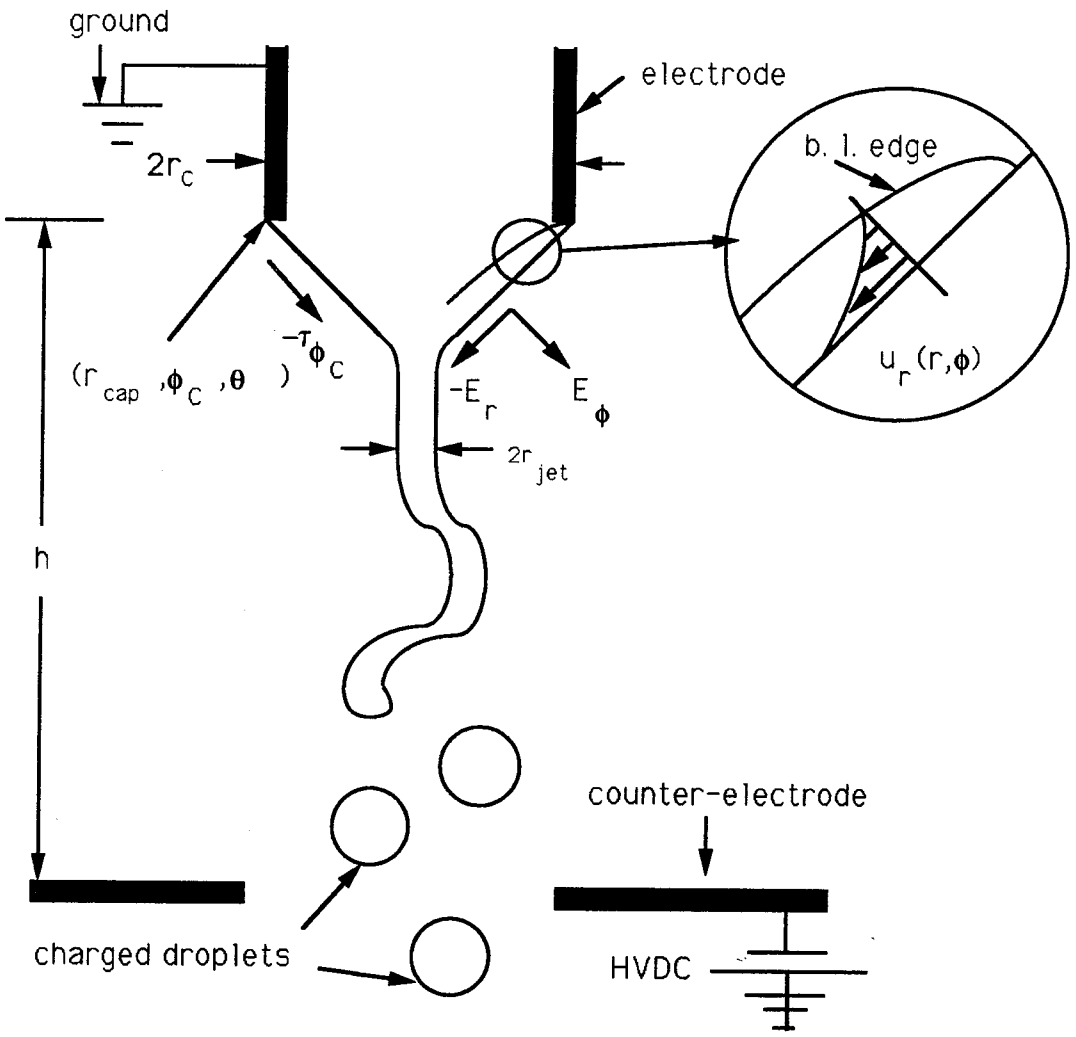

Figure 1.1: Schematic drawing of the Taylor cone and liquid jet.

1.1 Introduction

When a liquid is sprayed, the size of droplets produced is determined by the competition between surface tension forces and dynamic forces. Efforts to produce smaller droplets have led investigators to employ electrostatic and electrokinetic forces to augment dynamic forces in a process known as electrospray atomization. The use of electrical forces to overcome surface forces is not new. As early as 1745, researchers demonstrated that electrical forces alone were sufficient to spray a liquid [2]. Over the

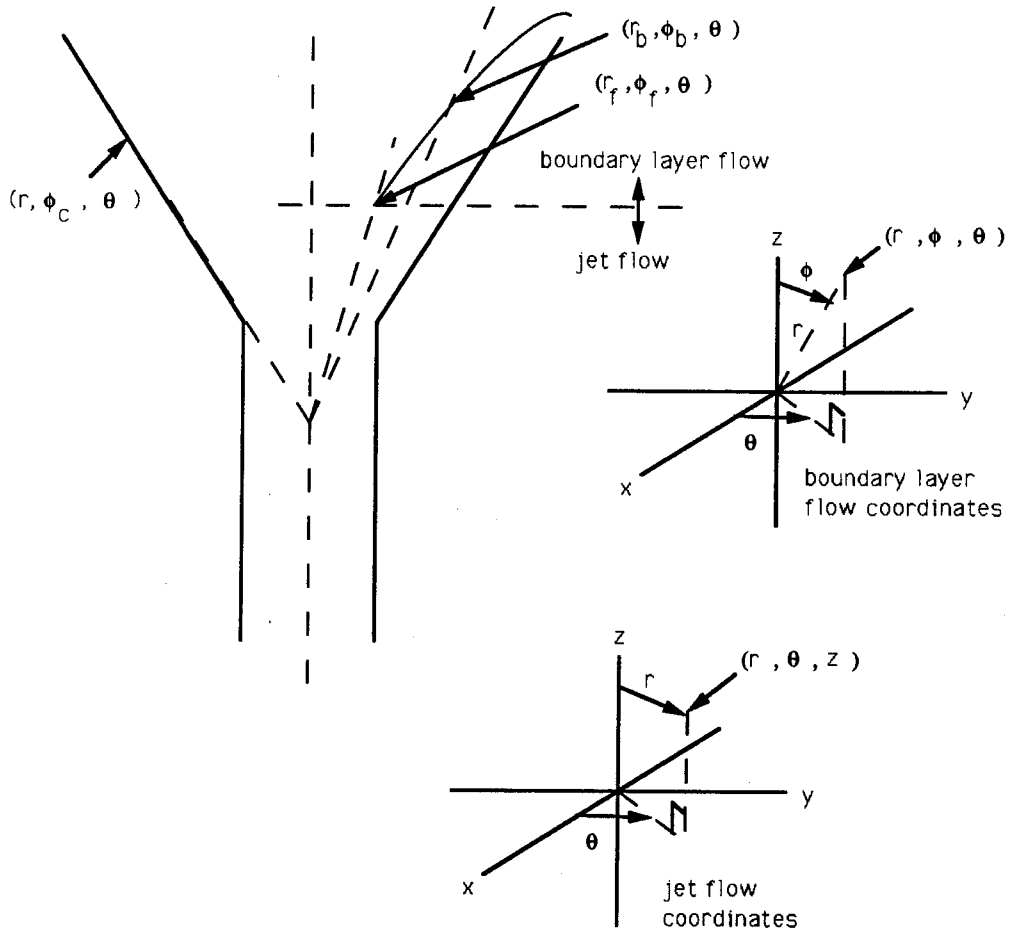

Figure 1.2: Coordinate systems. Spherical coordinates are used for the boundary layer analysis. Cylindrical coordinates are used for the jet flow analysis.

years, electrically induced or augmented sprayers have been applied to paint spraying, spacecraft thruster designs, and ink-jet printers. Interest in electrospray has grown in recent years as applications to materials processing [3], mass spectroscopy of large biomolecules [4], and liquid metal ion sources (LMIS) [5] have emerged. These latter applications represent an important limiting case in electrically enhanced spray technology, one in which the dominant forces involved in spray production are electrical.

Taylor [1] pioneered the theory of electrosprays with an explanation of the origin of the sharp conical tip that forms on a droplet placed in a strong electric field (Fig. 1.3). It is from the tip of the so-called Taylor cone that droplets or ions are emitted. Taylor's theory only describes the static cone and does not describe the production of droplets or ions.

Two broad categories of phenomena describe the emission of liquid from the tip of a Taylor cone. In one category, ions, neutral atoms, and droplets are emitted from the liquid surface due to instabilities brought on by the intense electric field present at the tip of the cone. Emission of droplets by growth of unstable surface deformations is an example [6] and field emission of ions utilized in liquid metal ion sources [5] are examples. In another category, the liquid is ejected due to momentum and mass fluxes created by the fluid mechanical stresses exerted on the whole cone. An example is the formation of a jet of liquid which breaks into droplets after some length, observed in the electrospray of moderately conductive (10^{-11} to 10 mhos/m) liquids by us (Fig. 1.3) and others [7, 8].

In this paper we perform a fluid mechanical analysis which indicates substantial mass and momentum fluxes of liquid reaching the tip of the Taylor cone for electrolytic solutions. These fluxes are sufficient to account for the observed electrospray

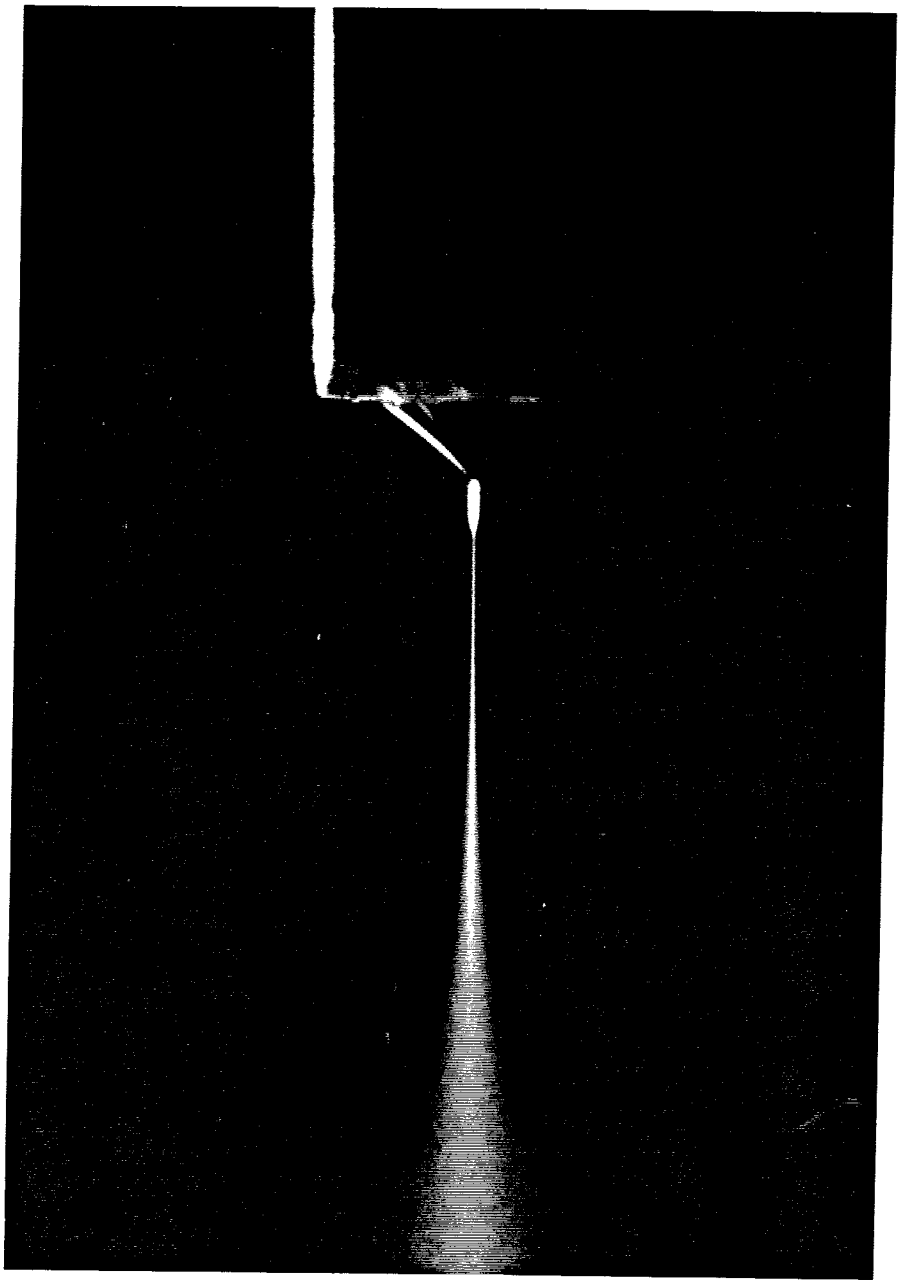

Figure 1.3: Photograph of a Taylor cone with jet. The solution was 2.4×10^{-5} g/ml of methylene blue ($C_{16}H_{18}ClN_3S{\cdot}3H_2O$) in 23% isopropyl alcohol/77% distilled water (by volume) (r_c=0.45 mm, V = +10.4 kV, h=15 mm).

behavior. We therefore neglect possible emission of ions or droplets through interfacial instabilities and concentrate on momentum and mass flux modelling.

De la Mora et al. [8] formulated a scaling law relating the jet radius r_{jet} (Fig. 1.1) to the volumetric flow rate Q, surface tension T, and density ρ. The derivation assumed that convection of charge is the major source of electrical current flow near the cone's tip. It also made use of an empirical finding from insulating liquid experiments that the dimensionless group $[2T\pi^2 r_{\text{jet}}^3/\rho Q^2]^{1/3}$ is always of order one. They applied Bernoulli's equation between a point far upstream of the cone's tip and a point in the jet. Their results gave qualitative agreement for r_{jet} as a function of Q and γ for $r_{\text{jet}} > 2.8$ microns. The finding is not useful in the present work where the effect of varying the specific electrical conductivity is studied. Also, the work of de la Mora does not predict the volumetric flow rate as a function of the liquid properties.

Other researchers have concentrated on predicting the size distribution of the droplets eminating from the electrospray. Kelly treated droplet formation as a purely random process that disperses the input mass and charge, producing droplets with a range of charges and sizes [9]. The charge distribution was assumed to be governed by Fermi-Dirac statistics, while the mass distribution was described using Maxwell-Boltzmann statistics. Equations for charge and mass distributions were derived in terms of several undetermined variables that were empirically fit to data involving surface tension, density, viscosity, specific electrical conductivity, applied electric field strength, mass flow rate, and electrical current. The results showed good agreement with experimental measurements of charge to mass ratio versus droplet radius for several conductive and nonconductive liquids. Implicit in his derivation was the assumption that the formation of charged droplets at the tip of the Taylor cone is

chaotic and an equilibrium state process so that droplet size and charge distributions can be determined by maximizing the number of states in the system. Kelly's work does not predict the volumetric flow rate or electrical current as functions of the liquid properties.

This paper presents a new model of the electrospray. Our goal is to determine the liquid flow rate, current, and droplet size as functions of the liquid being sprayed, as well as the applied electric field strength and geometry of the atomizer. To do this, we hypothesize that the flow is driven by shear stresses on the surface of the cone as described by Smith [7] (Fig. 1.1). As the Taylor cone begins to form, the intense electric field at the tip of the cone causes the emission of charge, through corona discharge if the cone is immersed in an electrically active gas, through field emission of electrons or ions, or through emission of charged liquid droplets. In any case, the loss of charge prevents the cone from being in electrostatic equilibrium. A current flows down the cone as a result of the charge loss, creating a shear stress which drives liquid toward the tip of the cone. The moving liquid forms a jet which disintegrates into charged droplets, establishing an electric current that causes the process to continue.

Smith derived scaling laws to relate the current and mass flow rate to the specific electrical conductivity and surface tension, but an error was made in applying conservation of charge so the results obtained were unusable. In this paper, we present a method to compute the current, mass flow rate, and jet radius based on the concept of the shear stress on the surface of the cone.

1.2 Theory

Using a boundary layer integral method, we find the liquid mass and momentum fluxes that result from the shear stress on the face of the cone. The acceleration of the jet that is formed from those fluxes toward its terminal velocity is described. Finally, the jet disintegrates and breaks up into charged droplets due to longitudinal instability.

1.3 The Boundary Layer

An electric field is applied to the liquid/gas interface at the exit of the electrode tube by applying a potential difference between the electrode and counter-electrode (Fig. 1.1). Taylor showed that the liquid interface can exist in equilibrium when the inward surface tension pressure $\frac{T\cot(\phi_c)}{r}$ is counterbalanced by the outward electric field pressure [1] $\frac{\epsilon_0 E_\phi^2(r,\phi_c)}{2}$ where ϵ_0 is the permittivity of free space, ϕ_c is the cone half-angle, r is the radial coordinate in spherical coordinates (Fig. 1.2), and ϵ_0 is the permittivity of free space. Solving Laplace's equation in spherical coordinates for the electrical potential in the region outside the interface (assuming an equipotential interface) shows that the counterbalance occurs only when the interface assumes a conical shape with half-angle $\phi_c = 49.3°$ [1]. The required potential is [7]

$$V_s = 0.667[\frac{2Tr_c\cos(\phi_c)}{\epsilon_0}]^{1/2}\ln(\frac{4h}{r_c}) \tag{1.1}$$

with the associated normal electric field at the interface

$$E_{\phi_s}(r,\phi_c) = (\frac{2T\cos(\phi_c)}{\epsilon_0 r_c})^{1/2}, \tag{1.2}$$

[1] Recently, de la Mora et al. showed that the cone can assume other angles if the space charge due to the sprayed droplets is included in the calculation [10]. The space charge is neglected in this paper however, as the cone angle used in experiments was always near the 49.3° calculated for zero space charge.

where T is the surface tension, r_c is the electrode radius, and h is the electrode to counter-electrode spacing. [2] The actual electrospray potential is generally higher, i.e., $V = PV_s$, where P is the over-potential ratio ($1.1 \leq P \leq 1.5$). Thus $E_\phi(r_c, \phi_c) = PE_{\phi_s}(r_c, \phi_c)$ The factor of 0.667 was found empirically [7].

The charge per unit area induced on the interface is[3]

$$\epsilon_0 E_\phi(r, \phi_c), \tag{1.3}$$

where ϵ_0 is the permittivity of free space. To use this expression when a liquid flow is present we must assume that the time scale of charge induction is much less than the time scale of liquid motion in the cone and that sufficient numbers of charge carriers are present in the liquid to provide the surface charge. The validity of these assumptions are checked *a posteriori* in Section 1.5. As remarked above, there is a tangential component of the electric field, $E_r(r, \phi_c)$, which causes the ions composing the surface charge to move relative to the liquid with speed

$$u_i(r) - u_r(r, \phi_c) = n_i e E_r(r, \phi_c)/f, \tag{1.4}$$

where $u_i(r)$ and $u_r(r, \phi_c)$ are the r-components of the ion and liquid velocities at the cone's surface, respectively, n_i is the number of elementary charges per ion, e is the elementary charge and $f = kT/D$ is the ionic friction factor, where k is Boltzmann's constant and D is the ion diffusivity. The surface current due to the migrating ions is

$$I_{sur}(r) = 2\pi r \sin(\phi_c) u_i(r) \epsilon_0 E_\phi(r, \phi_c). \tag{1.5}$$

[2]Note that Eqn. (1.2) applies to the case where no tangential electric field exists. In Appendix A we show that it is still accurate if the tangential component of the electrical field is sufficiently small, allowing us to apply the electrostatic solution to the electrospray problem.

[3]Steady-state conditions are assumed except at the tip of the cone.

Because the ions are moving relative to the liquid, a shear stress on the interface arises,

$$\tau_{\phi_c}(r) = \frac{\epsilon_o E_\phi(r,\phi_c) f}{n_i e}[u_i(r) - u_r(r,\phi_c)]. \tag{1.6}$$

The shear stress arises due to the action of the r-component of the electric field on the surface charge, so that

$$\tau_{\phi_c}(r) = \epsilon_o E_\phi(r,\phi_c) E_r(r,\phi_c). \tag{1.7}$$

Combining Eqns. (1.6) and (1.7), we obtain the radial electric field

$$E_r(r,\phi_c) = \frac{f}{n_i e}[u_i(r) - u_r(r,\phi_c)]. \tag{1.8}$$

The liquid interface thus has finite normal and tangential electric field components.

The field inside the liquid (beneath the charged interface [4]) is described by Laplace's equation

$$\nabla \cdot E(r,\phi) = 0. \tag{1.9}$$

Boundary conditions for Eqn. (1.9) must be specified in three regions: (1) the inside surface of the capillary electrode, (2) the interface away from the tip of the cone, and (3) the interface at the tip of the cone. In region (1), $V \approx PV_s$=const. In region (2) $E_\phi(r,\phi_c) \approx 0$ and $E_r(r,\phi_c)$ is given by Eqn. (1.8). In region (3), E_r and E_ϕ depend on the details of the droplet formation and charging processes, which are described in Section 1.3.2 for the case of electrolytic solutions.

The r-component of the electric field gives rise to the conduction current

$$I_{\text{cond}}(r) = \sigma \int_A E_r(r,\phi)\text{dA}, \tag{1.10}$$

[4] It is assumed that the diffuse layer of charge at the interface is very thin compared to the overall cone dimensions.

where σ is the specific electrical conductivity of the bulk fluid and A is the cross sectional area (normal to the r-direction) inside the cone. Equation (1.10) assumes that the space charge in the bulk liquid is zero and that positive and negative ions have the same mobility so that no current is created by liquid motions inside the cone [12]. The total current is

$$I_{\text{total}} = I_{\text{sur}}(r) + I_{\text{cond}}(r).$$

Note that in a steady electrospray, I_{total} is neither a function of time nor of r. This follows from a balance on charge in a spherical shell control volume.

Rather than solving Eqns. (1.9) and (1.10) to compute the conduction current, we assume that $E_r(r,\phi)$ is geometrically self-similar such that $E_r = E_r(r,\phi_c)g(\phi)U(\phi_f/\phi_b)$, where $g(\phi_c) = 1$, $U(\phi_f/\phi_b) = \left\{ \begin{array}{ll} 0 & \text{for } \phi_b/\phi_f > 1 \\ 1 & \text{for } \phi_b/\phi_f \leq 1 \end{array} \right\}$, ϕ_b is the boundary layer angle, and ϕ_f is the boundary layer angle when the flow changes from a boundary layer flow to a jet flow (see Fig. refsc). The conduction current is thus estimated to be

$$\begin{aligned} I_{\text{cond}}(r) &\approx \int_{\theta=0}^{2\pi}\int_{\phi=0}^{\phi_c} \sigma E_r(r,\phi_c)g(\phi)U(\phi_f/\phi_b) r\sin(\phi) r d\phi \\ &= E_r(r,\phi_c)U(\phi_f/\phi_b)2\pi r^2\sigma \int_{\phi=0}^{\phi_c} g(\phi)\sin(\phi)d\phi \\ &= E_r(r,\phi_c)2\pi r^2\sigma A_1, \end{aligned} \tag{1.11}$$

where $A_1 = U(\phi_f/\phi_b)\int_{\phi=0}^{\phi_c} g(\phi)\sin(\phi)\mathrm{d}\phi = \text{const}$. The parameter A_1, called the "electric field penetration efficiency," will be found empirically. The effect of the step function $U(\phi_f/\phi_b)$ is to disallow conduction current except near the tip of the cone. This is a reasonable approximation because the conduction current is expected to be greatest in the region where droplets are formed and charged according to the scheme described in Section 1.3.2.

The system couples to the liquid motion through the quantity $u_r(r, \phi_c)$ appearing in Eqn. (1.6). Thus equations of motion for the liquid are needed. Conservation of mass requires [14]

$$\frac{\partial \rho}{\partial t} + \frac{1}{r^2}\frac{\partial}{\partial r}(\rho r^2 u_r) + \frac{1}{r\sin\phi}\frac{\partial}{\partial \phi}(\rho u_\phi \sin\phi) + \frac{1}{r\sin\phi}\frac{\partial}{\partial \theta}(\rho u_\theta) = 0, \tag{1.12}$$

where ρ is the liquid density, and u_r, u_ϕ and u_θ are the r, ϕ, and θ-components of the liquid velocity, respectively.

Conservation of r-momentum requires (for constant ρ and μ)

$$\rho(\frac{\partial u_r}{\partial t} + u_r\frac{\partial u_r}{\partial r} + \frac{u_\phi}{r}\frac{\partial u_r}{\partial \phi} + \frac{u_\theta}{r\sin\phi}\frac{\partial u_r}{\partial \theta} - \frac{u_\phi^2 + u_\theta^2}{r}) =$$
$$-\frac{\partial p}{\partial r} + \mu[\frac{1}{r^2}\frac{\partial^2}{\partial r^2}(r^2 u_r) + \frac{1}{r^2\sin\phi}\frac{\partial}{\partial \phi}(\sin\phi\frac{\partial u_r}{\partial \phi}) + \frac{1}{r^2\sin^2\phi}\frac{\partial^2 u_r}{\partial \theta^2}] + \rho g_r, \tag{1.13}$$

where μ is the absolute viscosity, p is the pressure, and g_r is the r-component of the body force. We shall assume a steady flow with no azimuthal variations, and no body force.

Defining the dimensionless variables $\hat{r} = r/L$, $\hat{u}_r = u_r/U$, $\hat{u}_\phi = u_\phi/U$, $\hat{p} = p/\rho U^2$, and $\hat{t} = t/(L/U)$, Eqns. (1.12) and (1.13) become

$$\frac{1}{\hat{r}^2}\frac{\partial}{\partial \hat{r}}(\hat{r}^2\hat{u}_r) + \frac{1}{\hat{r}\sin\phi}\frac{\partial}{\partial \phi}(\hat{u}_\phi\sin\phi) = 0 \tag{1.14}$$

and

$$\hat{u}_r\frac{\partial \hat{u}_r}{\partial \hat{r}} + \frac{\hat{u}_\phi}{\hat{r}}\frac{\partial \hat{u}_r}{\partial \phi} - \frac{\hat{u}_\phi^2}{\hat{r}} = -\frac{\partial \hat{p}}{\partial \hat{r}} + \frac{1}{\mathrm{Re}}[\frac{1}{\hat{r}^2}\frac{\partial^2}{\partial \hat{r}^2}(\hat{r}^2\hat{u}_r^2) + \frac{1}{\hat{r}^2\sin\phi}\frac{\partial}{\partial \phi}(\sin\phi\frac{\partial \hat{u}_r}{\partial \phi})], \tag{1.15}$$

where $L = r_{\mathrm{cap}}$, U is the boundary layer speed scale, and $\mathrm{Re} = \rho UL/\mu$.

We shall assume that a thin boundary layer exists near the surface of the cone and scale the equations accordingly. This assumption will be checked *a posteriori*. In the boundary layer flow, the flow is confined to a narrow region near the surface of

the cone, so Eqn. (1.14) becomes

$$\frac{1}{\hat{r}^2}\frac{\partial}{\partial \hat{r}}(\hat{r}\hat{u}_r) + \frac{\partial}{\partial \phi}(\hat{u}_\phi) = 0. \tag{1.16}$$

If the boundary layer thickness is δ, then $\frac{\partial \hat{u}_\phi}{\partial \phi} \sim \frac{L}{\delta}\hat{u}_\phi$. Equation (1.16) then gives $\hat{u}_r \sim \frac{L}{\delta}\hat{u}_\phi$. Using this result in Eqn. (1.15) and balancing the viscous and inertial terms gives $\mathrm{Re} \sim (L/\delta)^2$. Typically in the spraying of electrolytic solutions, $\rho \sim 10^3\ \mathrm{kg\,m^{-3}}$, $U \sim 1\ \mathrm{m\,s^{-1}}$, $L \sim 10^{-3}$ m, and $\mu \sim 10^{-3}\ \mathrm{kg\,m^{-1}\,s^{-1}}$ so $\mathrm{Re} \sim 10^4$ which implies $\delta/L \sim 1/100$. Retaining only the largest terms in Eqn. (1.15) gives

$$\hat{u}_r\frac{\partial \hat{u}_r}{\partial \hat{r}} + \frac{\hat{u}_\phi}{\hat{r}}\frac{\partial \hat{u}_r}{\partial \phi} + \frac{\partial \hat{p}}{\partial \hat{r}} - \frac{1}{\mathrm{Re}}\frac{1}{\hat{r}^2}\frac{\partial^2 \hat{u}_r}{\partial \phi^2} = 0. \tag{1.17}$$

The pressure gradient arises due to the imbalance between the surface tension pressure $2T\cot\phi_c/r$ and the electric field pressure $\epsilon_0 E_\phi^2/2$ at locations away from the base of the cone. At the base of the cone the two effects are nearly balanced. The normal component of the electric field is bounded near the tip of the cone due to the charged jet [15]. Assuming that the surface tension dominates the pressure near the tip, the pressure gradient can be approximated as

$$\frac{\partial \hat{p}}{\partial \hat{r}} \approx -\frac{\hat{T}\cot\phi_c}{\hat{r}^2}, \tag{1.18}$$

where $\hat{T} = T/\rho U^2 L$. Combining this result with Eqns. (1.15) and (1.16) gives

$$\frac{\partial \hat{u}_r^2}{\partial \hat{r}} + \frac{1}{\hat{r}}\frac{\partial \hat{u}_r\hat{u}_\phi}{\partial \phi} + \frac{2}{\hat{r}}\hat{u}_r^2 - \frac{1}{\hat{r}\mathrm{Re}}\frac{\partial^2 \hat{u}_r}{\partial \phi^2} - \frac{\hat{T}\cot\phi_c}{\hat{r}^2} = 0. \tag{1.19}$$

Multiplying by $\hat{r}$ and integrating across the boundary layer gives

$$-\int_{\phi_b}^{\phi_c}\frac{\hat{T}\cot(\phi_c)}{\hat{r}}\mathrm{d}\phi + \int_{\phi_b}^{\phi_c}[\hat{r}\frac{\partial}{\partial \hat{r}}(\hat{u}_r^2) + 2\hat{u}_r^2 - \frac{1}{\mathrm{Re}}\frac{\partial^2 \hat{u}_r}{\partial \phi^2}]\mathrm{d}\phi = -\hat{u}_\phi(\phi_c)\hat{u}_r(\phi_c) + \hat{u}_\phi(\phi_b)\hat{u}_r(\phi_b), \tag{1.20}$$

where ϕ_b is the boundary layer edge (Fig. 1.2). The right-hand-side is zero since $\hat{u}_\phi(r, \phi_c)$ and $\hat{u}_r(r, \phi_b)$ are zero.

The velocity profile is approximated by

$$u_r(r, \phi) = \frac{\tau_{\phi_c} r}{2\mu} \frac{[\phi - \phi_b(r)]^2}{\phi_c - \phi_b(r)}. \tag{1.21}$$

This profile enforces zero velocity and zero stress at the boundary layer edge and the stress matching condition

$$\frac{\mu}{r} \frac{\partial u_r}{\partial \phi}(\phi_c) = \tau_{\phi_c}. \tag{1.22}$$

Using Eqn. (1.21) in Eqns. (1.5) and (1.6) leads to

$$I_{\text{sur}}(r) = I_{\text{total}} \left\{ 1 + \frac{\sigma r (1 - \cos\phi_c) A_1}{\epsilon^2 E_\phi^2(r, \phi_c) \sin(\phi_c) [e n_i / \epsilon_o E_\phi(r, \phi_c) + r(\phi_c - \phi_b(r))/2\mu]} \right\}^{-1} \tag{1.23}$$

and

$$\tau_{\phi_c} = \frac{I_{\text{sur}}(r)}{2\pi \epsilon_o E_\phi(r, \phi_c) r \sin\phi_c [e n_i / \epsilon_o E_\phi(r, \phi_c) + r(\phi_c - \phi_b(r))/2\mu]}. \tag{1.24}$$

Substituting Eqns. (1.21), (1.23), and (1.24) in Eqn. (1.20) leads to a nonlinear differential equation for $\phi_b(r)$. As an approximation to simplify the algebra, we take $E_\phi(r, \phi_c)$ to be constant in r, equal to the value given by Eqn. (1.2) multiplied by the overpotential ratio P. This is a reasonable level of approximation because the presence of the jet and charged droplets are not accounted for in Eqn. (1.2). The algebra is involved and was solved using the symbolic manipulator *Mathematica*. The result is the following governing equation for $\phi_b(r)$:

$$\frac{\mathrm{d}\phi_b}{\mathrm{d}r} = \frac{\Phi_3 + \Phi_1 \Phi_4}{1 - \Phi_2 \Phi_4}. \tag{1.25}$$

where

$$\Phi_1 = -\frac{b_1}{b_2(b_3 + b_4 + b_5 + b_6 + b_7)} - \frac{b_8(b_9 + b_{10} + b_{11} + b_{12})}{\pi r (b_{14} + b_{15} + b_{16} + b_{17} + b_{18})^2}$$

b_1	$\epsilon_o E_\phi(r,\phi_c) f I_{\text{total}} \mu$	b_2	πr^2
b_3	$2A_1 f \mu r \sigma$	b_4	$-2A_1 f \mu r \sigma \cos(\phi_c)$
b_5	$2e\epsilon_o E_\phi(r,\phi_c)\mu \sin(\phi_c) n_i$	b_6	$\epsilon_o^2 E_\phi^2(r,\phi_c) f \phi_c r \sin(\phi_c)$
b_7	$-\epsilon_o^2 E_\phi^2(r,\phi_c) f r \sin(\phi_c)\phi_b$	b_8	$\epsilon_o E_\phi(r,\phi_c) f I_{\text{total}} \mu$
b_9	$2A_1 f \mu \sigma$	b_{10}	$-2A_1 f \mu \sigma \cos(\phi_c)$
b_{11}	$\epsilon_o^2 E_\phi^2(r,\phi_c) f \phi_c \sin(\phi_c)$	b_{12}	$-\epsilon_o^2 E_\phi^2(r,\phi_c) f \sin(\phi_c)\phi_b$
b_{13}	$-\epsilon_o^2 E_\phi^2(r,\phi_c) f r \sin(\phi_c)$	b_{14}	$2A_1 f \mu r \sigma$
b_{15}	$-2A_1 f \mu r \sigma \cos(\phi_c)$	b_{16}	$2e\epsilon_o E_\phi(r,\phi_c)\mu \sin(\phi_c) n_i$
b_{17}	$\epsilon_o^2 E_\phi^2(r,\phi_c) f \phi_c r \sin\phi_c$	b_{18}	$-\epsilon_o^2 E_\phi^2(r,\phi_c) f r \sin(\phi_c)\phi_b$
b_{19}	$-10\mu^2 \phi_c T$	b_{20}	$10\mu^2 T \phi_b$
b_{21}	$-10\mu^2 r \tan(\phi_c)\tau_{\phi_c}$	b_{22}	$2\phi_c^3 r^3 \rho \tan(\phi_c)\tau_{\phi_c}^2$
b_{23}	$-6\phi_c^2 r^3 \rho \tan(\phi_c)\phi_b \tau_{\phi_c}^2$	b_{24}	$6\phi_c r^3 \rho \tan(\phi_c)\phi_b^2 \tau_{\phi_c}^2$
b_{25}	$-2r^3 \rho \tan(\phi_c)\phi_b^3 \tau_{\phi_c}^2$	b_{26}	$\phi_c^3 r^4 \rho \tan(\phi_c)\tau_{\phi_c}$
b_{27}	$-3\phi_c^2 r^4 \rho \tan(\phi_c)\phi_b \tau_{\phi_c}$	b_{28}	$3\phi_c r^4 \rho \tan(\phi_c)\phi_b^2 \tau_{\phi_c}$
b_{29}	$-r^4 \rho \tan(\phi_c)\phi_b^3 \tau_{\phi_c}$	b_{30}	$3r^4 \rho \tan(\phi_c)(\phi_c - \phi_b)^2 \tau {\phi_c}^2$

Table 1.1: Terms in the boundary layer growth equation.

$$\Phi_2 = -\frac{b_8 b_{13}}{\pi r (b_{14} + b_{15} + b_{16} + b_{17} + b_{18})^2}$$

$$\Phi_3 = \frac{2(b_{19} + b_{20} + b_{21} + b_{22} + b_{23} + b_{24} + b_{25})}{b_{30}}$$

$$\Phi_4 = \frac{2(b_{26} + b_{27} + b_{28} + b_{29})}{b_{30}}.$$

The values of b_i are given in Table 1.1.

The initial condition for Eqn. (1.25) is $\phi_b(r_{\text{cap}}) = \phi_c$, where r_{cap} is the value of r at the electrode edge (Fig. 1.2). There is a singular point at $r = r_{\text{cap}}$ where $\mathrm{d}\phi_b/\mathrm{d}r$ is unbounded. Therefore the initial condition used for numerical integration is $\phi_b(r = r_{\text{cap}}) = \alpha\phi_c$ where $1 - \alpha << 1$.

As the boundary layer grows, it depletes liquid from the inner part of the cone. If A_b and A_i are the cross-sectional areas of the boundary layer and inner flows, respectively, then conservation of mass dictates that $\Delta(\rho \bar{u_b} A_b) = \Delta(\rho \bar{u_i} A_i)$ where $\bar{u_b}$ and $\bar{u_i}$ are the average velocities in the boundary layer and inner flows, respectively. (The speed in the inner flow is assumed to be small compared to the speed in the boundary layer flow so that Eqn. (1.21) is valid.) Thus, $\Delta\bar{u_i} = \Delta\bar{u_b} A_b / A_i$, so a

change in average velocity in the boundary layer flow causes a change in average velocity in the inner flow which increases as A_b/A_i increases. But there is no stress to produce the associated change in momentum in the inner flow, which is of the order $\rho A_i \bar{u}_i \Delta\bar{u}_i$. Therefore, when $A_b \sim A_i$ the flow no longer behaves as a boundary layer flow. Hence, Eqn. (1.25) is integrated until the arbitrary stopping condition $A_b = A_i$, which corresponds to $\phi_f = \cos^{-1}[1/2 - \cos(\phi_c)/2]$. At this stage the flow in the cone is approaching full development and begins to accelerate as a whole.

1.3.1 Acceleration of the Jet

The momentum flux resulting from the boundary layer flow is

$$P_m = 2\pi\rho r^2 \int_{\phi_f}^{\phi_c} u_r^2 \sin(\phi) \mathrm{d}\phi \tag{1.26}$$

and the mass flow rate is

$$\dot{m} = 2\pi\rho r^2 \int_{\phi_f}^{\phi_c} u_r \sin(\phi) \mathrm{d}\phi. \tag{1.27}$$

Using Eqn. (1.21) with ϕ_b replaced with ϕ_f, P_m is found to be

$$\begin{aligned}
P_m = & -\tfrac{\pi r^4 \tau_{\phi_c}^2}{2\mu^2(\phi_c-\phi_f)^2}(24\cos\phi_c - 12\phi_c^2\cos\phi_c \\
& +\phi_c^4\cos\phi_c + 24\phi_c\phi_f\cos\phi_c \\
& -4\phi_c^3\phi_f\cos\phi_c - 12\phi_f^2\cos\phi_c \\
& +6\phi_c^2\phi_f^2\cos\phi_c - 4\phi_c\phi_f^3\cos\phi_c + \\
& +\phi_f^4\cos\phi_c - 24\cos\phi_f + 24\phi_c\sin\phi_c - 4\phi_c^3\sin\phi_c - 24\phi_f\sin\phi_c + \\
& +12\phi_c^2\phi_f\sin\phi_c - 12\phi_c\phi_f^2\sin\phi_c + 4\phi_f^3)\sin\phi_c,
\end{aligned} \tag{1.28}$$

and $\dot{m}$ is

$$\dot{m} = -\frac{\rho\pi r^3 \tau_{\phi_c}}{\mu(\phi_c - \phi_f)}(-2\cos\phi_c + \phi_c^2\cos\phi_c - 2\phi_c\phi_f\cos\phi_c \quad + \\ \phi_f^2\cos\phi_c + 2\cos\phi_f - 2\phi_c\sin\phi_c + 2\phi_f\sin\phi_c). \tag{1.29}$$

Since the flow is accelerating as a whole, we approximate that the z-component of the velocity is uniform across the jet, i.e., $u_z \neq u_z(r)$, where we now use cylindrical coordinates (Fig. 1.2). The initial jet velocity is $u_{z_o} = P_{\rm m}/\dot{m}$, and the initial jet radius is $r_{\rm jet_o} = (\dot{m}/\rho u_{z_o})^{1/2}$. Following a development similar to that used for the boundary layer, the surface shear stress on the jet is found to be

$$\tau = \frac{\epsilon_o E_{\rm p} f}{e}(u_{\rm c} - u_z) = \epsilon_o E_{\rm p} E_z, \tag{1.30}$$

where $E_{\rm p}$ and E_z are the perdendicular and parallel components of the electric field, respectively, u_c is the charge velocity, u_z is the z-component of the liquid velocity and $r_{\rm jet}$ is the jet radius. The magnitude of $E_{\rm p}$ is found by approximating the geometry as a semi-infinite line of charge perpendicular to a flat plate [16]. Using the result from Eqn. (1.2),

$$E_{\rm p} = A_2 E_\phi(r, \phi_c)\frac{r_{\rm c}}{r_{\rm jet}}\frac{\log(4h/r_{\rm c})}{\log(4h/r_{\rm jet})}. \tag{1.31}$$

The "jet electric field factor," A_2, is introduced to correct any errors arising due to the approximate geometry.

The surface current is $I_{\rm sur} = 2\pi r_{\rm jet}\epsilon_o E_p u_c$ and the conduction current is $\pi r_{\rm jet}^2 \sigma E_z$, where it is assumed that the z-component of the electric field is uniform across the jet. Thus we find

$$I_{\rm sur} = \frac{I_{\rm total} + f\pi r_{\rm jet}^2 \sigma u_z / e n_{\rm i}}{1 + r_{\rm jet}\sigma f / 2 e n_{\rm i}\epsilon_{\rm o} E_{\rm p}(r_{\rm jet})} \tag{1.32}$$

and

$$\tau = \frac{\epsilon_o E_p}{e}\left(\frac{I_{sur}}{2\pi r_{jet}\epsilon_o E_p} - u_z\right). \tag{1.33}$$

From a momentum balance on the accelerating jet, we find

$$\frac{du_z}{dz} = \frac{2\pi r_{jet}\tau}{\dot{m}}, \tag{1.34}$$

where $u_z(z=0) = u_{z_o}$ and $r_{jet}(z=0) = r_{jet_o}$. The jet accelerates until it reaches a terminal speed. At this speed the conduction current is zero and the induced surface charge moves at the same speed as the liquid.

1.3.2 Jet Break-up and Droplet Charging

The jet breaks up into droplets due to an instability driven by surface tension and electric field forces on the jet surface. Saville [17] derived expressons for the rate of growth of various axisymmetric and non-axisymmetric perturbations on the surface of a liquid cylinder subjected to surface tension and electric field forces including the effects of viscosity and inertia. We shall use a general finding from Saville's work that the wavelength which ultimately divides the jet longitudinally ranges roughly from 1 to 1.4 times the circumference of the jet. Thus, for purposes of this model we shall assume that the droplet radius is twice the jet radius, i.e., $r_d = 2r_{jet}$. In making this assumption we forfeit the ability to predict the droplet size distribution, but trends of droplet size should be useful.

The droplets carry a charge corresponding to the total current flowing in the system. The steady-state charge per drop is

$$q_{d_{steady}} = 9\sqrt{2}\pi\epsilon_o r_d^2 E_p(r_{jet}) = CV, \tag{1.35}$$

where C is the droplet capacitance and V is the applied voltage. The steady charge is not reached instantaneously, however, because there is a resistance to the flow of

charge through the jet and into the droplet. The system forms a simple resistance capacitance circuit so the droplet charges approximately as

$$q_{\rm d} = [1 - \exp(\frac{-A_3 t_{\rm f} \sigma}{\epsilon})] q_{\rm d_{steady}}, \tag{1.36}$$

where $t_{\rm f}$ is the droplet formation time (equal to the charging time) and A_3 is an empirical constant called the "geometric charging factor." In actuality the droplet charge is influenced by the charged droplets formed ahead of it, but the details of how the droplet capacitance varies with jet diameter and length have been neglected in Eqn. (1.37). As the σ and $t_{\rm f}$ increase, the droplet charge reaches a larger fraction of $q_{\rm steady}$.

The maximum charge a droplet can carry, $q_{\rm limit}$, is given by the Rayleigh charge limit [18],

$$q_{\rm limit} = (64\pi^2 \epsilon_0 T r_{\rm d}^3)^{1/2}. \tag{1.37}$$

The droplet is unstable to perturbations in its surface shape for charges greater than $q_{\rm limit}$. The Rayleigh charge limit fraction, Z, is defined by $Z = q_{\rm d}/q_{\rm limit}$.

The volume specific charge, ξ, is defined by $\xi = q_{\rm d}/v_{\rm d}$ where $v_{\rm d}$ is the droplet volume.

We now have the necessary equations to solve for the mass flow rate, electrical current, jet radius, and droplet size for the steady electrospray. A guess for $I_{\rm total}$ is made and Eqn. (1.25) is integrated until $\phi_{\rm b}$ reaches $\phi_{\rm f}$. Then Eqn. (1.35) is integrated until the jet reaches a steady speed and breaks up into droplets due to the longitudinal instability. The droplets carry a current equal to $I'_{\rm total} = q_d/t_f$. When $I'_{\rm total} = I_{\rm total}$ the solution is obtained. In practice the system is solved by a numerical bisection method to determine the current [19].

concentration (g/l)	conductivity (mhos/m)
0.6179	0.00684
0.8491	0.0090
2.339	0.0202
5.284	0.0376
6.041	0.0429
8.609	0.0568
9.074	0.0588
17.95	0.1030
37.43	0.195
75.82	0.356

Table 1.2: Specific electrical conductivity of NaI in n-propyl alcohol at 25°C.

1.4 Experiment

Solutions of anhydrous NaI [5] in n-propyl alcohol [6] were selected for experimental validation studies because its surface tension is low enough to allow spraying at potentials below the breakdown potentials in nitrogen and air. This eliminates the need for a surfactant that is generally required to operate the electrospray with aqueous solutions. Also, sodium iodide is sufficiently soluble in n-propyl alcohol to allow testing of a wide range of concentrations [20]. The specific electrical conductivity was measured using an Omega model CDH-70 conductivity meter. [7] Table 1.2 shows the results, corrected by the probe to 25°C.

Experiments were performed using the atomizer shown in Fig. 1.4 (h=10.3 mm and r_c=0.826 mm). The experimental system illustrated in Fig. 1.5 allowed measurement of the volumetric flow rate, total electrical current, and size distribution of dried solute particles. Solution was supplied to the atomizer by either a syringe pump (Sage Instruments Model 355) or a gravity feed reservoir with pipette and air-filled

[5] EM Science, extra pure grade
[6] Fisher Scientific
[7] Omega Engineering, Inc.

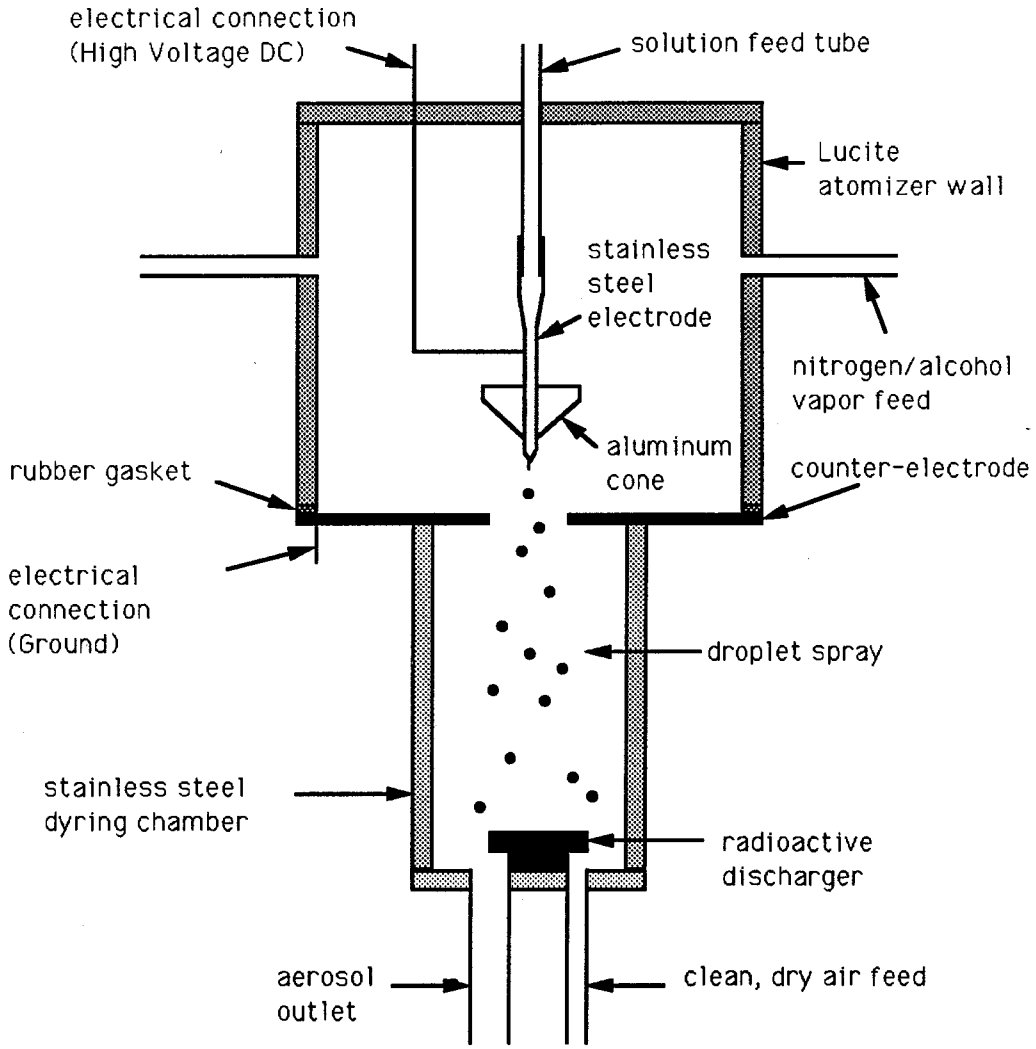

Figure 1.4: Schematic of the electrospray atomizer.

syringe to measure the flow rate by timing the passage of a small air bubble through a known volume [21]. The liquid was carried by plastic tubing into the atomizer. A stainless steel tube with a wire attached was placed at the end of the tube to become the electrode. The electrode was connected to a Spellman WRM15P1500D power supply. The range of potentials at which the Taylor cone could be established was enhanced by mounting a 25 mm diameter aluminum cone with semi-vertex angle 49.3° (providing an extension of the Taylor cone geometry) on the electrode. Flowrates were increased approximately four-fold when this cone was added. The aluminum cone was mounted 2.5 mm away from the end of the electrode to prevent liquid from moving up the sides due to capillarity. The atomizer sides were constructed of flat, clear plexiglass so that the cone and spray could be observed using a Questar model QM1 long range microscope placed 0.76 m away. An aluminum plate mounted 10 mm from the tip with a 10 mm diameter hole and grounded through an ammeter sensitive to ±10 nA (Hewlett-Packard model 3465A) formed the bottom of the atomizer and the counter-electrode. A chamber on the downstream side of the counter-electrode was supplied with clean, dry air (8.7 to 10.6 lpm) to reduce the solvent partial pressure to facilitate the production of dry solute particles.

When spraying particularly concentrated electrolytic solutions, the solute gradually precipitated on the capillary tip. To prevent this, the space between the capillary and the counter-electrode was purged with nitrogen that had been saturated with solvent vapor by passing it through a bubbler. The flow was typically 90 cm^3 $min.^{-1}$. A filter was used to remove any particles created in the bubbler. Nitrogen was used as the carrier gas to prevent ignition of solvent vapors in the event of sparkover.

Corona discharge occurring in gases surrounding the tip of the Taylor cone have

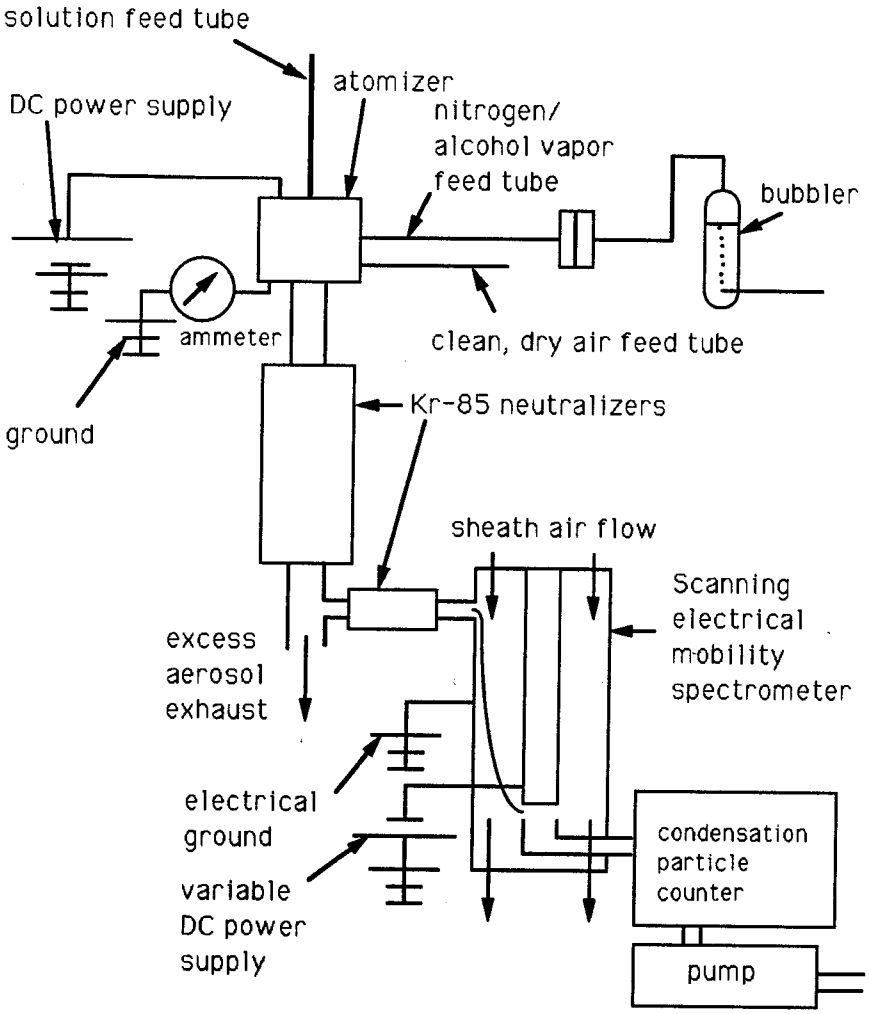

Figure 1.5: Schematic of the overall experimental apparatus.

been observed when operating at very high potentials [22]. Such phenomena obviously complicate the situation and were strictly avoided in the experiments reported here.

Because the droplets were highly charged, their electrical mobility was high. The strong electric fields in the vicinity of the hole in the counter-electrode plate resulted in substantial droplet deposition. To increase the throughput efficiency, a Nuclespot[8] static discharger was placed in a stainless steel chamber [23]. The Nuclespot has a 5 mCi source of polonium-210 (half-life 138.4 days) which emits 5.407 MeV α-particles that ionize the gas in the drying chamber, thereby neutralizing the charge on the electrosprayed droplets. This design increased the overall throughput efficiency by one to two orders of magnitude as described below.

The ionized gas in the drying chamber resulted in some flow of current between the electrode and counter-electrode when an electric field was applied without liquid flow. The measured currents indicated that the ions were probably intercepted by droplets when liquid was being sprayed.

To establish a spray, the potential on the counter-electrode was adjusted until a Taylor cone formed, V_s. Then the potential was increased to 1.1 to 1.4 times V_s, i.e., $P = 1.1$ to 1.4, to establish a steady spray. In order to make quantitative comparisons between different solutions or potentials it is necessary to keep the cone angle constant. Thus to measure the volumetric flow rate and current for a given solution, we adjusted the feed rate of liquid to the atomizer until cone angle of 40 $\pm$ 2° was obtained as observed through the long range microscope using a reticle eyepiece. The flow rate and current were then recorded.

The aerosol flowed into a TSI model 3054 Krypton-85 bipolar charger and 1.6 lpm

[8]Static Control Products, NRD, Inc., Grand Island, New York

Parameter	Value
permittivity (F m^{-1})	1.8×10^{-10}
density (kg m^{-3})	803.5
absolute viscosity (kg $m^{-1}s^{-1}$)	0.00198
surface tension (N m^{-1})	0.0238
ion drag coefficient (N s m^{-1})	$2.373x10^{-12}$
spacing (m)	0.065

Table 1.3: Properties of sodium iodide in n-propyl alcohol

was drawn through a TSI model 3077 bipolar charger and subsequently into a Scanning Electrical Mobility Spectrometer (based on the TSI Model 3071 Differential Mobility Classifier and Model 3761 Condensation Particle Counter) for size distribution analysis [24]. The remainder of the aerosol was ejected into the laboratory exhaust system.

1.5 Results

The solution properties used in the numerical simulations are given in Table 1.3 [25] [13]. Some values are approximate. For example, no variations of surface tension, density, or viscosity with solute concentration are considered due to a lack of data. The ionic friction factor was calculated from [14]

$$f = kT/D = 4\pi R_A \mu, \tag{1.38}$$

where k is Boltzmann's constant, D is the ion diffusivity, and R_A is the ion radius (0.95 Angstroms for Na^+ [26]) [9]

The volumetric flow rate, total electrical current, volume-mean dried particle size, volume-mean droplet size, specific charge, and Rayleigh charge limit fraction are plotted as functions of specific electrical conductivity in Figs. 1.6-1.11. The droplet size

[9]Empirical alternatives to Eqn. (1.39) are available which attempt to account for solute-solvent interactions and relative size effects between solute and solvent molecules [27]. These, however, are not necessarily more accurate for this system.

was computed assuming that fully dense NaI particles formed upon solvent evaporation ($\rho = 3667$ kg m^{-3}). Then the volume-mean particle size measured using SEMS was multiplied by the appropriate factor to account for the solvent originally present when the droplet formed.

Three potentials were used, giving three values of P ($V_s = +5590$ volts). The values of A_1, A_2, and A_3 were found by fitting the volumetric flow rate, volume-mean droplet size, and total electrical current, respectively, at one value of the specific electrical conductivity. The model was then used to compute the curves shown in Figs. 1.6 through 1.11.

The largest experimental error in these experiments arose from the difficulty of setting the cone to a predetermined angle by adjusting the feed rate of liquid. The uncertainty in the volumetric flow rate was about $\pm 10\%$. The magnitude of errors for current and droplet size data were similar.

The volumetric flow rate, volume-mean dried particle size, volume-mean droplet size, and fraction of the Rayleigh charge limit all decreased with increasing specific electrical conductivity. The total electrical current and specific charge increased with increasing specific electrical conductivity. The model predicted these trends except for the Rayleigh charge limit fraction. The predicted dependence of volumetric flow rate on specific electrical conductivity was stronger than observed. The predicted total electrical current and particle and droplet sizes agree well with the measurements. The Rayleigh charge limit fraction was predicted to increase with increasing specific electrical conductivity, but the data shows an opposite trend. We attribute this discrepancy to the overly strong volumetric flow rate dependence suggested by the model. The model gives a lower flow rate than measured at high conductivities. This

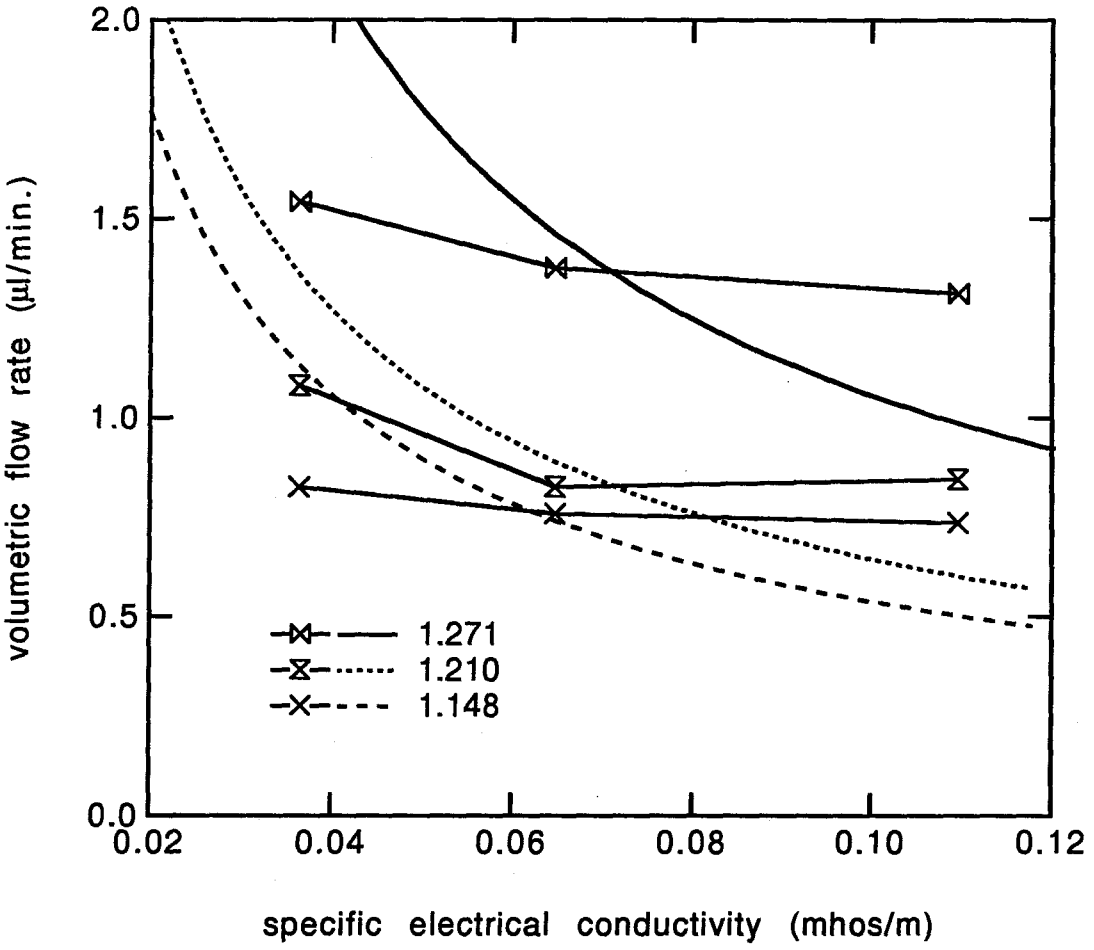

Figure 1.6: Volumetric flow rate of liquid versus specific electrical conductivity for three values of P.

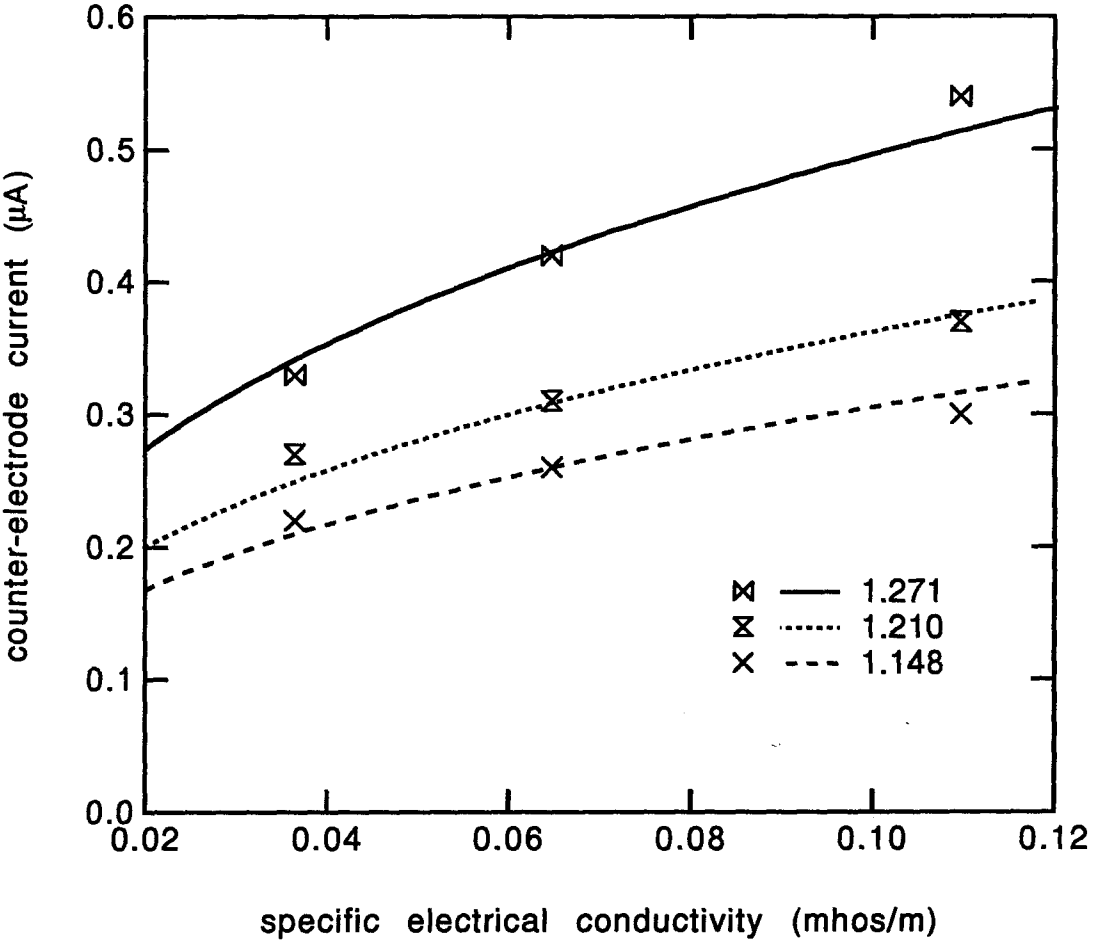

Figure 1.7: Total electrical current versus specific electrical conductivity for three values of P.

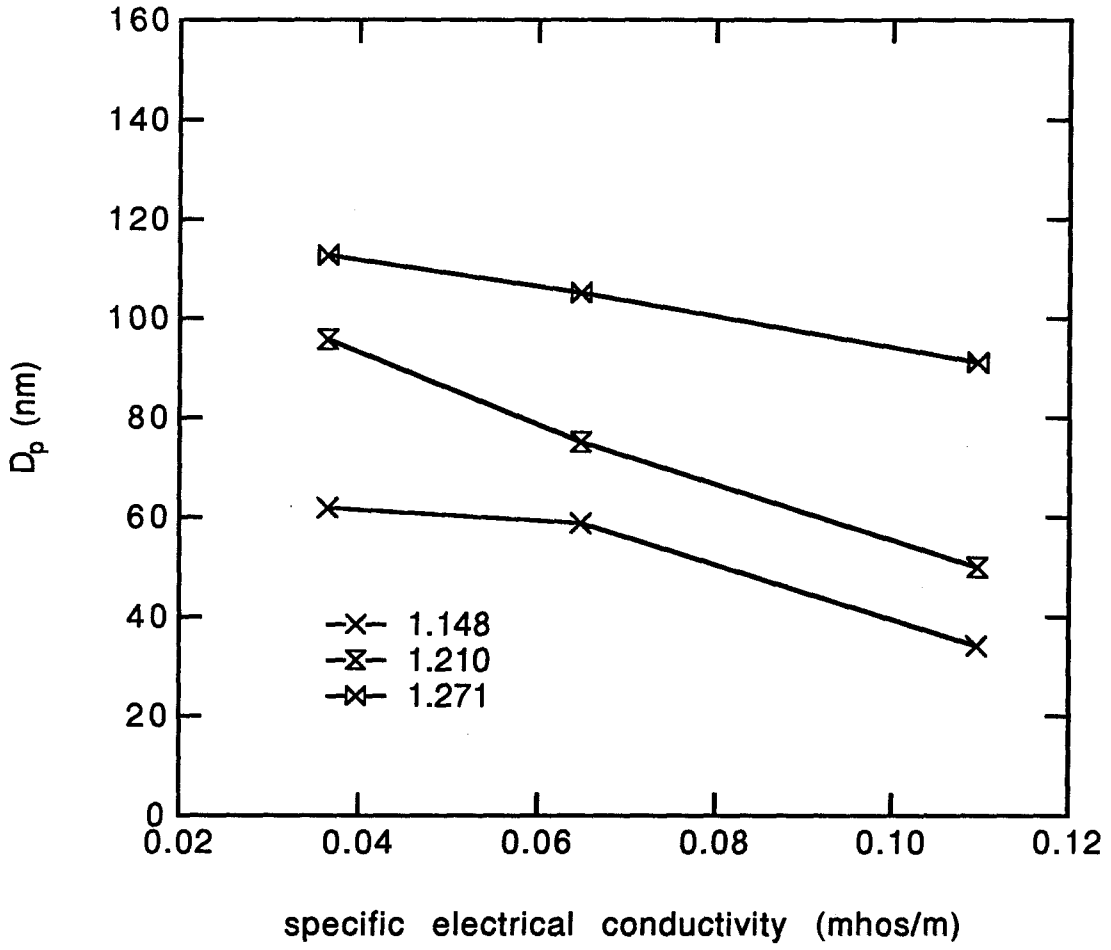

Figure 1.8: Volume-mean dried particle size versus specific electrical conductivity for three values of P.

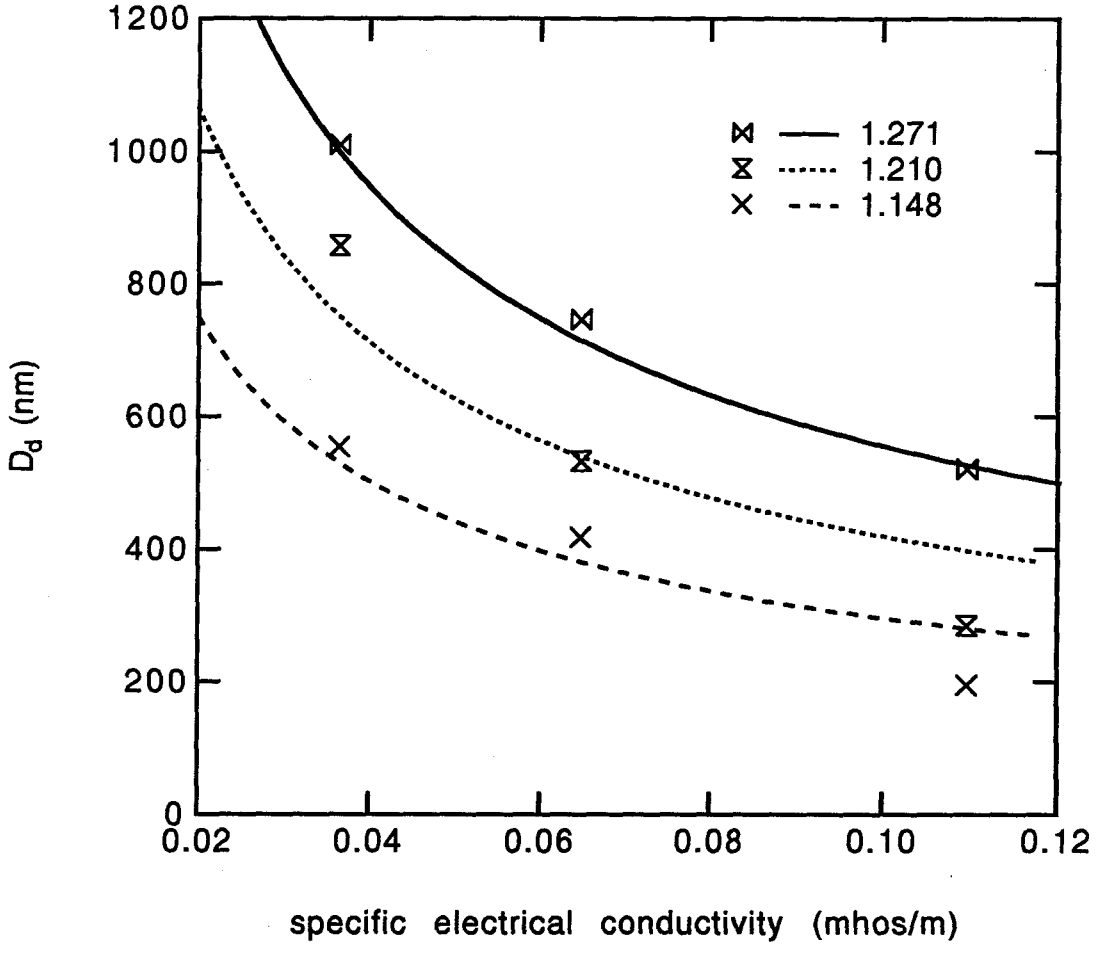

Figure 1.9: Volume-mean droplet size versus specific electrical conductivity for three values of P.

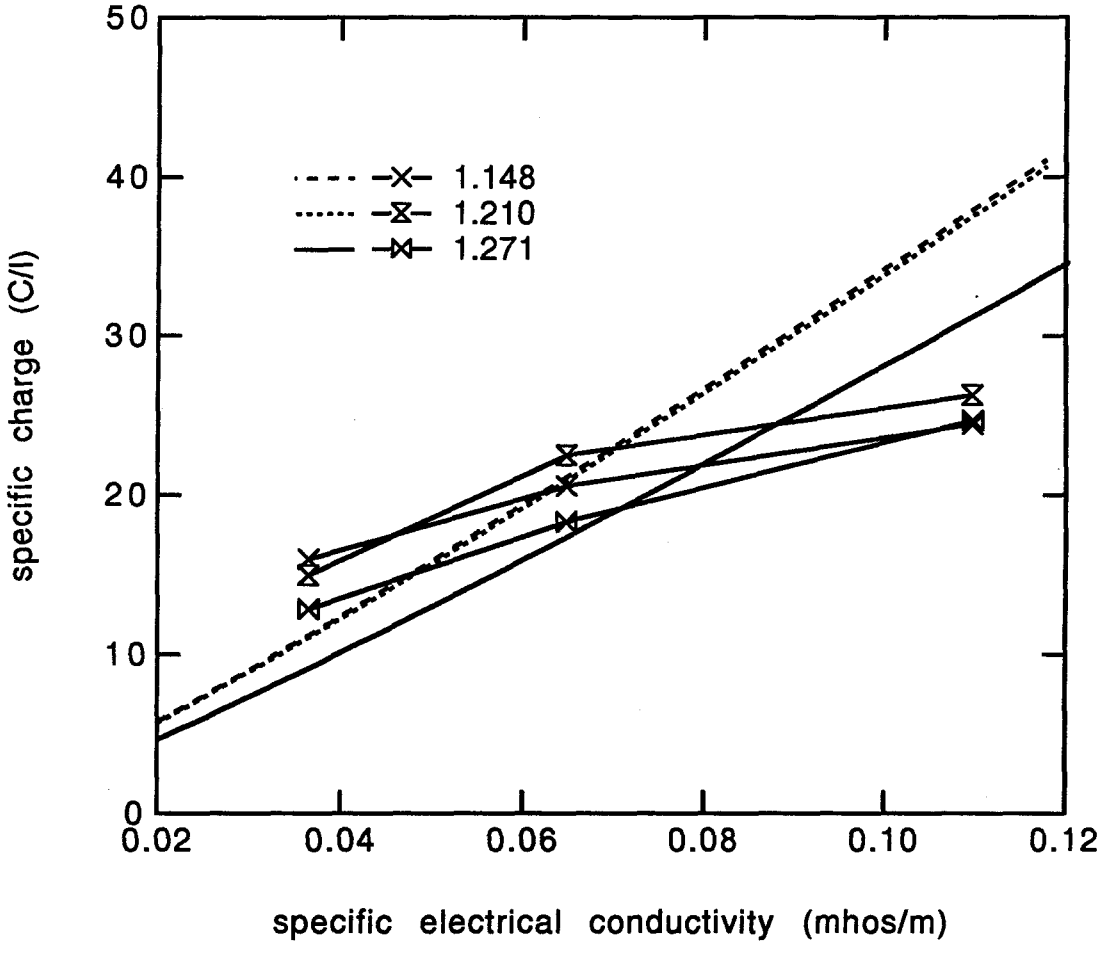

Figure 1.10: Specific charge versus specific electrical conductivity for three values of P.

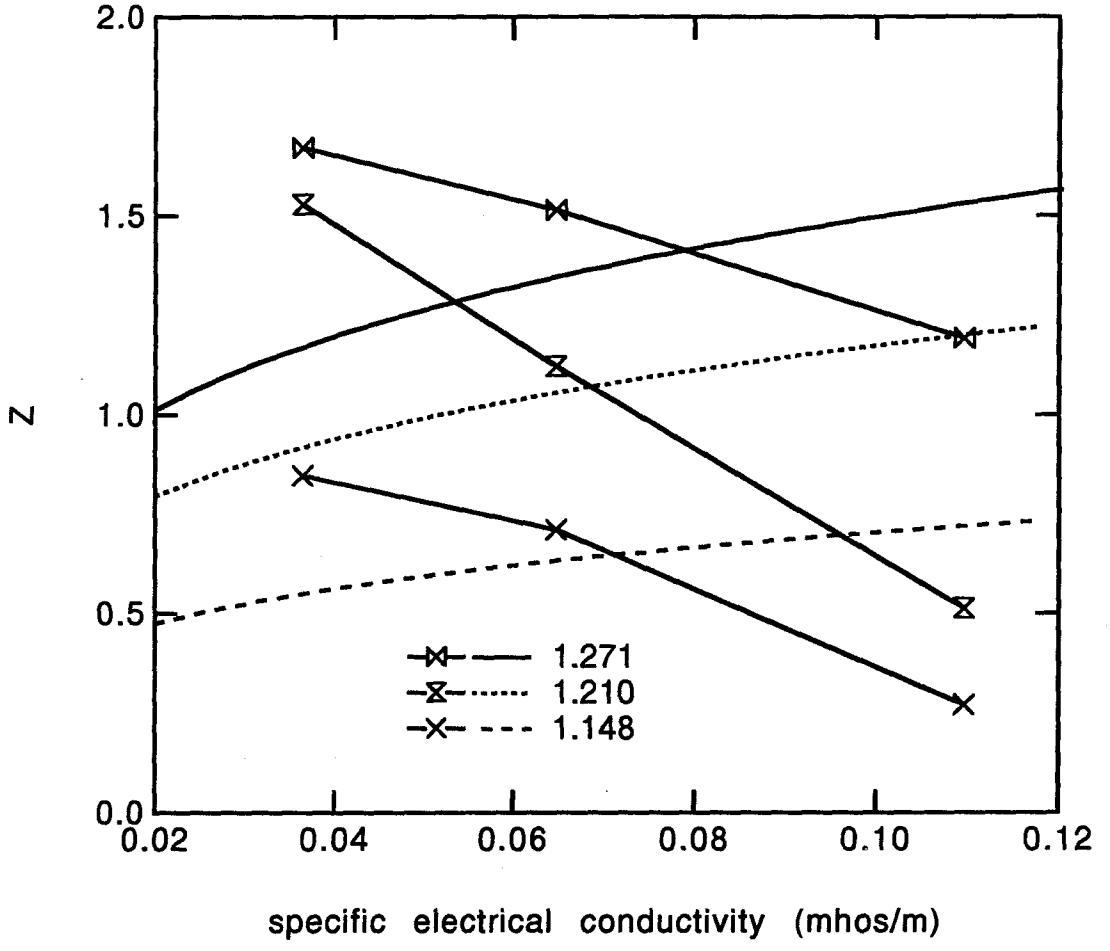

Figure 1.11: Rayleigh charge limit fraction versus specific electrical conductivity for three values of P.

corresponds to a higher charge to mass ratio, thus leading to a higher fraction of the Rayleigh charge limit. Some measured values of Z exceed unity. This is physically impossible since a liquid droplet cannot exist above the Rayleigh limit and is due to the experimental error arising in this indirect measurement.

We may now check the validity of the assumption that the induction of free surface charge on the cone occurs over much faster time scales than the motion of liquid. This condition is required in order to use Eqn. (1.3). The time scale for conduction is ϵ/σ and the time scale of liquid motion is r_c/U. Here, $r_c \sim 0.001$ m, $U \sim 1$ m s^{-1}, $\epsilon \sim 10^{-10}$ F m^{-1}, and $\sigma \sim 0.1$ mhos /m. Thus $\frac{(1)(10^{-10})}{(10^{-3})(10^{-1})} = 10^{-6} \ll 1$ so the assumption is valid for the present case. The specific charge was limited to about 30 C/l for all experiments. Referring to Table 1.2 we see that sufficient number of charge carriers were present to supply the total electrical current. This condition is also required to use Eqn. (1.3).

If the charge induction lags sufficiently or if insufficient numbers of charge carriers are present, then the liquid may not be sprayed by the present mechanism at all. In that case a charge *injection* system must be used to provide the surface charge. See, for example, the system of Bankston et al. [28] used for liquid hydrocarbon fuels with conductivities as low as $\sigma \sim 10^{-11}$ mhos/m.

When the model results were matched to the data, the electric field penetration factor A_1 was found to vary with P (Fig. 1.12). This is not surprising since P appears in Eqn. (1.9) and would thus affect the value of A_1 in the approximate expression for the internal electric field. The jet electric field factor A_2 was directly proportional to P. The charging geometry factor A_3 was inversely proportional to P.

P	c (g/l)	D_v (nm)	$D_{g,n}$ (nm)	$D_{g,a}$ (nm)	$D_{g,v}$ (nm)
1.15	5.09	62	54	65	71
	10.3	59	51	62	67
	19.7	34	31	35	38
1.21	5.09	96	81	101	108
	10.3	75	65	79	85
	19.7	50	44	52	57
1.27	5.09	113	89	120	127
	10.3	105	85	112	119
	19.7	91	72	98	107

Table 1.4: Dried NaI particle size distribution statistics.

Typical dried NaI particle size distributions are shown in Figs. 1.13 and 1.14. The volume-mean diameter (D_v), the geometric mean diameters based on number (D_g, n), area ($D_{g,a}$), and volume ($D_{g,v}$) are given in Table 1.4. The geometric standard deviations based on number ($\sigma_{g,n}$), area ($\sigma_{g,a}$), and volume ($\sigma_{g,v}$) are given in Table 1.5.

The particle size clearly increases with increasing P and decreasing σ. Thus the *addition* of solute to the solution results in *smaller* dried aerosol particles. This is due to the decreasing droplet size with increasing specific electrical conductivity. The total number concentration (N_{total}) and volume-based throughput efficiencies (η) are given in Table 1.5. Larger droplets resulted in higher throughput efficiencies. This was probably due to their increased momentum which allowed them to deviate from electric field lines and avoid deposition more readily than smaller droplets.

1.6 Conclusions

A model has been presented which utilizes a boundary layer integral method to describe the development of the boundary layer near the surface of a Taylor cone. A shear stress due to the flow of surface ions is the driving force for the liquid flow.

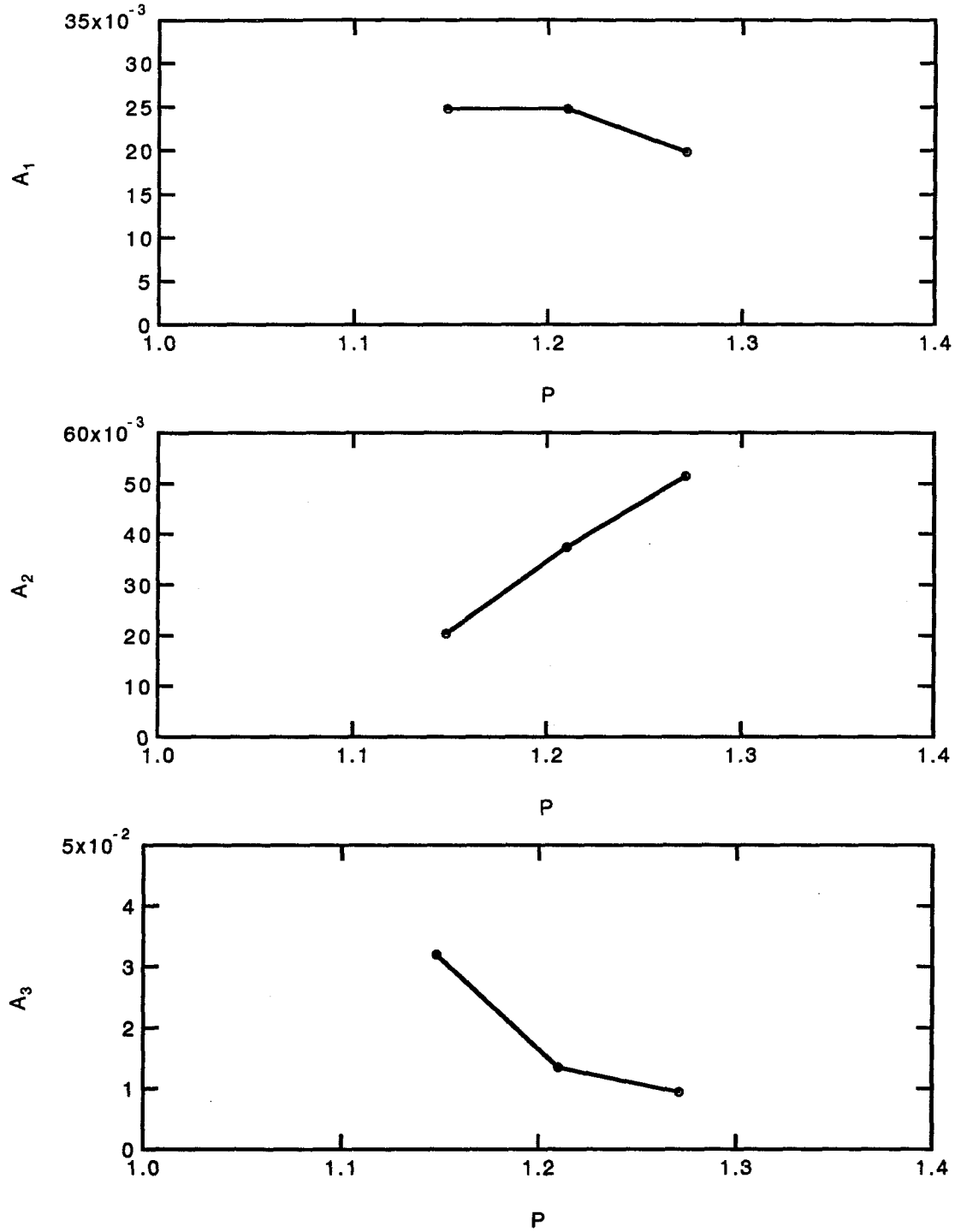

Figure 1.12: Electric field penetration factor (top), jet electric field factor (middle), and charging geometry factor (bottom) versus P.

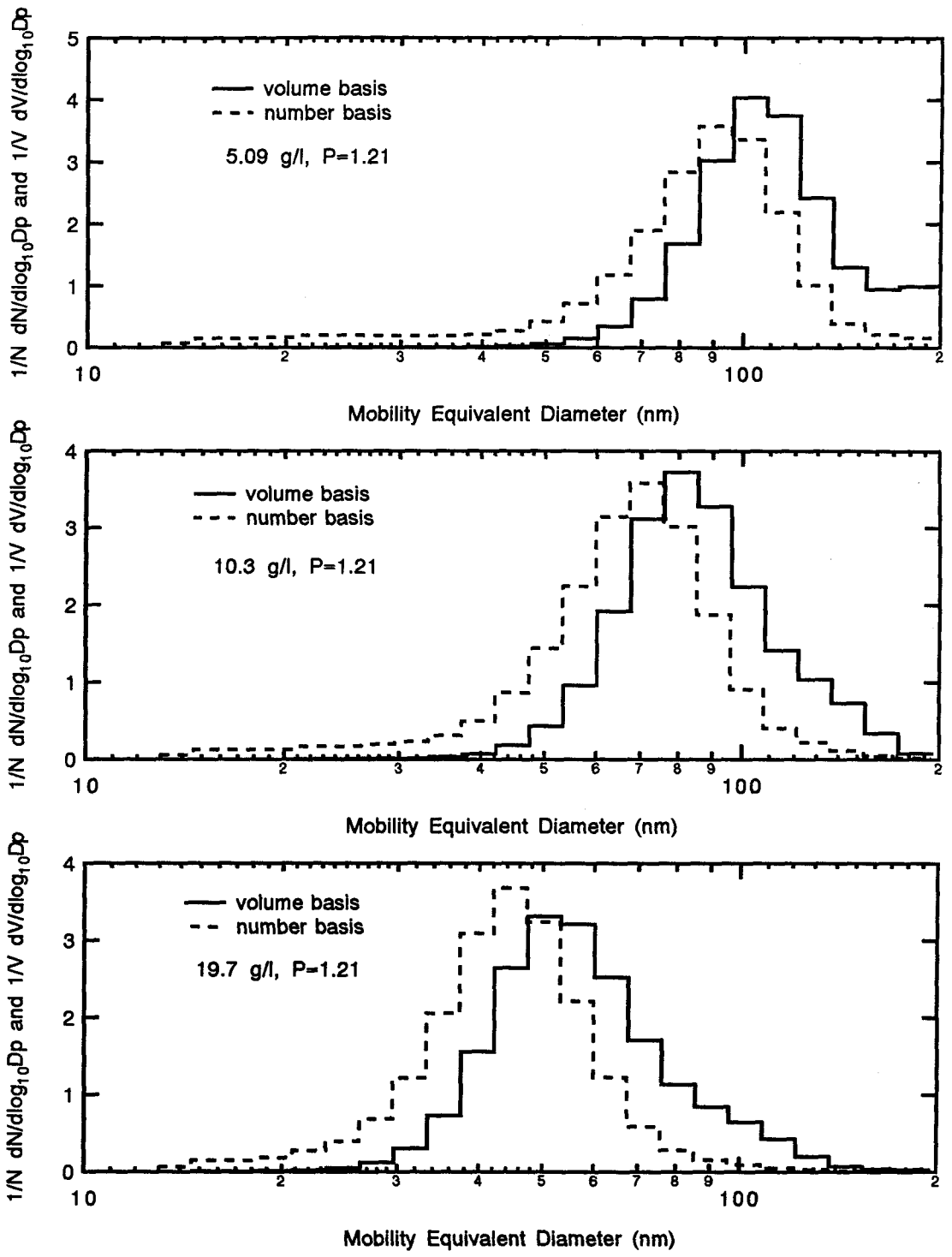

Figure 1.13: Dried NaI particle size distribution measured by SEMS. Variable concentration.

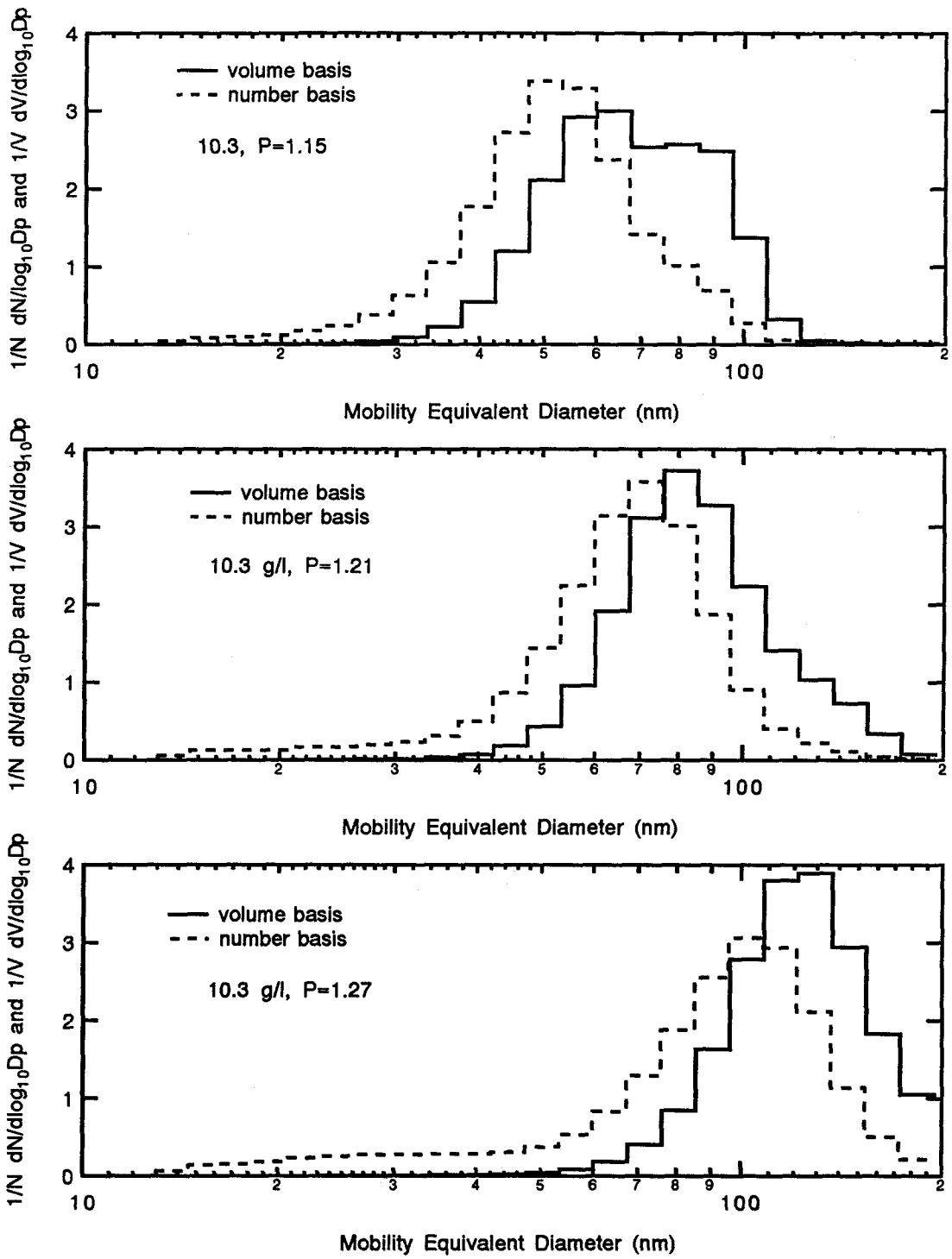

Figure 1.14: Dried NaI particle size distribution measured by SEMS. Variable P.

P	c (g/l)	$\sigma_{g,n}$	$\sigma_{g,a}$	$\sigma_{g,v}$	η %	N_{total} (10^5 cm^{-3})
1.15	5.09	1.4	1.3	1.4	14	1.5
	10.3	1.4	1.3	1.4	11	2.4
	19.7	1.3	1.3	1.3	1.3	2.8
1.21	5.09	1.5	1.3	1.3	47	1.7
	10.3	1.4	1.3	1.3	24	2.8
	19.7	1.4	1.3	1.4	2.8	2.6
1.27	5.09	1.7	1.3	1.3	50	1.6
	10.3	1.6	1.3	1.3	34	2.5
	19.7	1.7	1.4	1.3	14	2.7

Table 1.5: Further dried NaI particle size distribution statistics.

When the boundary layer grows to sufficient thickness, the liquid begins to accelerate as a jet. It continues to accelerate until it reaches a steady speed and then divides longitudinally into charged droplets due to longitudinal instability.

Many assumptions simplify the analysis. The flow is assumed to consist of a thin boundary layer of moving liquid at the liquid interface with the interior of the cone quiescent. The exact geometry of the cone, jet, and space charge resulting from sprayed droplets is not taken into account when computing the electric field at the cone's surface. The conduction current flowing inside the cone depends on the r-component of the electric field, which is governed by the Poisson equation, but here the electric field is assumed to be self-similar such that the conduction current is proportional to the cone cross-sectional area and the r-component of the electric field at the cone's surface with constant of proportionality A_1. The constant of proportionality is found by fitting the results of the model to experiment. It is seen that A_1 varies with applied electric field strength but not with the specific electrical conductivity.

The jet accelerates until it reaches a steady speed. The electric field at the jet's surface is approximated as that for a semi-infinite line of charge perpendicular to a

flat plate. A second empirical factor, A_2, appears in the jet electric field formulation to account for the approximate geometry and space charge effects.

The droplets are assumed to be charged by induction as they are formed. They do not reach the full charge, however, because the charging is limited by the flow of current through the jet, forming a simple resistance-capacitance circuit. Therefore an exponential factor involving the droplet formation time and specific electrical conductivity is used to find the actual charge acquired by the droplets. A third empirical constant, A_3, appears in this factor.

Despite these major simplifications, the model correctly predicts the dependence of volumetric flow rate, current, and droplet size on specific electrical conductivity. Increasing the conductivity decreases both the droplet size and volumetric flow rate and increases the total electrical current and specific charge.

Acknowledgements

This work was supported by the National Science Foundation, grant numbers CBT8813006 and CTS9113191.

Chapter 2

Further Data on Volumetric Flow Rate and Current in Electrospray Atomization of Electrolytic Solutions

The electrospray data obtained using the atomizer with the polonium discharger in the drying chamber have been reported (Chapter 1). This chapter reports experiments performed using an atomizer having no discharger (Fig. 2.1). Size distribution measurements could not be made using this atomizer because the volume-based throughput efficiency was less than 1%. Measurements of volumetric flow rate and total electrical current, however, were made which extend the range of specific electrical conductivity σ, over-potential ratio P, and capillary radius r_c. For modelling purposes the jet electric field factor A_2 was taken from a linear fit to the data obtained using the atomizer with the discharger because no droplet size data was measured. Values of A_1 and A_3 were then determined from a fit to the volumetric flow rate and current at one value of σ (Table 2.1).

The volumetric flow rate, total electrical current, and specific charge as functions of σ and P are plotted in Figs. 2.2, 2.3, and 2.4, respectively. The volumetric flow rate, total electric current, and specific charge all increased with increasing specific

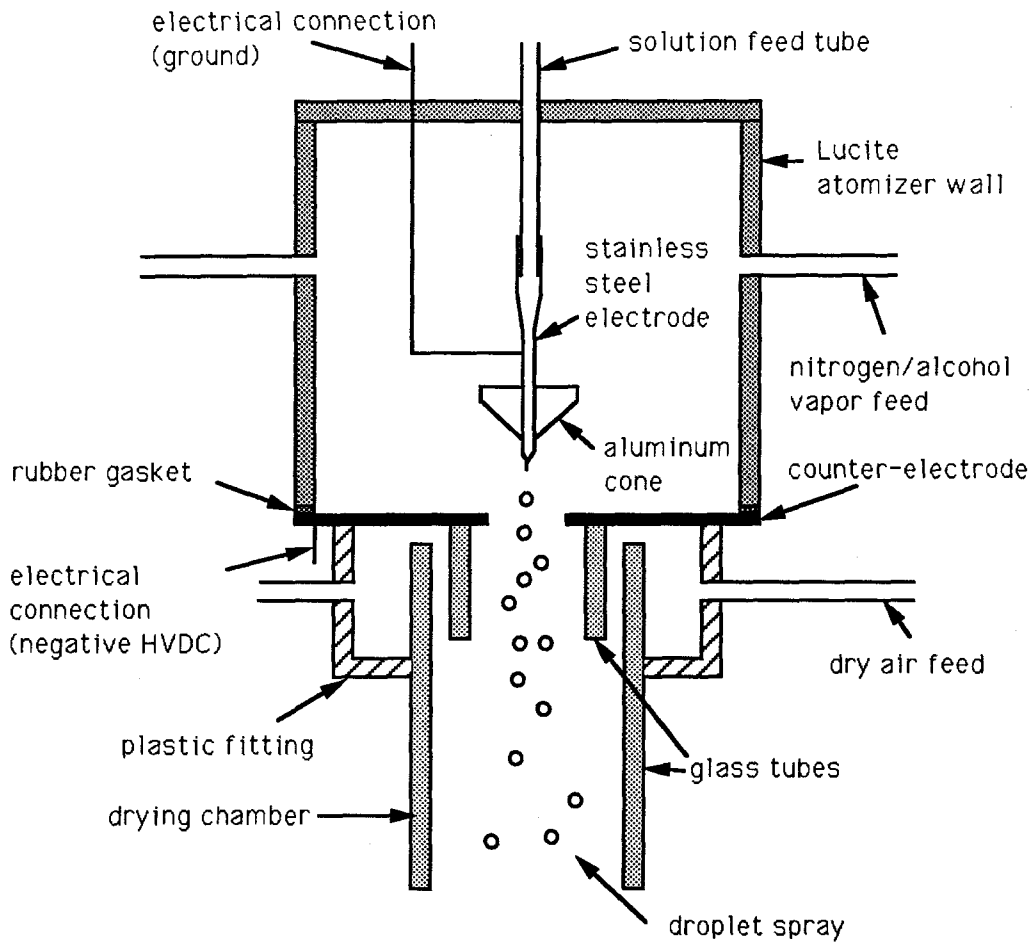

Figure 2.1: Schematic of the electrospray atomizer without a discharger in the drying chamber.

P	A_1	A_2	A_3
1.263	0.0700	0.049594	0.0123
1.342	0.0452	0.068704	0.00795
1.421	0.0290	0.087814	0.00580

Table 2.1: Values of A_1, A_2, and A_3 for experimentally tested values of P.

electrical conductivity. The volumetric flow rate increased and the specific charge decreased with increasing P. This result at first appears paradoxical because more charge is expected to be induced on liquid surface as P is increased. The volumetric flow rate increased fast enough to counter this effect, resulting in lesser specific charge.

These data are similar to those measured for the atomizer with the discharger, and are extended to higher values of σ and P. The boundary layer model (Chapter 1) predicted the trends well.

Experiments using various electrode radii r_c were also performed. Figures 2.5 through 2.7 show that increasing the capillary radius increased the volumetric flow rate, the total electrical current, and the droplet size ($\sigma = 0.0684 mhos/m$, $P = 1.493$). It was assumed that A_1 varied inversely with the square of the capillary radius, i.e., the fraction of cross-sectional area available for conduction current flow depended on the capillary diameter. In fact, with the inverse square rule, the *absolute* area available for conduction current flow remains constant and it appears that the tangential electric field penetration depth is nearly independent of the electrode diameter. This assumption leads to better agreement between theory and experiment than one obtains if A_1 is held constant. Its validity must be verified by a full solution of the Poisson equation inside the cone.

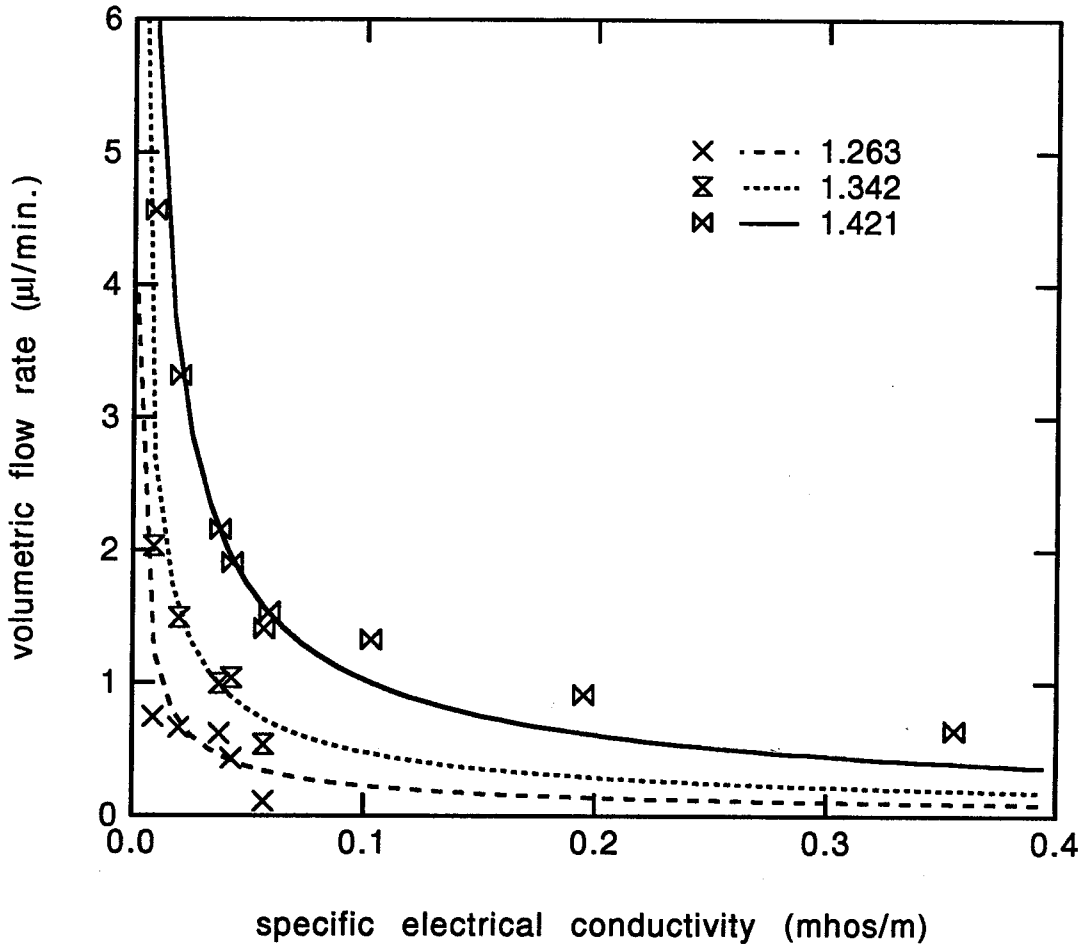

Figure 2.2: Volumetric flow rate of liquid versus specific electrical conductivity for three values of P for the atomizer without the discharger.

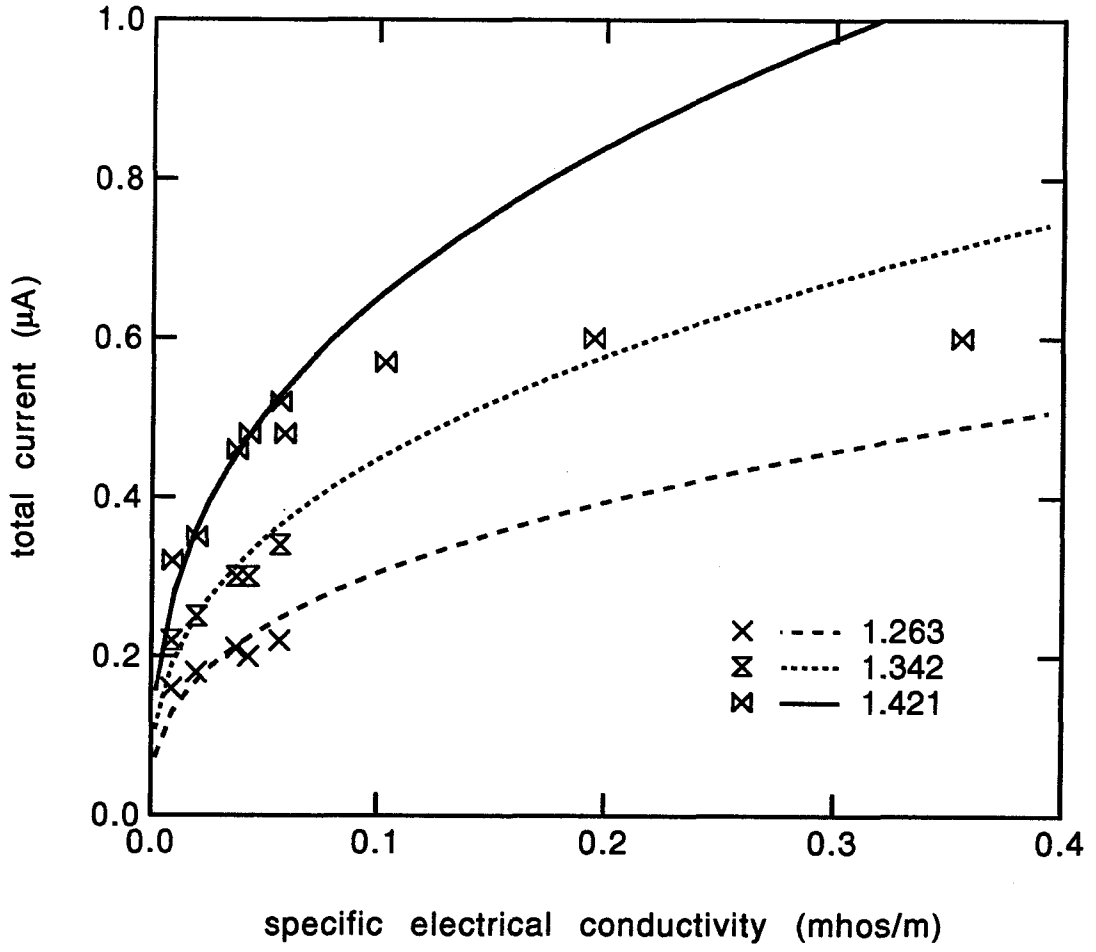

Figure 2.3: Total electrical current versus specific electrical conductivity for three values of P for the atomizer without the discharger.

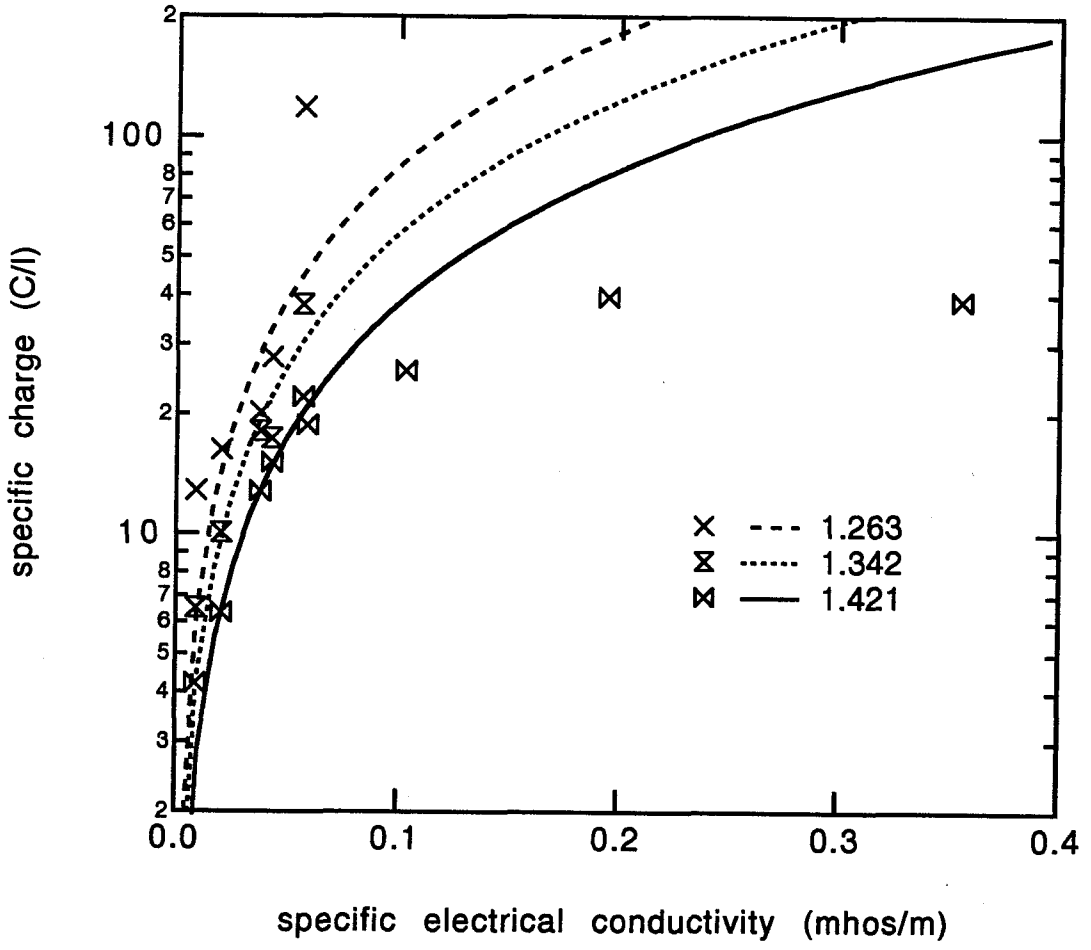

Figure 2.4: Specific charge versus specific electrical conductivity for three values of P for the atomizer without the discharger.

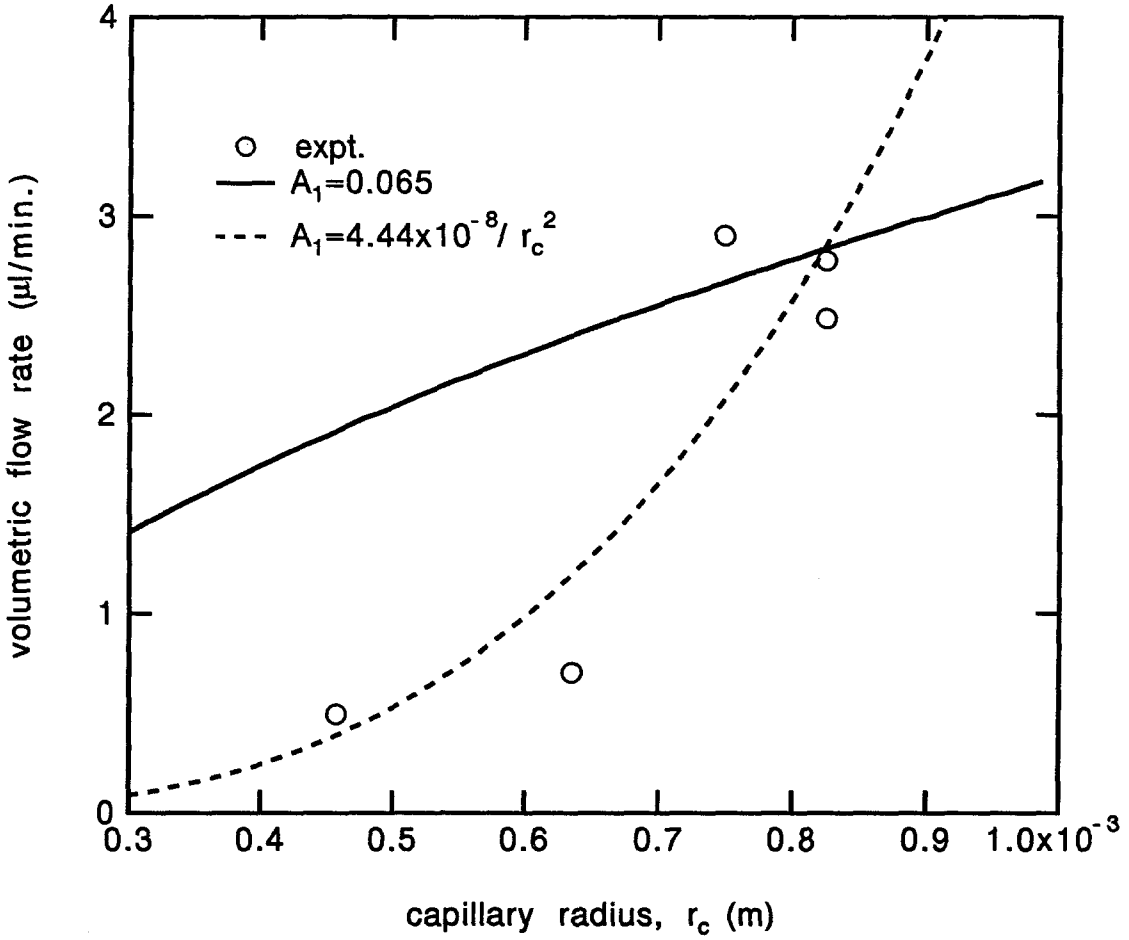

Figure 2.5: Volumetric flow rate of liquid versus electrode radius for the atomizer without the discharger.

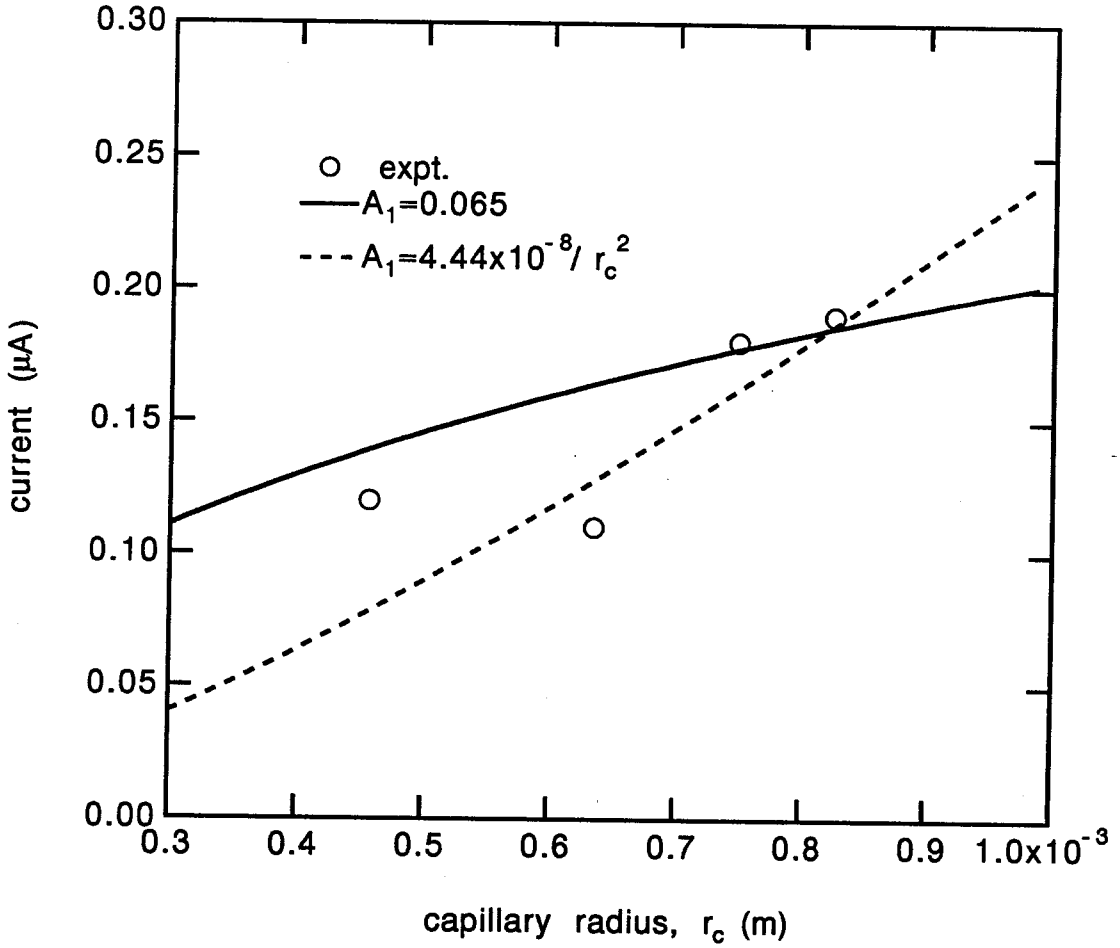

Figure 2.6: Total electrical current versus electrode radius for the atomizer without the discharger.

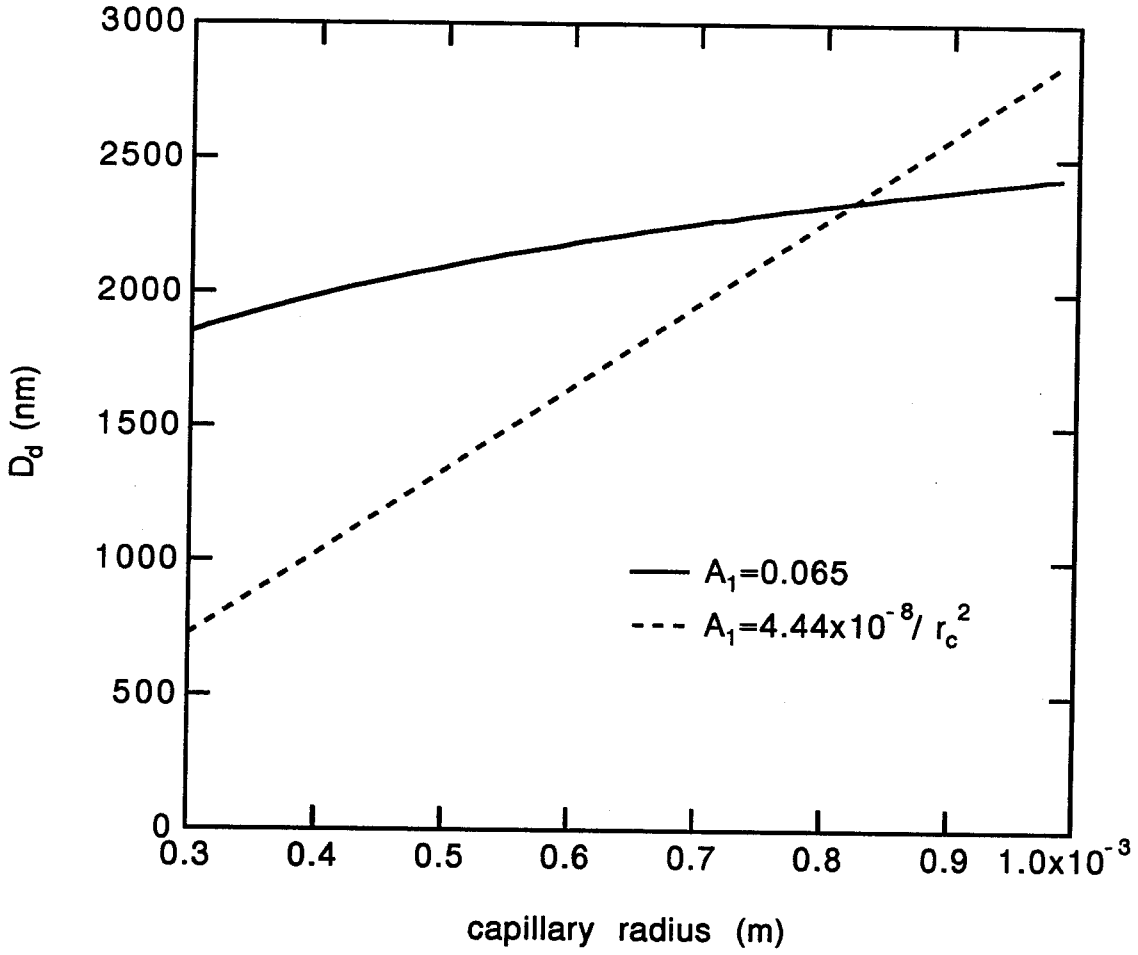

Figure 2.7: Predicted droplet size versus electrode radius for the atomizer without the discharger.

Chapter 3

Evaporation of Charged Droplets

In many electrospray applications the liquid used contains a volatile solvent. As the liquid droplets evaporate, their charge to mass ratio increases. The maximum charge a droplet can carry is given by the Rayleigh charge limit [18],

$$q_{\max} = (64\pi^2 \epsilon_0 T r_d^3)^{1/2}, \tag{3.1}$$

where ϵ_0 is the permittivity of free space, T is the surface tension, and r_d is the droplet radius. If q_d is reached, disturbances in the droplet surface shape grow exponentially and the primary droplet disrupts into several smaller droplets. Thus the size of the droplet changes during drying due to both evaporation and disruptions. We wish to predict the size distribution of the particles resulting from the evaporation and disruption of charged solution droplets.

Several researchers have analyzed the disruption process [30, 31, 32, 33]. The methods used to date include energy minimization and energy balance methods applied to the pre- and post-disrupted droplet systems. The model used by Roth [30] is relatively simple to implement. A primary droplet charged to the Rayleigh limit is assumed to disrupt into a mother droplet and two to seven identical sibling droplets. A balance of surface energy, electrostatic energy, and kinetic energy before and after

the disruption is used to predict the parent and sibling masses and charges. The model predicts that the number of siblings formed must range from two to seven, but it gives no method to determine that number. The data of Elghazaly [33], however, show that the number of siblings formed is nearly random, i.e., there appears to be a nearly equal likelihood of forming all numbers of siblings. This random nature will be used to predict the size distribution of droplets resulting from the disruption of one drop.

We begin with a newly-sprayed primary droplet with radius r_o, charge Q_o, Rayleigh charge limit fraction Z, mass M_o, and solute concentration C_o. For purposes of the present calculations the droplet is assumed to evaporate until $Z = 1$ unless the solute concentration reaches $C_{\max}$ at which point the solute precipitates. (The actual situation may be more complex. Some solutions form a gel at high concentrations. Or, a droplet may form a precipitated crust over a portion of its surface while the open surface may still disrupt.) After disruption the charge Q_2 and radius r_2 of each of the n sibling droplets, and charge Q_1 and radius r_1 of the mother droplet are given by the following set of equations [30] which are derived by balancing mass and energy (surface, electrostatic, and kinetic) before and after the disruption:

$$2\frac{r_o}{r_1}(\frac{Q_1}{Q_o})^2 + (\frac{r_1}{r_o})^2 + 2n\frac{r_o}{r_2}(\frac{Q_2}{Q_o})^2 + n(\frac{r_2}{r_o})^2 + \frac{n\mathrm{E_k}}{4\pi\gamma r_o^2} - 3 = 0 \tag{3.2}$$

$$\frac{Q_2}{Q_o} = \frac{1}{n}(1 - \frac{Q_1}{Q_o}) \tag{3.3}$$

$$(\frac{r_2}{r_o})^3 = \frac{1}{n}(1 - \frac{r_1^3}{r_o^3}) \tag{3.4}$$

$$\frac{Q_1}{Q_o} = \frac{1}{1 + n^{1/3}(r_o^2/r_1^2)(1 - r_1^3/r_o^3)^{1/3}}, \tag{3.5}$$

where E_k is the kinetic energy of the sibling droplets immediately after the disruption

event (the mother droplet is assumed to remain stationary). The sibling droplets are assumed to be emitted in a symmetrical pattern around the mother droplet, so that

$$\mathrm{E}_k = \frac{nQ_1Q_2}{4\pi\epsilon_o d_i} + \frac{n^2Q_2^2 f_n}{8\pi\epsilon_o d_i}, \tag{3.6}$$

where f_n is a geometrical factor describing the emission pattern, given by

$$f_n = -0.28290 + 0.35415n - 0.04385n^2 \quad 2 \leq n \leq 7. \tag{3.7}$$

As a droplet evaporates it may undergo many disruptions, creating sibling droplets which may also disrupt, etc. The process ceases when all of the solute has precipitated. The model may be conveniently implemented by numerical solution of Eqns. (3.2) through (3.7). This is particularly simple if the sibling droplets do not disrupt themselves during drying. Then the primary droplets are the only possible sources of new droplets through their multiple disruptions. The number of siblings produced at each disruption is assumed to be an integer randomly distributed such that $[2 \leq n \leq 7]$. For each simulation the equations are solved multiple times to ensure adequate statistical representation of the random distribution of particles resulting from one primary droplet. It was found during trial runs that 10,000 realizations were enough for convergence of the size distributions to within $\pm$ 3% from one realization to the next.

To see the effects of disruptions during drying, we considered a hypothetical system where T=0.040 N/m, solution and solute densities equal to 1000 kg m^{-3}, $C_{\mathrm{max}} = 0.3$, and $r_0 = 0.5\mathrm{x}10^{-6}$ m at various initial concentrations. The droplets begin at one-half the Rayleigh charge limit. If the secondary effects of the dependence of surface tension and density dependence on solute concentration are ignored, then the initial droplet size does not affect the results; the mother and sibling droplet radii and charges are proportional to the primary droplet radius and charge.

Figure 3.1 shows the size distribution resulting from two concentrations of the hypothetical solution. For $C_o = 0.1$, no disruptions occur. For $C_o = 0.01$ one or two disruptions occur depending on the number of siblings formed in the first disruption. The average number of particles resulting from each primary droplet in this case is 8.525. For $C_o = 0.001$ the average number is 14.520. These results indicate that large numbers of small droplets are created when Rayleigh disruptions occur.

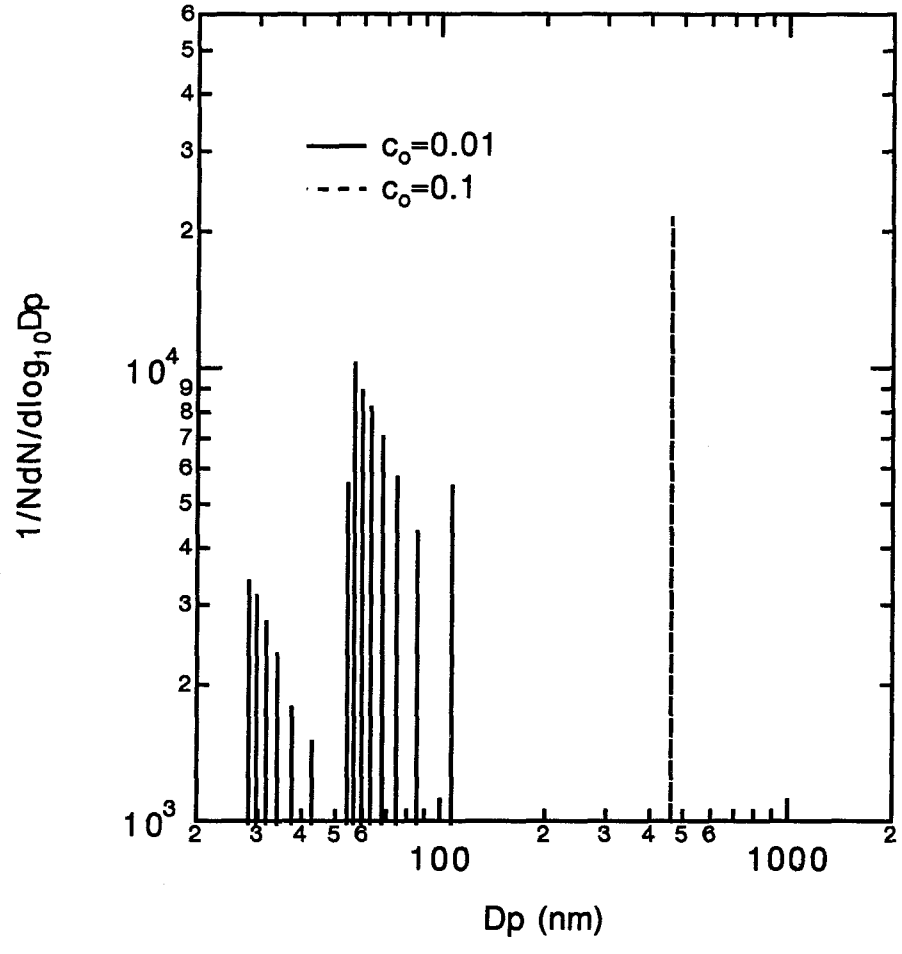

Figure 3.1: Size distributions of dried solute particles resulting from one initial droplet of 1 μm diameter for two initial solution concentrations. The width of the histogram bars in the $C_o = 0.1$ cases and $C_o = 0.01$ case are 0.05 and 0.015 nm, respectively.

Chapter 4

Synthesis of Lanthana-doped Yttria by Electrospray Pyrolysis

Abstract

Electrospray atomization of high concentration chemical precursor solutions was applied to the synthesis of yttria powders. Conditions were found which led to high quality powders, composed of dense, spheroidal, submicron, and nanocrystalline oxide particles. The precursor solutions were hydrated lanthanum and yttrium nitrates dissolved in n-propyl alcohol at concentrations ranging from 44.1 to 455 g/l. Electrospray atomization produced submicron precursor droplets which were dispersed in air and carried through an electric furnace for thermal decomposition at temperatures ranging from 550 to 725°C for several seconds residence time. X-ray powder diffraction patterns indicated the expected cubic phase. Transmission electron micrographs showed that the particle structure varied with solution composition, ranging from hollow, inflated spheres for six-hydrated nitrates to dense spheroids for five-hydrated nitrates. The use of 6-hydrated nitrates in the solutions appeared to form gas-impermeable particle surfaces during thermal decomposition, leading to hollow, inflated spheres.

4.1 Introduction

Ceramic objects are often produced by sintering powder compacts [34]. The quality of the ceramic object depends strongly on the quality of the powder from which it was formed. To avoid the mechanical flaws where catastrophic failure in stressed ceramics usually begins, the powder must be homogeneous and free of hard particle agglomerates, oversize particles, angular structures, and local composition variations [35]. Powder handling and sintering considerations require that the particles have an average size between 0.1 and 1.0 μm. In order to avoid excessive shrinkage during sintering, the particles should be dense, rather than hollow or porous. Synthesis of ceramic powders that satisfy these requirements is receiving considerable attention, with many of the efforts focused on the gas phase reactions of volatile precursors [36]. While vapor precursors are available for many materials, for some ceramics suitable reactants are either too costly or totally unavailable. Control of particle stoichiometry is also difficult in the production of multicomponent particles. Thus, for the production of advanced ceramics such as lanthana-doped yttria, alternate synthesis routes are required.

Spray pyrolysis has the potential to satisfy the above criteria for many ceramic materials [37, 38, 39, 40]. Ceramic particles are generated by spraying a liquid ceramic precursor and reacting the aerosol droplets in a furnace. Precursors are typically aqueous solutions of metal salts. Thermal decomposition in air or nitrogen converts the salts to metal oxides after evaporation of the solvent. The atomizer determines the size distribution of the precursor droplets and hence the size distribution of the cured ceramic particles. A fully dense ceramic particle produced by curing a droplet with initial diameter D_d has diameter $D_p = C^{1/3}D_d$ where C is the volume fraction

of ceramic material in the solution. An atomizer which produces 5 μm diameter droplets requires a solution with $C = 0.001$ to produce ceramic particles 0.5 μm in diameter. Unfortunately, nonvolatile impurities inevitably present in solvents limit the compositional purity of the ceramic particle, because these are concentrated as the solvent evaporates. For example, if there are 10 ppm (by volume) nonvolatile impurities present in a solution with $C = 0.001$, the ceramic particle will contain 1% (by volume) impurities–a value which is far too high for advanced ceramics applications. For optical ceramics, such as lanthana-doped yttria considered in this paper, impurity levels must be limited to roughly 10 ppm or less.

What is needed, then, is an atomizer that produces droplets in the submicron range from concentrated precursor solutions so that little concentration of nonvolatile impurities takes place, leading to submicron and sufficiently pure ceramic particles. Electrospray atomization is known to produce droplets in the submicron range [41] (Chapter 1). This paper describes the use of electrospray atomization in spray pyrolysis, i.e., *electrospray pyrolysis*, to produce particles of lanthana-doped yttria.

4.2 Experiment

A modified version of the electrospray atomizer described in Chapter 1 was used to spray solutions of hydrated yttrium nitrate and hydrated lanthanum nitrate in n-propyl alcohol (Fig. 4.1). The liquid was introduced by gravity feed into a 1.57 mm (outside diameter) stainless steel capillary (the electrode), which was placed 8 mm from a flat, stainless steel plate with a 10 mm diameter hole (the counter-electrode). The counter-electrode current, I_g, was measured by grounding it through a Hewlett Packard model 3465A Digital Multimeter, sensitive to $\pm$ 10 nA. A potential was

applied to the electrode using Spellman high voltage power supplies [1] which induced charges on the surface of the liquid. The resulting electrostatic forces balance surface tension forces leading to the formation of a Taylor cone [1]. Liquid is driven toward the tip of the cone by tangential electric field stresses, described in detail in Chapter 1. A charged jet of liquid is emitted from the tip of the cone, accelerates, and breaks up into charged droplets under the action of longitudinal instabilities. The electrode current, I_e, is measured by floating a Metex model M- 3800 Multimeter to the electrode potential. To prevent corona discharge at the Taylor cone, the upper part of the atomizer is purged with 90 cm^3/minute SF_6 gas. To prevent solvent at the cone from evaporating and forming a solute crust, the SF_6 is saturated with n-propyl alcohol by passing it through a bubbler.

When using the gravity feed method, the Taylor cone was disturbed by pressure fluctuations in the surrounding gas. To quiet these fluctuations, a pressure feedback tube in the SF_6 flow system was connected from the SF_6 feed line just upstream of the atomizer to a point just above the gravity feed reservoir (Fig. 4.1).

Electrospray atomization is influenced by the properties of the liquid, i.e., the specific electrical conductivity, absolute viscosity, surface tension, and density (Chapter 1). The specific electrical conductivity was measured using an Omega model CDH-70 conductivity meter. The absolute viscosity was measured using a capillary viscometer built in our laboratory. The surface tension was measured by the capillary rise method. The density was measured by weighing a known volume.

To establish a spray, the potential was increased until a Taylor cone was established at the electrode, V_s. The potential was then increased to 1.1 to 1.5 times V_s.

[1] Model Nos. RM6N1500D and WRM15P1500D

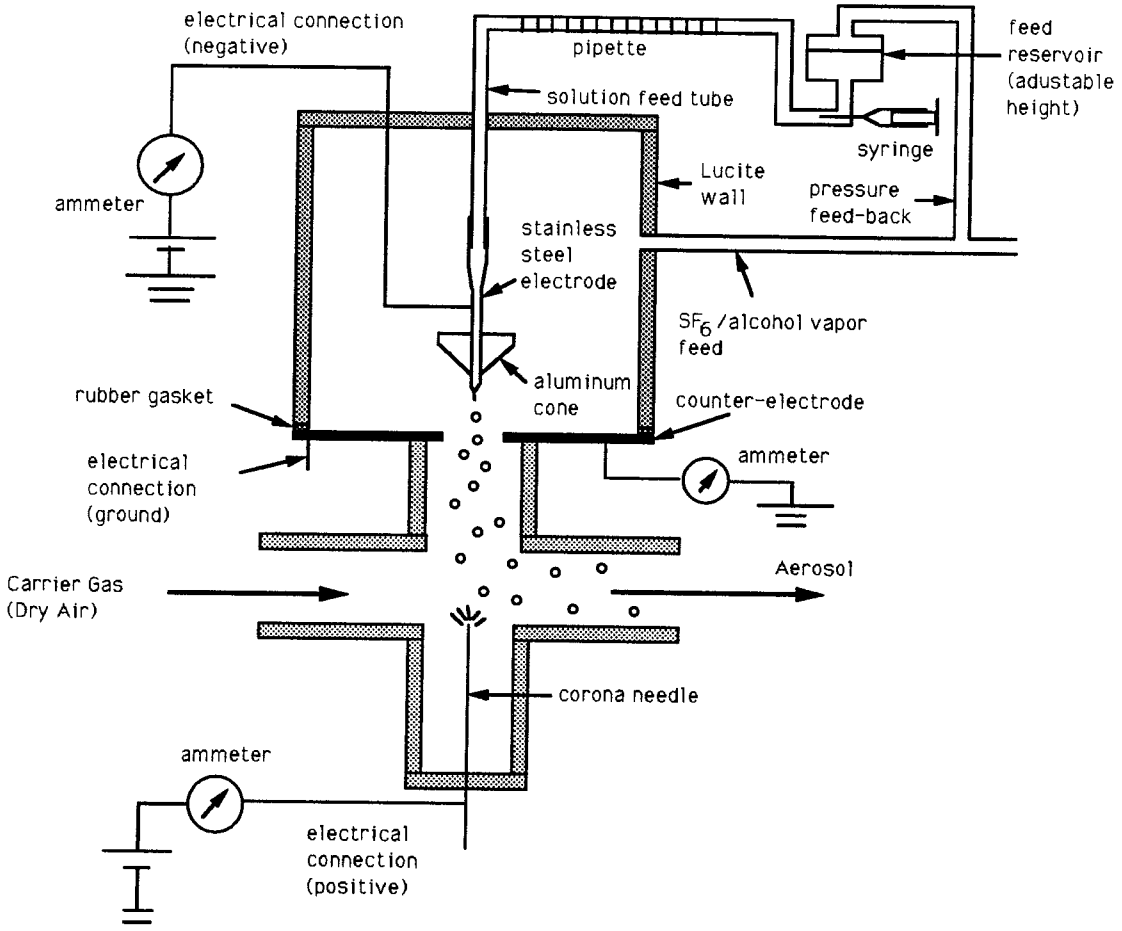

Figure 4.1: Schematic of the electrospray atomizer.

The height of the feed reservoir was adjusted until the cone semi-vertex angle was $30 \pm 2°$ to $33 \pm 2°$. The liquid passed through a pipette with 1 microliter graduations (Fig. 4.1). A syringe and hypodermic needle were placed at one end of the pipette so that a small air bubble could be introduced for flow rate measurement by timing its passage through a known volume [42].

The method of Meesters et al.[22] was used to minimize deposition of the highly charged droplets on the counter-electrode or nearby surfaces. A corona needle at high potential opposite to that of the electrode was placed beneath the counter-electrode. The corona needle deflected the charged droplets away from the counter-electrode and discharged them with ions of opposite sign. The corona needle current, I_c, was measured by floating a Metex model M-3800 Multimeter to the corona needle potential. The throughput efficiency of the atomizer was maximized by setting the corona needle potential such that the net current to ground was near zero ($I_g \leq 10$ nA). This was achieved by balancing the electrode current I_c and the corona needle current I_c, i. e., $I_c = -I_e$. The aerosol leaving the atomizer then has zero net charge. Droplets with excessive charge deposit on the counter-electrode or nearby surfaces. No deposits were seen on the corona needle even after many hours of operation. As discussed below, the volume throughput efficiency of the atomizer reached roughly 50 % when optimized in this way.

Dry purified air flowed through the lower portion of the atomizer at 5.8 lpm to dry and carry the droplets into a TSI model 3054 bipolar charger to reduce the charge on any particles that escaped neutralization in the atomizer.

The thermal decomposition was carried out in a 56 mm (inside diameter) alumina tube, 1.5 m long, surrounded by an electric furnace 64 cm long. The residence time

in the heated zone depended on the furnace temperature. For 5.89 lpm total gas flow through the atomizer (measured at 1 atm, 25°C), the residence times were 5.7, 5.1, and 4.7 seconds for furnace temperatures of 550, 656, and 725°C, respectively.

The cured aerosol was sampled for size distribution measurement by passing it through a TSI model 3077 Krypton-85 bipolar charger and subsequently through a Scanning Electrical Mobility Spectrometry (SEMS) [24] based on the TSI model 3071 Differential Mobility Classifier and Model 3761 Condensation Particle Counter. Samples for transmission electron microscopy (TEM) were obtained on 300 mesh holey-carbon grids using an in-line sampler which held the grid like a small filter and allowed aerosol to pass through it, or on 300-mesh formvar grids using a thermophoretic sampler. Bulk samples for x-ray diffraction and powder compaction were collected on Nuclepore polycarbonate membrane filters with 50 nm pore size.

X-ray diffraction patterns were obtained on an INEL diffractometer. Micrographs were obtained on Phillips 201 and 430 Tranmission Electron Microscopes. Micrographs were used both for particle structure determination and to augment size distribution data obtained using SEMS.

4.3 Results and Discussion

4.3.1 Undoped Yttria

Two solutions of yttrium nitrate pentahydrate ($Y(NO_3)_3 \cdot 5H_2O$) in n-propyl alcohol (44.2 g/l and 450 g/l) and one solution of yttrium nitrate hexahydrate ($Y(NO_3)_3 \cdot 6H_2O$) in n-propyl alcohol (93.4 g/l) were electrosprayed and cured at 550°C with a furnace residence time of 5.7 seconds. The absolute viscosity, density, surface tension, and specific electrical conductivity are plotted as functions of solute concentration in

Figs. 4.2, 4.3, and 4.4, along with curve fits through the data that are used in numerical simulations described below. In using these curve fits we make the approximation that the rheological differences are small between equal mass concentrations of yttrium nitrate pentahydrate and yttrium nitrate hexahydrate in n-propyl alcohol. The absolute viscosity and density increased with increasing concentration. The surface tension was nearly independent of concentration. The specific electrical conductivity increased with increasing concentration rapidly at first, then more slowly at higher concentrations. To spray these three solutions, a positive potential was applied to the electrode with $V/V_s = 1.04$, $V_s = +4600$ volts, and $\phi_c = 33°$. Negative potential was applied to the corona needle at -6000 volts. The cone and corona needle currents were too low to measure precisely with the multimeters used, but ranged from 0.1 to 0.2 microamps for all three solutions. The ground current I_g was less than 10 nA.

The volumetric flow rate of liquid is shown in Fig. 4.5. It first decreases with increasing concentration because of the increasing specific electrical conductivity, a trend which was observed in studies of sodium iodide in n-propyl alcohol (Chapter 1). The modelling results for low concentration shown in Fig. 4.5 was computed using our previous model with $A_1 = 0.0151$, $A_2 = 0.0197$, $A_3 = 0.0331$, and $n_i = 3$. With higher concentrations the volumetric flow rate began to increase, possibly due to the increasing absolute viscosity. Our previous model (Chapter 1) that predicts the volumetric flow rate of liquid is not applicable for low Reynolds numbers, i. e., when the absolute viscosity is too high for a thin boundary to form near the surface of the Taylor cone. We now extend that model to the limit of high absolute viscosity.

In the low Re limit, the liquid flow in the cone will have no transverse velocity gradients. The fluid thus accelerates as a jet immediately upon exiting the electrode.

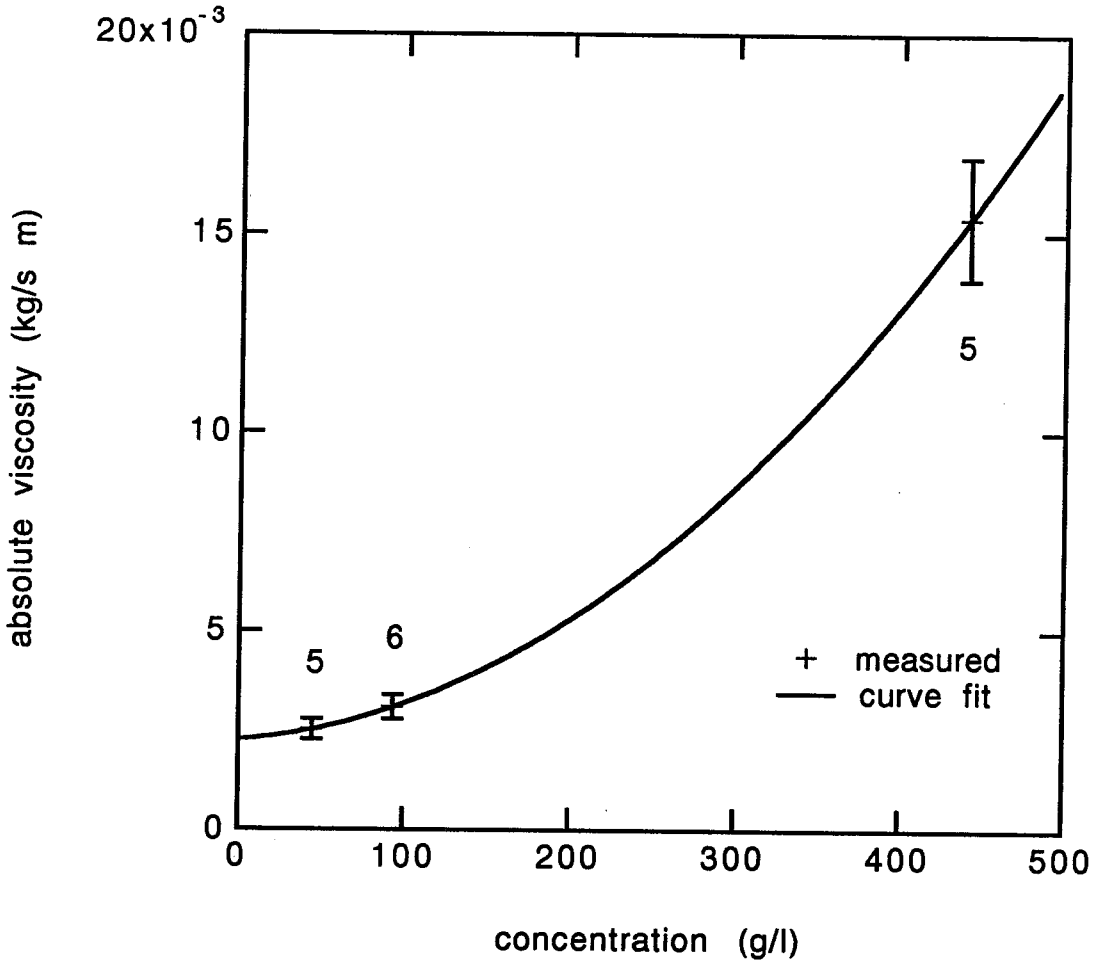

Figure 4.2: Absolute viscosity of solutions of hydrated yttrium nitrate in n-propyl alcohol at 24°C. The number next to each point gives the hydration level.

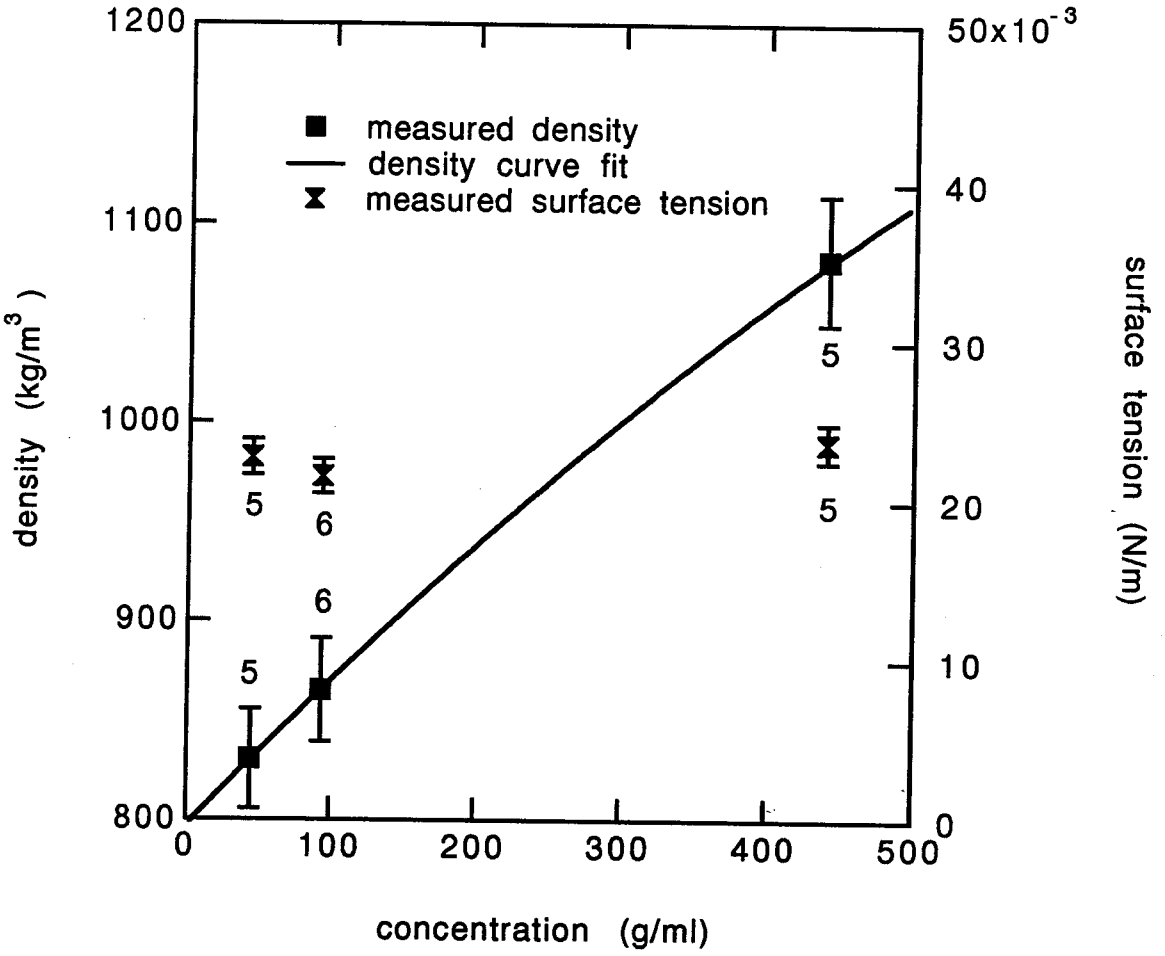

Figure 4.3: Density and surface tension of solutions of hydrated yttrium nitrate in n-propyl alcohol at 24°C. The number next to each point gives the hydration level.

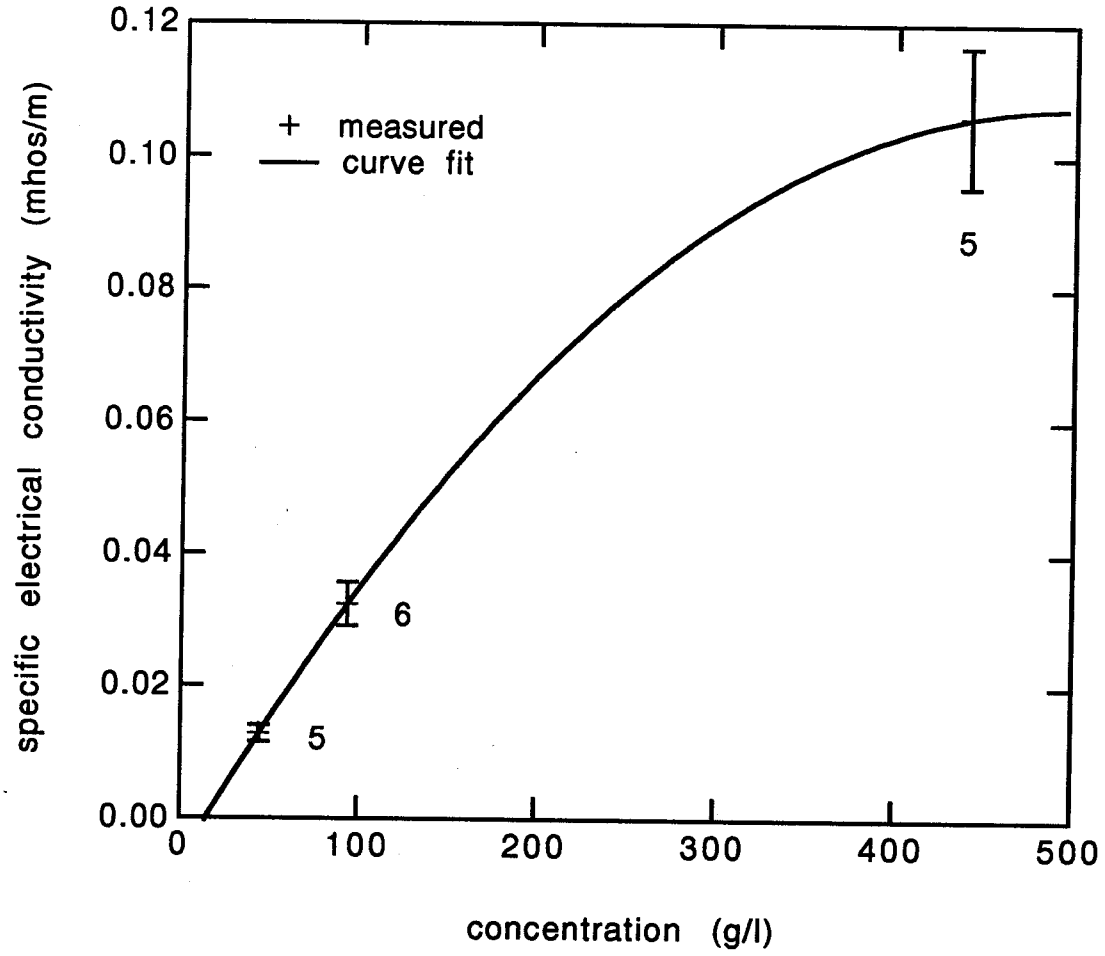

Figure 4.4: Specific electrical conductivity of solutions of yttrium nitrate hexahydrate in n-propyl alcohol at 25°C. The number next to each point gives the hydration level.

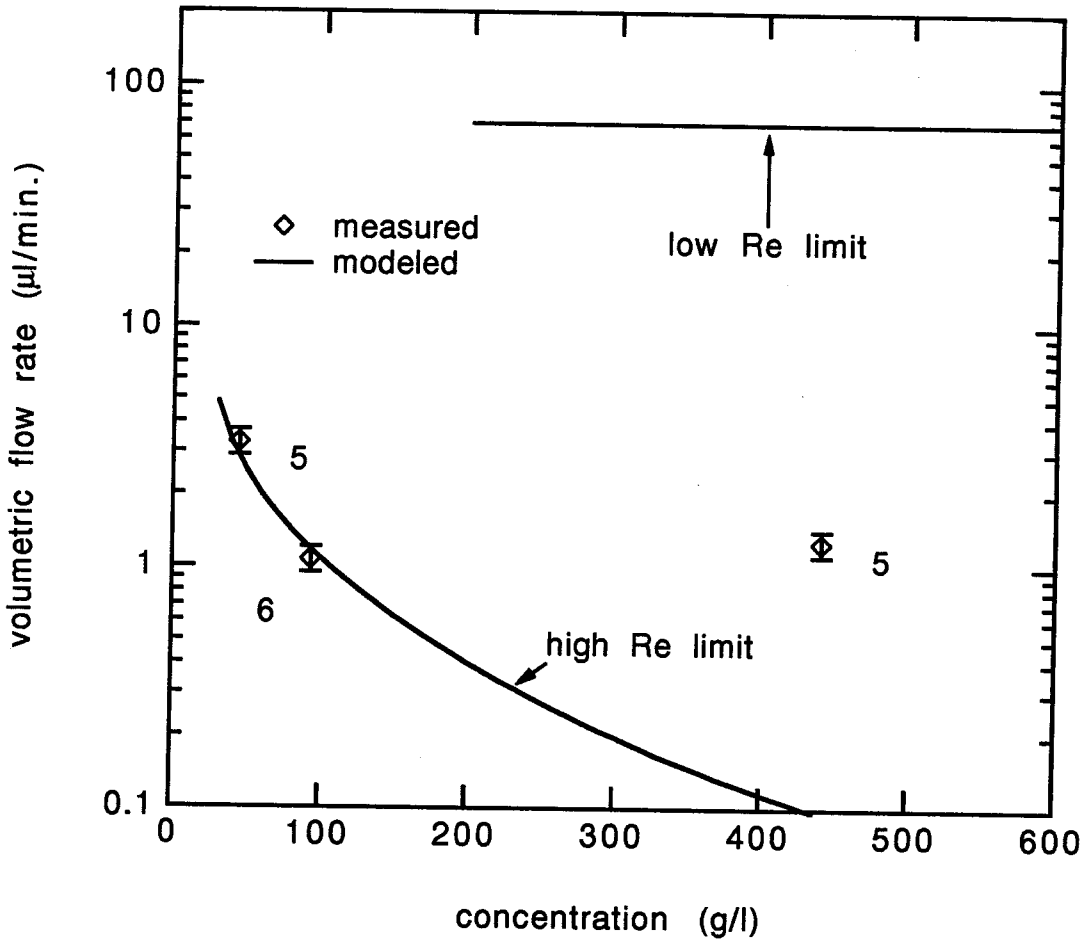

Figure 4.5: Volumetric flow rate of liquid versus concentration of hydrated yttrium nitrate in n-propyl alcohol. The number next to each point indicates the hydration level.

Using a treatment similar to the jet acceleration portion of our previous model, we solve for the volumetric flow rate which results in a cone angle of ϕ_c =33°, defined by the angle between the tangent to the cone's surface at $r/r_{cap} = 1/2$ and the z-axis (Fig. 4.6). Using the specific electrical conductivity, density, and surface tension for the 441 g/l solution, and using the ion friction factor $f = 1.8 \times 10^{-9}$ N s m^{-1}, and $A_1 = 0.0151$, $A_2 = 0.0197$, $A_3 = 0.0331$, and $n_i = 3$ as inputs to our model we obtain $Q =$ 69 μl/min. This is clearly higher than the observed value of 1.27 μl/min. In reality, the flow is somewhere between the thin boundary regime and the jet acceleration regime, and a more sophisticated fluid mechanical model is needed to predict the volumetric flow rate.

The droplet size also increases in the low Reynolds number limit, as shown in Fig. 4.7.

The mass flow rate of yttrium oxide is $F = Qc_1c_2$, where c_1 is the mass concentration of hydrated yttrium nitrate in n-propyl alcohol and c_2 is the mass fraction of yttrium oxide in the hydrated yttrium nitrate (0.29 for hexahydrate, 0.31 for pentahydrate), and is shown in Fig. 4.8. It begins at about 2.5 mg/hour and first decreases with increasing concentration due to the decrease of volumetric flow rate, but then increases to nearly 10 mg/hour at high concentration.

The size distributions of oxide particles produced using these solutions and spray conditions are shown in Fig. 4.9. In each plot, the dashed line indicates the number size distribution, and the solid line indicates the volume size distribution. The SEMS instrument covered the range of 20 to 200 nm, and hand-measured diameters from transmission electron micrographs were used to extend the range to the largest particles observed. The two sets of data were matched at the size bin in the histograms

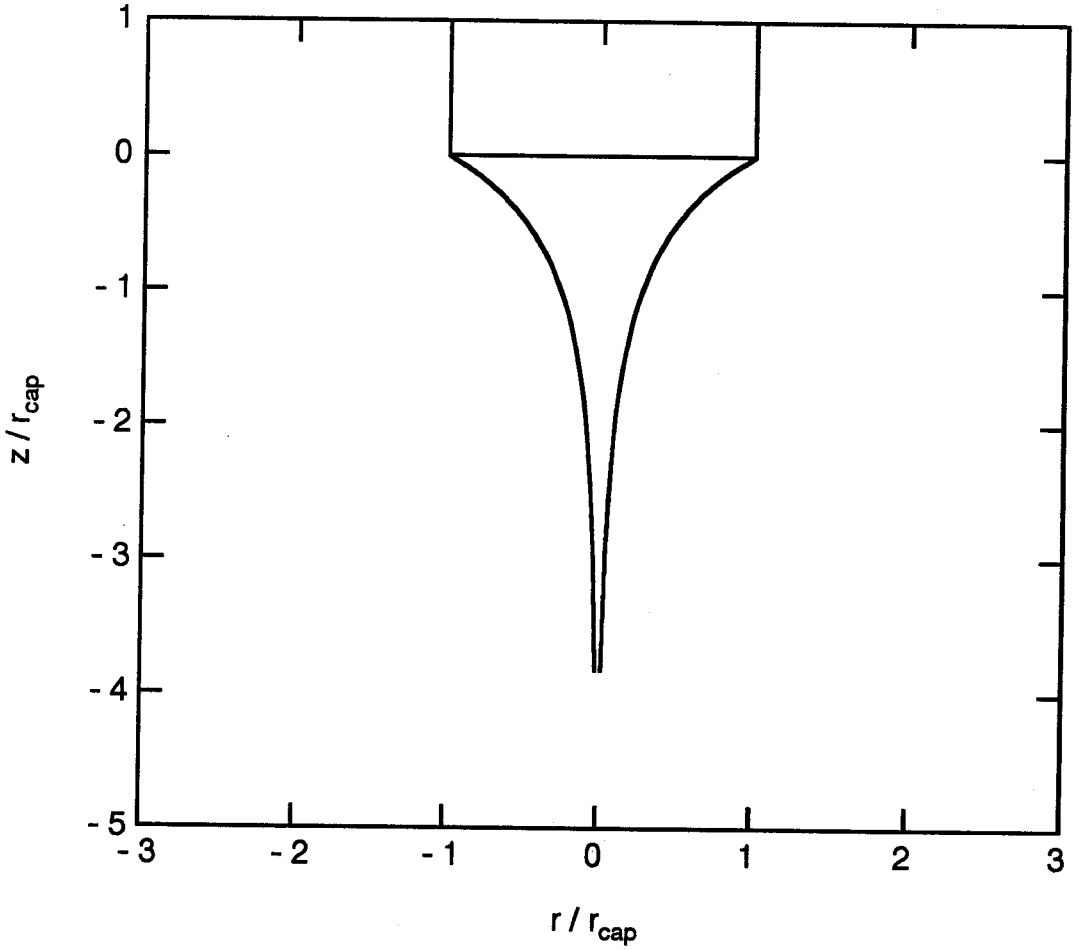

Figure 4.6: Computed profile of yttrium nitrate pentahydrate in n-propyl alcohol being accelerated according to the low Reynolds number approximation.

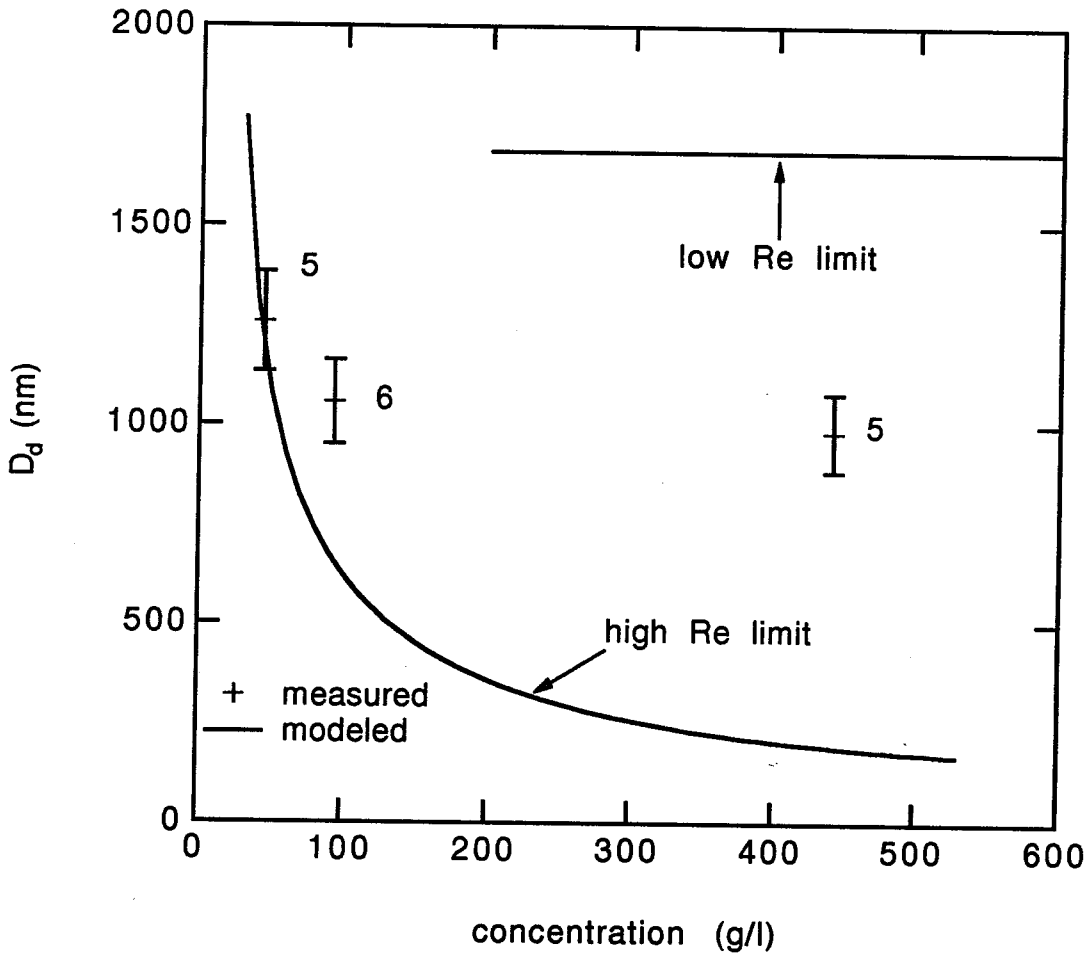

Figure 4.7: Volume-mean droplet size versus concentration of hydrated yttrium nitrate in n-propyl alcohol. The number next to each point gives the hydration level.

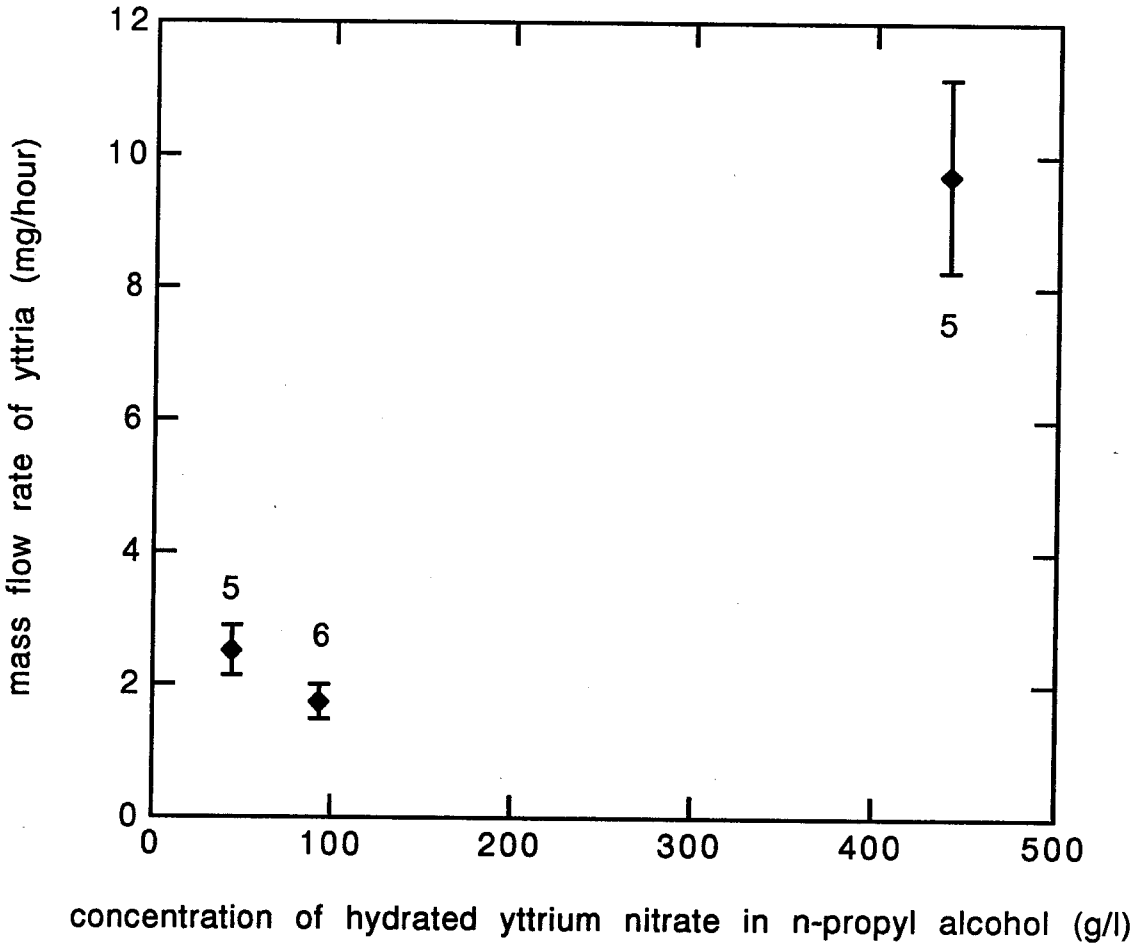

Figure 4.8: Mass throughput of yttrium oxide for solutions of hydrated yttrium nitrate in n-propyl alcohol. The number next to each point gives the hydration level.

with left hand boundary at 150 nm. Then the combined data were normalized by the total number or total volume. The particle counting efficiency of the TSI Model 3761 Condensation Particle Counter is nominally 50% at 20 nm, and decreases as the particle size decreases. Because of the large counting efficiency correction, the size distribution data for $D_p < 20$ nm is subject to high uncertainty.

Figure 4.9(top) shows the size distributions of oxide particles derived from the 44.2 g/l yttrium nitrate pentahydrate solutions in n-propyl alcohol. The number distribution was bimodal. The fine particle mode occurred below the range measured using SEMS. The volume distribution was monomodal. The volume geometric mean diameter and geometric standard deviation were 170 nm and 1.3, respectively. Figure 4.10 shows that the yttria particles were thick shells, with the wall thickness approximately one third to one fourth of the diameter. The surfaces are irregular, but the overall shape is spheroidal. A particle with wall thickness one third the diameter is 96.3% dense, and if sintered to full density the diameter would shrink to 98.7% of its original value. Therefore these particles very nearly achieve the desired particle shape and structure described in Section 4.1.

Figure 4.9(bottom) shows the size distributions of oxide particles derived from the 441 g/l yttrium nitrate pentahydrate in n-propyl alcohol. The number distribution was bimodal. The volume distribution was monomodal. The volume geometric mean diameter and geometric standard deviation were 290 nm and 1.5, respectively. Figure 4.11 shows that the particle surfaces were irregular, but the overall shape was spheroidal. No shell structure is evident, but this may due to the large size of the particles which interferes with internal imaging by transmission electron microscopy.

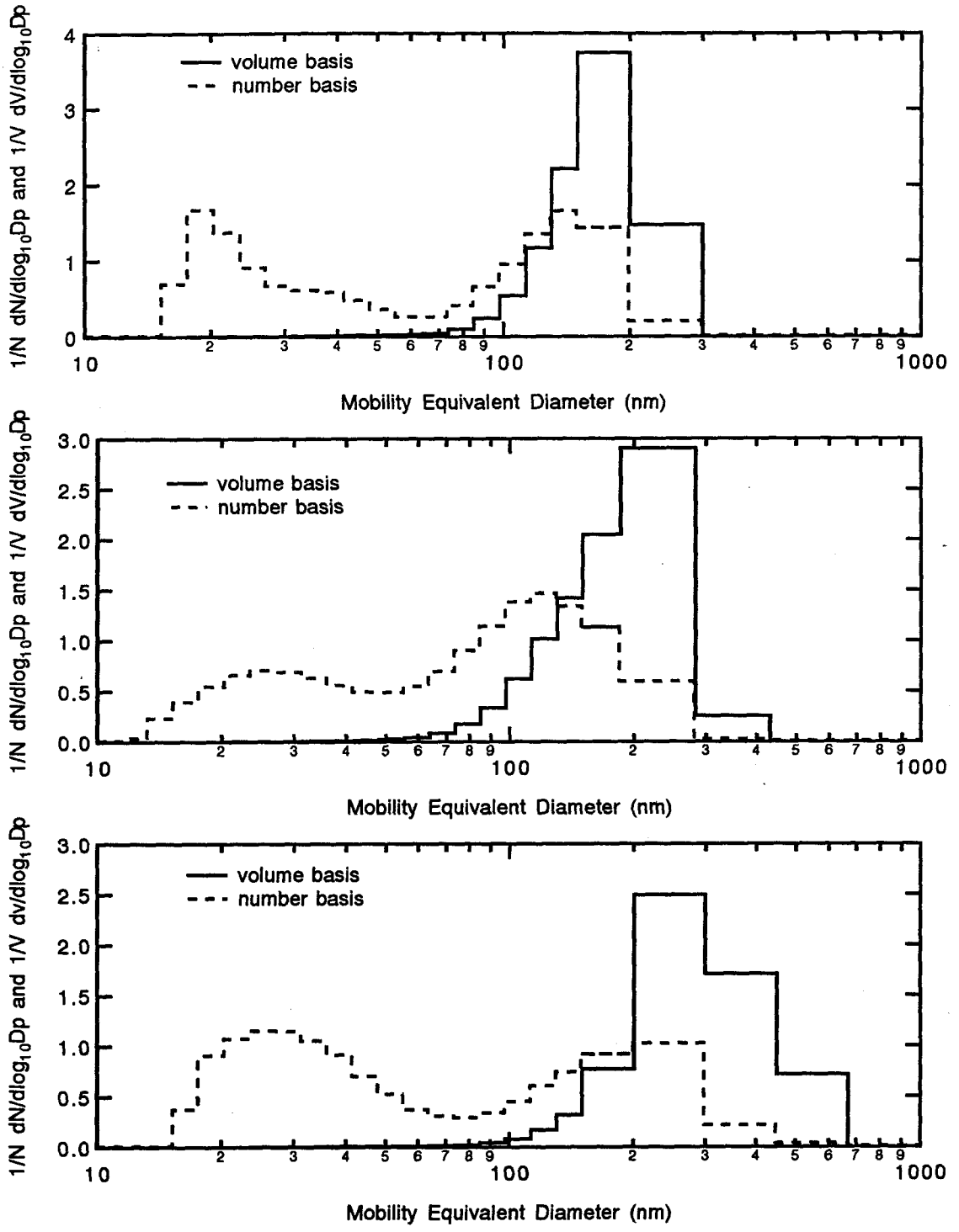

Figure 4.9: Size distribution of yttrium oxide particles synthesized from yttrium nitrate pentahydrate in n-propyl alcohol, cured at 550°C for 5.7 seconds. Top: 44.2 g/l. Middle: 93.4 g/l. Bottom: 441 g/l.

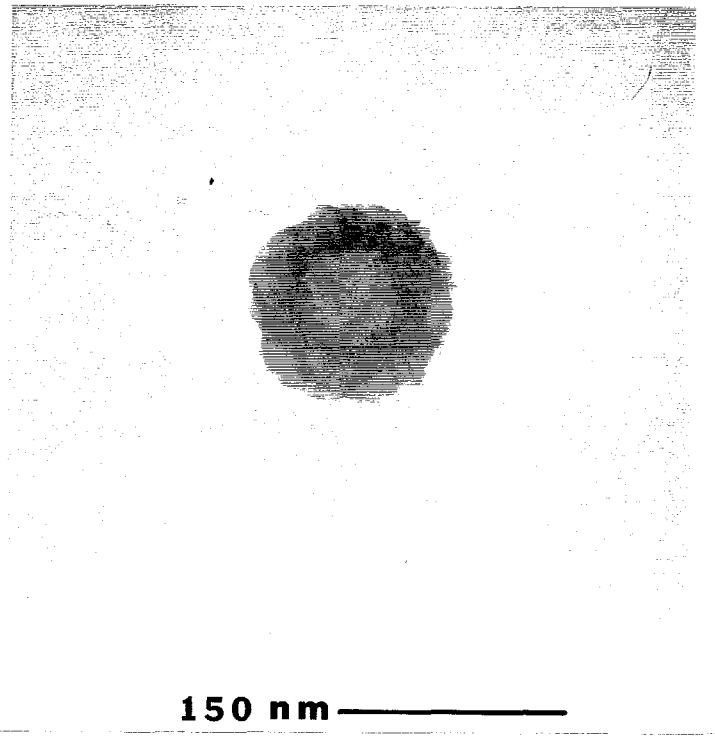

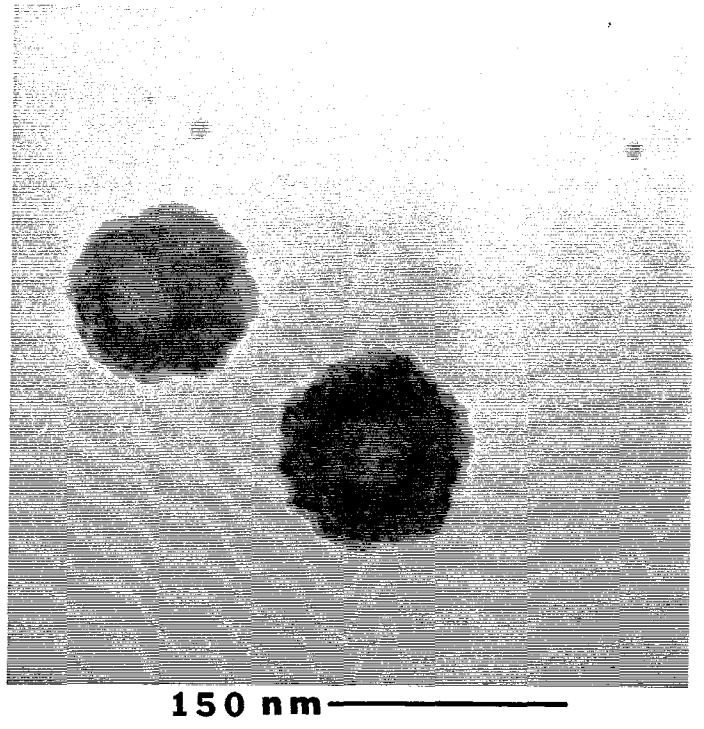

Figure 4.10: Transmission electron micrographs of yttria particles synthesized from 44.2 g/l yttrium nitrate pentahydrate in n-propyl alcohol, cured at 550°C for 5.7 seconds.

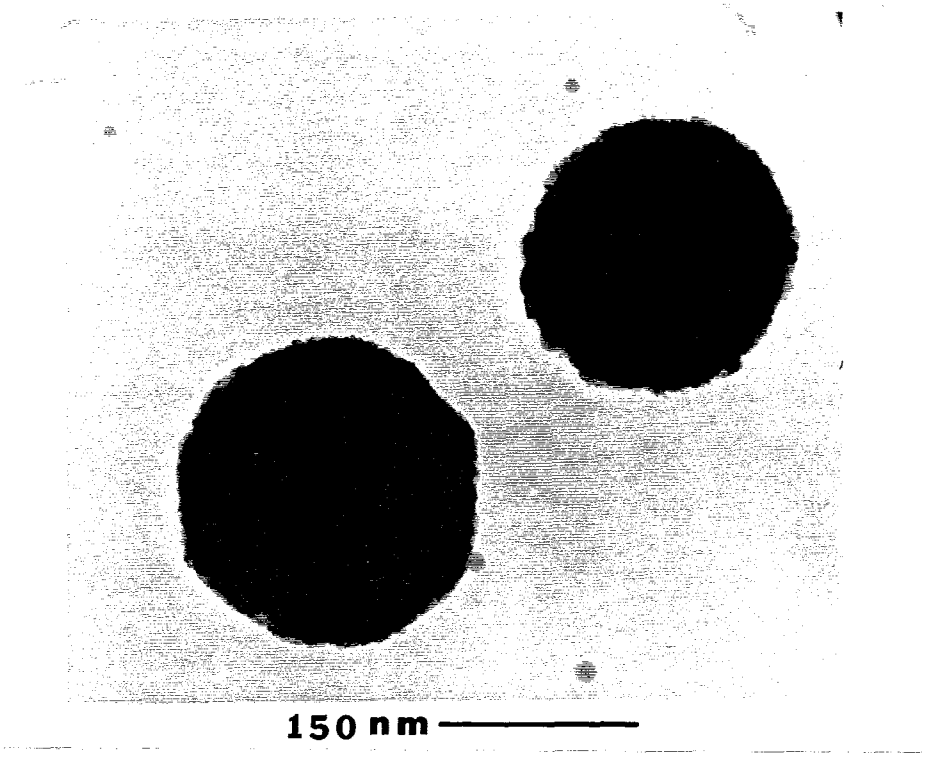

Figure 4.11: Transmission electron micrographs of yttria particles synthesized from 441 g/l yttrium nitrate pentahydrate in n-propyl alcohol, cured at 550°C for 5.7 seconds.

Figure 4.9(middle) shows the size distributions of oxide particles derived from the 93.4 g/l yttrium nitrate hexahydrate in n-propyl alcohol. The volume distribution was monomodal. The volume geometric mean diameter and geometric standard deviation were 190 nm and 1.4, respectively. Although the size distributions were similar to those of Figs. 4.9(top) and 4.9(bottom), the particle structure was different as shown in Figs. 4.12 and 4.13. The particles are shells with the wall thickness roughly one tenth of the diameter. These particle are therefore much less dense than those made from hexahydrated yttrium nitrates. Also, the surfaces are smoother than those of the previous two cases. The dark field micrograph (Fig. 4.12, bottom) shows individual crystallites in each particle. These are roughly 50 Å across and can also be seen in Fig. 4.13 as rows of crystal planes.

Charlesworth and Marshall [43] and Leong [44, 45, 46] considered the factors affecting the morphology of solute particles precipitated from evaporating solution droplets. As the droplet evaporates, there is an increased concentration of solute near the surface. The associated concentration gradient causes solute to diffuse toward the center of the droplet. If the droplet is small, the diffusion time scale is short enough to avoid precipitation at the droplet surface. If the droplet is large, the diffusion of solute is too slow to avoid precipitation and a solute shell form. Although there are many factors to consider in the evaporation and precipitation process, a general finding from Leong's work is that shells will not tend to form if the solute mass in a droplet is below an equivalent solid particle diameter of about three microns. Since the present particles lie below this size, the evaporation and precipitation process is not expected to produce shell particles.

Therefore the observed difference in structure is probably due to the difference in

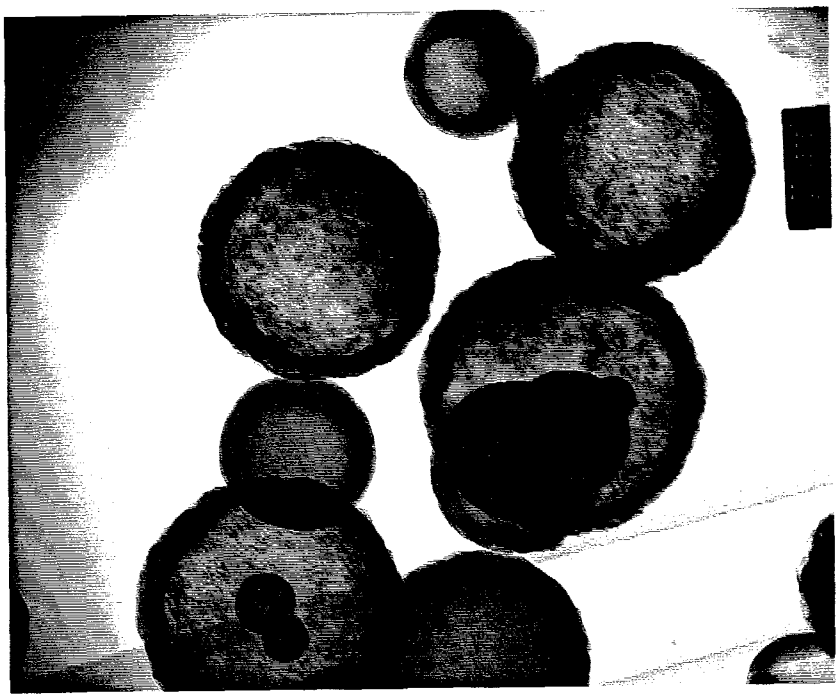

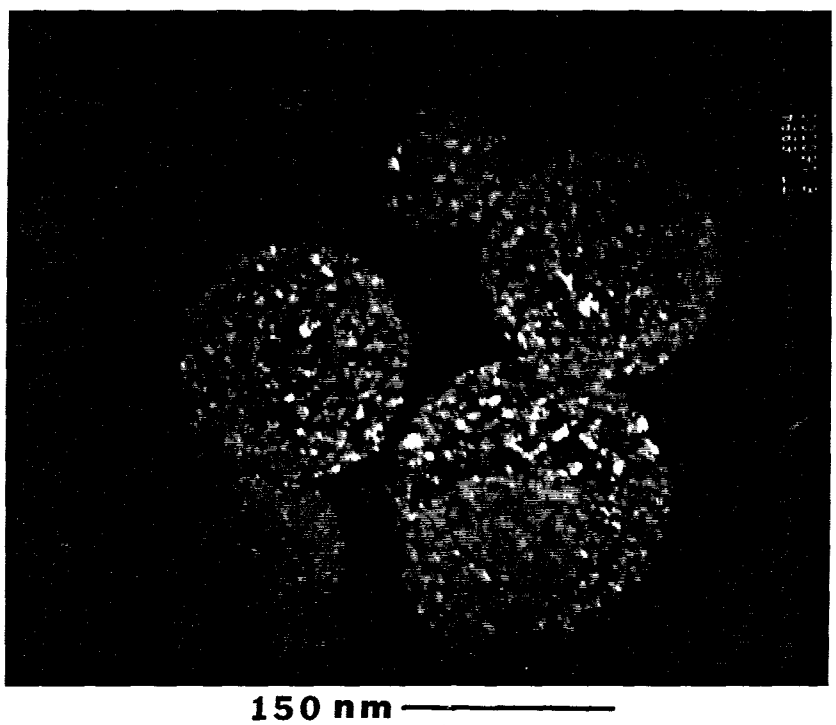

Figure 4.12: Transmission electron micrographs of yttria particles synthesized from 93.4 g/l yttrium nitrate hexahydrate in n-propyl alcohol, cured at 550°C for 5.7 seconds. Top: bright field micrograph. Bottom: Dark field micrograph.

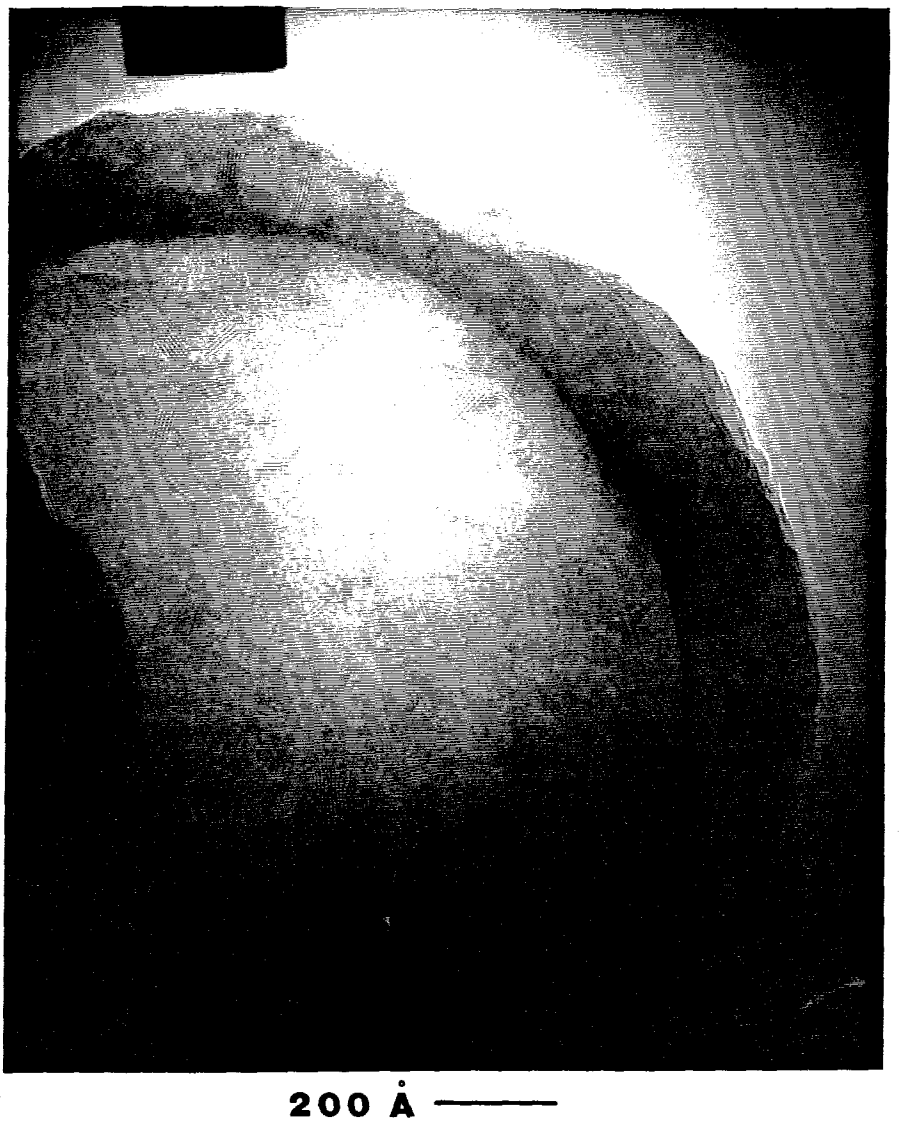

Figure 4.13: Transmission electron micrograph of yttria particles synthesized from 93.4 g/l yttrium nitrate hexahydrate in n-propyl alcohol, cured at 550°C for 5.7 seconds.

the level of hydration of the yttrium nitrate. For the 44.2 and 441 g/l cases, the level of hydration was 5, while for the 93.4 g/l case it was 6. The higher level of hydration appears to result in a particle surface which is impermeable to the alcohol vapor being given off during evaporation and thermal decomposition. The trapped vapor causes the particle to inflate during curing, resulting in the thin-walled and smooth shell structures (Fig. 4.14a). The hydration level of 5 does not appear to result in an impermeable surface, since the particles collapse into lower density structures during curing (Fig. 4.14b). This explanation is supported by experiments done on bulk solutions. A solution of 6-hydrated yttrium nitrate in n-propyl alcohol forms blisters of yttrium oxide several millimeters across after curing in a crucible heated to 550°C, while a 5-hydrated one does not.

Zhang and Messing [47] found similar results for the conditions necessary to form dense particles during spray pyrolysis. In synthesizing zirconia, use of zirconyl nitrate in aqueous solution gave hollow, shell structures while use of zirconyl chloride and zirconyl hydroychloride resulted in denser structures. They explained their results in terms of the formation of a gas-impermeable particle surface in the case of the nitrate salt.

The efficiency of the atomizer and aerosol flow system in spraying the above solutions was approximately 2 percent–that is, the amount of yttria collected on the Nuclepore filter in a given time was 2 percent of the amount known to be flowing in the liquid precursor into the atomizer. It was found that the efficiency could be increased by an order of magnitude by taking two steps: 1) increasing the hydrostatic head supplying liquid to the cone such that the cone semi-vertex angle decreased to 30°, i.e., the cone length increased, and 2) exchanging the power supplies so that a negative

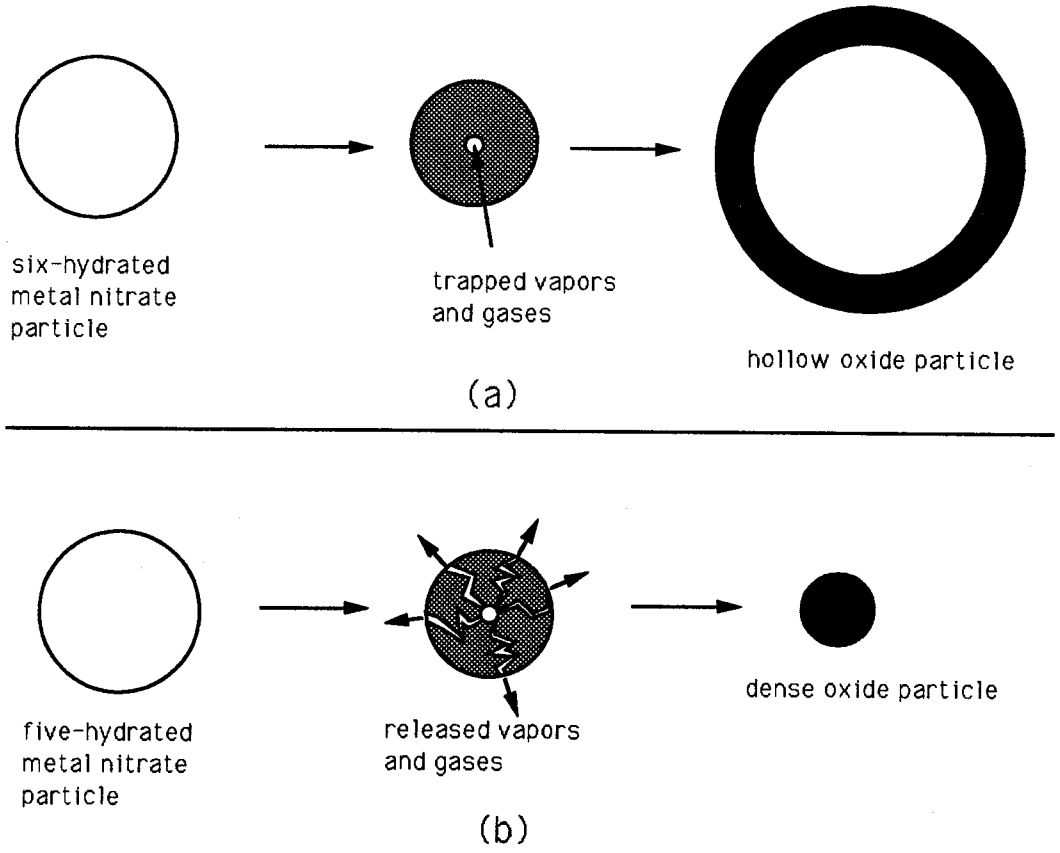

Figure 4.14: Schematic explanation of the dependence of particle structure on hydration level in yttrium and lanthanum nitrates.

6000 volts of electrical potential was applied to the electrode, i.e., $V/V_0 = 1.3$, and +11000 volts was applied to the corona needle. For the 441 g/l solution, the electrode current decreased from -0.1 to -1.0 μA, the corona needle current increased from 0.1 to 1.0 μA, and the volumetric flow rate of liquid increased from 1.27 to 1.60 μl/min. The increased corona discharge current and electric field strengths increased the overall aerosol flow system efficiency to 25 percent. Estimating the thermophoretic losses downstream of the furnace indicates that the atomizer efficiency was near 50 percent. The atomizer efficiency was very sensitive to the exact cone angle used, but no attempt to fine tune the potentials and cone angle was made, other than to operate at the higher potential just reported, and at the cone semi-vertex angle of 30°.

The size distribution of yttria powder collected under these conditions is shown in Fig. 4.15. The number distribution was bimodal. The volume size distribution was monomodal. The volume geometric mean diameter and geometric standard deviation were 480 nm and 1.4, respectively. This size distribution is similar to those for the lower efficiency atomization conditions, except that the volume distribution is shifted to larger particle diameters. The structure of these particles is shown in Fig. 4.16. The particles are shells with wall thickness roughly one third of the diameter. This is similar to the other particles made from the other 5-hydrated yttrium nitrate salt solutions.

Bulk samples were collected for x-ray diffraction. A 5 mg powder sample was spread on a glass microscope slide and placed in an INEL diffractometer using Cobalt k-α radiation (1.7902 Å). The powder diffraction pattern, shown in Fig. 4.17, is that of cubic yttrium oxide. The standard is shown below the data. No other phase is indicated. This is the expected phase of yttria below 2350°C [48]. There is consid-

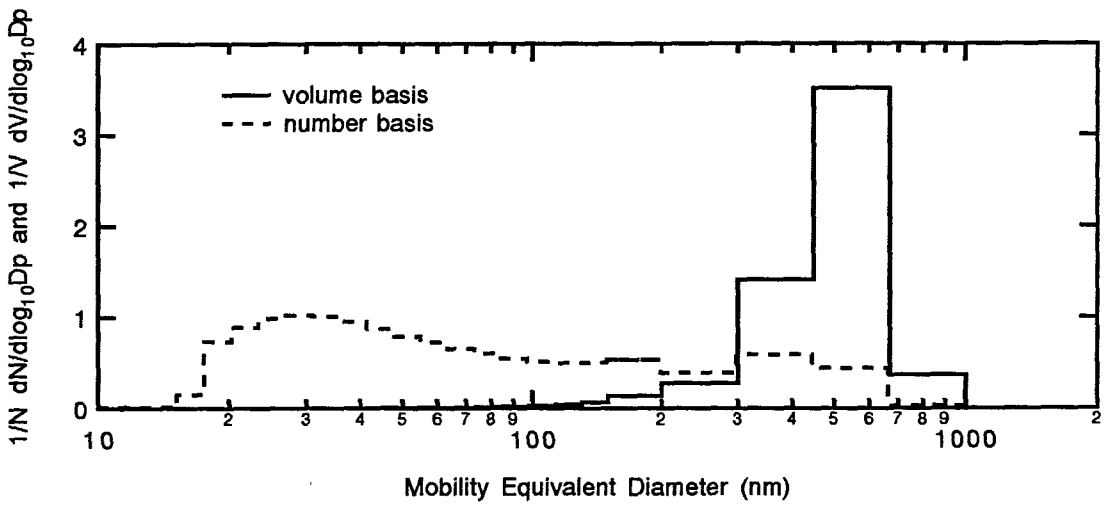

Figure 4.15: Size distribution of yttrium oxide particles synthesized from 441 g/l yttrium nitrate pentahydrate in n-propyl alcohol, cured at 550°C for 5.7 seconds, high efficiency case.

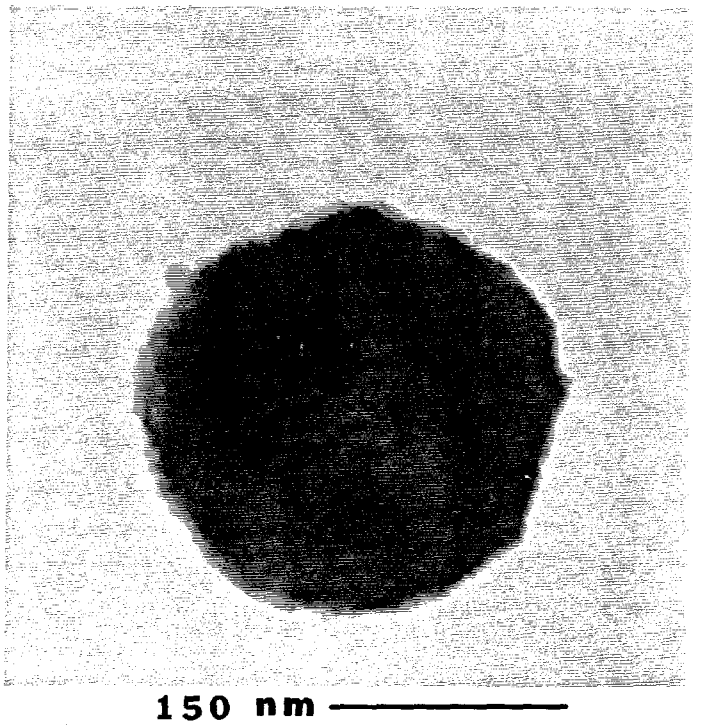

Figure 4.16: Transmisson electron micrograph of an yttria particle synthesized from 441 g/l yttrium nitrate pentahydrate in n-propyl alcohol, cured at 550°C for 5.7 seconds, high efficiency case.

erable scatter from the glass substrate because the powder sample was thin, which caused the overall higher intensity on the low angle side of the plot. The peaks in the diffraction pattern were broadened significantly due to the small size of crystallites making up each particle. Using Scherrer's formula [49] to estimate the crystallite size gives 32 Å. This is uncorrected for instrument broadening and is, therefore, an underestimate. The high resolution transmission electron micrographs (bright field and dark field) of the 93.4 g/l case show crystallite sizes of the same order of magnitude (Figs. 4.12 and 4.13).

4.3.2 Lanthana-doped Yttria

The favored method for producing optically transparent yttria is to dope it with 9 mole percent lanthana [48]. The lanthana is a sintering aid which allows the material to be sintered to very near zero porosity. A hexagonal phase precipitates in the cubic phase at high temperature ($\sim 2100°C$). The hexagonal phase effectively pins the grain boundaries, making it impossible for grains to swallow pores, and allowing the pores to sinter via grain boundary sintering mechanisms. After holding in the two-phase region to remove the pores, the hexagonal phase can be removed by annealling or retained for mechanical toughening.

To produce lanthana-doped yttria via the electrospray method, we combined lanthanum nitrate hexahydrate and yttrium nitrate pentahydrate in n-propyl alcohol to produce the required mole percentage of lanthana in the oxides. The solution used had 20.5063 g yttrium nitrate pentahydrate and 2.5296 g lanthanum nitrate hexahydrate in n-propyl alcohol to make 455 ml of solution. This should result in 9.42 mole percent lanthana in the oxides after thermal decomposition.

The rheological properties of this solutions are as follows: absolute viscosity,

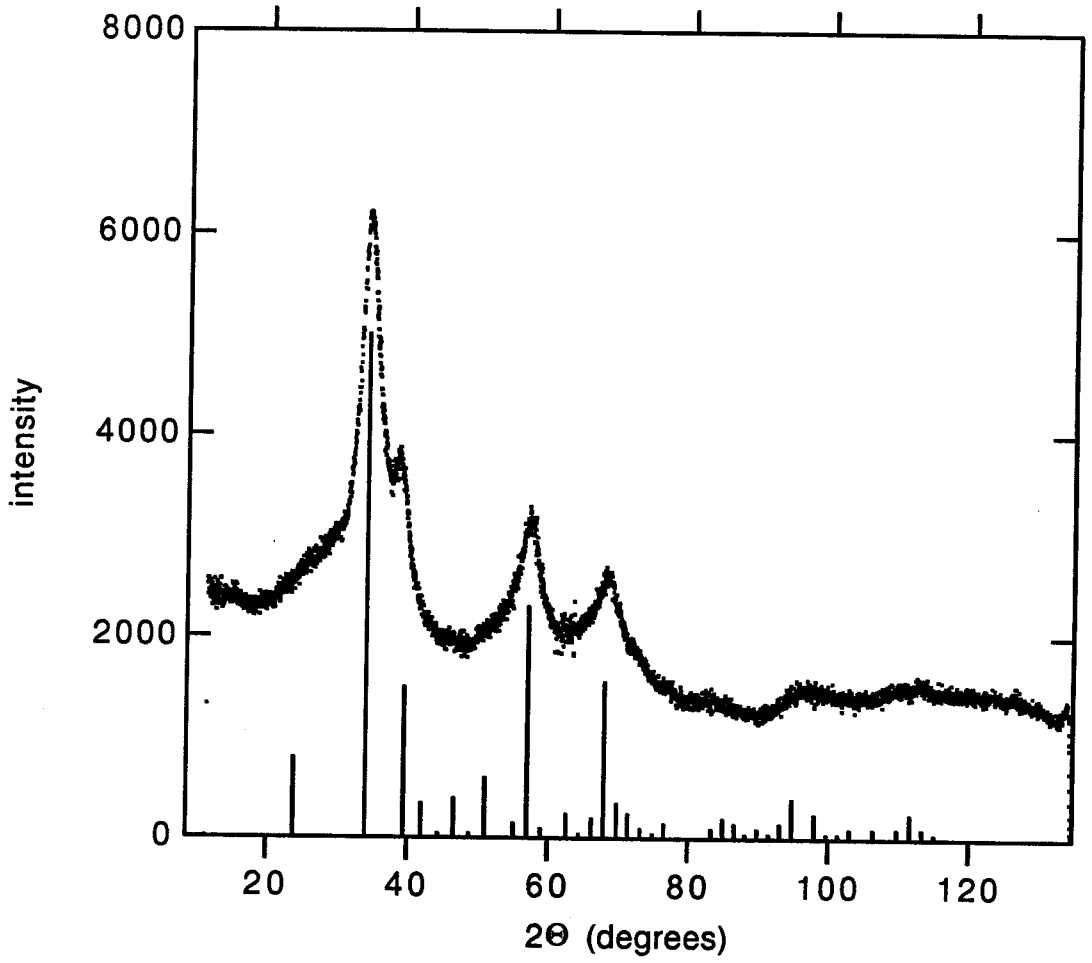

Figure 4.17: X-ray diffraction pattern for undoped yttria powder synthesized from 441 g/l yttrium nitrate pentahydrate in n-propyl alcohol electrosprayed at P=1.3, cured at 550°C for 5.7 seconds, high potential case.

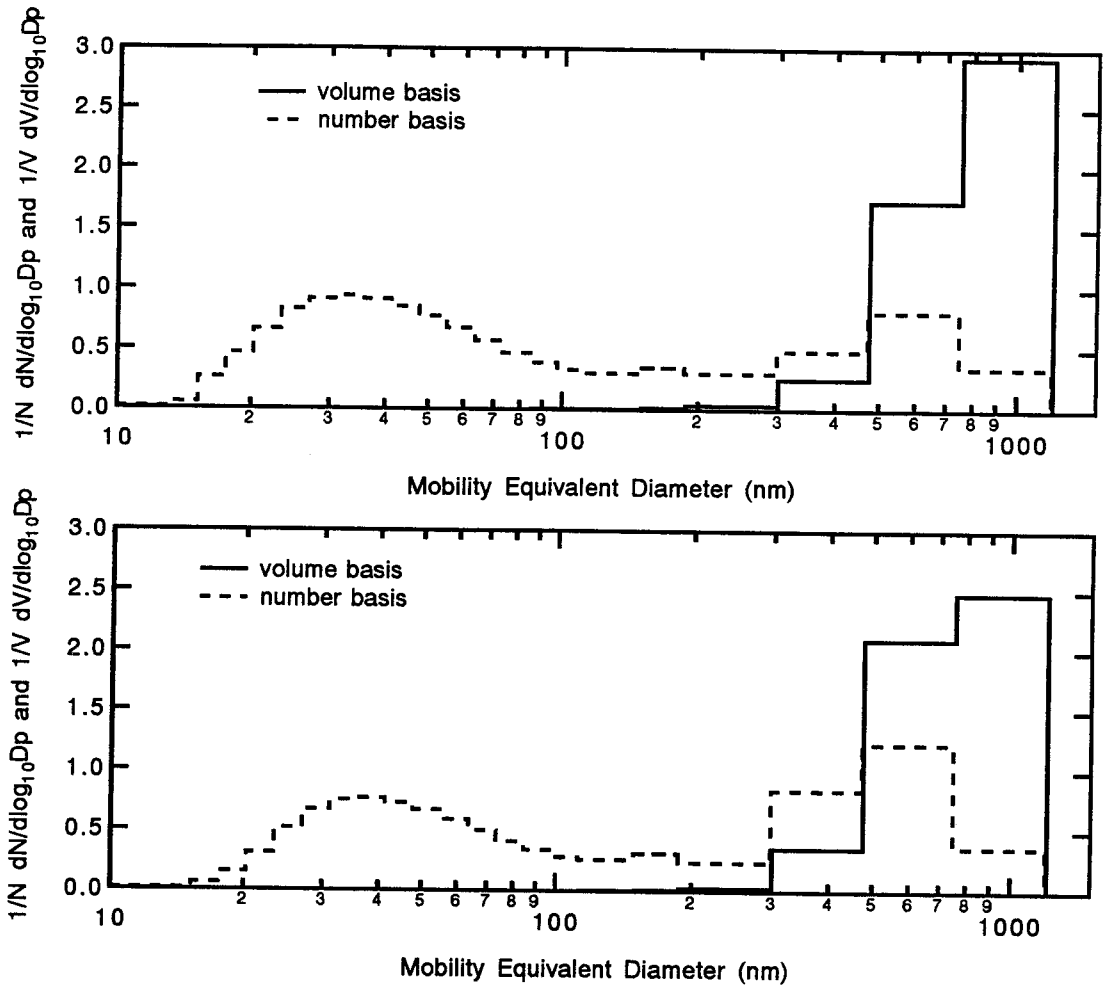

Figure 4.18: Size distribution of lanthana-doped yttria particles synthesized from 445 g/l hydrated metal nitrates in n-propyl alcohol, cured at 656°C for 5.1 seconds (top) or 725°C for 4.7 seconds (bottom).

0.014 kg s^{-1} m^{-1}; specific electrical conductivity, 0.0994 mhos/m; surface tension, 0.021 N/m; density, 983 kg m^{-3}.

Two furnace temperatures were used. The size distribution obtained for a curing temperature of 656°C is shown in Fig. 4.18(top). As for all of the size distributions reported, the number distribution was bimodal. The volume distribution was monomodal. The volume geometric mean diameter and geometric standard deviation were 780 nm and 1.4, respectively.

This powder contains a mix of structures, as seen in Fig. 4.19. Some 44 ± 10%

particle type	mole percentage of lanthanum
dense	10.7 ± 0.3
dense	10.5 ± 0.3
dense	10.2 ± 0.3
hollow	11.8 ± 0.4
hollow	11.3 ± 0.3

Table 4.1: Correlation between oxide particle structure and lanthanum content.

of the particles appear dense in the transmission electron micrographs (counted over several hundred particles ranging in size from 150 nm to 1200 nm), and the remaining particles appear to be shell structures. The origin of the shell structures in this powder is probably the formation of a gas-impermeable particle surface during thermal decomposition, as occurred with the 6-hydrated yttrium nitrate.

We selected particles randomly and measured the mole percentage of lanthana in particles of each type to see whether there was a correlation between particle structure and lanthana content. The mole percentage of lanthanum was measured using EDAX energy dispersive x-ray analysis in combination with a Phillips 430 transmission electron microscope. Because the measurements were time-consuming, only five particles were tested. The results are shown in Table 4.1. There is an average of 10% more lanthanum in hollow particles compared to dense particles. This indicates that the excess of lanthanum nitrate hexahydrate probably contributed to gas-impermeable particle surfaces during curing.

Note that both particle types have greater mole percentages of lanthana than the original solution, which was mixed to give 9.42 mole percent. This difference may be due to uncertain hydration levels in the solutes which would introduce errors when the materials were weighed. Another explanation is possible: The flow of charge in the electrospray must ultimately originate with electrolytic reactions on the inside

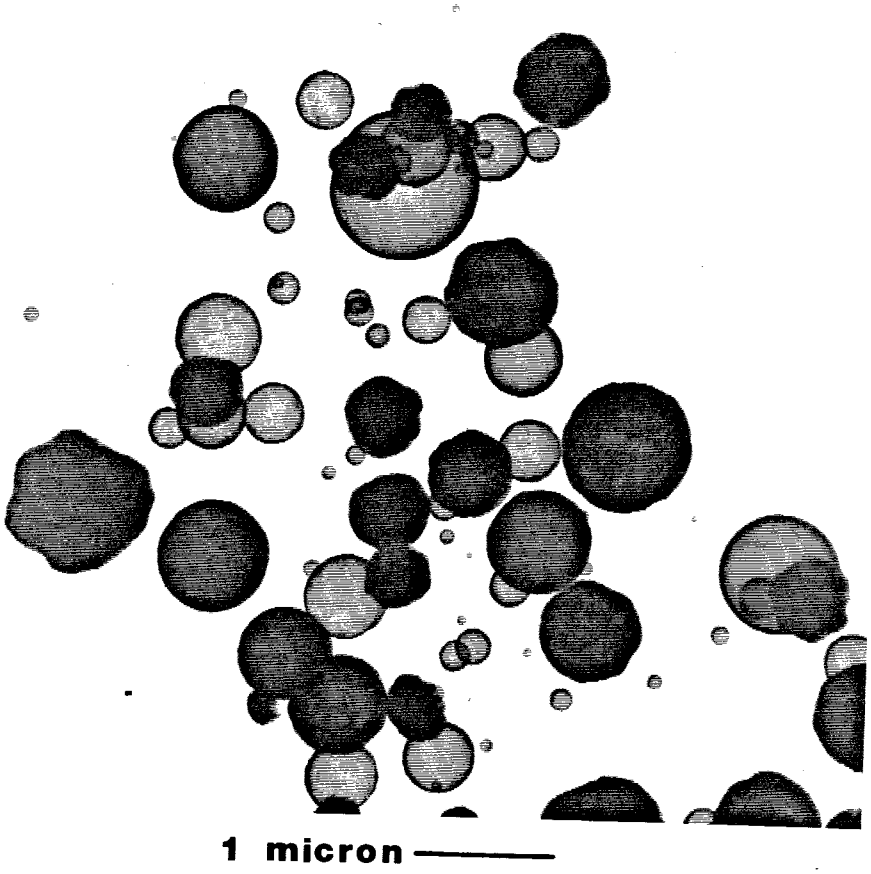

Figure 4.19: Transmission electron micrograph of lanthana-doped yttria particles synthesized from 445 g/l hydrated metal nitrates in n-propyl, cured at 656°C for 5.3 seconds.

face of the capillary electrode. In these experiments the electrospray had a negative current, i.e., the droplets had a negative charge. Therefore, reduction reactions must have occurred at the interface between the solution (hydrated lanthanum and yttrium nitrates in n-propyl alcohol) and the stainless steel capillary electrode. A variation in the rate constants of the electrolytic reactions may also account for the deficit of yttrium in the ceramic.

Differences in ionic mobility between Y^{3+} and La^{3+} may have caused the observed difference in lanthanum content from one particle to the next. As droplets are formed in the electrospray, liquid surfaces are exposed to periodically varying electric field strengths. The liquid supplied to the electrospray, however, has a constant concentration of solute ions. Electrical separation may, therefore, occur in a fluctuating manner within the bulk of the liquid, particularly near the end of the jet where droplets are being formed. Such separation may have led to the observed variation of lanthanum content from one particle to the next.

The x-ray diffraction pattern obtained for this powder is shown in Fig. 4.20. The material is cubic, as is the case for the undoped yttria. The presence of 9.42 mole percent of lanthana had no effect on the phase of material, as expected for temperatures less than about 2100°C. The peak broadening in the x-ray diffraction indicates an average crystallite size of 36 Å, uncorrected for instrument broadening. This is larger than the crystallite size found for undoped yttria cured at 550°C.

Particles from this solution were also cured at a furnace temperature of 725°C. The size distribution appears very similar to that for a furnace temperature of 656°C (Fig. 4.18(bottom)). The number distribution was bimodal. The volume distribution was monomodal. The volume geometric mean diameter and geometric standard

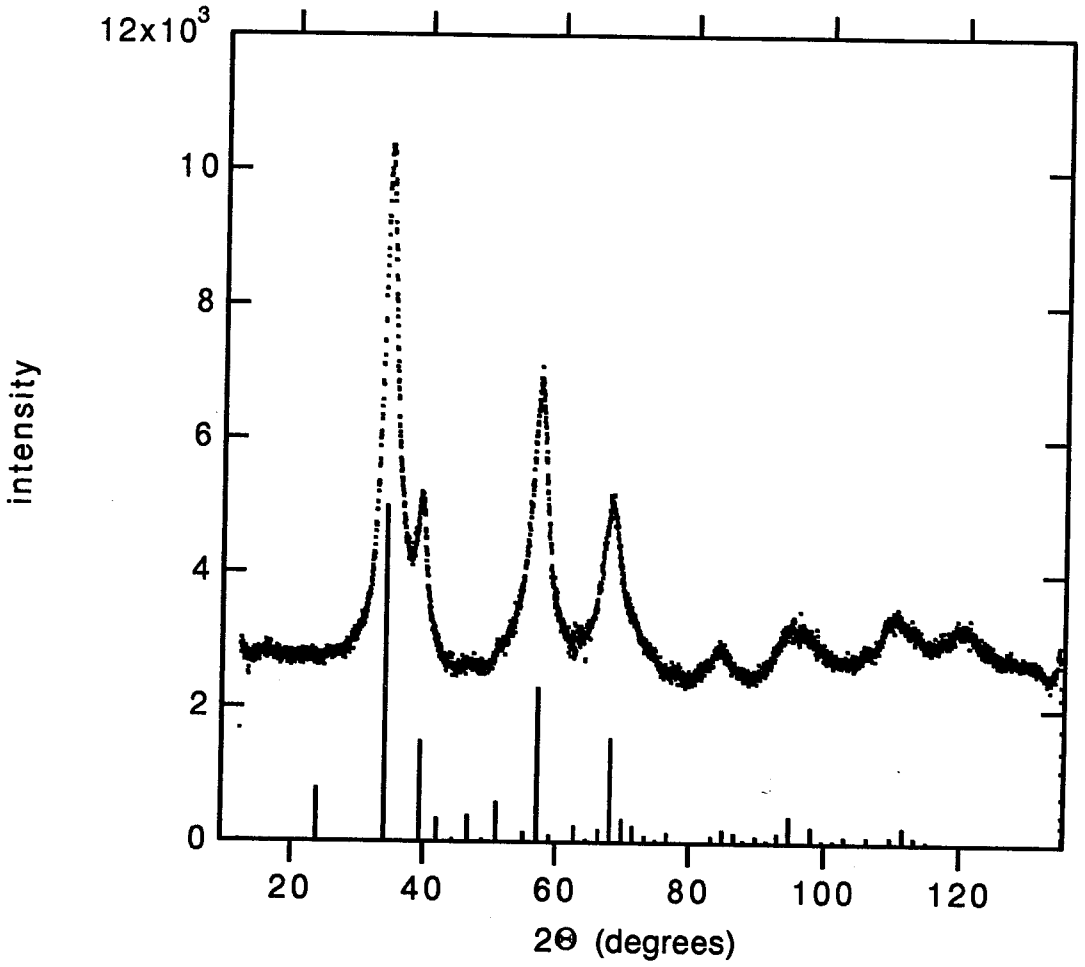

Figure 4.20: X-ray diffraction pattern for lanthana-doped yttria powder synthesized from 445 g/l hydrated metal nitrates in n-propyl alcohol, cured at 656°C for 5.3 seconds.

deviation were 740 nm and 1.4, respectively.

The structures of these particles, seen in Figs. 4.21 and 4.22, was very similar to the 656°C case, with 41 ± 10% of the particles appearing dense in the transmission electron micrographs (counted over several hundred particles ranging in size from 150 nm to 1200 nm), the remaining particles appear to be shell structures. The explanation given above for the observed mix of particles involving the separation of yttrium and lanthanum nitrate by electrical separtion applies here as well. The fact that nearly the same fraction of particles appear dense for both 656°C and 725°C cases indicates that the particle structure was not dependent on temperature, and so was not an artifact of incomplete curing.

The x-ray diffraction pattern obtained for this powder is shown in Fig. 4.23. The material is again cubic, as expected. The peak broadening indicates an average crystallite size of 55 Å, uncorrected for instrument broadening. There is therefore a correlation between the furnace temperature and the crystallite size. Higher furnace temperatures result in larger crystallite sizes. This is due to the growth of crystallites, i.e., grain growth, while the oxide particles are in the furnace.

4.4 Conclusions

Electrospray pyrolysis was used to synthesize powders comprising submicron, spheroidal, nanocrystalline particles of undoped and lanthana-doped yttria from very highly concentrated solutions of hydrated yttrium nitrate and hydrated lanthanum nitrate in n-propyl alcohol. These were atomized using electrospray atomization. The resulting aerosol droplets were then thermally decomposed in a flow tube reactor with air as the carrier gas. Success was achieved in synthesizing powders which satisfy the criteria

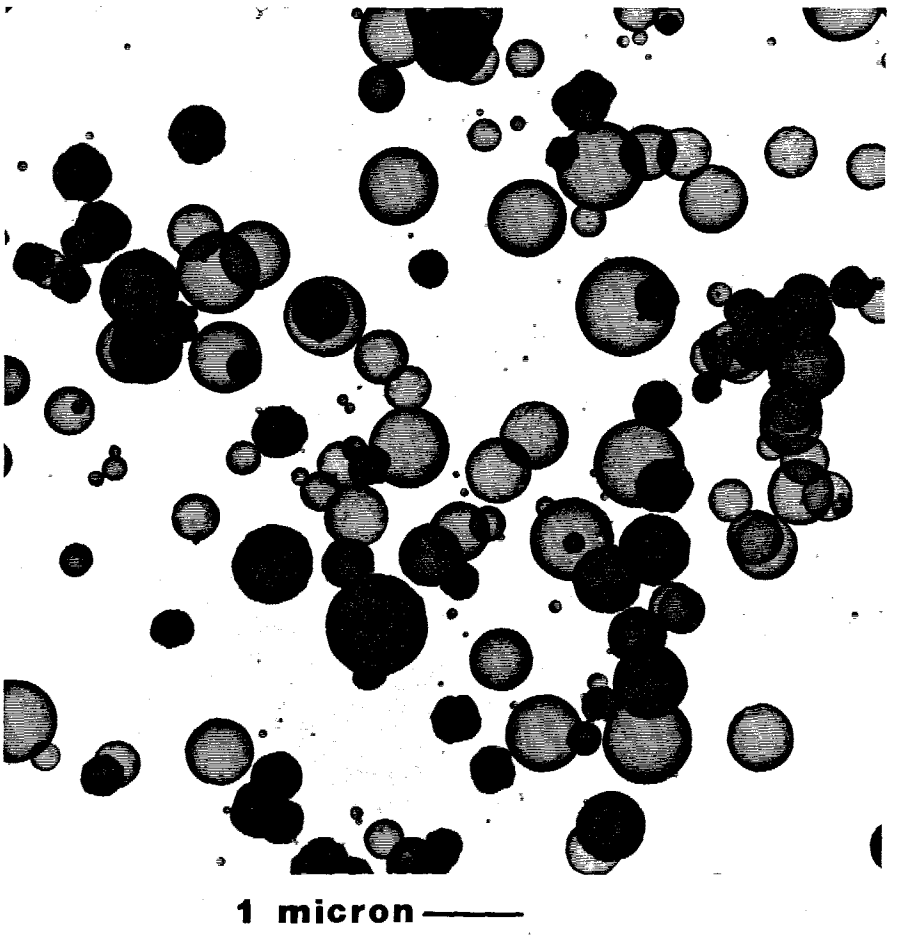

Figure 4.21: Transmission electron micrograph of lanthana-doped yttria particles synthesized from 445 g/l hydrated metal nitrates in n-propyl alcohol, cured at 725°C for 4.7 seconds.

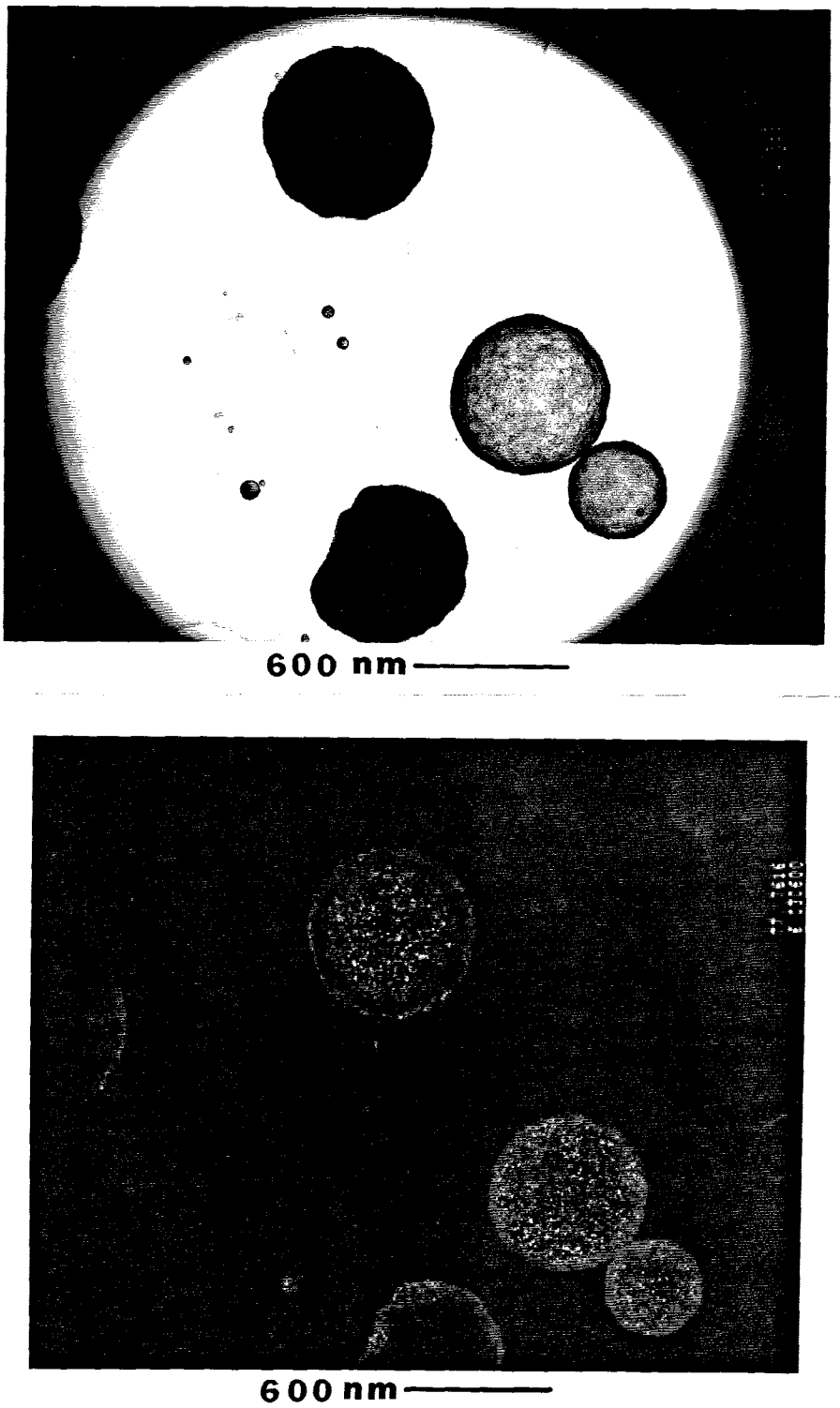

Figure 4.22: Transmission electron micrographs of lanthana-doped yttria particles synthesized from 445 g/l hydrated metal nitrates in n-propyl alcohol, cured at 725°C for 4.7 seconds. Top: Bright field image. Bottom: Dark field image.

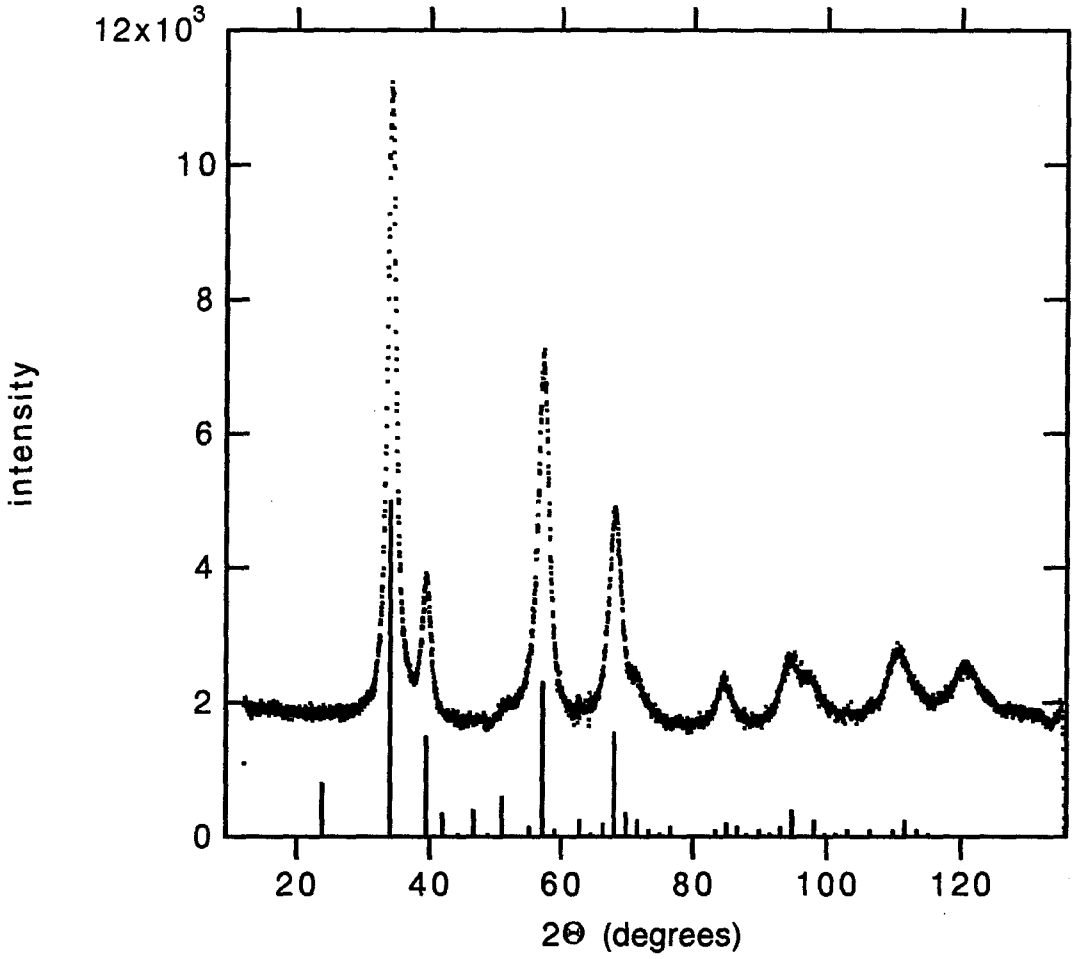

Figure 4.23: X-ray diffraction patterns for lanthana-doped yttria powder synthesized from 445 g/l hydrated metal nitrates in n-propyl alcohol, cured at 725°C for 4.7 seconds.

for production of high-quality ceramic components by consolidation and sintering, i. e., the particles were dense, spherical, and submicron. Three solutions in n-propyl alcohol were tested for the undoped yttria case: 41.1 and 441 g/l yttrium nitrate pentahydrate, and 93.4 g/l yttrium nitrate hexahydrate. The number size distribution of powders made from these three solutions were all bimodal. The volume size distributions were all monomodal, with the volume geometric mean diameters ranging from 170 to 290 nm. The volume geometric standard deviations ranged from 1.3 to 1.5.

The choice of chemical precursor strongly affected the structure of particles synthesized using electrospray pyrolysis. The yttrium oxide particles made from 5-hydrated yttrium nitrate salts appeared to have dense structures. The particles made from 6-hydrated yttrium or lanthanum solutions were shells. The shells were due to the formation of a gas-impermeable particle surface which trapped the gases given off in thermal decomposition, thus inflating the particles. Evidently, the 5-hydrated yttrium nitrate formed a gas-permeable particle surface during decomposition while the 6-hydrated yttrium nitrate did not.

The x-ray diffraction pattern for the 441 g/l derived yttria showed the expected cubic phase. Dark field transmission electron micrographs indicated a crystallite size of 150 Å.

One solution for producing lanthana-doped yttria was tested. It contained the appropriate amount of lanthanum nitrate hexahydrate to give 9.42 mole percent of lanthana in the oxides and had 455 g/l total solutes. Two furnace temperatures were used. The size distributions were similar to those for the undoped yttria case, with a bimodal number distribution and a monomodal volume distribution. A mix of

particle structures was seen. Some 44 ± 10% of the particles in the 656°C case were dense, and 41 ± 10% in the 725°C case were dense, while the remaining particles were shells. There was a correlation between particle structure and lanthana content such that hollow particles had higher percentages of lanthana content than dense ones. The lanthanum nitrate hexahydrate appeared to have the same tendency to form a gas-impermeable shell as the yttrium nitrate hexahydrate, emphasing the importance of precursor selection in spray pyrolysis. The variation of lanthanum content from one particle to the next may be due to electrical separation of La^{3+} and Y^{3+} in the atomization process.

Acknowledgments

This work was supported by the National Science Foundation, grant numbers CBT8813006 and CTS9113191. Support was also provided by GTE Laboratories, Inc., Waltham, MA.

Chapter 5

Scale-up of Electrospray Atomization using Linear Arrays of Taylor Cones

Abstract

Linear arrays of Taylor cones were established on capillary electrode tubes opposite a slotted flat plate counter-electrode to investigate the feasibility of increasing the liquid throughput rate in electrospray atomizers. It was found that individual Taylor cones could be established on each capillary over a wide range of the capillary radius to spacing ratio R/S. The onset potential, V_s, required to establish the cones varied directly with R/S, but the liquid flow rate per cone and current per cone were nearly independent of R/S for a given overpotential ratio $P = V/V_s$. Only six working capillaries were used, but the results per cone are applicable to larger arrays of cones since end effects were minimized.

5.1 Introduction

Electrospray atomization is a method of dispersing a liquid into droplets or ions by overcoming surface tension forces with electrical forces. Droplets or ions are emitted from the tip of a Taylor cone [1], which is the equilibrium shape of a free liquid

surface at the end of a capillary electrode in a sufficiently intense electric field. It has been applied to production of ceramic powders (Chapter 4) [50], production of aerosol standards [22], application of coatings [51], dispersion of pesticides [52], space thrusters [53], and mass spectrometry [54]. Technologies such as ceramic powder production by spray pyrolysis require large liquid throughputs to be economically feasible. A single Taylor cone, however, processes only several microliters per minute of typical ceramic precursors (Chapter 4).

The liquid throughput in electrospray atomization can be increased by operating a number of Taylor cones in parallel. This paper reports the liquid throughput and electrical current as a function of capillary spacing for a linear array of Taylor cones.

5.2 Experiment

A linear array of capillary electrodes opposite a slotted flat plate counter-electrode was constructed to test the operation of a multiple-cone sprayer (Fig. 5.1). Capillaries were made by squaring the tips of stainless steel hypodermic needles. Up to eight capillaries could be mounted at any spacing between two aluminum angle beams, one of which had a rubber strip on its face to provide holding friction. The counter-electrode was constructed from two stainless steel plates connected with a thin stainless steel sheet. A slot was maintained between the two plates by mounting them on a Lucite frame which also held the aluminum beams and capillaries. The capillaries were thus electrically insulated from the plates. A Spellman model WRM15P1500D positive high voltage ower supply was attached to the capillaries. The counter-electrode assembly was grounded through an ammeter sensitive to $\pm$ 10 nA.

Liquid was supplied to each capillary using a syringe pump which compressed

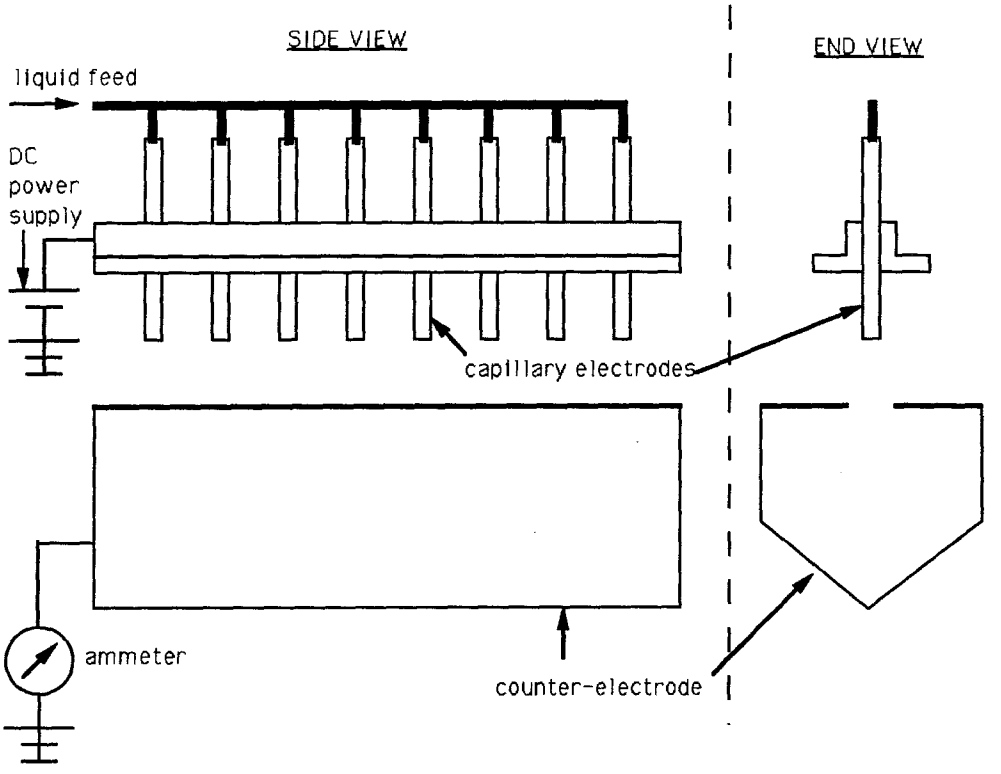

Figure 5.1: Multiple electrode electrospray apparatus.

syringes in parallel. Thus each capillary sprayed the same volumetric flow rate of liquid. Although the capillaries were all at the same potential, they did not experience the same electric field due to end effects. To reduce the end effects, capillaries without liquid flow were added at each end of the array.

To establish the electrospray, the electrical potential on the capillaries was increased until Taylor cones formed on each capillary, V_s, and then further increased to an overpotential ratio of $P = V/V_s = 1.39$ or 1.6. The liquid flow rate was adjusted to obtain a cone half angle of $37.5 \pm 2°$ on the middle two cones in the array. The total electrical current, I_{total}, was measured by the current arriving at the counter-electrode. The average current per cone was thus I_{total}/n, where n is the number of capillaries supplied with liquid.

The liquid used in these tests was a solution of 0.618 g/l sodium iodide in n-propyl alcohol. The specific electrical conductivity was 0.00684 mhos/m. The surface tension was 0.0238 N/m.

5.3 Results and Discussion

The electric field required to establish a Taylor cone at the end of a capillary (the electrode) opposite a flat plate (the counter-electrode) is [7]

$$E_s(r_c) = (2T\cos\theta/\epsilon_0 r_c)^{1/2}, \tag{5.1}$$

where r_c is the capillary radius, T is the liquid surface tension, θ is the cone semi-vertex angle, and ϵ_0 is the permittivity of free space. The cone is only in equilibrium when the cone semi-vertex is 49.3°, ignoring space charge effects (De la Mora [10] examines the role of space charge). The potential difference between the electrode

and counter-electrode required to reach this field strength is

$$V_s = 0.667(2Tr_c \cos\theta/\epsilon_0)^{1/2} \ln(4h/r_c) \tag{5.2}$$

where h is the electrode to counter-electrode spacing. Thus the required potential increases with increasing surface tension, electrode radius, and electrode to counter-electrode spacing.

With a linear array of capillary electrodes the onset potential V_s is greater than that for a single electrode since neighboring electrodes reduce the electric field strength. The onset potential as a function of R/S is shown in Fig. 5.2. The $R/S = 0$ case corresponds to infinite spacing and was approximated using a single capillary. The onset potential increased from 4800 volts to 7400 volts as R/S increased from 0 to 1.6. Thus closer capillary spacing required a higher potential to form Taylor cones.

The liquid forming the cones responds to the electric field, not the potential level. Therefore if the potential is set to give the same electric field at different values of R/S, the flow of liquid and current will remain the same, assuming that the asymmetric electric field components at each capillary are small compared to the symmetric ones. The measured value of V_s provides an experimental determination of the electric field, and a reference value by which to set a constant electric field strength for operation of the cones. This was done by operating at fixed values of P as R/S varied.

The average current and volumetric flow rate per cone are plotted as functions of R/S in Figs. 5.3 and 5.4. For $P = 1.39$, the current varied by only 25 percent as R/S increased from 0 to 1.6. Similarly, the volumetric flow rate varied by about 33 percent. Most of the variation in current and volumetric flow rate was due to experimental inconsistencies in establishing the predetermined cone semi-vertex angle of $37.5 \pm 2°$ by adjusting the volumetric flow rate. Note that the dip in current occurring at

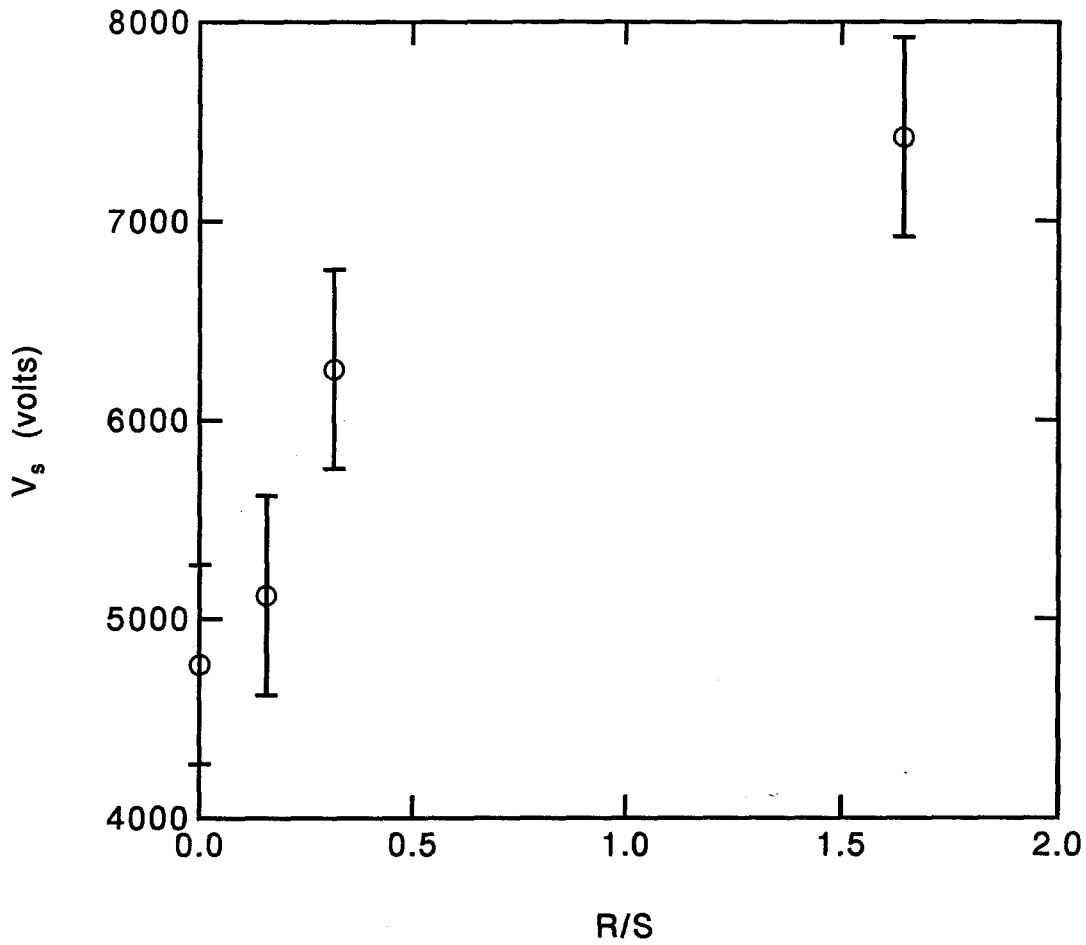

Figure 5.2: Onset potential of Taylor cones versus capillary radius to spacing ratio.

$R/S = 0.2$ correlated with a dip in volumetric flow rate.

Photographs of arrays of Taylor cones operating at various spacings are shown in Figs. 5.5 through 5.10.

Figure 5.5 shows a cone established on a single capillary, which corresponds to the case $R/S = 0$. Neither the cone's shape nor its behavior was influenced noticeably by the asymmetric electric field applied to it by the slotted counter-electrode.

Figure 5.6 shows cones established on capillaries spaced such that $R/S = 0.16$. Although the onset potential was greater for this array compared to that of a single cone, these cones did not differ in appearance or behavior from a cone established in an axially symmetric elecrical field once they were established.

Figure 5.7 shows cones established on capillaries spaced such that $R/S = 0.31$. Even with this closer spacing, the cones in the center of the array did not differ in appearance from a single cone. End effects, however, become noticeable on cones located at the edges of the array. Figure 5.8 shows two cones on the right hand side of the array. The end cone is deflected to the right, following the electric field. One end-effect capillary is present on each end of the array to reduce this effect. No liquid was supplied to the end-effect capillaries. To further reduce the field distortion, one might introduce conical tips on these guard electrodes. This would provide the influence of the Taylor cone, although it would not reproduce space charge effects.

Figure 5.9 shows cones established on capillaries spaced such that $R/S = 1.6$. Figure 5.10 shows five cones on the right hand side of the array. The two end cones are deflected to the right more strongly than in the $R/S = 0.31$ case.

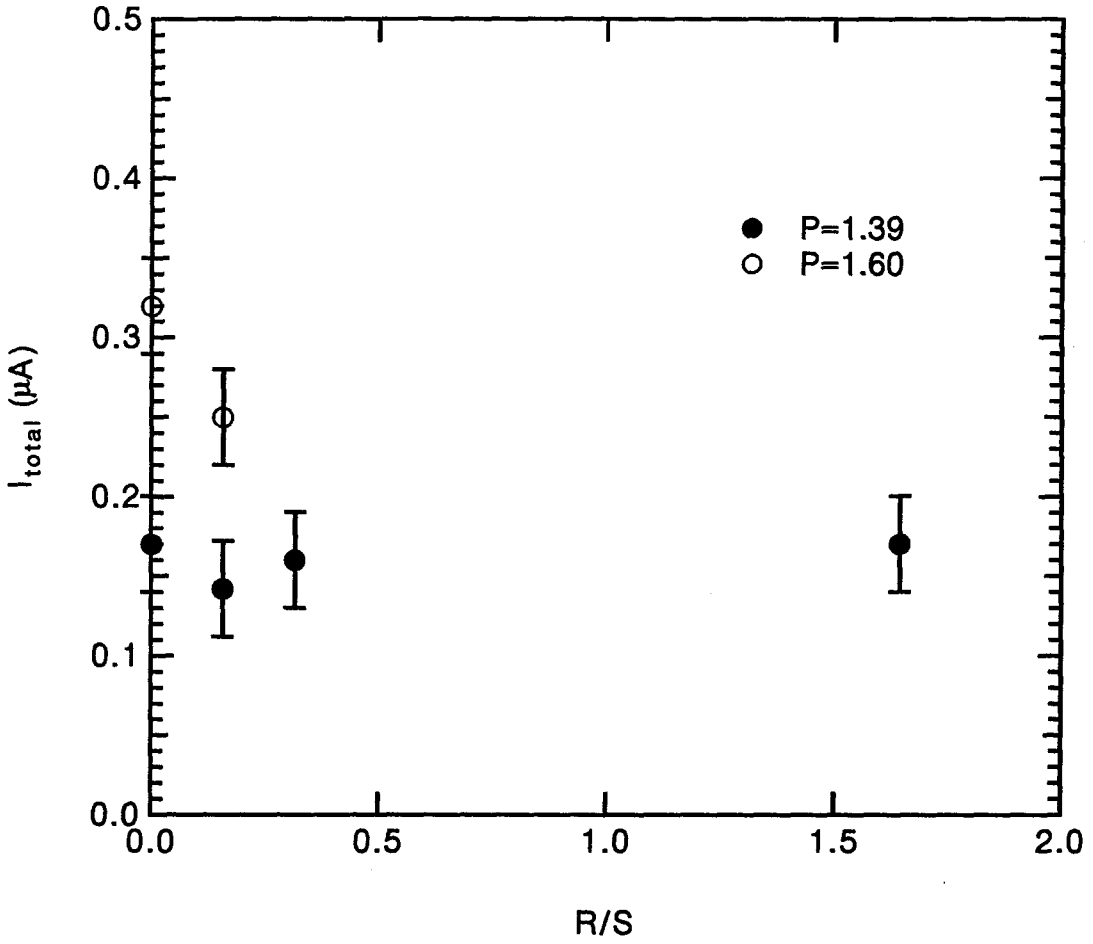

Figure 5.3: Average electrical current per cone versus capillary radious to spacing ratio.

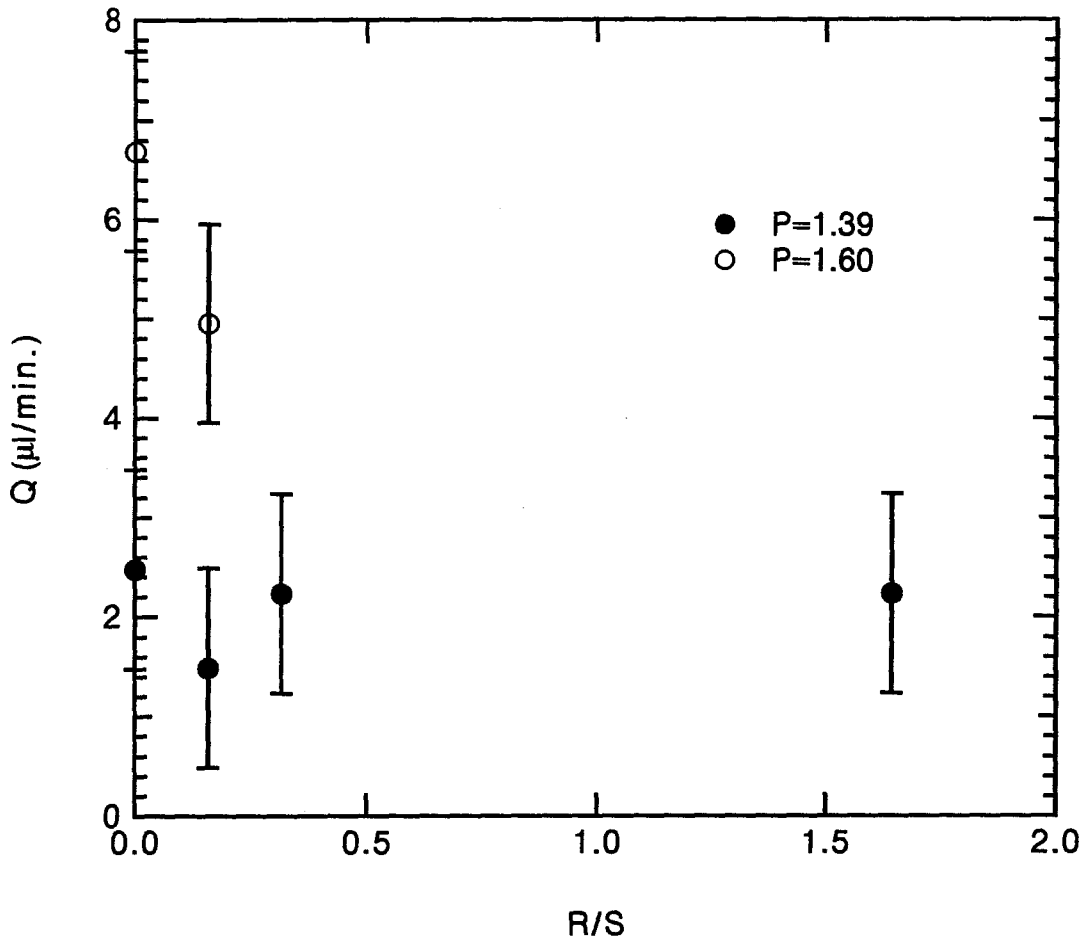

Figure 5.4: Volumetric flow rate per cone versus capillary radius to spacing ratio.

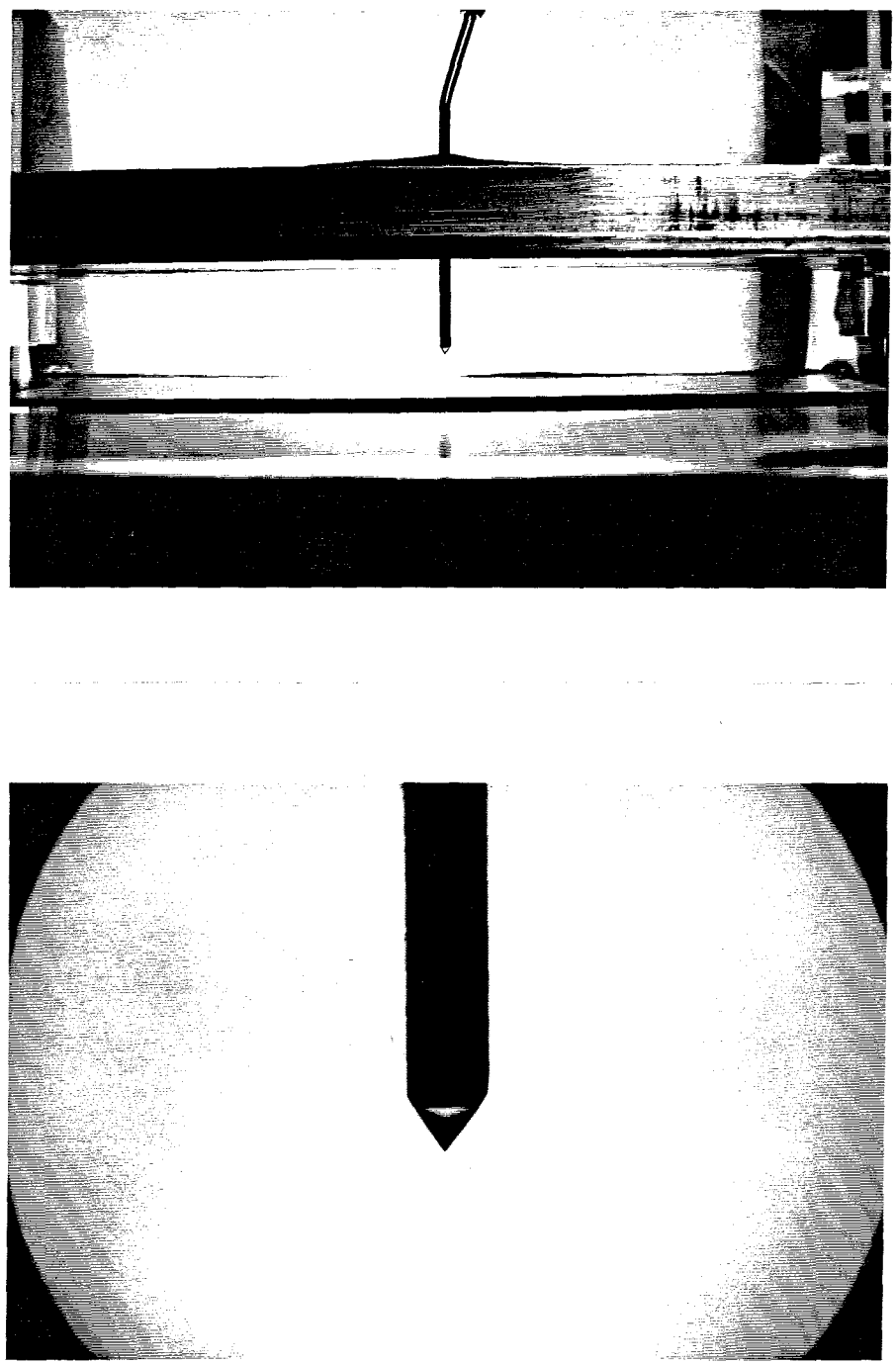

Figure 5.5: Photographs of a Taylor cone established on a capillary electrode placed opposite a slotted flat plate electrode. $R/S \rightarrow 0$, $P = 1.39$.

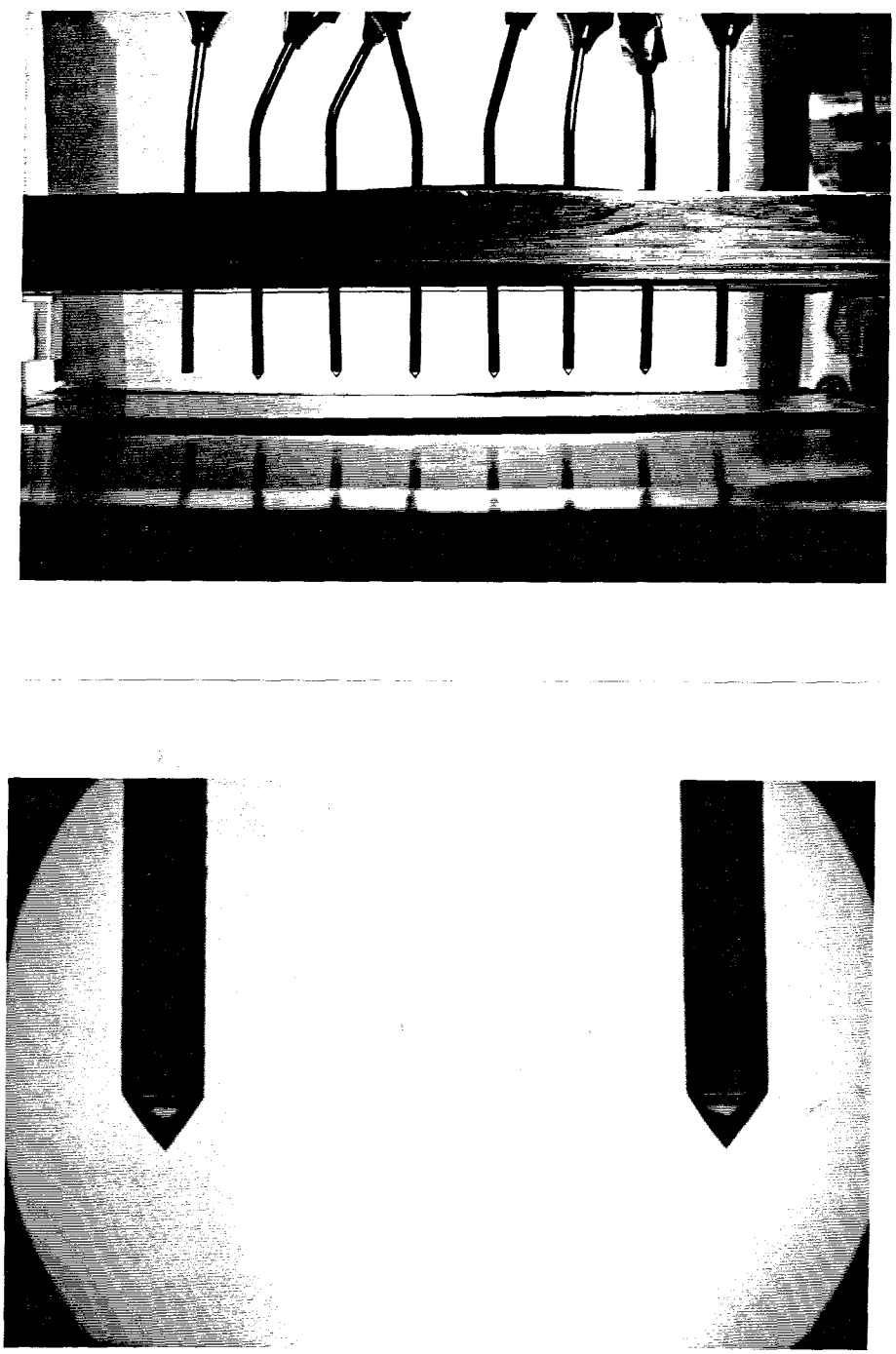

Figure 5.6: Photographs of a linear array of Taylor cones established on capillary electrodes placed opposite a slotted flat plate electrode. $R/S = 0.16$, $P = 1.39$.

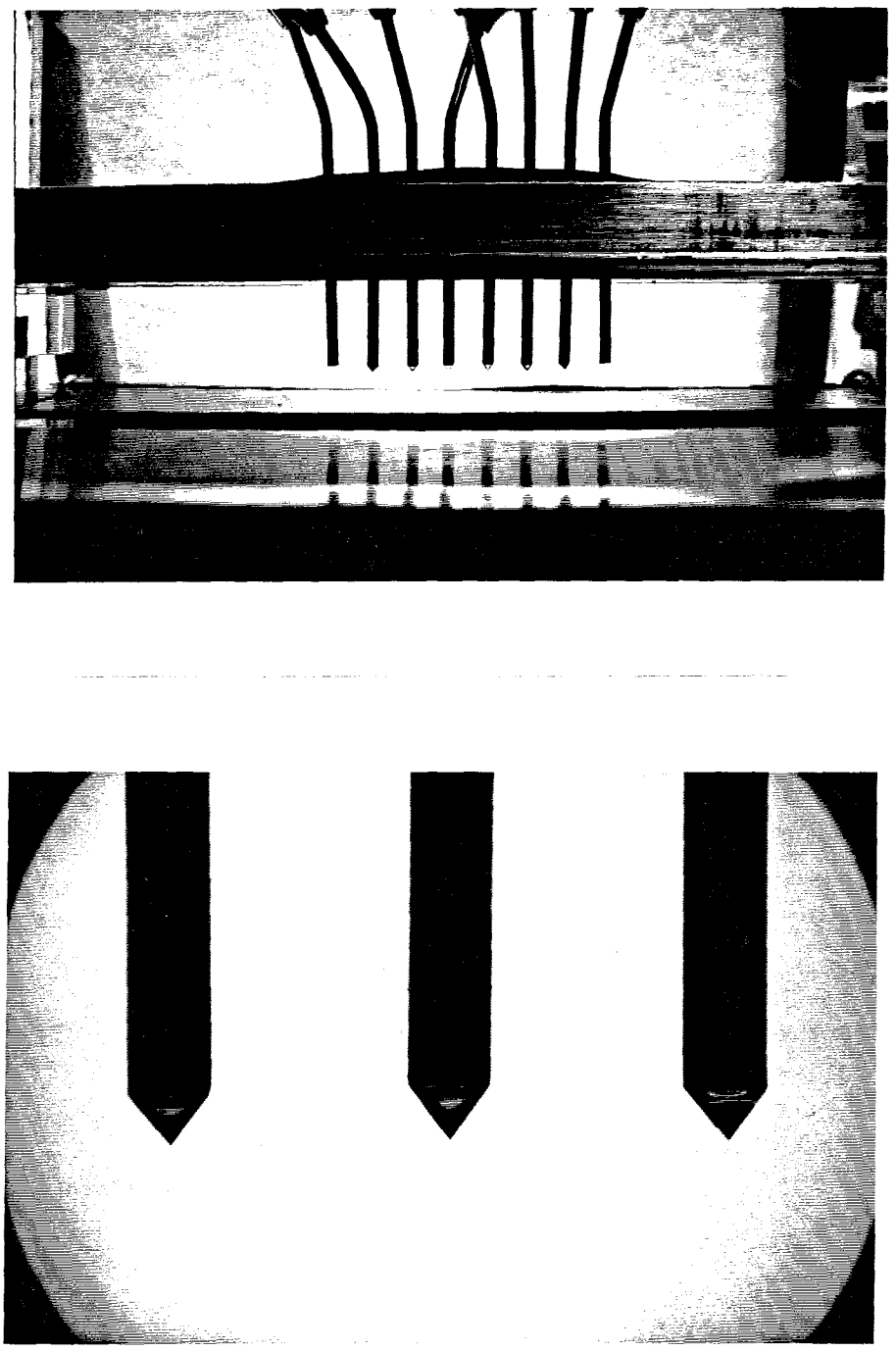

Figure 5.7: Photographs of a linear array of Taylor cones established on capillary electrodes placed opposite a slotted flat plate electrode. $R/S = 0.31$, $P = 1.39$.

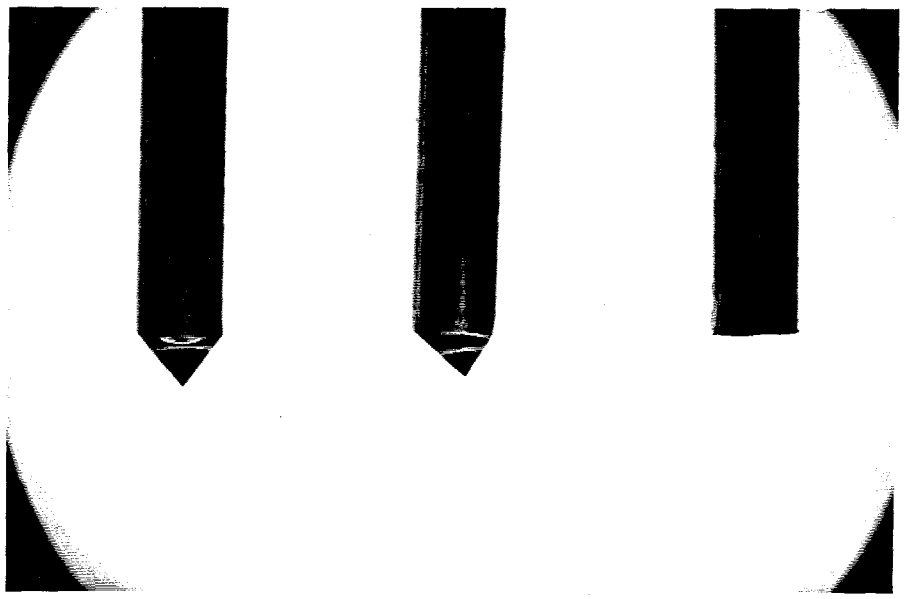

Figure 5.8: Photograph of the right-hand side of a linear array of Taylor cones established on capillary electrodes placed opposite a slotted flat plate electrode. $R/S = 0.31$, $P = 1.39$.

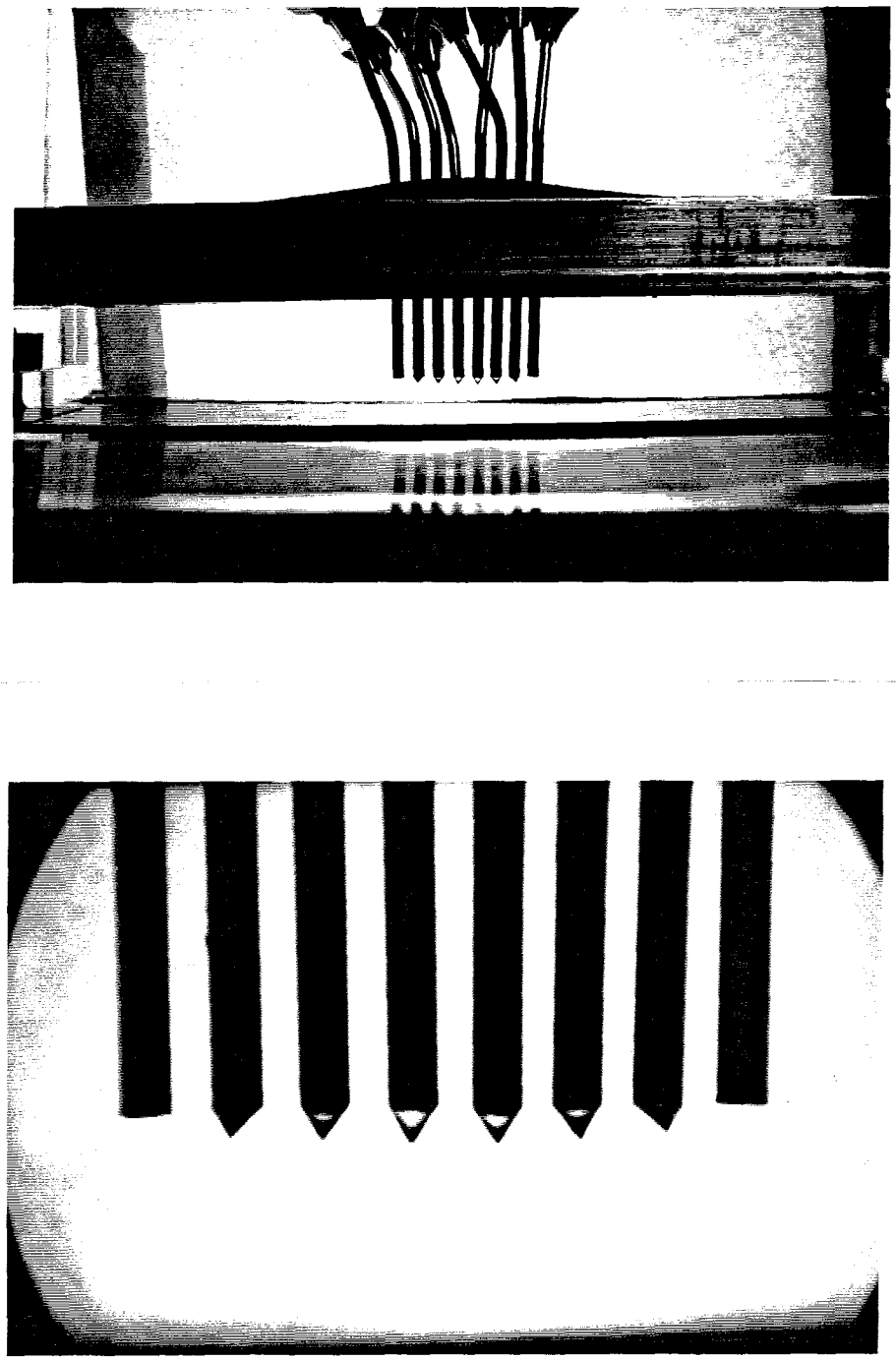

Figure 5.9: Photographs of a linear array of Taylor cones established on capillary electrodes placed opposite a slotted flat plate electrode. $R/S = 1.6$, $P = 1.39$.

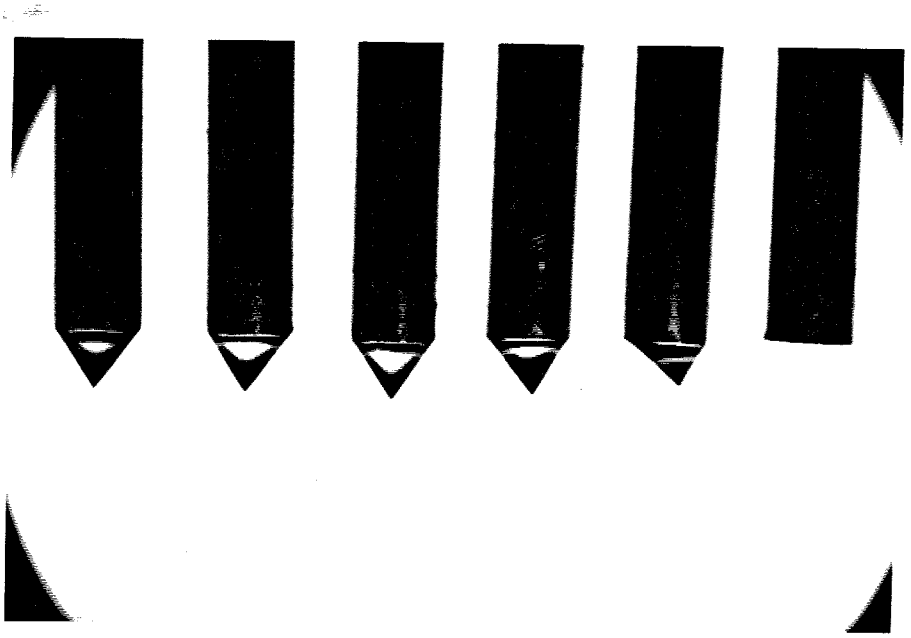

Figure 5.10: Photograph of the right-hand side of a linear array of Taylor cones established on capillary electrodes placed opposite a slotted flat plate electrode. $R/S = 1.6$, $P = 1.39$.

5.4 Conclusions

Linear arrays of Taylor cones were established on capillary electrodes with various radius to spacing ratios R/S, placed opposite a slotted flat plate electrode. The onset potential to establish the cones varied inversely with capillary spacing. Operation of the cones at a constant overpotential ratio $P = V/V_s = 1.39$ (independent of capillary spacing) resulted in nearly constant values of volumetric flow rate per cone and electrical current per cone, indicating that the electric field determines the electrospray properties and not the applied electrical potential, as expected.

Photographs show that the cones at the ends of the array were deflected due to end effects in the electric field. The feasibility, however, of establishing the electrospray at several capillary electrodes arranged in a linear array opposite a slotted flat plate is demonstrated. This provides a means of greatly increasing the throughput of liquid in electrospray atomization.

Acknowledgements

This work was supported by NSF grant number CTS9113191.

Chapter 6

Ablation of Silicate Particles in High-speed Continuum and Transition Flow with Application to the Collection of Interplanetary Dust Particles

Abstract

A model for the ablation and deceleration of spheres in continuum and slip flow is presented. Experiments were conducted in which initially spherical 7.1 μm diameter soda-lime glass particles were launched from vacuum at 4500 m/s through a 0.5 mil (13 μm) plastic film into a capture chamber containing xenon at 0.1 and 0.2 atm and 295 K. Samples of ablated particles were collected and inspected using scanning electron microscopy (SEM). It was found that the ratio of the ablated particle radius (R_f) to the initial radius (R_0) depends on the gas pressure such that at 0.1 atm, $R_f/R_0 = 0.67 \pm 0.08$ and at 0.2 atm, $R_f/R_0 = 0.88 \pm 0.08$. The model agrees with these results if the heat of ablation Q is set to 1.5 $\pm$ 0.2 MJ/kg. This value of Q approximately corresponds to the energy needed to raise the particle temperature from 295°K to 1300°K, the working point of soda-lime glass. This indicates that the

mechanism of ablation is melting and blowing of material from the particle's surface.

6.1 Introduction

New instruments are needed to capture and analyze interplanetary dust particles (IDPs). Capture of the particles in a gas is attractive since the particle could be conveyed electrostatically to a planchet for detailed analysis, e. g., mass spectroscopy. An instrument using gas deceleration would have the gas confined within a thin plastic or metal membrane. High speed (~10 km/s) dust particles would penetrate the membrane and then be stopped by gas drag and ablation. The gas cell must be large enough to accommodate the deceleration length of the incoming particles. The extent of ablation must be minimized if compositional analysis of single particles is to be undertaken. System mass and the mass of gas carried must be minimized for space-borne missions. Gas pressure and temperature are design parameters that may be varied in the instrument optimization.

A detailed understanding of ablation processes and the aerodynamic forces acting on the particle is needed to design this instrument. Since the instrument will operate in the continuum and slip flow regimes, knowledge of ablation and deceleration is needed there. The ablative deceleration of particles entering an atmosphere at high velocity has been studied extensively to relate the radiant intensity and duration to the mass, density, and velocity of objects which intercept the Earth in order to constrain the contribution from different sources (e.g., comets and asteroids) [55, 56, 57, 58, 59]. That work focuses primarily on ablation of particles in high velocity free molecular flow, such as occurs in the atmosphere at high altitudes and is, therefore, not directly applicable for the design of this instrument.

This paper presents a study of ablative deceleration of particles in the continuum and slip flow regime. The theory of ablative deceleration in free molecular flow (i.e., meteor theory) is reviewed and extended to the continuum and slip flow regimes. An experimental investigation of ablative deceleration is then reported and compared with meteor theory and the revised theory derived in this paper.

6.2 Ablation and Deceleration

The deceleration and ablation of an object can be described by momentum and energy conservation equations:

$$m\frac{du_1}{dt} = -\frac{1}{2}\rho_1 u_1^2 C_D A_p, \tag{6.1}$$

where m is the particle mass, u_1 is the free stream speed of the particle, ρ_1 is the free stream gas density, C_D is the drag coefficient, A_p is the particle projected area, and

$$Q\frac{dm}{dt} = -\frac{1}{2}\rho_1 u_1^3 C_E A_p, \tag{6.2}$$

where Q is the heat of ablation, and C_E is the energy transfer coefficient. Note that even though Eqns. (6.1) and (6.2) involve the free stream values ρ_1 and u_1 the values of C_D and C_E given below take into account the shock wave which is present due to the supersonic and hypersonic speeds.

The heat of ablation Q is the energy per unit mass needed to remove material from the particle and eject it into the free stream. Implicit in Eqn (6.2) is the assumption that all of the energy reaching the particle is used to remove material (none is conducted into the interior of the particle). Thus, the time scale over which ablation occurs, τ_a, is assumed to be no greater than the Fourier conduction time τ_c. Thus we require

$$\tau_a < \tau_c \sim R^2/D_t, \tag{6.3}$$

where R is the particle radius and D_t is the thermal diffusivity. If the assumption given by Inequality (6.3) is not valid, then heat is absorbed throughout the particle body rather than concentrating at the surface, and Eqn. (6.2) would not apply. For the particles examined in this paper, τ_c is approximately 6 microseconds. As will be seen below the model incorporating this assumption predicts that most of the ablation occurs during the first few microseconds of flight. Therefore the assumption leads to a reasonable level of approximation.

In the meteor literature C_E is usually called the "heat transfer coefficient." In this paper this term is reserved for the usual fluid mechanical quantity h,

$$h = \frac{q}{A(T_f - T_s)}, \tag{6.4}$$

where q/A is the heat per unit time per unit area transferred to a surface, A is the surface area, T_s is the temperature of the surface, and T_f is the temperature of the fluid. In Eqn. (6.4), q is taken to be positive if heat flows into the particle surface. There is some question about the validity of this equation since it will be used for a very large temperature difference $T_f - T_s$. It will be used as a first approximation however.

If the particle is assumed to remain spherical throughout its entire flight, then

$$m = \frac{4}{3}\pi R^3 \rho_p, \tag{6.5}$$

where R is the particle radius and ρ_p is the particle density, and

$$A_p = \pi R^2. \tag{6.6}$$

Substituting Eqns. (6.5) and (6.6) into Eqns. (6.1) and (6.2) gives

$$\frac{du_1}{dt} = -\frac{3\rho_1 u_1^2 C_D}{8\rho_p R} \tag{6.7}$$

and

$$\frac{dR}{dt} = -\frac{\rho_1 u_1^3 C_E}{8\rho_p Q}, \tag{6.8}$$

respectively. The particle's density is assumed to remain constant throughout its flight.

Now we introduce the dimensionless variables $\hat{R} = R/R_0$, $\hat{t} = tv_0/R_0$, and $\hat{M}_1 = M_1/M_{1_0} = u_1/v_0$, where "0" subscripts indicate the state before ablation or deceleration begin and v_0 is the initial free stream speed. Thus Eqn. (6.7) becomes

$$\hat{R}\frac{d\hat{M}_1}{d\hat{t}} = -\frac{3\rho_1 C_D \hat{M}_1^2}{8\rho_p}, \tag{6.9}$$

and Eqn. (6.8) becomes

$$\frac{d\hat{R}}{d\hat{t}} = -\frac{\rho_1 v_0^2 C_E \hat{M}_1^3}{8\rho_p Q}. \tag{6.10}$$

The initial conditions for Eqns. (6.9) and (6.10) are $\hat{R}(0) = 1$ and $\hat{M}_1(0) = 1$.

In order to solve Eqns. (6.9) and (6.10), expressions are needed for C_D and C_E. In meteor science it is commonly assumed that $\sigma = C_E/QC_D$ is constant over the flight of the particle. The parameter σ is known in meteor science [60] as the "ablation parameter." If σ is constant then Eqns. (6.9) and (6.10) may be integrated directly. Dividing Eqn.(6.10) by Eqn. (6.9) gives

$$\frac{d\hat{R}}{\hat{R}} = \frac{1}{3} v_0^2 \sigma \hat{M}_1 d\hat{M}_1. \tag{6.11}$$

Integrating over the flight of the particle,

$$\ln(\frac{R}{R_0}) = \frac{1}{6} v_0^2 \sigma (\hat{M}_1^2 - \hat{M}_{1_0}^2) = \frac{1}{6}\sigma(u_1^2 - v_0^2), \tag{6.12}$$

or

$$\frac{R}{R_0} = \exp(\frac{1}{6}\sigma(u_1^2 - v_0^2). \tag{6.13}$$

In general, the drag coefficient C_D and the energy transfer coefficient C_E are functions of the instantaneous Reynolds number, $\mathrm{Re}_1 = 2\rho_1 u_1 R/\mu_1$, and Mach number, $M = u_1/a_1$, where a_1 is the speed of sound in the gas. Since the gas density ρ_1 and viscosity μ_1 and speed of sound depend on the pressure and temperature of the gas, σ must be a function of pressure and temperature. Meteor theory gives no way of predicting the dependence, however.

A previously reported expression for C_D and a derivation for C_E will now be used to develop a more general description of the ablative deceleration of small particles. Forney et al. [61] report a formula for C_D as a function of M_1 and Re_1. The expression is

$$C_D = (C_{D_0} - 2)\exp[-3.07\gamma^{1/2}\frac{M_1}{\mathrm{Re}_1}g(\mathrm{Re}_1)] + \frac{h(M_1)}{\gamma^{1/2}M_1}\exp(-\frac{\mathrm{Re}_1}{2\mathrm{M}_1}) + 2 \quad , \tag{6.14}$$

where

$$C_{D_0} = \frac{24}{\mathrm{Re}_1}(1 + 0.158\mathrm{Re}_1^{2/3}), \tag{6.15}$$

$$g = \exp\{2.88[1 + \tanh(0.33\ln(\mathrm{Re}_1) - 1.92)]\}, \tag{6.16}$$

$$h = 2.3 + 1.7(T_s/T_f)^{1/2} - 2.3\tanh(0.51M_1), \tag{6.17}$$

where γ is the ratio of specific heats, T_s is the particle surface temperature, and T_f is the fluid temperature. Equation (6.14) includes theoretically predicted trends and also fits the available experimental data to which it was fitted to within plus or minus 10 percent for $10 < \mathrm{Re}_1 < 1000$ and $M_1 = 3$ [62]. This range of Re_1 covers the present cases. The accuracy of C_D at higher M_1 has not, however, been experimentally tested so the uncertainty is larger at higher Mach numbers.

Equation (6.14) includes effects of non-continuum flow since any two of the three parameters M_1, Re_1, and the Knudsen number Kn_1, determine the third. The Knudsen number is the ratio of the gas mean free path, λ, to the particle radius and can be expressed as [63],

$$\mathrm{Kn}_1 = (\frac{\gamma\pi}{2})^{1/2}\frac{M_1}{\mathrm{Re}_1}. \tag{6.18}$$

A flow is arbitrarily taken to behave as a continuum flow if $\mathrm{Kn} < 0.01$, as a free molecular flow if $\mathrm{Kn} > 10$, and as a transition flow if $0.01 < \mathrm{Kn} < 10$. Thus the flow is a continuum flow in the limit of $M_1/\mathrm{Re}_1 << 1$ or a free-molecular flow in the limit $M_1/Re_1 >> 1$. In the first limit (continuum flow) Eqns. (6.14) through (6.17) give $C_D = C_{D_0}$. The second limit (free-molecular flow) to Eqns. (6.14) through (6.17) yields $C_D = 2$, the value that corresponds to reflections of incoming molecules off the sphere's surface. Figure 6.1 shows the variation of C_D with Re_1 for $M_1 = 0$, 1, 2, 10, and 20. Sonic and supersonic flow reduce C_D for $\mathrm{Re}_1 < 30$ and increase C_D for $\mathrm{Re}_1 > 30$.

To derive an expression for C_E, the high speed gas flow must be understood. In continuum and near-continuum flow, ablation occurs at the particle surface due to intense heating from the surrounding fluid. The fluid is hot because it has passed through a bow shock in front of the particle (Fig. 6.2). The primary assumption of the present model is that the bow shock may be replaced by a normal shock for purposes of computing the fluid state surrounding the particle. This approximation is useful in that it greatly simplifies the problem of computing the heat transfer at the particle's surface which is a complicated phenomena involving boundary layer formation and the velocity and temperature fields behind the curved bow shock. This approximation will not be valid if the fluid is too rarefied to form a shock. Thus use of this model

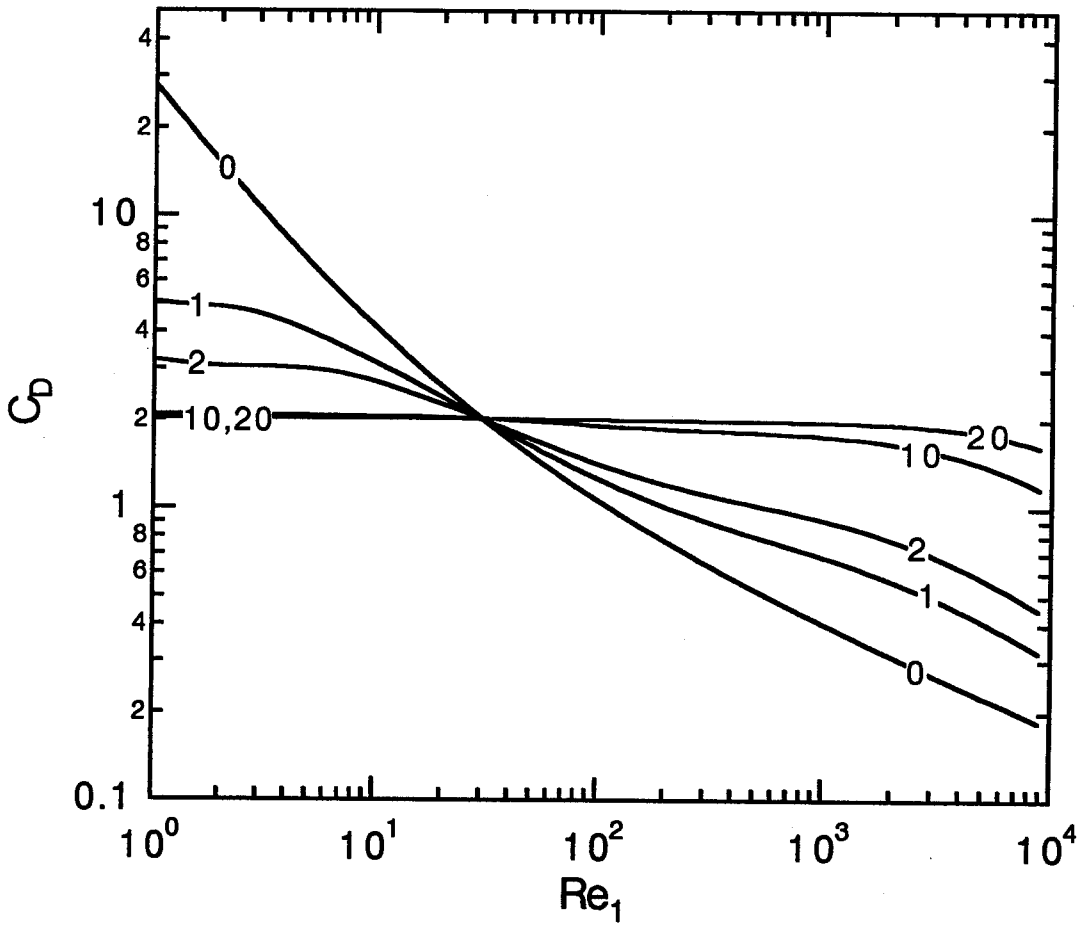

Figure 6.1: Drag coefficient C_D for a sphere as a function of Re_1 for various M_1.

is restricted to $0 \leq \mathrm{Kn} \leq \mathrm{Kn_{cr}}$ where $\mathrm{Kn_{cr}}$ is the maximum Kn for formation of a bow shock. Bronshten [60] gives $\mathrm{Kn_{cr}} = 1/3$. The experimental conditions examined in this paper and the present IDP instrument satisfy this condition but meteor entry into the atmosphere may not. The fluid state behind the shock (region 2 in Fig. 6.2b) is thus uniquely determined by the normal shock relations and fluid state 1 ahead of the shock. For strong shocks the fluid can be expected to relax into its ionized state behind the shock after a sufficient number of collisions between its constituent molecules or atoms. This significantly modifies the state of the gas sufficiently far downstream of the shock. It is assumed here, however, that the fluid surrounding the particle has had insufficient time to relax and is therefore "frozen."

The heat flux to the particle is given by Eqn. (6.2) as $\frac{1}{2}\rho_1 u_1^3 C_E A_p$. The same quantity can also be expressed as

$$q = h_2(T_2 - T_s)A, \tag{6.19}$$

where T_s is the particle surface temperature, A is the particle total surface area, h_2 is the heat transfer coefficient for the fluid in state 2. By equating these we obtain

$$C_E = \frac{4h_2(T_2 - T_s)}{\frac{1}{2}\rho_1 u_1^3}. \tag{6.20}$$

The heat transfer coefficient, h_2, can be obtained from the surface-averaged Nusselt number $\mathrm{Nu_2}$ as

$$h_2 = \frac{\mathrm{Nu_2} k}{2R_p}, \tag{6.21}$$

where k is the fluid thermal conductivity. In practice k is evaluated at the average temperature of the fluid and particle surface.

To evaluate $\mathrm{Nu_2}$ the results of an analysis presented in [63] are used. If the fluid is rarefied, then the temperature of the particle surface will not exactly match that of

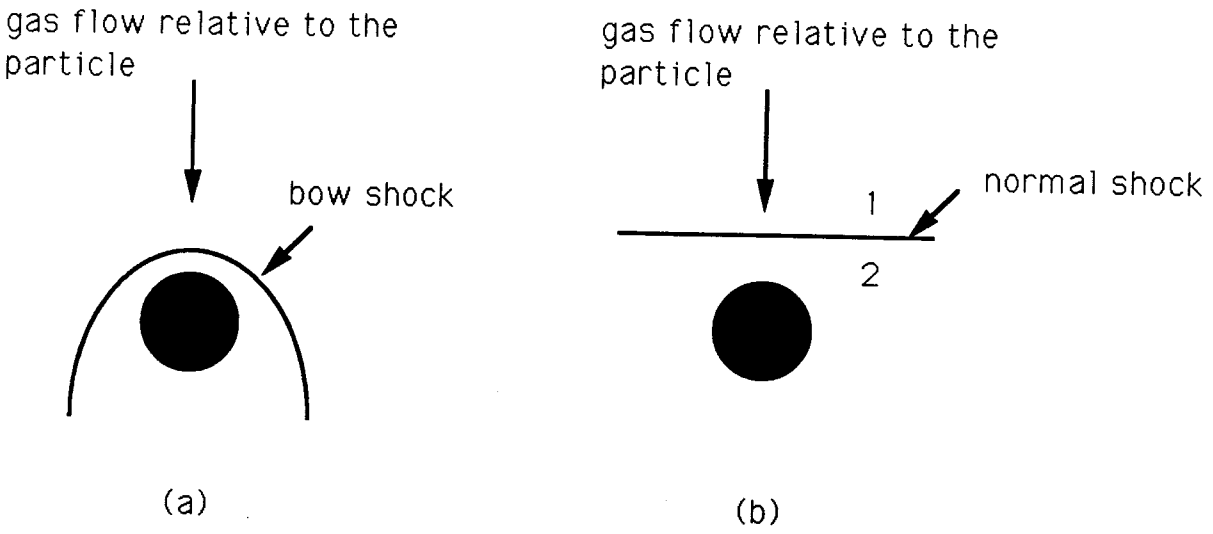

Figure 6.2: (a) Schematic diagram of the bow shock through which the gas must pass to reach the particle. (b) Approximation of the bow shock by a normal shock of the same Mach number. The fluid state upstream of the shock is denoted as 1. The fluid downstream of the shock is denoted as 2.

the fluid at the surface. This temperature jump discontinuity modifies the continuum Nusselt number Nu_{2_0} such that

$$Nu_2 = Nu_{2_0}/[1 + (\frac{\gamma\pi\theta^2}{2})^(1/2)\frac{M_2}{Re_2Pr_2}Nu_{2_0}], \tag{6.22}$$

where

$$\theta = 1.996\frac{2-\alpha_s}{\alpha_s}\frac{\gamma}{\gamma+1}\frac{1}{Pr_2}, \tag{6.23}$$

$Pr_2 = \mu_2 C_{p_2}/k_2$ is the Prandtl number of the gas at state 2, C_{p_2} is the gas specific heat at constant pressure, and α_s is the thermal accomodation coefficient.

The continuum Nusselt number for a sphere surrounded by a laminar velocity distribution is [63]

$$Nu_{2_0} = 2 + \frac{2}{\pi}\int_0^\infty \frac{[1+\exp(-\beta^2\pi)](1+\beta^4)^{-1}}{[J_1^2(\alpha_1\beta)+Y_1^2(\alpha_1\beta)]\beta}d\beta, \tag{6.24}$$

where

$$\alpha_1 = (2Re_2Pr_2)^{1/2} \tag{6.25}$$

and J_1 and Y_1 are Bessel functions of the first and second kind, respectively.

Equation (6.24) can be integrated numerically for various α_1 to obtain Nu_{2_0} as a function of α_1. This integration was conducted for $3.65 \leq \alpha_1 \leq 115$ which covers a wide enough range of Re_2 and Pr_2 for the present purpose. A curve was then fit to the results which has a maximum deviation of 1.4% over this range of α_1,

$$Nu_{2_0} = \sum_{i=1}^{10}\delta_i x^{i-1}, \tag{6.26}$$

where

$$x = \log_{10}[(2Re_2Pr_2)^{1/2}]$$

$$\delta_1 = 2.19280$$

$$\delta_2 = 0.39345$$

$$\delta_3 = 0.50523$$

$$\delta_4 = 1.39274$$

$$\delta_5 = 0.60924$$

$$\delta_6 = -1.48578$$

$$\delta_7 = -0.06673$$

$$\delta_8 = 0.66629$$

$$\delta_9 = -0.26443$$

$$\delta_{10} = 0.03258.$$

Equation (6.26) is plotted in Fig. 6.3 as a function of Re_2 for M_2 =0.2, 0.6, and 1.0 for a monatomic gas and for $\alpha_s = 0.8$. The lower limit of $M_2 = 0.2$ is used since it is the limiting downstream Mach number in a very strong shock in a monatomic gas. The reduction of Nu_{2_0} due to slip can be seen by considering increasing M_2 at a fixed Re_2 on Fig. 6.3.

The viscosity μ_2 is needed to calculate Re_2. Kinetic theory gives an approximate expression [64],

$$\mu_2 = 8.44 \times 10^{-25} \frac{(MT_2)^{1/2}}{\sigma^2}, \tag{6.27}$$

where M is the molecular weight of the gas and σ is the hard sphere collision diameter. The thermal conductivity k_2 is also obtained from kinetic theory as [64],

$$k_2 = 2.632 \times 10^{-23} [\frac{(T_2 - T_s)}{2M}]^{1/2} / \sigma^2, \tag{6.28}$$

where both μ_2 and k_2 are in mks units.

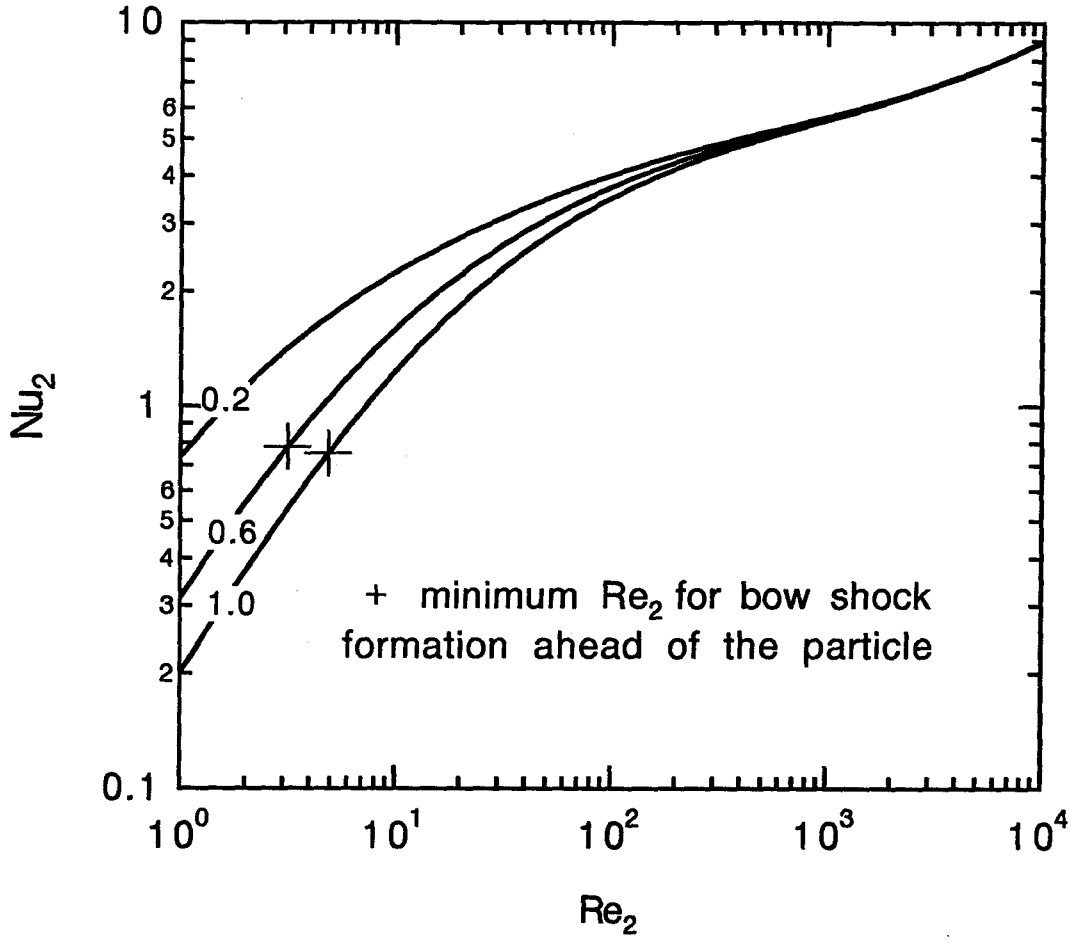

Figure 6.3: Nusselt number Nu_2 for a sphere versus Re_2 for various M_2 and for Pr = 2/3 (monatomic gas). The minimum value of Re_2 needed to satisfy the condition that a bow shock forms ahead of the particle is indicated by the crosses. This corresponds to the condition that $Kn_1 \leq 0.33$. In the $M_2 = 0.2$ case, the minimum Re_2 is less than 1.

The Prandtl number

$$\mathrm{Pr}_2 = \frac{\mu_2 C_{p_2}}{k_2} \tag{6.29}$$

can be computed using Eqn. (6.27), (6.28), and the following expression for C_{p_2}:

$$C_{p_2} = \frac{\gamma}{\gamma - 1} R, \tag{6.30}$$

where R is the gas constant.

In Eqn. (6.30) it is assumed that γ is constant; we consider this approximation reasonable for the present model. Note that for xenon, which was employed in the present experiments, $\gamma = 5/3$. The gas temperature in the shocked state is calculated using the ideal gas, normal shock relation [65]

$$\frac{T_2}{T_1} = 1 + \frac{2(\gamma - 1)}{(\gamma + 1)^2} \frac{\gamma M_1^2 + 1}{M_1^2} (M_1^2 - 1), \tag{6.31}$$

as is the pressure

$$\frac{p_2}{p_1} = 1 + \frac{2\gamma}{\gamma + 1} (M_1^2 - 1). \tag{6.32}$$

The density then follows from the ideal gas law.

The velocity downstream of the normal shock is

$$u_2 = u_1 \frac{\rho_1}{\rho_2} \tag{6.33}$$

and the Mach number is

$$M_2^2 = \frac{1 + [(\gamma - 1)/2] M_1^2}{\gamma M_1^2 - [(\gamma - 1)/2]}. \tag{6.34}$$

Equations (6.9) and (6.10) can now be integrated numerically with the initial conditions $\hat{M}_{1_{n=0}} = 1$ and $\hat{R}_{n=0} = 1$. C_{D_n} and C_{E_n} are evaluated from Eqns. (6.14) and (6.26).

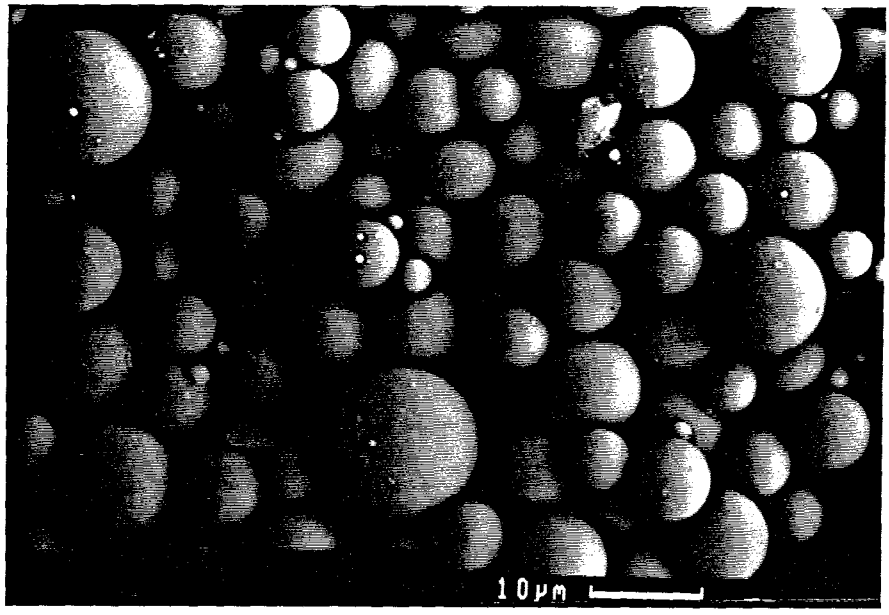

Figure 6.4: Scanning electron micrograph of the original (unablated) soda-lime glass spheres. The mean diameter is 7.1 μm.

6.3 Experiment

Experiments were performed on soda-lime glass particles obtained from Duke Scientific Corp. A scanning electron micrograph of the particles as received shows that the particles are very nearly spherical (Fig. 6.4). Direct measurement of the diameters of the particles taken from several scanning electron micrographs gave the size distribution shown in Fig. 6.5. In order to isolate the effects of varying sphere diameter on ablation, monosized particles would be desired. However, no attempt was made to size classify the particles in the original samples. The mean diameter was 7.1 μm. The nominal density was 2420 kg m^{-3}.

The particles were launched using the Ames Vertical Gun Range (AVGR) at NASA Ames Research Center, Moffet Field, California. AVGR consists of a light gas gun,

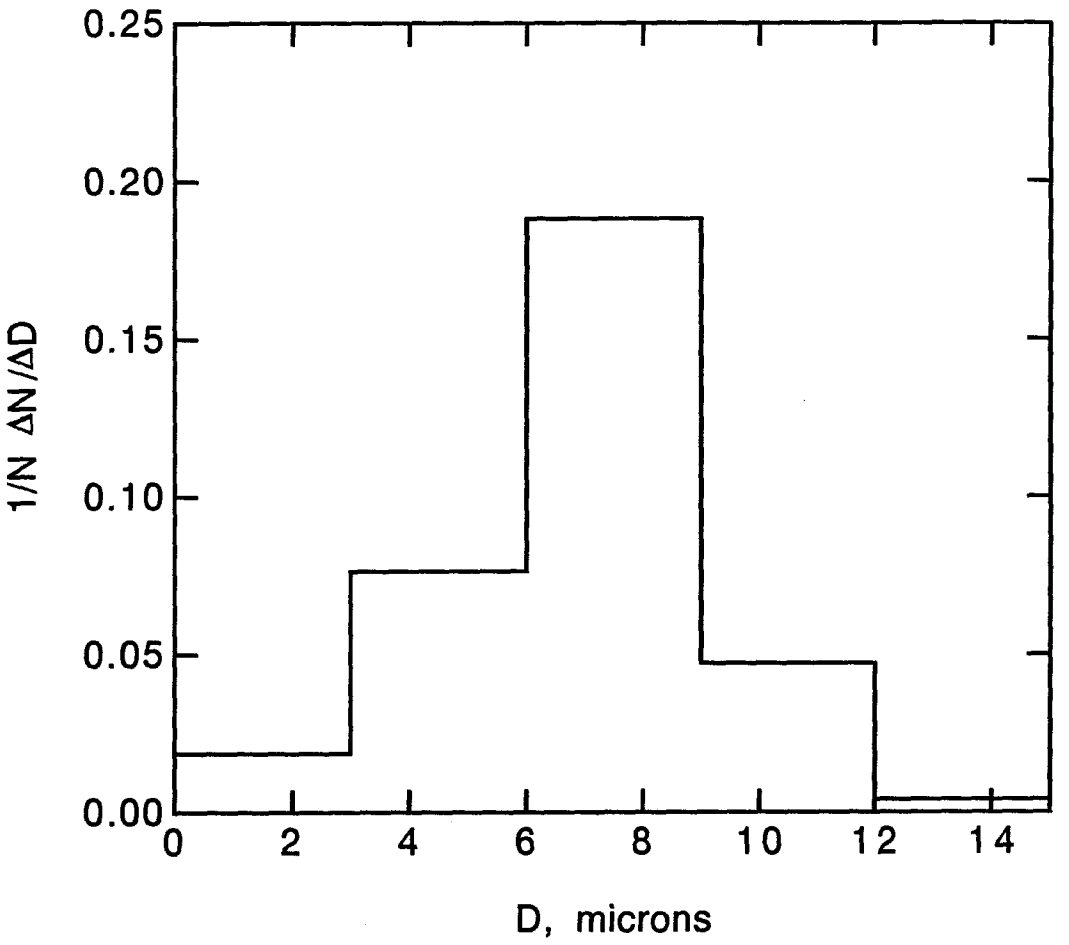

Figure 6.5: Size distribution of original (unablated) soda-lime glass spheres. The size distribution represents the diameters of 503 spheres measured by hand from SEM micrographs.

launch tube, blast chamber, high voltage spark gap velocity chamber, and vacuum impact chamber. In the light gas gun, a gunpowder charge is fired to drive a piston into a pump tube. The piston compresses hydrogen gas ahead of it into a high pressure coupling. The hydrogen pressure and temperature increase until a diaphragm breaks, allowing the high pressure hydrogen gas to accelerate the projectile down the launch tube toward the vacuum impact chamber. In this case the projectile consisted of an aluminum cup which held approximately 5 mg of particles. An advantage of this particle launching system over systems which use electrostatic forces to accelerate the particles is its capability of launching relatively large particles. The cup is held in a plastic sabot, which fits in the gun barrel. The gun barrel is rifled so that the projectile assembly spins as is travels toward the impact vacuum tank. Centrifugal force breaks the sabot up and the pieces fly outward and are stopped by an impact sabot catcher before reaching the impact vacuum tank. Centrifugal force also forces some of the particles out and away from the cup. When the cup and particles reach the target, some of the particles are several centimeters away (radially) from the cup.

The target, shown in Fig. 6.6, consisted of a xenon-filled Lucite capture chamber with a 10 cm x 10 cm particle acceptance aperture, and 37 cm length. The center of the capture chamber had a 2.5 cm tube to allow the aluminum cup to pass without disturbing the experiment. Xenon is an appropriate gas for use in stopping IDPs because it is dense, and chemically inert. Moreover, it is not an abundant constituent of IDPs so it will not interfere with compositional analysis. A steel blast plate beneath the capture chamber stops the cup. The top of the capture chamber was sealed with 0.5 mil (13 μm) Mylar or 0.5 mil cellulose triacetate film. The film was fastened to the capture chamber edges and central tube with contact cement. The capture chamber

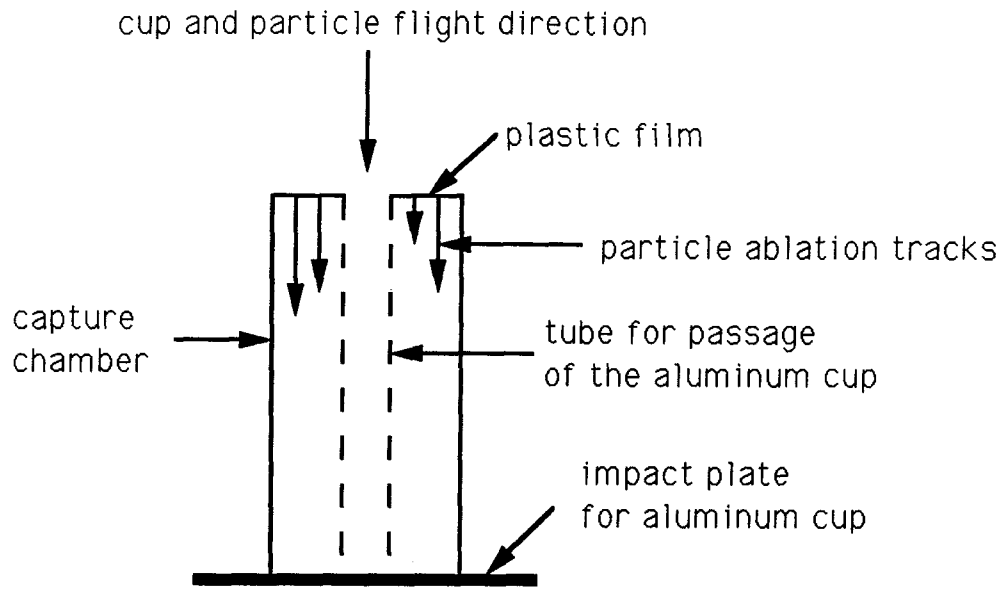

Figure 6.6: Schematic of the capture chamber used in the ablation experiments. The particles and aluminum cup move downward. The cup travels through the central tube while the particles penetrate the plastic film and enter the xenon gas. The particles settle to the bottom of the chamber to be collected on a Teflon sheet. The sheet is then divided and mounted on electron micrograph stubs.

could hold 0.2 atm internal pressure (Mylar) or 0.5 atm (cellulose triacetate) before the film ruptured. The gas pressure was adjusted in the capture chamber before an experiment by valves outside the impact vacuum tank (Fig. 6.7). Valve 2 was left open and 1 was closed while the impact vacuum tank was evacuated to 1 mm Hg or less. Then valve 2 was closed and xenon was bled through valve 1 until the desired pressure was reached. Then all valves were closed and the gun was fired.

The bottom of the capture chamber was fitted with a Teflon sheet on which ablated particles settled after being stopped in the gas at the top of the chamber. After the experiment the Teflon was removed and divided into squares which fit on 13 mm electron microscope stubs.

The gun powder load in the powder chamber was designed to produce a projectile speed of approximately 5 km/s. The actual projectile velocity was measured using

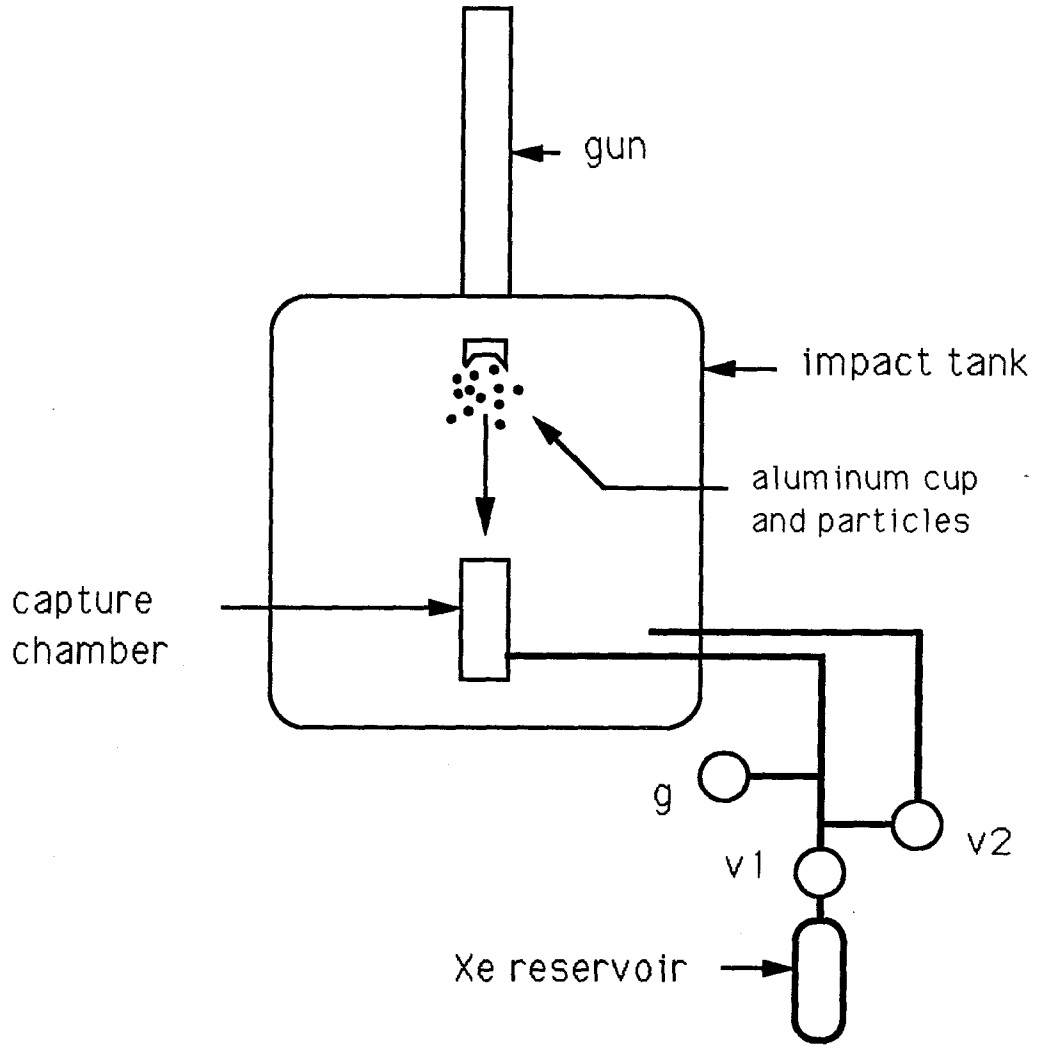

Figure 6.7: Schematic of the system used to adjust and maintain xenon gas pressure inside the capture chamber while the impact vacuum tank is evacuated. The gun is fired in the vertical position. The impact tank is evacuated to $\sim$ 1 Torr.

the spark gap velocity chamber. Three shots each were conducted at 0.1 and 0.2 atm.

A CamScan Series 2 Scanning Electron Microscope fitted with a Tracor Northern TN5500 Energy Dispersive X-Ray Analyzer (EDS) was used to analyze the collected particles. Since gun blast debris also entered the capture chamber during a shot, it was necessary to use the EDS to verify that each measured particle was soda-lime glass. After a particle was positively identified as soda-lime glass, it was photographed. The particle diameter was determined using the equivalent area method.

In order to determine whether the particles were damaged as they penetrated the capture chamber films, particle capture tests were performed with the capture chamber evacuated so that no gas ablation could occur. Spheres launched through the film were subjected to the same SEM inspection as the ablated particles. No major damage is seen on these particles (Fig. 6.8). Thus, we conclude that any damage or reduction in diameter resulted from gas ablation. Nearly circular perforations in the film made by the particles are seen in Fig. 6.9.

Only a small fraction of the original particles were thrown far enough from the projectile to penetrate the membrane rather than passing through the central tube. Particle deposition on surfaces other than the Teflon sheet further reduced the number of particles analyzed. Twenty three particles were located, unambiguously identified, photographed and sized in the 0.1 atmosphere experiment. The 0.2 atmosphere experiment yielded 22 particles. The average velocity of the projectile for the 0.1 atm case was 5000 m/s and for the 0.2 atm case was 4900 m/s. The main reason so few particles were located is that only a small fraction of them were located far enough away radially from the cup to enter the chamber and not pass through the central tube.

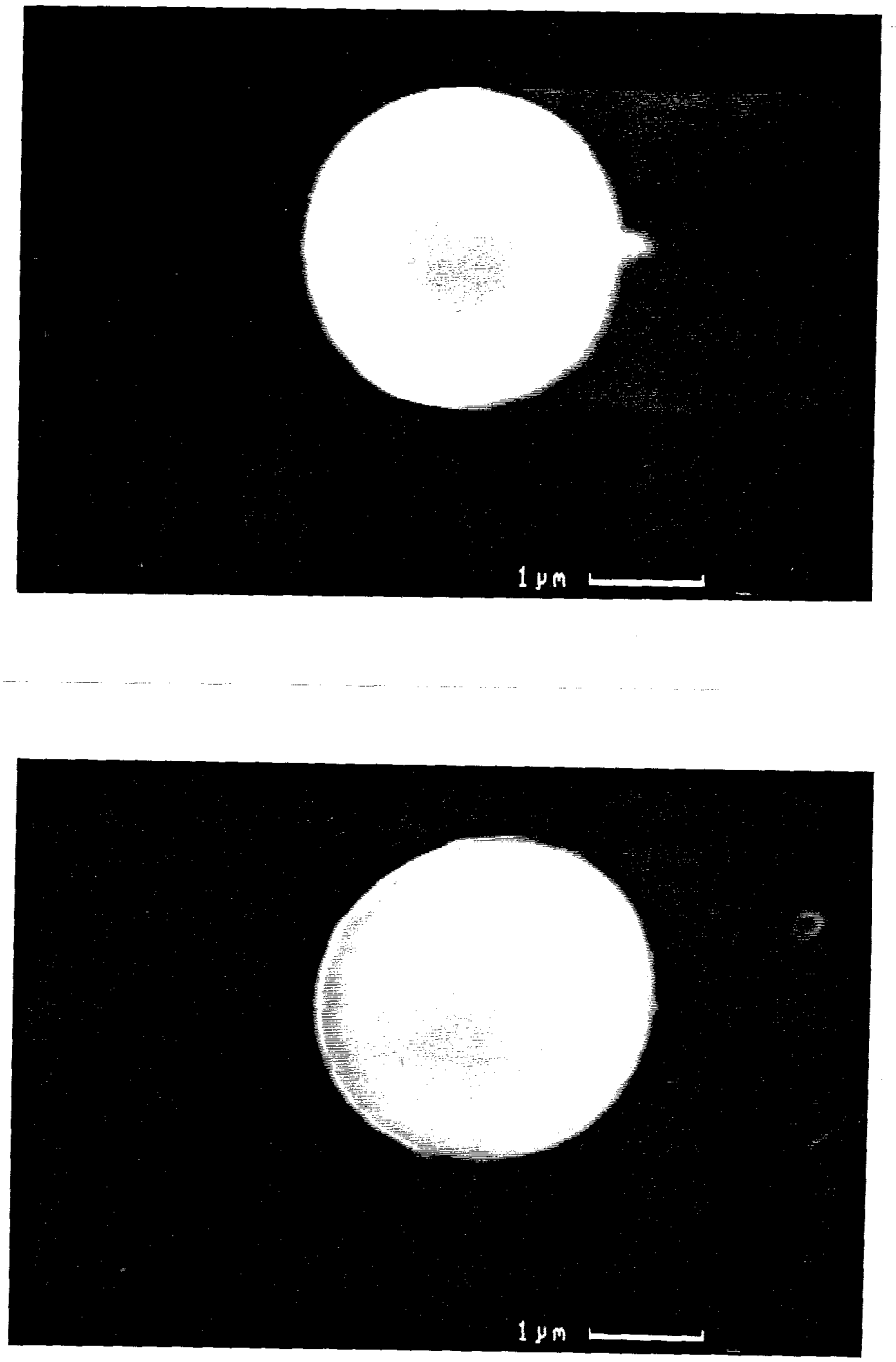

Figure 6.8: Typical scanning electron micrographs of particles which perforated the film but were not exposed to gas, so that no ablation could occur. The particles are undamaged, indicating that the reduction of diameter described below must be due to ablation. The small white square seen on the micrographs is an aiming aid for the EDS system.

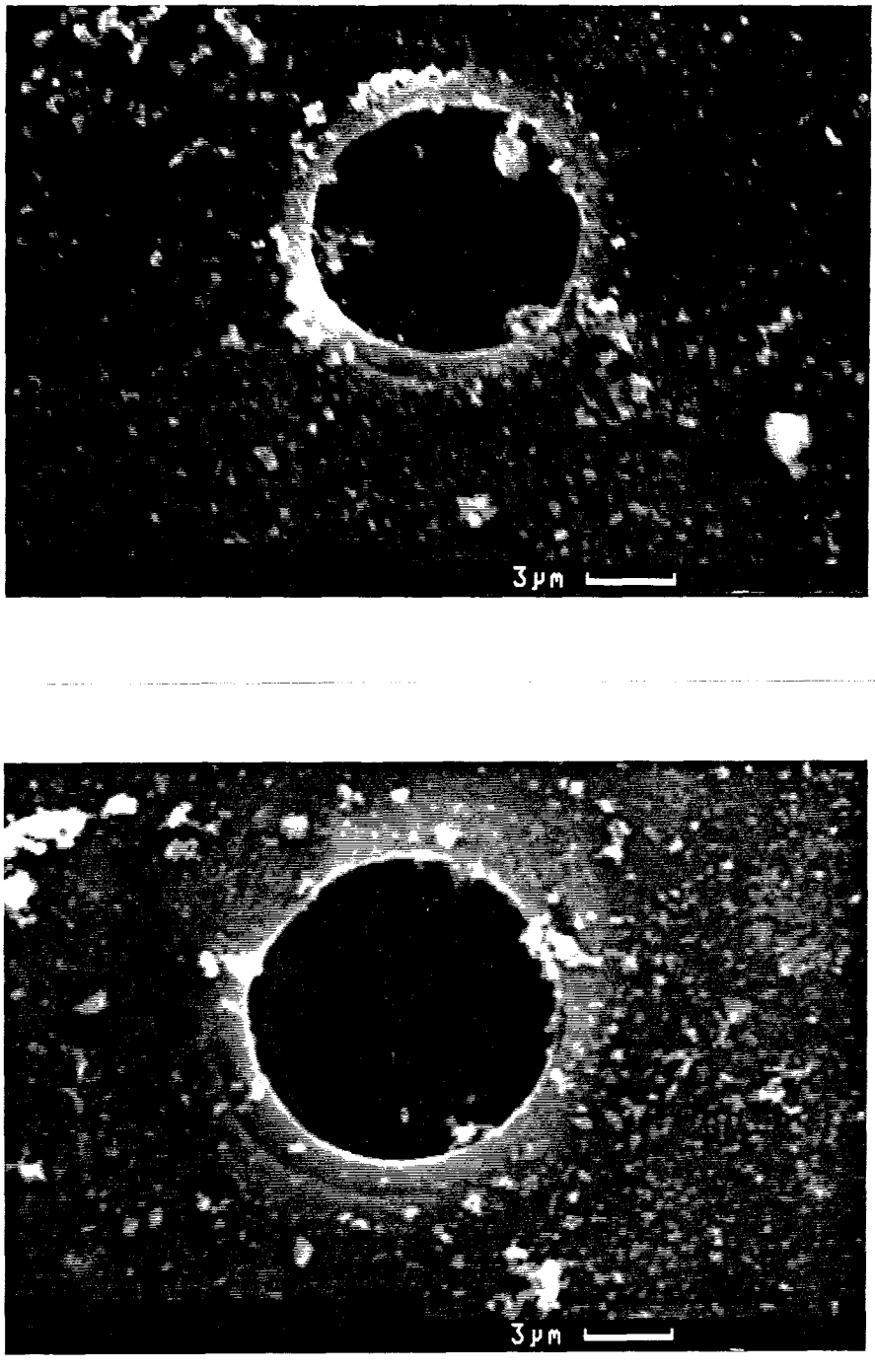

Figure 6.9: Typical scanning electron micrographs of film perforations made by high-speed particles. The film is 13 μm thick. The debris seen on the film is from the gun blast, and is not related to the glass particles.

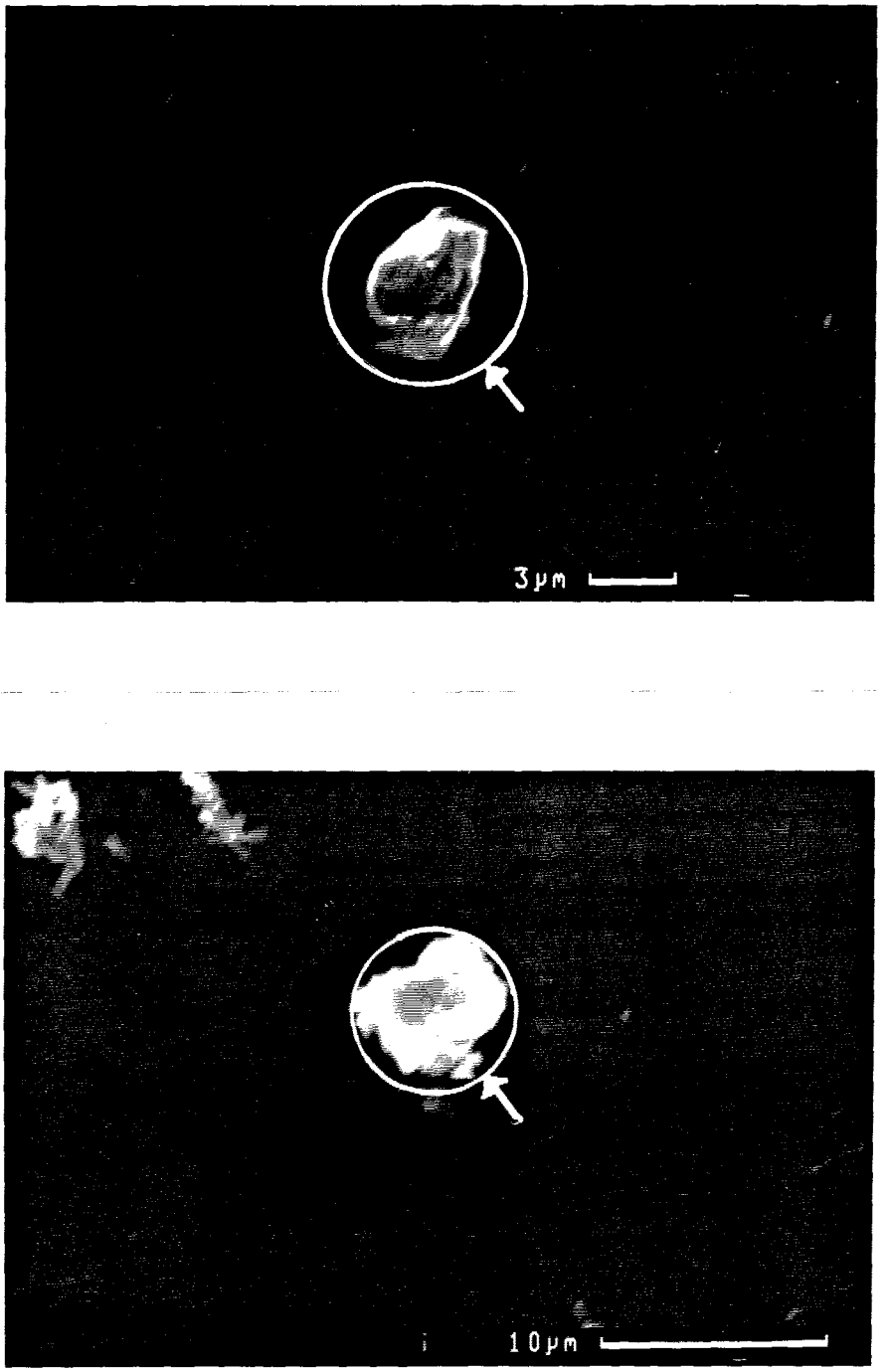

Figure 6.10: Scanning electron micrographs of soda-lime glass particles ablated in 0.1 atm (top) and 0.2 atm (bottom) Xe gas at 295 K. The initial speed was approximately 4500 m/s. The initial sizes (arrowed), calculated for these particles by the average ratios of final to initial radius for each pressure, are indicated for comparison.

6.4 Results

The average diameter of the particles ablated at 0.1 atm was 4.7±0.6 μm, and for 0.2 atm was 6.2±0.6 μm. Views of two ablated particles are given in Fig. 6.10. The initial size is shown for comparison. The ratios of the ablated radius to initial radius were $R_f/R_0 = 0.67 \pm .08$ and $0.88 \pm .08$ for 0.1 and 0.2 atm, respectively. It is of interest to compare the prediction of the model described above with these results. The only parameter in the model which has not been determined is Q, the heat of ablation. There are two main mechanisms of ablation: vaporization and spraying of melted material. If the heats of fusion and vaporization of a material are h_f and h_v respectively, then the heat of ablation is roughly

$$Q = h_f + \epsilon h_v, \tag{6.35}$$

where ϵ is the fraction of the mass that is lost by vaporization, $0 \leq \epsilon \leq 1$. Thus, Q is restricted to $h_f \leq Q \leq h_f + h_v$. Equations (6.9) and (6.10) were solved numerically assuming $T_a = 1300$ K (the working point of soda-lime glass [66]) and $v_0 = 4500$ m/s (the reduction in velocity from the measured projectile velocity approximates the deceleration of the particles through the film at the top of the capture chamber) for $p_1 = 0.1$ and 0.2 atm. The working point of an amorphous material such as glass is defined to be the temperature at which the viscosity is 10^4 P. It is the approximate temperature at which the glass may be formed. The curve of R_f/R_0 versus xenon gas pressure can be computed using various values of Q (Fig. 6.11). It was found that a value of Q= 1.5 ± 0.2 MJ/kg gives the results within experimental error for R_f/R_0 at both pressures. The curve for $Q = 0.81$ MJ/kg does not extend below about 7×10^3 Pa because the requirement that $\mathrm{Kn}_1 \leq 0.33$ would be violated during

part of the particle's flight. Note that lower gas pressure leads to more ablation. This is mainly due to the fact that at lower pressures the particle is at speeds high enough to cause ablation for a longer time. Thus more material is removed.

We may now compare the experimentally determined value of Q with the energy needed to raise the temperature of the soda-lime glass material from 295 K to 1300 K. An expression is available for the average heat capacity C_p as a function of temperature for soda-lime glasses [66]. At 1300 K the average heat capacity is 1.00×10^3 J/kg K which gives 1.3 MJ/kg. This roughly corresponds to the value of $Q = 1.5 \pm 0.2$ MJ/kg indicating that ablation occurs primarily by melting and blowing of material from the particle's surface. This indicates that the forces tending to resist ablation from the liquid phase (surface tension and viscosity) are overcome and vaporization is not required to remove material. This conclusion is reached if T_a is greater than about 1100 K. It is difficult to determine T_a since this involves determining when the glass is soft enough ,i.e., has low enough viscosity, that the aerodynamic forces can blow material from the particle's surface. If T_a is 1100 K, then Q is approximately 50% higher than the energy required to heat the particle from 295 K to 1100 K, and one would begin to think that vaporization as an ablative mechanism is important in these experiments. Our best estimate for T_a (= 1300 K) however, indicates that vaporization is unimportant.

Also indicated in Fig. 6.11 is the best available result from meteor theory, which normally assumes $\sigma = C_E/QC_D = \text{const}$. Clearly, meteor theory is inadequate to explain the results of these experiments.

The Kn_1 number histories for typical conditions are shown in Fig. 6.12. The Kn_1 number increases as the particle ablates. Clearly, the lower pressure cases bring about

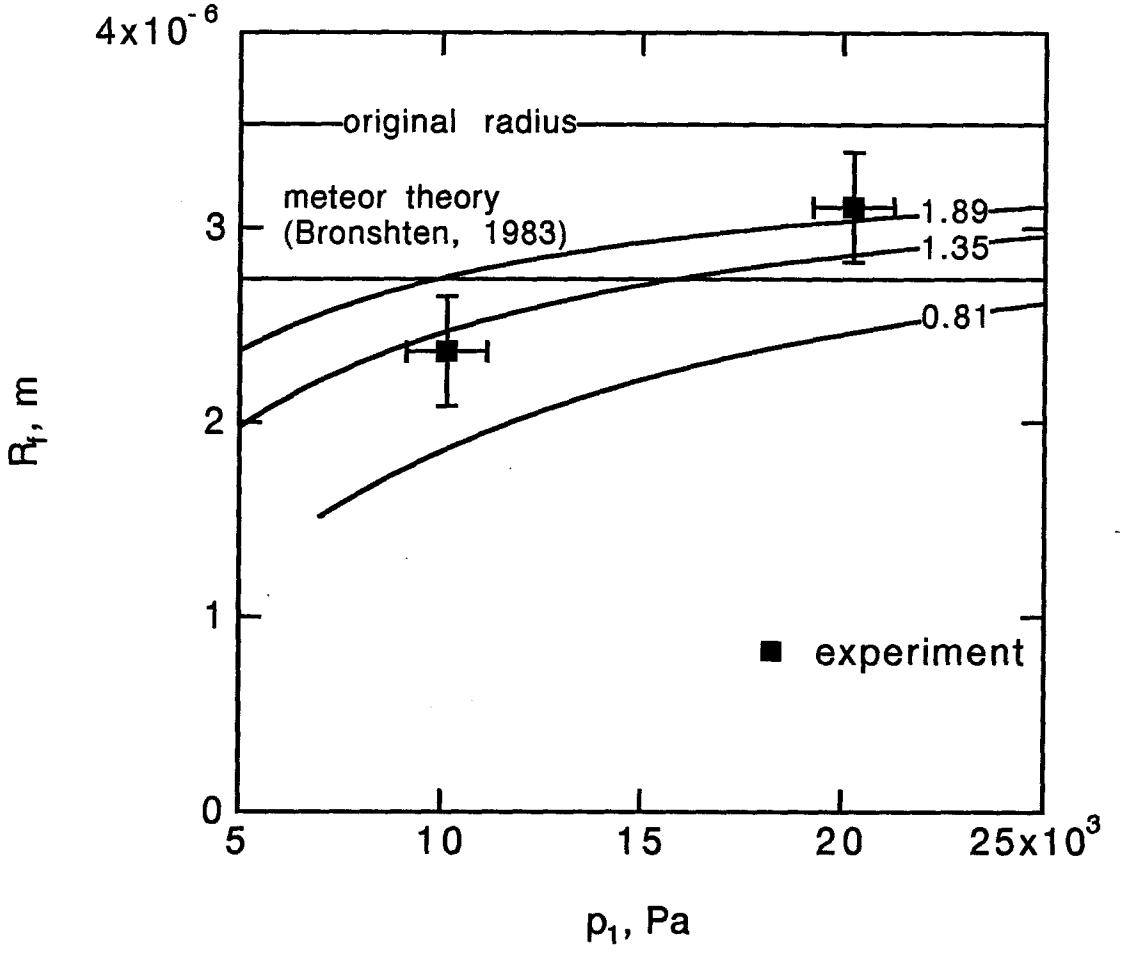

Figure 6.11: Ablated radius R_f for xenon at 295 K versus pressure p_1 for various Q (MJ kg^{-1})(ρ_p =2420 kg m^{-3} and v_0 = 4500 m s^{-1}). The two experimental values of v_0 were of slightly different values (4540 m s^{-1} for p_1 = 0.1 atm and 4300 m s^{-1} for p_1 = 0.2 atm). The meteor theory curve is calculated assuming no variation of σ with gas pressure. There is agreement between the present model and the experiment results for $Q = 1.5 \pm 0.2$ MJ kg^{-1}.

higher Kn numbers as the particle is more extensively ablated.

The numerical simulations also show that R_f/R_0 is dependent on R_0 and v_0 (Fig. 6.13). Smaller and faster spheres are ablated more. Again, the assumption that σ = const. gives no dependence on R_0. The curves are terminated on the left hand side where the restriction that $\mathrm{Kn}_1 \leq 0.33$ would be violated.

The time-resolved motion and ablation are computed for the two pressures used in the experiments (Fig. 6.14). At 0.1 atm it takes approximately 22 microseconds to slow the sphere to the speed where it no longer ablates. At 0.2 atm it takes 13 microseconds. The reason that more ablation occurs at 0.1 atm is that the sphere is decelerated more slowly, thus exposing it to high fluid temperatures for a longer time, allowing more material to be removed. Most of the ablation occurs during the first several microseconds for both 0.1 and 0.2 atm. The measured extent of ablation agrees with the calculated final radii at both pressures within experimental error.

Since various mineralogies of IDPs are expected to be encountered in space, the dependence of R_f/R_0 on the particle density and heat of ablation has been investigated (Fig. 6.15). As ρ_p increases, R_f/R_0 decreases. Also, particles with greater heats of ablation are not as extensively ablated.

Because of the difficulty of the experimental method only two data points are given. The model presented here is therefore not strongly tested. There are many assumptions and simplifications discussed in the derivation. To improve the model would require a more detailed analysis of the gas flow and temperature fields around the particle as well as an analysis of the temperature and material phase fields within the particle. The variation of ablated radius with gas pressure is brought out, however, and this is a step forward.

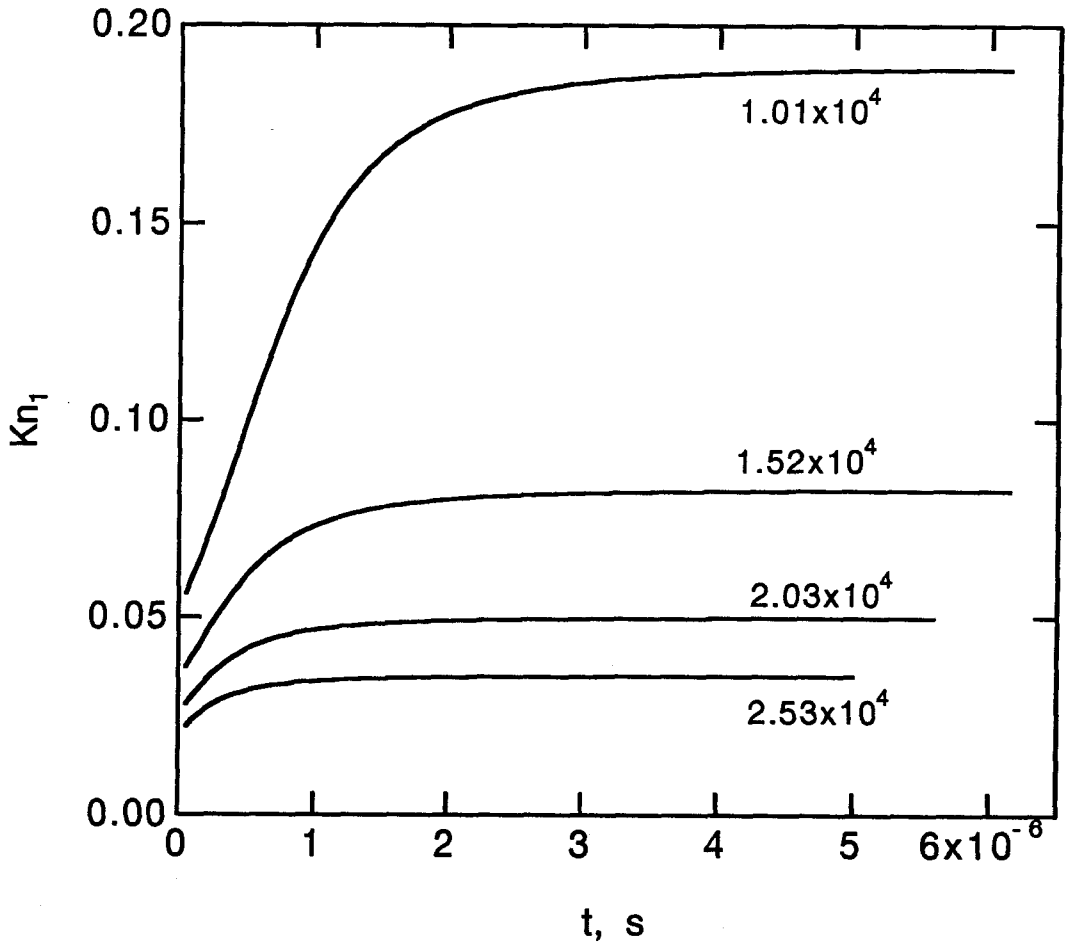

Figure 6.12: Free-stream Knudsen number Kn_1 histories for particles ablating in various free-stream gas pressures (Pa) (Q =1.9 MJ kg^{-1}, $\rho_p = 10^{-3}$, $v_0 = 10$ km s^{-1}, and $R_0 = 5$ μm).

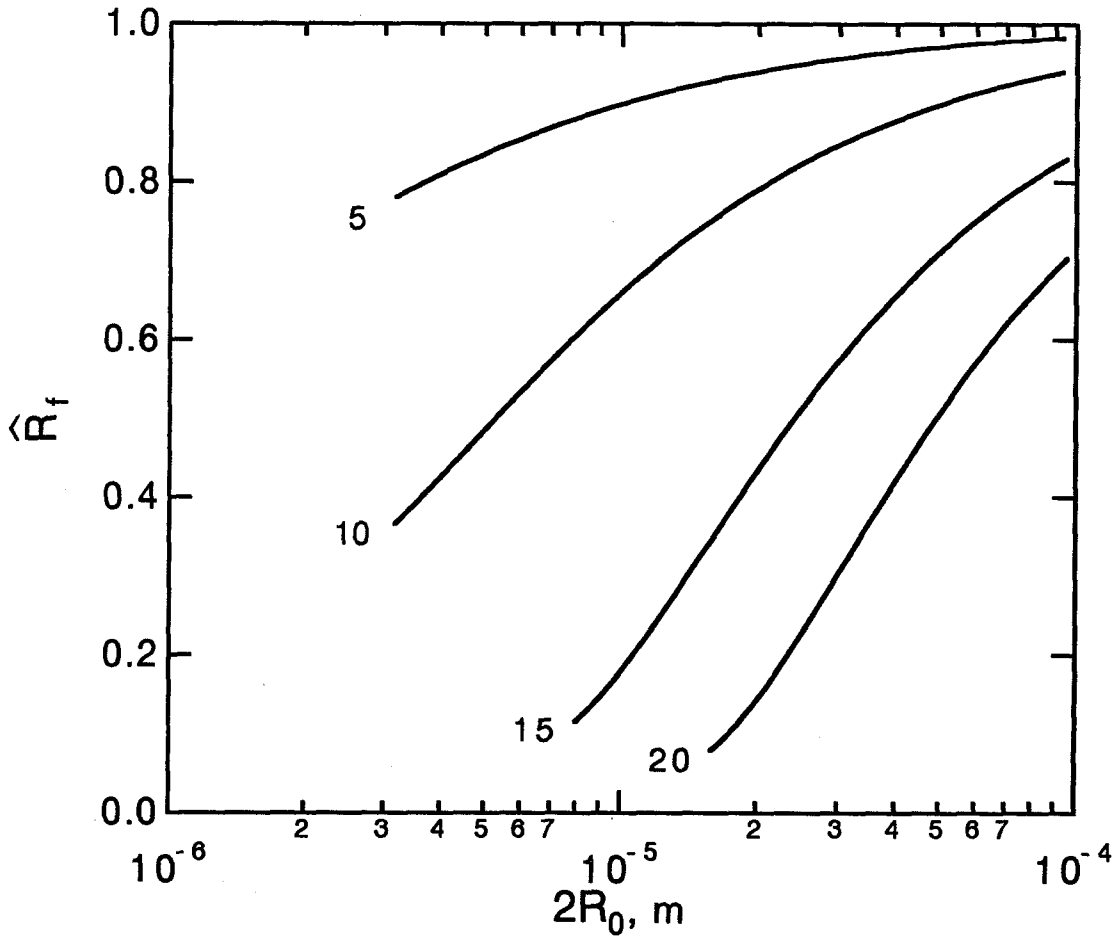

Figure 6.13: $\hat{R}_f$ versus $2R_0$ for various values of v_0 (km s^{-1})($Q = 1.9$ MJ kg^{-1}, $\rho_p =$ 1000 kg m^{-3}). The curves are terminated on the left-hand side where the condition that a bow shock forms ahead of the particle, i.e., $\mathrm{Kn}_1 \leq 0.33$, is violated.

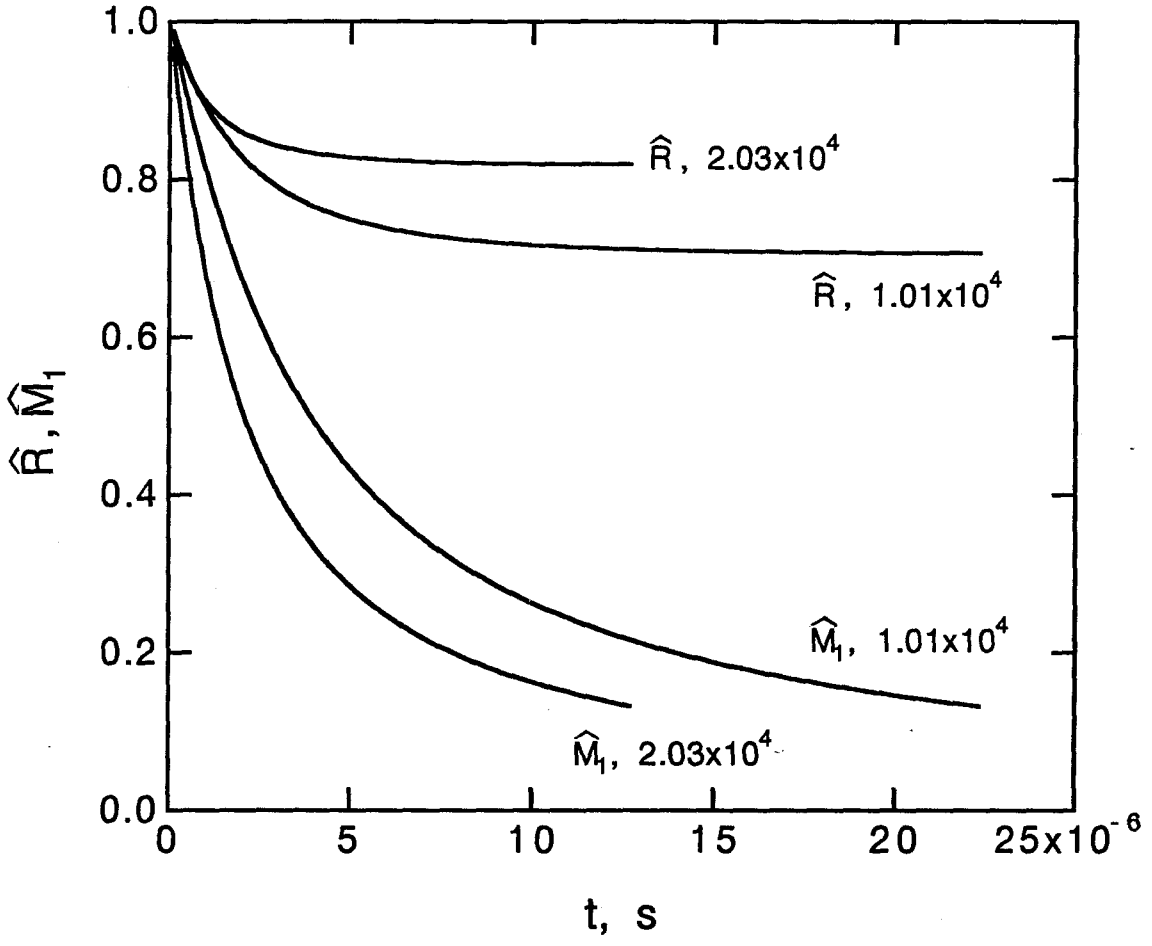

Figure 6.14: $\hat{R}$ and $\hat{M}_1$ versus t for two pressures (Pa)(Q = 1.35 MJ kg^{-1}, ρ_p =2420 kg m^{-3}, v_0 = 4.5 km s^{-1}, and R_0 = 3.53 μm).

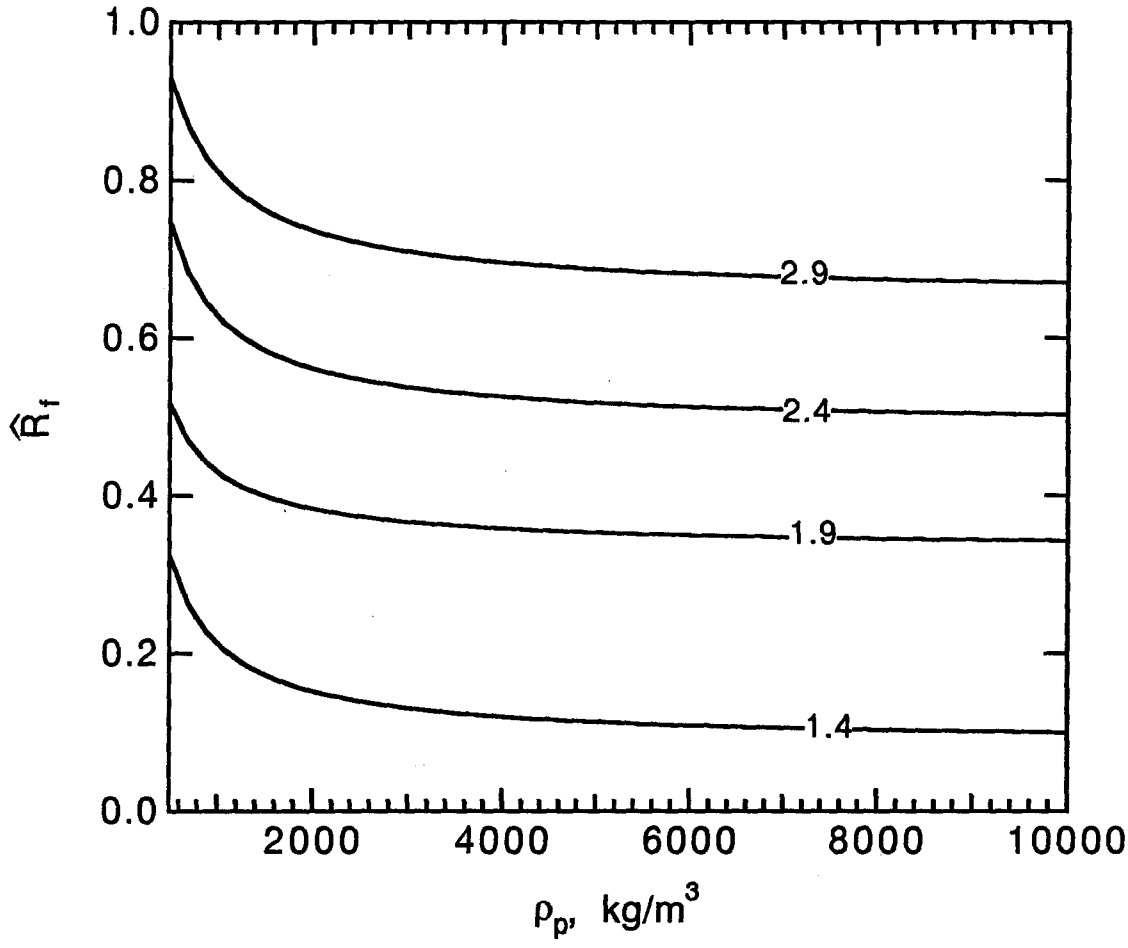

Figure 6.15: $\hat{R}_f$ versus ρ_p for various Q (MJ kg^{-1}) (v_0 =10 km s^{-1}, $R_0 = 5$ μm, and $p_1 = 0.2$ atm.

6.5 Conclusions

A model has been developed to describe the ablation and deceleration of spheres in continuum and slip flow. The model accounts for the variation of the particle drag coefficient and energy transfer coefficient with Reynolds and Mach numbers. The mass loss by ablation is pressure dependent according to this theory. Experiments performed using the NASA Ames Vertical Gun Range show the predicted dependence. The ratio of final to initial radii was 0.88 $\pm$ .08 for deceleration of silicate particles of 3.5 μm initial radius in 0.2 atm Xe gas, and decreased to 0.67 $\pm$ .08 in 0.1 atm gas. The mass loss increases with decreasing pressure mainly because the reduced particle drag leads to longer exposure to high temperatures. The heat of ablation was estimated to be 1.5 $\pm$ 0.2 MJ/kg, approximately corresponding to the energy required to raise the particle temperature from 295 K to 1300 K, the working point of the glass. This heat of ablation suggests that the primary mechanism of mass loss is aerodynamic entrainment of molten material from the surface of the particle, and that vaporization plays only a minor role in ablation under the present experimental conditions. Parametric studies of ablation using the model suggest that the mass loss will increase with an increase in particle density, velocity, and radius, mainly due to the increased time required to slow the particle, or with decreasing energy of ablation.

Acknowledgements

We thank W. Logsden, B. Langedyk, and J. Vongraey at NASA- Ames Research Center and B. Barber at the California Institute of Technology for technical assistance.

This research was supported in part by NASA grant NAGW1941, National Science Foundation Grant Number CTS-8813006, and the California Institute of Technology. Contribution #4870, Division of Geological and Planetary Sciences.

Chapter 7

Inward Electrostatic Precipitation of Particles in Spherical and Cylindrical Chambers

Abstract

An inward precipitator collects particles initially dispersed in a gas throughout either a cylindrical or spherical chamber onto a small central planchet. The instrument is effective for particle diameters greater than about 1 μm. One use is the collection of interplanetary dust particles (IDPs) which are stopped in a noble gas (xenon) by drag and ablation after perforating the wall of a thin-walled spacecraft-mounted chamber. First, the particles are positively charged for several seconds by the corona production of positive xenon ions from inward facing needles placed on the chamber wall. Then an electric field causes the particles to migrate toward the center of the instrument and onto the planchet. The collection time (of the order of hours for a 1 m radius spherical chamber) is greatly reduced by the use of optimally located screens which reapportion the electric field. Some of the electric field lines terminate on the wires of the screens so a fraction of the total number of particles in the chamber is lost. This loss can be minimized by using screens with small wire diameter and large

mesh size. The operation of the instrument is demonstrated by experiments which show the migration of approximately 1 μm carbon soot particles (initially dispersed throughout a 5 cm diameter cylindrical chamber with a +10 kV DC power supply) toward a 3.2 mm central collection rod.

7.1 Introduction

The motivation for the development of the present instrument which collects particles onto a small planchet stems from our work in which we use a thin-walled chamber filled with a noble gas (xenon) to stop interplanetary dust particles (IDPs) by gas drag and ablation (Chapter 6)(Fig. 7.1). Xenon is used since it is dense and chemically inert. The chamber is mounted on a spacecraft. A particle, after penetrating the chamber wall and being stopped in the gas, is collected by electrostatic precipitation. Conventional electrostatic precipitation is often used to remove particles from flue gases in power plants. In typical applications the particles are driven outward in a cylindrical geometry from a central wire which is also used as the charge source by operating a corona discharge around it. The particles migrate to the outer electrode. It would be exceedingly difficult to locate the particles for study via microscopy or other means in this scheme if the total number of particles is small since the particles are spread over a large area. Thus a means of driving a particle to a small area planchet is desired.

In a spherical geometry used for IDP collection it is natural to place the planchet at or near the center of the chamber since the direction from which the IDPs enter is unknown. The inward precipitator of Fig. 7.2a has a small spherical planchet at the center of a spherical cavity. The particle enters the chamber at hypersonic velocities

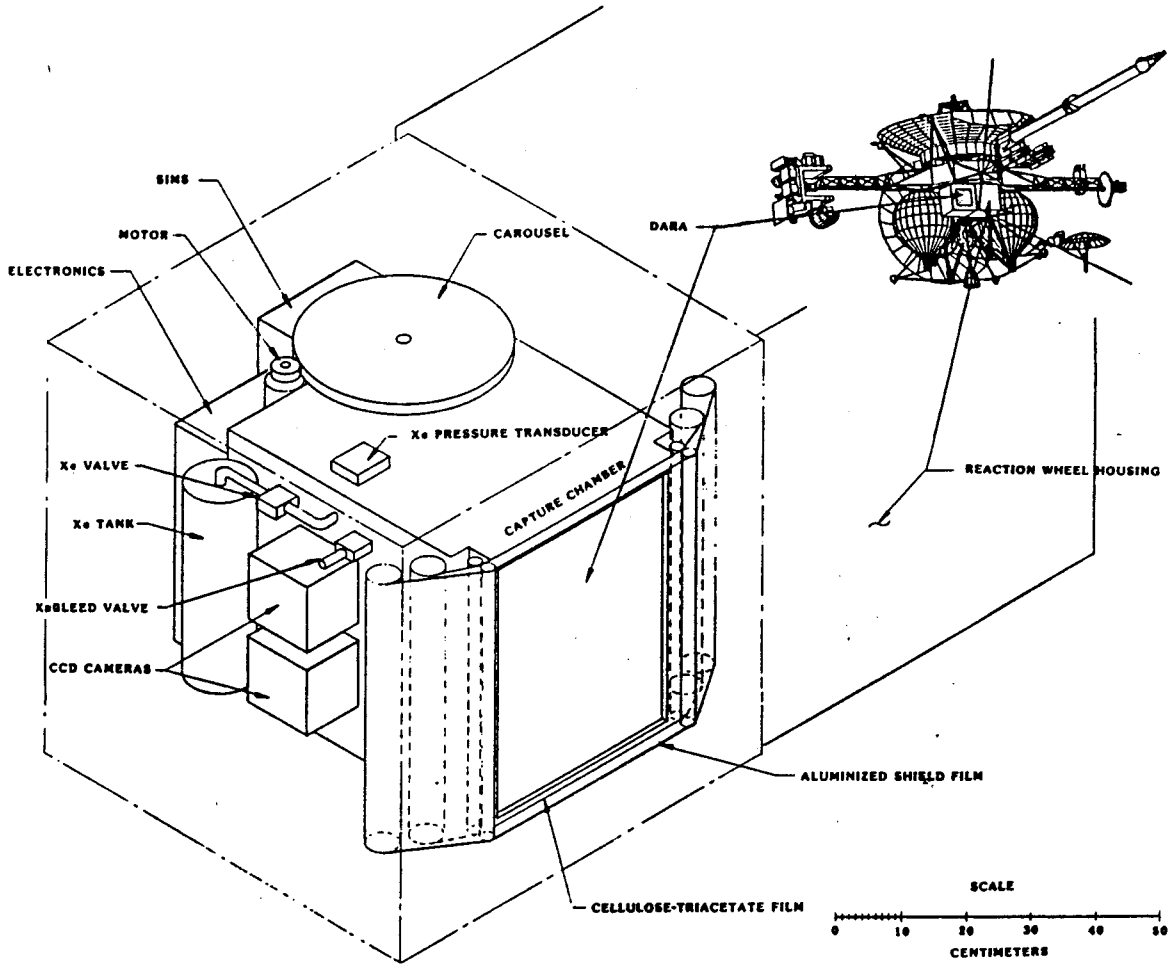

Figure 7.1: Concept drawing for the Dust and Ring Analyzer (DARA).

and is decelerated. This is represented by the dashed segment of the trajectories shown in Fig. 7.2. After the particle is stopped, numerous corona needles placed on the wall act to charge the IDPs positively by producing a flood of positive ions inside the chamber when an electrical potential of about +20 kV is applied for several seconds. Positive ions are used since xenon is a poor absorber of electrons and thus would be ineffective for particle charging if used with a negative corona . An electric field E is oriented to drive the particles to the planchet after they are charged. This is represented by the dotted segment of the trajectories shown in Fig. 7.2. The geometry of Fig. 7.2a has limitations in that E is too weak in regions far from the planchet and the migration speed of the particle is low there, resulting in long collection times (~1000 hrs for 5 micron particles in a 1 m radius spherical chamber). Thus one or more intermediate reapportioning screens are added which, when appropriately charged, adjust the electric field to speed the particle when it is in the region near the wall (Fig. 7.2b). As will be shown below the screens are very effective and reduce the collection time by more than two orders of magnitude.

This paper presents the techniques used for particle charging and a detailed analysis needed to determine the positions of the reapportioning screens which minimize the collection time in both the cylindrical and spherical geometries. Results of some preliminary experiments with a working cylindrical model are presented and compared with theoretical performance.

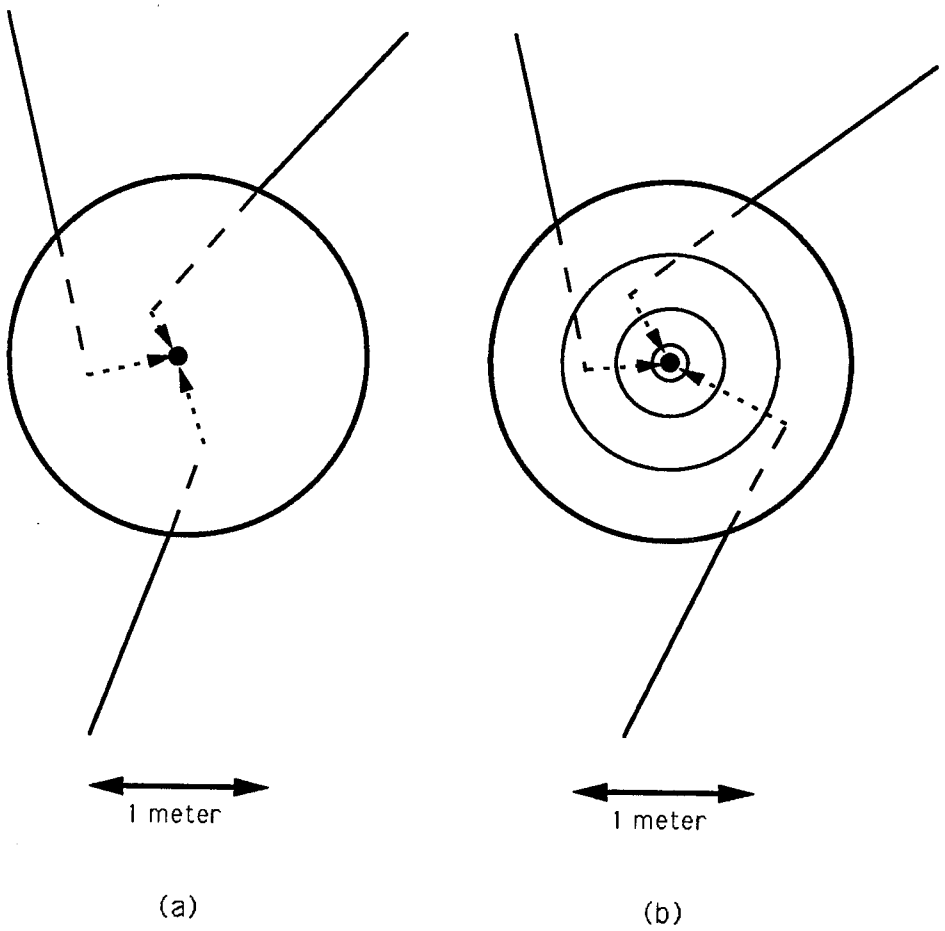

Figure 7.2: Geometry of the inward electrostatic precipitator. Particles dispersed throughout the chamber after being slowed by gas drag and ablation are collected by charging them and applying an electric field to force them toward the small planchet at the center. Solid lines indicate trajectories of IDPs in space. Dashed lines indicate trajectories during deceleration. Dotted lines indicate trajectories during electrostatic precipitation.

7.2 Theory

7.2.1 Particle Charging in a Gas

A micron-size dielectric particle suspended in a gas can be charged with tens or hundreds of elementary charges using corona field charging techniques.

Consider the situation at the end of a sharp needle which is held at a positive potential and surrounded by xenon gas at 0.2 atm and 300°K. The electric field lines are directed outward and the small amounts of thermally-excited free electrons always present in the gas are accelerated toward the needle. If the potential is high enough then these electrons will reach sufficient energy (~12 eV) to ionize xenon atoms. Each collision liberates additional electrons and positive xenon ions. Thus a positive corona is established around the needle tip. The positive xenon ions are repelled from the needle and out into the surrounding gas. It is these positive ions which attach to and charge the IDPs in the gas.

It is also possible to operate negative coronas by applying a negative potential to the needle, but for particle charging applications this requires a surrounding gas that is an efficient absorber of electrons. Since noble gases are not efficient absorbers of electrons due to their low electron affinities [67], the negative corona is not used.

Field charging occurs when the positive ions created by the corona migrate along electric field lines and impinge on the particle. As the charge on the particle increases the electric field in the vicinity is altered and eventually incoming positive ions are deflected and further field charging does not occur. At this time the particle has received the saturation field charge q_s. The time required to reach q_s is [68]

$$\tau_c = \frac{4\epsilon_o}{eB_i N_{i_\infty}}, \tag{7.1}$$

where τ_c is the time scale for complete field charging, ϵ_o is the permittivity of free space, e is the elementary charge, B_i is the ion mobility, and N_{i_∞} is the background ion number concentration. Equation (7.1) gives, under typical electrostatic precipitation conditions, $\tau_c = 0.1$ s. As will be seen below this time is much less than the overall collection times in a chamber of the size being considered (which is of the order of 1 meter in radius) so the particles can be assumed to have the saturation field charge after a negligible amount of time. The saturation charge q_s is [68]

$$q_s = 4\pi\epsilon_o \frac{3k}{k+2} E_\infty R_p^2, \tag{7.2}$$

where k is the dielectric constant of the particle, E_∞ is the magnitude of the background electric field, and R_p is the particle radius. Equation (7.2) is derived assuming a spherical and homogeneous particle. Typical values of k for mineral particles as might be encountered in interplanetary space range from approximately 2 to 10. Values for metallic particles would be higher.

As long as the background xenon ions are present the charge on the particle continues to increase beyond the value given by Equation (7.2) by diffusion charging [68]. It is assumed here, however, that potentials high enough to cause electrical discharges at the corona needles will be applied only long enough (several seconds) to reach the field charging saturation charge q_s. Negligible diffusion charging will occur during this time so q_s is the final particle charge. The ion migration time through a 1 meter radius chamber with three screens is about 3 seconds, assuming an ion mobility of 10^{-4} m^2 V^{-1} s^{-1} and $V_T = 20$ kV.

7.2.2 Particle Motion

Spherical Case

In order to describe the migration of a particle in the spherical chamber the electric field must be known throughout. With an absence of space charge the potential between two concentric spheres is given by Laplace's equation in spherical coordinates with radial dependence only,

$$\frac{1}{r^2}\frac{\partial}{\partial r}[r^2\frac{\partial V}{\partial r}] = 0 \tag{7.3}$$

with $V = V_i$ at $r = r_j$ and $V = V_j$ at $r = r_j$. Note that $r_j > r_i$ where r_i and r_j are the radii of the spheres which are held at potentials V_i and V_j, respectively. The solution to Eqn. (7.3) is

$$V(r) = \frac{1}{r_j - r_i}[\frac{r_i r_j}{r}(V_i - V_j) + r_j V_j - r_i Vi] \tag{7.4}$$

with $r_i \leq r \leq r_j$.

The electric field is

$$E(r) = -\frac{\partial V}{\partial r} \tag{7.5}$$

which gives

$$E(r) = \frac{1}{r^2}[\frac{V_i - V_j}{r_j - r_i}]r_i r_j. \tag{7.6}$$

Equation (7.6) gives the electric field strength in any part of the spherical cavity provided the location and potential of each screen is known.

The particles, having been charged positively to the field charge saturation level, will move toward the sphere center under the action of the electric field. For Stokesian particles (Re $= 2u_p R_p \rho/\mu < 0.1$, where u_p is the particle speed, R_p is the particle radius, ρ is the gas density, and μ is the absolute viscosity) the equilibrium speed is

[68]

$$\mid u_p \mid = \frac{\mid q_s E \mid}{6\pi\mu R_p} = \mid \frac{\partial r}{\partial t} \mid, \tag{7.7}$$

where r is the radial position of the particle. Equation (7.7) is valid for approximately $1/2 < R_p < 5$ microns, which is the range of interest for this study. The lower limit is set by the requirement that the particle is much larger than the mean free path (which is about 0.3 microns for xenon at 0.2 atm and 300°K) and the upper limit is set by the Stokes flow regime (low Re) requirement. For particles outside this range, both Equations (7.2) and (7.7) would need to be modified.

Rearranging and integrating Eqn. (7.7) gives

$$\int_{r_i}^{r_j} \frac{6\pi\mu R_p}{\mid q_s E \mid} \mathrm{d}r = \mid \int_{t_i}^{t_j} \mathrm{d}t \mid = \mid t_j - t_i \mid . \tag{7.8}$$

To find the time $T = t_i - t_j$ for the particle to move from one screen to the next in the spherical chamber, we set r_i and r_j to the radial locations of the screens. Substituting Eqn. (7.6) gives

$$T = \int_{r_i}^{r_j} \frac{6\pi\mu R_p \mathrm{d}r}{\mid \frac{q_s}{r^2} \frac{V_i - V_j}{r_j - r_i} r_i r_j \mid}. \tag{7.9}$$

Since the particle is positively charged ($q_s > 0$), we must have $V_i < V_j$ to move the particle toward the sphere center. Thus

$$T = \frac{6\pi\mu R_p}{r_i r_j q} \frac{r_j - r_i}{V_j - V_i} \int_{r_i}^{r_j} r^2 \mathrm{d}r = \frac{2\pi\mu R_p}{q} \frac{r_j - r_i}{V_j - V_i} \frac{r_j^3 - r_i^3}{r_i r_j} > 0. \tag{7.10}$$

The total time T_T for the particle to pass from the outside of a spherical chamber with n internal screens to the central planchet is a sum over the $n + 1$ zones between the screens. Thus,

$$T_T = \frac{2\pi\mu R_p}{q_s} \sum_{i=0}^{n} \frac{r_{i+1} - r_i}{V_{i+1} - V_i} \frac{r_{i+1}^3 - r_i^3}{r_{i+1} r_i}. \tag{7.11}$$

where $r_{n+1} = R$ is the overall radius and $r_o = r_p$ is the planchet radius.

One way to set the potentials on each screen is to divide the total available potential V_T into even portions, so that $V_j - V_i = \text{const.} = V_T/(n+1)$. Thus $V_i = (i-1)V_T/(n+1)$. By fixing the voltages on the screen, the number of independent variables in the system available for minimizing T_T is reduced from $2n$ to n. Thus the minimum in T_T that is found will not be the absolute optimum, but the beneficial effect of the screens is still obvious and the calculation may be extended to include varying voltages in a straightforward manner–an example of this is given later. For now we have $V_{i+1} - V_i = \Delta V = V_T/(n+1)$ and Eqn. (7.11) becomes

$$T_T = \frac{2\pi\mu R_p(n+1)}{q_s V_T} \sum_{i=0}^{n} \frac{(r_{i+1} - r_i)(r_{i+1}^3 - r_i^3)}{r_{i+1} r_i}. \tag{7.12}$$

If we now define the dimensionless radial coordinate $\hat{r} = r/R$ and the dimensionless time

$$\hat{T}_T = \frac{T_T}{\frac{2\pi\mu R_p R^2}{q_s V_T}} \tag{7.13}$$

we obtain

$$\hat{T}_T = (n+1) \sum_{i=0}^{n} \frac{(\hat{r}_{i+1} - \hat{r}_i)(\hat{r}_{i+1}^3 - \hat{r}_i^3)}{\hat{r}_{i+1}\hat{r}_i}. \tag{7.14}$$

Proper positioning of the screens minimizes $\hat{T}_T$. The number of independent variables available for minimizing $\hat{T}_T$ is n, namely the screen positions $\hat{r}_1, \ldots, \hat{r}_n$, with the restriction

$$1 > \hat{r}_n > \hat{r}_{n-1} > \hat{r}_{n-2} > \ldots > \hat{r}_1 > \hat{r}_p. \tag{7.15}$$

The total time $\hat{T}_T$ in Eqn. (7.14) was minimized numerically for n =1, 2, and 3 and for $\hat{r}_p = 0.001$. This was done by systematically moving the screens throughout all of their allowed positions and noting the positions corresponding to minimum $\hat{T}_T$. Table 7.1 shows the results.

$\hat{T}_T$	number of screens	screen positions ($\hat{r}$)
999	0	-
17.7	1	0.135
7.47	2	0.069, 0.406
5.44	3	0.049, 0.254, 0.595

Table 7.1: Optimal screen positions for a spherical inward electrostatic precipitator.

By the addition of a single screen the collection time is reduced to 1.8% of its original value. Diminishing returns are seen with additional screens but with three screens the collection time is reduced to 0.54% of its original value. Thus the screens are very effective. The dimensionless electric fields $E/(V/R)$ versus $\hat{r}$ without screens and with three screens are shown in Fig. 7.3. The screens add electric field strength to the outer regions of the chamber where it is needed. The dimensionless particle motion characteristics for these two geometries are shown in Fig. 7.4 where $\hat{t} = tq_sV_T/(2\pi\mu R_pR^2)$ is the dimensionless time. Notice that the screens act to give the particle a more constant speed as it travels inward compared to the motion without screens. For a concrete example, consider particles in a 1 m radius chamber with three screens filled with xenon gas at 300°K and 0.2 atm and with +20 kV total available potential. The potentials are thus +20 kV, +15 kV, +10 kV, +5 kV and 0 kV on the outer wall, screens, and planchet, respectively. Collection times are shown as a function of particle size and dielectric constant in Fig. 7.5. The collection time is inversely proportional to the particle size and dielectric constant.

The dimensionless size of the planchet has an effect on the collection times and screen positions. For a planchets with radii of 0.05% and 0.2% of the overall sphere radius the dimensionless collection times for three screens are 5.75 and 5.11, respectively. Also, as given in Table 7.2 the optimum screen positions are such that the screens are placed closer to the planchet for the smaller planchet.

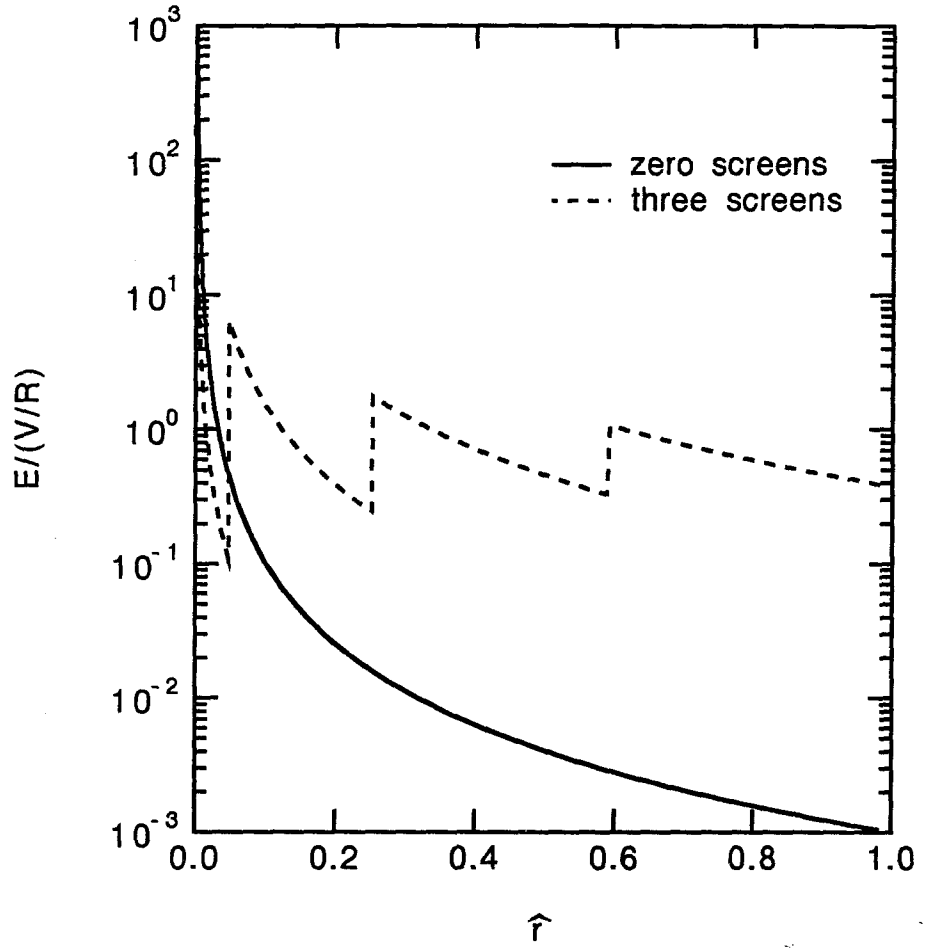

Figure 7.3: Dimensionless electric field strength versus dimensionless radial position for spheres with zero screens and three optimally positioned screens. The screens increase the field strength in the outer part of the chamber.

$\hat{T}_T$	number of screens (n)	screen positions ($\hat{r}$)
for $\hat{r}_p = 0.0005$:		
1999	0	–
5.75	3	0.038, 0.232, 0.579
for $\hat{r}_p = 0.002$:		
499	0	–
5.11	3	0.062, 0.277, 0.612

Table 7.2: Effect of dimensionless planchet size.

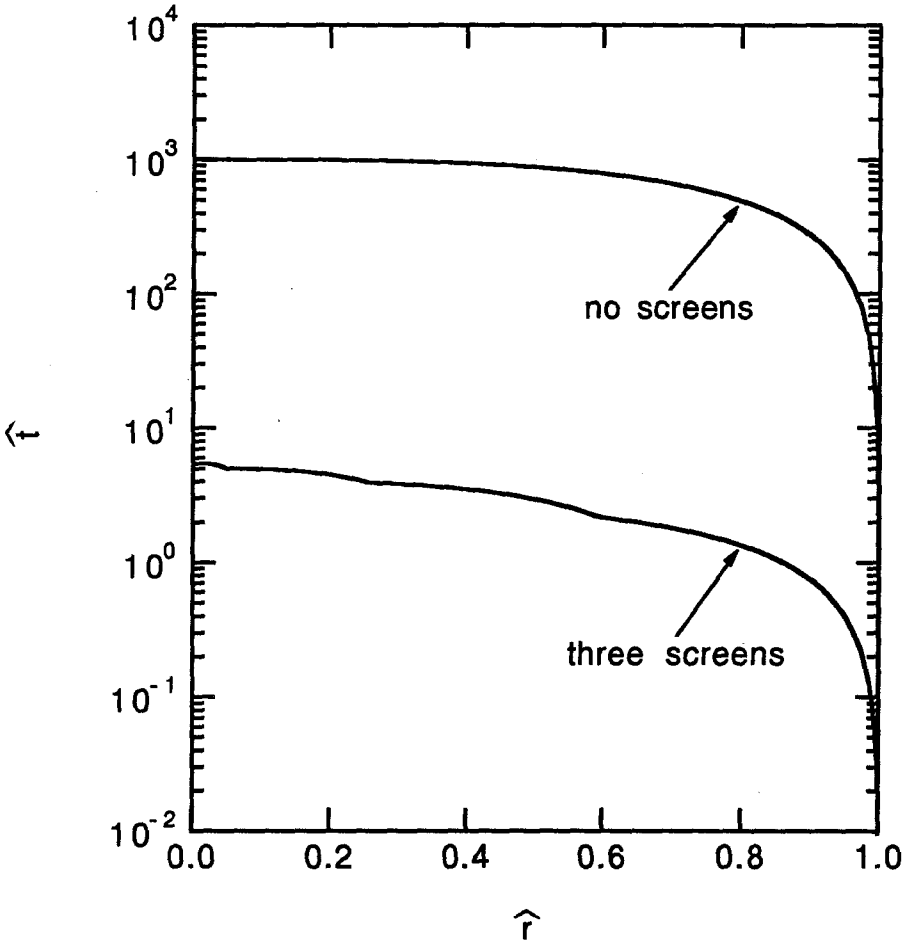

Figure 7.4: Dimensionless particle motion characteristics for a sphere with zero and three screens. The speed of the particle is more constant in the three screen case.

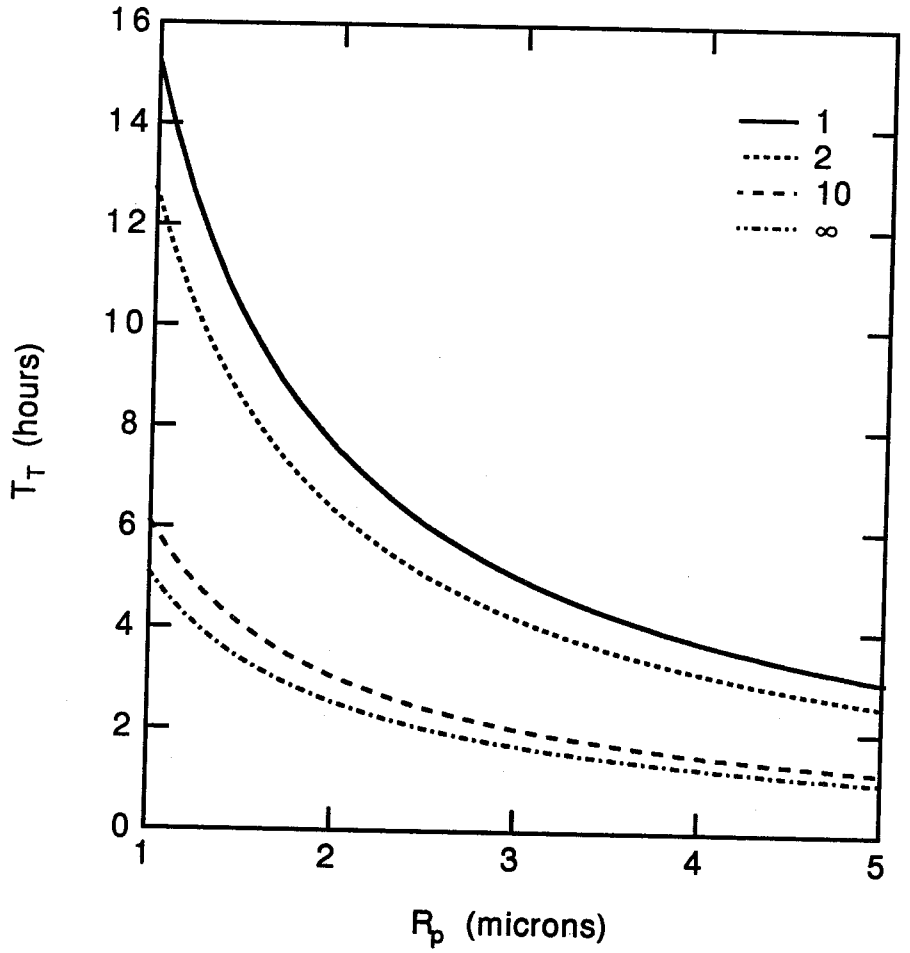

Figure 7.5: Collection time as a function of particle diameter and dielectric constant. Large particles with large dielectric constant are collected in the least amount of time ($\mu = 5 \times 10^{-5}$ kg m^{-1}s^{-1}, $E_\infty = 1.4 \times 10^4$ V/m, $R = 1$, V_T=20 kV, and $\hat{T}_T = 5.44$).

If we relax the restriction that the potential is equally divided over the zones of the chamber then $\hat{T}_T$ can be further reduced. For example, consider a spherical chamber with one internal screen ($n = 1$) and $\hat{r}_p = 0.001$. Both the screen position and potential are allowed to vary such that $\hat{T}_T$ is a function of $\hat{r}_2$ and $\hat{V}_2$, where $\hat{r}_1 < \hat{r}_2 < 1$ and $0 < V_2 < V_T$. For this case, $\hat{T}_T = 15.9$ with $\hat{r}_2 = 0.106$ and $V_2 = 0.272V_T$. This compares to the one screen case in Table 7.1, which has $\hat{T}_T = 17.7$, $\hat{r}_2 = 0.135$ and $V_2 = 0.500V_T$. Thus a reduction in $\hat{T}_T$ is obtained by reducing the potential on the screen and moving it slightly inward toward the planchet.

Cylindrical Case

The cylindrical geometry can also be treated using the above analysis. The governing equation for the potential is

$$\frac{1}{r}\frac{\partial}{\partial r}[r\frac{\partial V}{\partial r}] = 0 \tag{7.16}$$

with $V = V_i$ at $r = r_i$, $V = V_j$ at $r = r_j$ and $r_j > r_i$, where r_i and r_j are the radii of cylinders which are held at potentials V_i and V_j, respectively. The solution to Eqn. (7.16) is

$$V(r) = \frac{V_j \ln(r/r_j) - V_i \ln(r/r_j)}{\ln(r_j/r_i)} \tag{7.17}$$

for $r_i < r < r_j$. The electric field is

$$E(r) = \frac{V_i - V_j}{r \ln(r_j/r_i)}. \tag{7.18}$$

Eqn. (7.8) then gives

$$t_i - t_j = \int_{r_i}^{r_j} \frac{6\pi\mu R_p}{|\frac{q(V_i - V_j)}{r\ln(r_j/r_i)}|} \mathrm{d}r. \tag{7.19}$$

Assuming $q > 0$ and $V_j > V_i$ gives

$$t_i - t_j = \frac{6\pi\mu R_p \ln(r_j/r_i)}{q(V_j - V_i)} \int_{r_i}^{r_j} r\mathrm{d}r = \frac{3\pi\mu R_p \ln(r_j/r_i)}{q(V_j - v_i)}(r_j^2 - r_i^2) > 0. \tag{7.20}$$

$\hat{T}_T$	number of screens (n)	screen positions ($\hat{r}$)
10.4	0	–
4.83	1	0.301
3.98	2	0.179, 0.569
3.66	3	0.130, 0.400, 0.697

Table 7.3: Optimal screen positions for a cylinder.

The total collection time for the cylindrical chamber with n internal screens is

$$T_T = \frac{3\pi\mu r_p}{q}\sum_{i=0}^{n}\frac{\ln(r_j/r_i)}{V_j - V_i}(r_j^2 - r_i^2); \tag{7.21}$$

where $r_{n+1} = R$ and $r_0 = r_p$. If we set $V_j - V_i = \text{const.}$ then

$$T_T = \frac{3\pi\mu R_p(n+1)}{qV_T}\sum_{i=0}^{n}\ln(r_j/r_i)(r_j^2 - r_i^2). \tag{7.22}$$

Using the same dimensionless variables as previously defined in Eqn. (7.13) we obtain

$$\hat{T}_T = \frac{3}{2}(n+1)\sum_{i=0}^{n}\ln(\hat{r}_j/\hat{r}_i)(\hat{r}_j^2 - \hat{r}_i^2). \tag{7.23}$$

Table 7.3 shows the results of minimizing $\hat{T}_T$ for the cylindrical case for one, two, and three screens for $\hat{r}_p = 0.001$.

Note that a cylinder of the same radius as a sphere collects a particle in less time (Table 7.1). For example, with three screens the collection time for a cylindrical chamber is 67% that of a spherical one. The screens enhance the collection speed but not as effectively as for the spherical case. One screen reduces the collection time to 46.4% of the value for zero screens while three screens reduce it to 35.2%. The trends seen for the spherical geometry regarding the effect of the dimensionless planchet size and variable voltages apply to the cylindrical geometry as well.

7.2.3 Particle Loss to the Screens

Since a fraction of the electric field lines around the screen wires terminate on the wires, some particle losses will occur as particles migrate across the chamber. The

magnitude of this loss depends on the details of the screen mesh size and shape and wire size and shape. It also depends on the physical characteristics of the particles since there are aerodynamic and inertial forces involved in the migration. To illustrate how loss can occur we considered an infinite array of wires between two parallel plates. The upper plate (at $\hat{y} = 1$) is held at a potential $\hat{V}_3 = 1$ (where $\hat{V} = V/V_T$) and the lower plate (at $\hat{y} = 0$) is grounded. The wires (at $\hat{y} = y_2$) are held at a potential $\hat{V}_2$ where $\hat{V}_1 < \hat{V}_2 < \hat{V}_3$. A positively charged particle would thus migrate from the top plate toward the bottom plate. In both the cylindrical and spherical geometries considered above the screens strengthen the electric field in the outer part of the chamber and weaken it in the inner part. This can be simulated in the test geometry by setting, for example, $\hat{V}_2 = 0.5$ and $\hat{y}_2 > 0.5$. To obtain the field lines the potential field $\hat{V}(\hat{x}, \hat{y})$ must be solved. The governing equation, assuming no space charge, is the Laplace equation in rectangular coordinates

$$\frac{\partial^2 \hat{V}}{\partial \hat{x}^2} + \frac{\partial^2 \hat{V}}{\partial \hat{y}^2} = 0. \tag{7.24}$$

The boundary conditions for Eqn. (7.24) are $\hat{V}(\text{wire}) = \hat{V}_2$, $\hat{V}(\hat{y} = 1) = 1$, $\hat{V}(y = 0) = 0$, and $\frac{\partial \hat{V}}{\partial \hat{x}}(\hat{x} = 0, \hat{x} = 1) = 0$. Equation (7.24) was solved numerically using a finite-element method [69]. The wire surface is simulated by setting four points in the numerical grid equal to $\hat{V}_2$. The resulting field lines are shown in Fig. 7.6. In this example 40% of the field lines terminate on the surface of the wire. The percentage of particles lost, assuming that the starting position of particles is random, is also 40%. In the actual instrument an experimental calibration or full three-dimensional simulation is needed to quantify the loss.

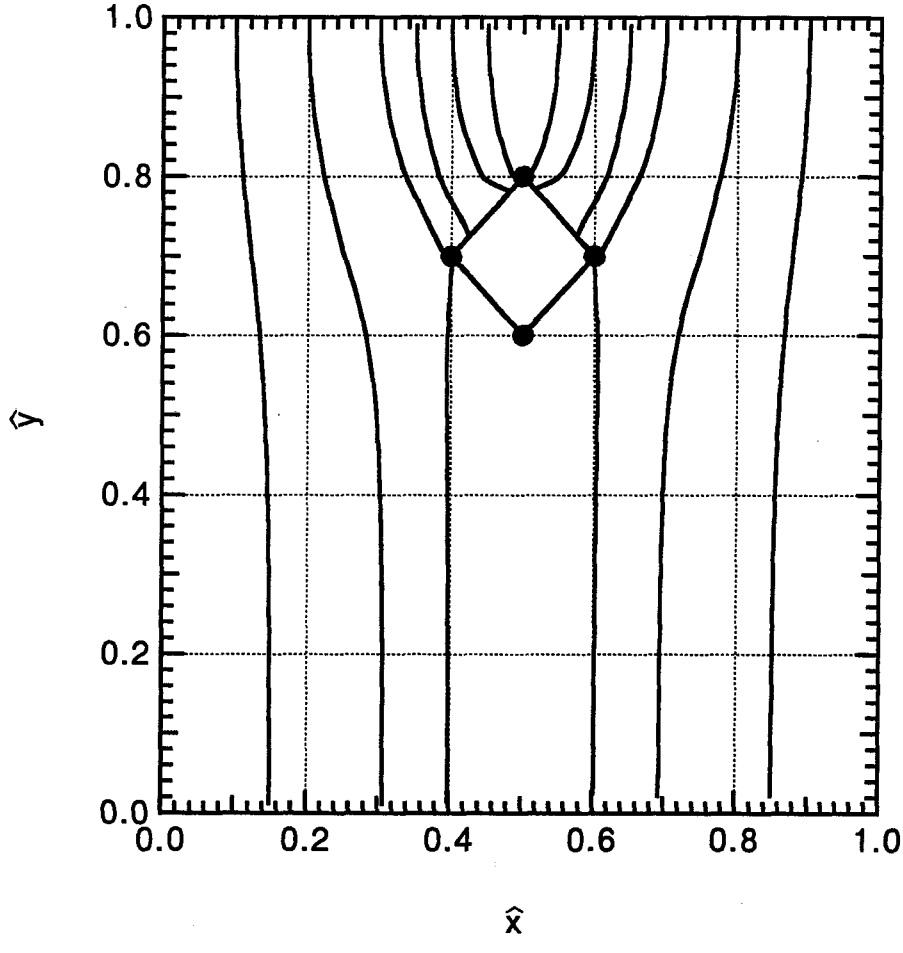

Figure 7.6: Field lines according to the finite element solution. One section of the periodic geometry that extends to infinity to the left and right is shown.

7.3 Experiments

To demonstrate the operation of the inward electrostatic precipitator, a cylindrical chamber was constructed (Fig. 7.7). A cylindrical geometry was chosen for ease of experiment and construction. The brass outer casing was 5.1 cm diameter. The ends and sides were fitted with clear Lucite ports to allow videotaping and He-Ne laser illumination of the particles. The particles were injected using a 50 cc syringe through a port in the side of the casing and allowed to diffuse throughout the interior of the chamber. A long range microscope (Questar QM1), CCD camera (COHU 4815-5000/0000) and video cassette recorder (Panasonic AG-1830 in S-VHS format) were used to record the motion of the particles (Fig. 7.8). The particles were charged by one to two seconds of corona discharge of positive ions from corona needles held at +10 kV and placed at the perimeter of the precipitator. After charging, the potential was reduced to +6 kV to stop the corona but maintain an electric field and the particles migrated toward the 3.2 mm diameter grounded collection rod. The single screen with 2.5 cm diameter was held at half the casing potential (i.e., +5 kV during charging and + 3 kV during collection).

The particles were carbon soot produced from a candle flame [70]. To obtain the particles, a glass container was placed over the flame until it extinguished, producing large amounts of soot in aerosol form. The particles were drawn out of the container and into the syringe with a 1/4 inch tube attached and subsequently injected into the cylindrical precipitator. Some large-scale motion occurred just after injection into the chamber but this ceased after approximately one minute. The appearance of particles in the chamber before any potential was applied is shown in Fig. 7.9 which is a photograph taken directly from a black and white monitor. On the original

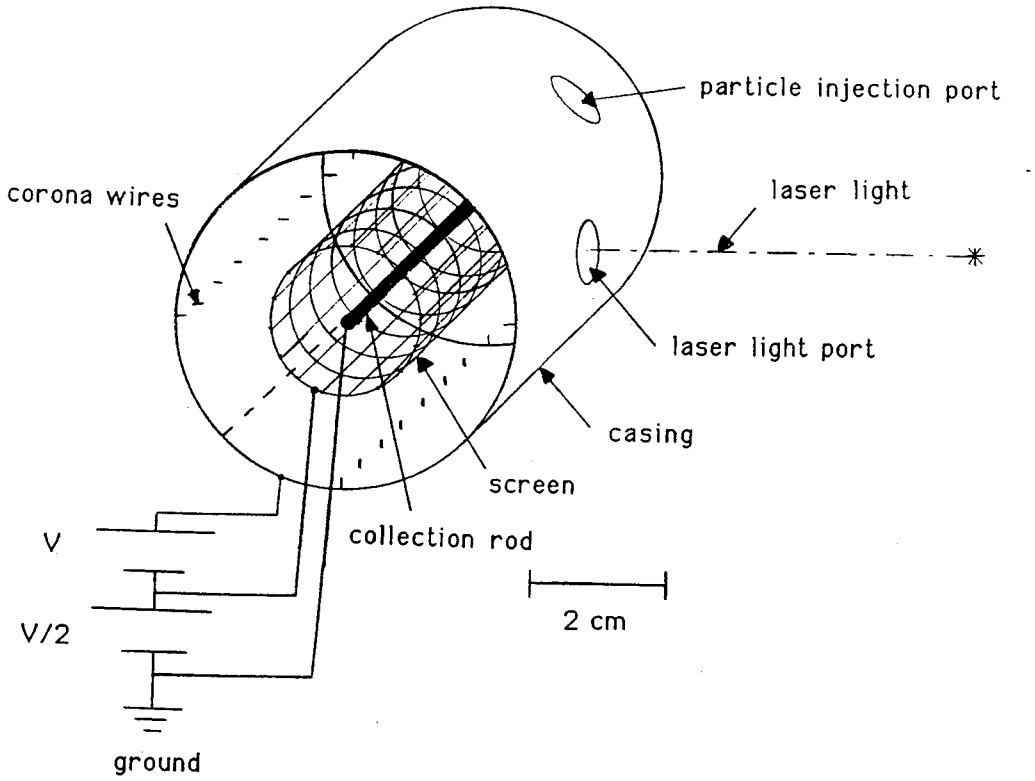

Figure 7.7: Schematic drawing of the cylindrical inward precipitator constructed for the experiments.

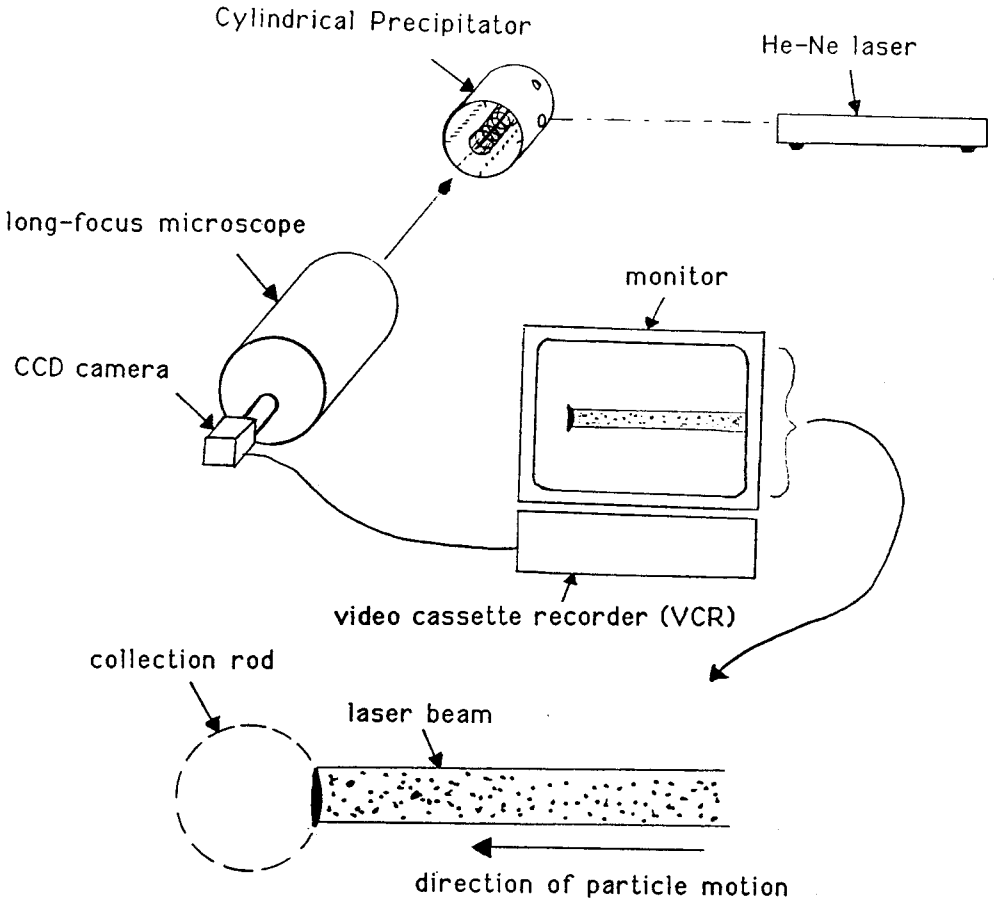

Figure 7.8: Overall experimental apparatus. The particle motion was recorded using a long range microscope and video cassette recorder.

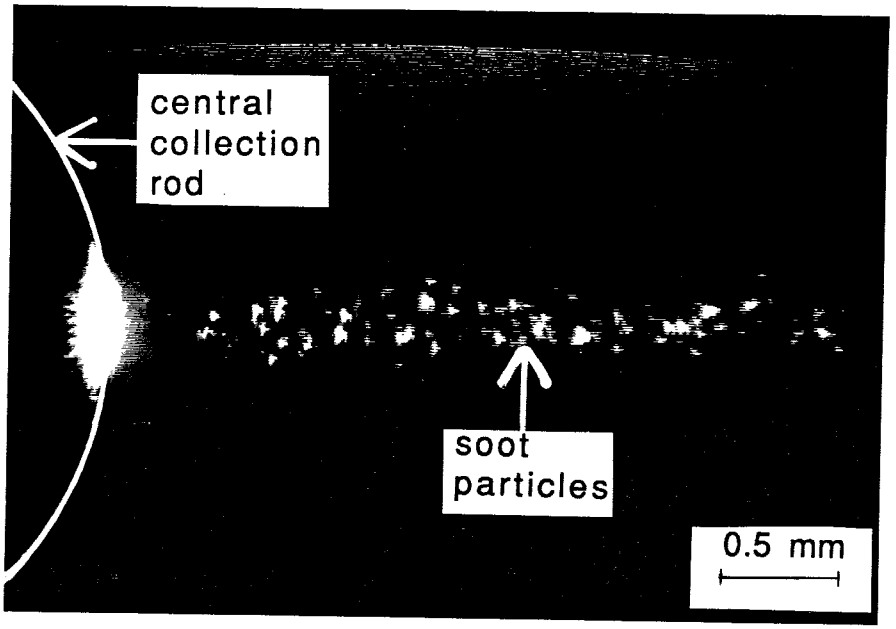

Figure 7.9: Photograph of particles near the central collection rod (end view). The outline of the collection rod is drawn. Scattered light from the laser is seen at the surface of the rod. No charge or electric field exist.

video recording, the particles were seen to move under Brownian motion and slow gravitiational settling, but all large-scale fluid motion had ceased.

After charging the motion of particles was seen clearly on the original recording as all particles migrated toward the collection rod. The speed varied from particle to particle due to the variation of size and charge. Figure 7.10 shows photographs of a particularly slow particle taken 0.17 s apart. The average speed was 4.5 mm/s. This particle was chosen for photographing since its slow speed facilitated better images for the figures in this paper.

The experimentally determined speed cannot be precisely compared with the theoretical predictions since the exact size and charge of the particle seen in the videotape was not known. By the observed settling speed of the particles in the chamber, the

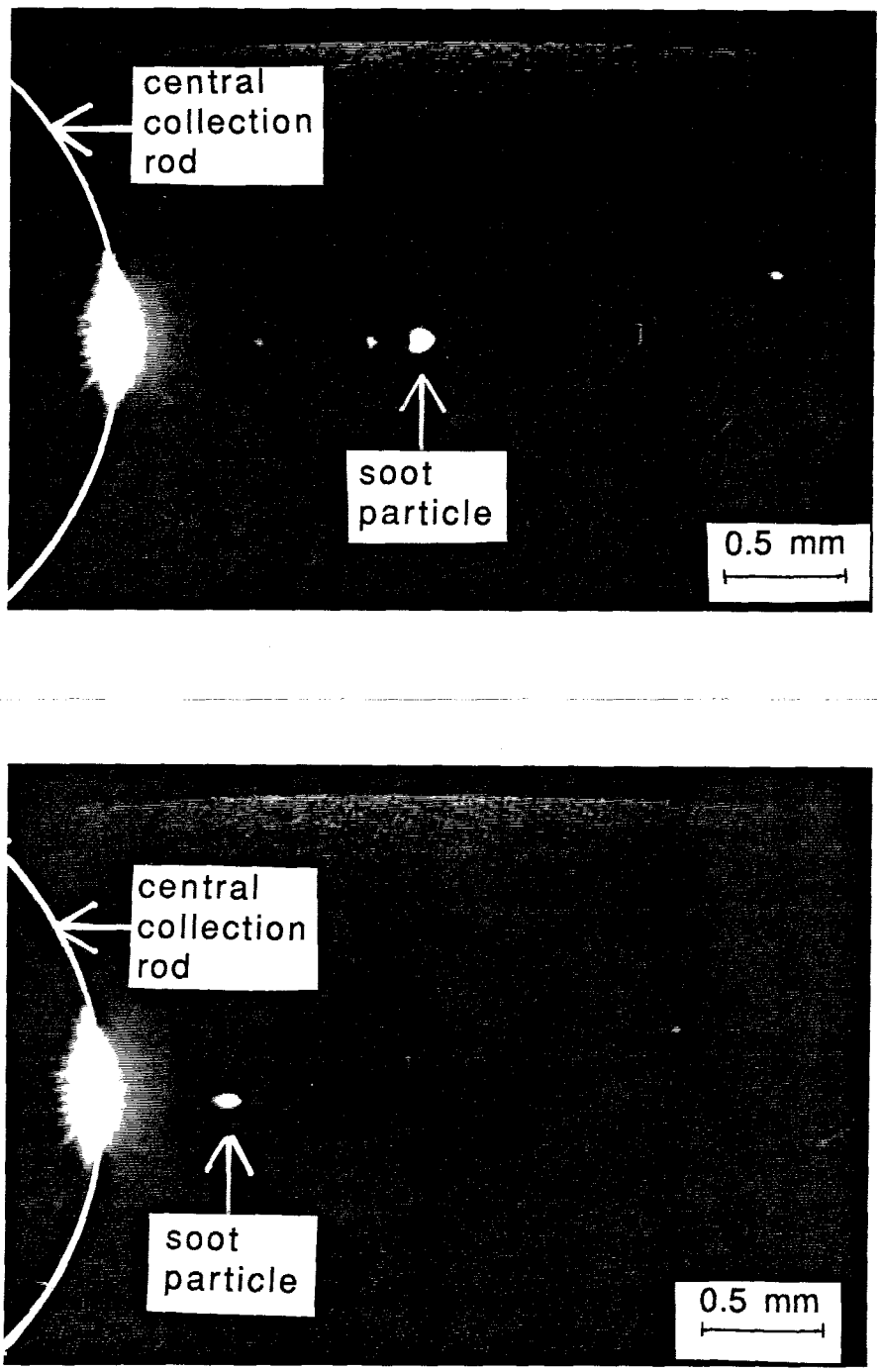

Figure 7.10: Photographs showing a particularly slow particle (chosen for photographic clarity) near the collection rod (end view) (top) 0 s, (bottom) 0.17 s. The particle was moving toward the rod with an average speed of 4.5 mm/s.

average particle diameter was roughly 1 μm. Using Eqn. (7.2) for the charge in the migration velocity calculation (Eqn. (7.7)) gives 43 mm/s, which is one order of magnitude higher than observed. The particle in Fig. 7.10 probably did not receive the full saturation charge given by Eqn. (7.2) due to its initial location in the chamber and anomalies in the spatial density of ions generated in the charging process. Other particles seen on the video but not photographed had speeds averaging 30 mm/s–roughly corresponding to the theoretical value of 43 mm/s.

Motion of particles through the electrified screen was also observed. Figure 7.11 shows photographs of a slow particle taken 1.0 seconds apart. The average speed of this particle was 1.5 mm/s. Again, the theoretically predicted value is higher than this by one order of magnitude, the difference being mainly due to charge anomalies. Other particles seen on the video but not photographed had speeds of the order of the theoretically predicted values.

7.4 Conclusions

The basic design concepts of the inward electrostatic precipitator have been described. The instrument is designed to collect interplanetary dust particles (IDPs) with diameters ranging from approximately 1 to 1000 microns initially dispersed throughout a large volume filled with xenon gas onto a planchet of small size so that the particles can be easily located for inspection and analysis. Particles below 1 micron are difficult to charge by field charging and particles above 1000 micron radius may be too large to move through the screens. (The calculations are valid for particles ranging from about 1 to 10 microns in diameter.) The analysis of the motion of charged particles in an electric field was used to optimize the positions of one, two, or three intermediate

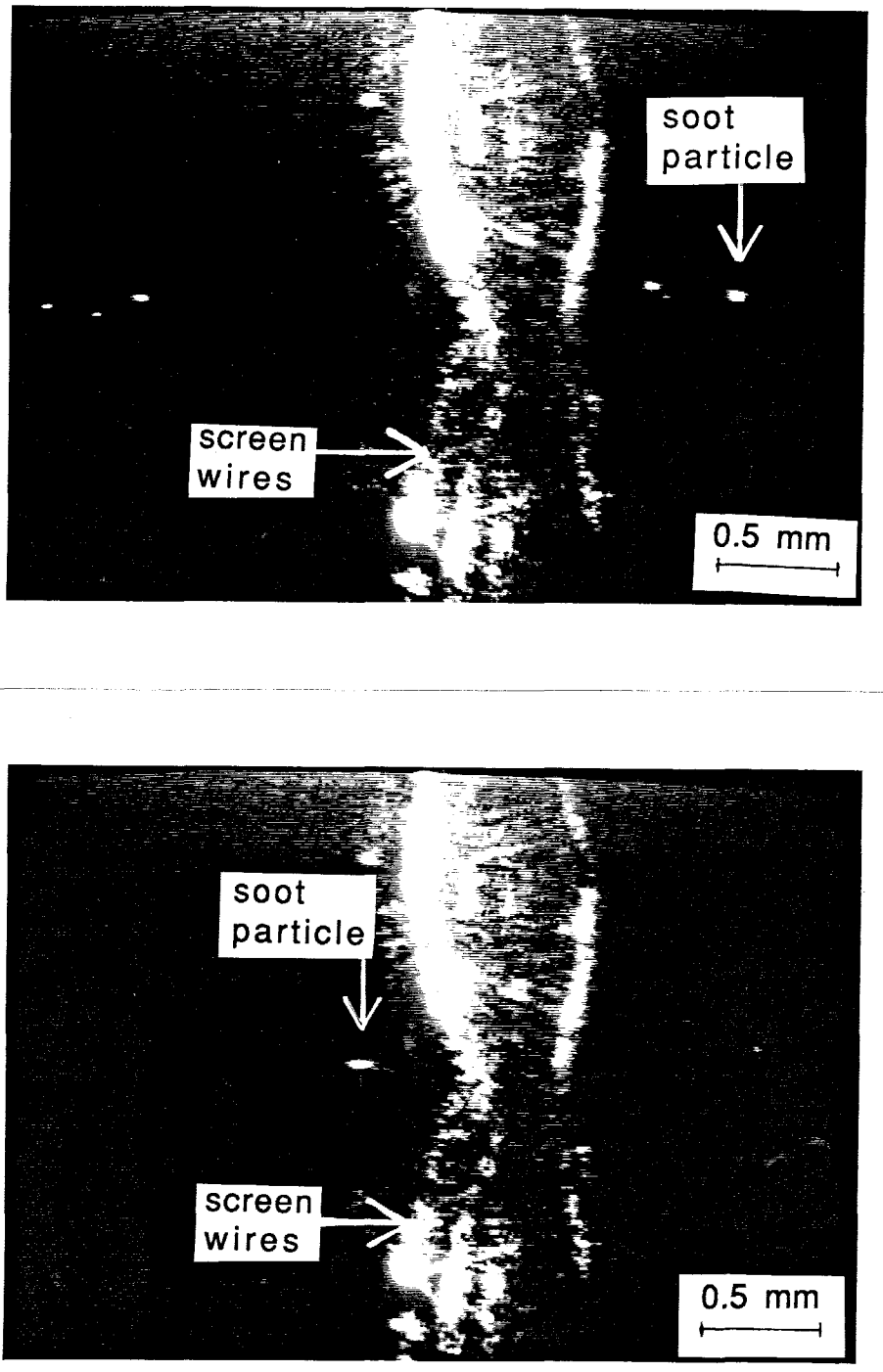

Figure 7.11: Photographs showing a particularly slow particle (chosen for photographic clarity) near the screen (end view) (top) 0 s (bottom) 1.00 s. The particle was charged and moving toward the screen and collection rod to the left (not shown) with an average speed of 1.5 mm/s.

screens which greatly enhance the collection speed. Three internal screens appropriately placed in a spherical inward precipitator decrease the collection time by a factor of 185. The collection time is inversely proportional to the particle size and dielectric constant. For example, a 10 μm diameter mineral particle (k $\sim$ 2) requires 0.78 hours and a conducting particle (k $\sim$ 10) requires only 0.47 hours, while a 1 μm diameter particle requires 7.8 hours and 4.7 hours, respectively.

The screens also decrease the collection time in a cylindrical precipitator and results are presented for this geometry as well. A cylindrical precipitator with three screens and with the same overall radius as a spherical precipitator with three screens can collect a particle in 67% of the time.

Because of the nature of the potential field around the wires in the screens, some particle loss will occur due to impingement. This effect is demonstrated with the use of a finite element solution of Laplace's equation which governs the potential field around an infinite array of wires between two parallel plates in the absence of space charge. The loss was 40% in this example.

A cylindrical inward precipitator was constructed for demonstration purposes. A long range microscope, CCD camera and video casette recorder showed $\sim$1 μm diameter particles moving through the screen and impinging on the central planchet at speeds of a approximately 30 mm/s, roughly equivalent to the value of 43 mm/s predicted by the theory.

Acknowledgements

This research was supported under NASA Grants NAG-1953 and NAGW-1941 and National Science Foundation Grant #CBT8813006. Contribution #5077, Division of

Geological and Planetary Science.

Appendix A: Pressure Difference Across a Conducting Liquid/Air Interface with an Applied Electric Field

Consider an interface with sum of reciprocal radii of curvature $1/r_{\text{curv}}$ formed by a conducting liquid with surface tension T, dielectric constant κ, and density ρ surrounded by air ($\epsilon \approx \epsilon_0$) and exposed to normal and tangential electric field components E_n and E_t, respectively. The pressure difference across the interface (neglecting electrostriction) is [11]

$$p_- - p_+ = \frac{T}{r_{\text{curv}}} - \frac{\epsilon_0}{2}(E_{n+}^2 + (\kappa - 1)E_{t+}^2),$$

where "-" indicates conditions inside the liquid and "+" indicates conditions outside the liquid. Usually in the electrospray atomization of conducting liquids, we have $E_{t+} << E_{n+}$. If we have $E_{t+} << E_{n+}/(\kappa - 1)^{1/2}$ then

$$p_- - p_+ \approx \frac{T}{r_{\text{curv}}} - \frac{\epsilon_0}{2}E_{n+}^2,$$

which was used by Taylor in his original analysis [1].

Appendix B: Program Listing–EHDA1.F

```
c     EHDA1.F
c
c     Written by Aaron J. Rulison, 3/8/91.
c
c     EHDA1.F solves for the volumetric flow rate,
c     total electrical
c     current, and droplet size using
c     the boundary layer model.
c
c     declare variables...
c
      double precision phistar,r,sig,itotal,
     *cap,e0,rcap,phic,phic0,spacing,
     *phislop,phideltar,odeltar,
     *deltar,interp,rold,oldphistar
     *,e,f,pi,tau,isur,z,zdrop,vel,phitest,a
     *,vdot,momdot,vel0,ephi,b,a2,ishould,istep,differ,
     *olddiffer,phif,pcheck,ephifac,rdrop,conc,a3,ni
c
      integer k,count
c
      character*8 outfile
c
      logical start,going
c
      real mu
      common t,rho,mu,rjet,efield,alpha
c
c     open set-up file...
c
      open(1,file="con1.inp")
c
c     read output file name and open it...
c
```

```
      read(1,15) outfile
 15   format(A8)
      open(2,file=outfile)
c
c     read run-specific variables...
c
c     absolute viscosity...
      read(1,20) mu
c     specific electrical conductivity...
      read(1,20) sig
c     density...
      read(1,20) rho
c     surface tension...
      read(1,20) t
c     capillary electrode radius...
      read(1,20) cap
c     electrode to counter-electrode spacing...
      read(1,20) spacing
c     ionic friction factor...
      read(1,20) f
c     initial guess for total electrical current...
      read(1,20) itotal
c     electric field penetration factor...
      read(1,20) a
c     cone half-angle
      read(1,20) phic
c     over-potential ratio...
      read(1,20) ephifac
c     flag for writing outputs to the terminal...
      read(1,20) pcheck
c     geometric charging factor...
      read(1,20) a3
c     jet electric field factor...
      read(1,20) a2
c     number of elementary charges per ion...
      read(1,20) ni
```

```
 20    format(e10.4)
 c
 c     define constants...
 c
       conc=30.0
       pi=3.141592654
       e0=8.85e-12
       e=1.6e-19*ni
       b=1.
       istep=0.1d-6
       start=.true.
       phic0=49.3*pi/180.
       going=.false.
 c
 c     begin a loop to solve the problem
 c     for a range of parameters...
 c
       do 1000 count=1,51
 c
 c     find initial boundary layer angle...
 c
 999   phistar=phic*0.9999
 c
 c     find value of r at the capillary edge...
 c
       rcap=cap/dsin(phic)
 c
 c     find final boundary layer angle...
 c
       phitest=acos((1.+dcos(phic))/2.)
 c
 c     initialize r...
 c
       r=rcap
 c
 c     find normal electric necessary to
```

```
c     establish the Taylor cone...
c
      ephi=(2.*t*dcos(phic0)/(e0*rcap*dsin(phic0)))**.5
c
c     find actual normal electric field...
c
      ephi=ephi*ephifac
c
c     call coef, the subroutine which
c     integrates the boundary layer
c     equations...
c
25    call coef(r,sig,phistar,phislop,
     *          e0,a,e,f,itotal,ephi,phic)
c
c     increment the boundary layer angle...
c
      phideltar=dabs(phic/1000./phislop)
      odeltar=r/1000.
      deltar=dmin1(odeltar,phideltar)
      phistar=phistar-deltar*phislop
      if(phistar.ge.phic) then
         phistar=0.9999*phic
      end if
      r=r-deltar
c
c     increment step counter...
c
      k=k+1
c
c     if more than 200,000 steps were taken, then quit and
c     update input parameters...
c
      if(k.gt.200000) then
         write(2,3456)
3456     format(' no solution')
```

```
         goto 1001
      end if
c
c     if the boundary layer has grown
c     to its final thickness, then
c     find the final value of r and move on...
c
      if(phistar.le.phitest) then
         interp=(phitest-oldphistar)/(phistar-oldphistar)
         r=rold+(r-rold)*interp
         goto 555
c
c     else continue integrating...
c
      else
         oldphistar=phistar
         rold=r
         goto 25
      end if
c
c     find volumetric flow rate and
c     momentum fluxes resulting from
c     the boundary layer flow...
c
c     find surface current...
c
555   isur=itotal/(1.+sig*r*(1.-
     *      dcos(phic))*a/(e0**2.*ephi**2.*
     *      dsin(phic)*(e/(e0*ephi*f)
     *      +r*(phic-phistar)/(2.*mu)
     *      )))
c
c     find shear stress on the surface...
c
      tau=isur/(2.*pi*e0*ephi*r*
     *   dsin(phic)*(e/(e0*ephi*f)
```

```
     *  +r*(phic-phistar)/(2.*mu)))
c
c     find volumetric flow rate...
c
      phif=phistar
      vdot=pi*r**3.*tau*(-2.*dcos(phic)
     *     +phic**2.*dcos(phic) -
     *     2.*phic*phif*dcos(phic)+phif**2.
     *     *dcos(phic)+2.*dcos(phif)-
     *     2.*phic*dsin(phic)+2.*phif
     *     *dsin(phic))/(mu*(phic-phif))
c
c     find momentum flux...
c
      momdot=-pi*r**4.*tau**2.*(24.*dcos(phic)
     *   -12.*phic**2.*dcos(phic)+
     *  phic**4.*dcos(phic)+
     *  24.*phic*phif*dcos(phic)-
     *  4.*phic**3.*phif*dcos(phic)-
     *  12.*phif**2.*dcos(phic)+6.*
     *  phic**2.*phif**2.*dcos(phic)-
     *  4.*phic*phif**3.*dcos(phic)+phif
     *  **4.*dcos(phic)-24.*dcos(phif)+
     *  24.*phic*dsin(phic)-4.*phic**3.
     *  *dsin(phic)-24.*phif*dsin(phic)+
     *  12.*phic**2.*phif*dsin(phic)-
     *  12.*phic*phif**2.*dsin(phic)+
     *   4.*phif**3.*dsin(phic))/(2.*mu**2.*(phic-phif)**2.)
c
c     find initial jet speed...
c
      vel0=momdot/vdot
c
c     sign convention change...
c
      itotal=-itotal
```

```
c
c     call the ehda2 subroutine which solves the jet
c     acceleration and returns total electrical current...
c
      call ehda2(vel0,sig,e0,e,f,itotal,
     *           b,a3,vdot,ephi,outfile,phic,ishould,vel
     *          ,rdrop,z,zdrop,spacing,cap,ephifac,a2)
c
c     if the total electical current has been found then
c     write the results to the output file...
c
      if(istep.lt.0.0001e-7) then
         write(2,998) sig,vdot*6.e10,itotal*
     *       1.e6,rdrop*1.e9,zdrop
     *       ,r/rcap
998      format(6(1x,e10.4))
c
c        go to update the input parameters...
         goto 1001
c
c     else if the total electrical current has not been found
c     yet then continue searching...
c
      else
         differ=(itotal-ishould)/dabs(itotal-ishould)
         if(start.eq..true.) then
            olddiffer=differ
            start=.false.
         end if
         if(differ.eq.-olddiffer) then
            going=.true.
         end if
         if(going.eq..true.) then
            istep=istep/2.
         end if
c
```

```
c        if the terminal print flag has been set then write
c        results to the terminal...
c
         if(pcheck.ne.0.) then
            write(6,682) vdot*1.e9*60.
682         format(e10.4)
            write(6,777) itotal,ishould,k,rdrop*1.e6,zdrop
777         format(2(1x,e14.8),i6,1x,e10.4,1x,e10.4)
         end if
c
c
         itotal=-itotal
         itotal=itotal+istep*differ
         if(itotal.ge.0.) then
            itotal=itotal-istep*differ
            itotal=itotal/2.
         end if
         k=0
         goto 999
      end if
c
c     update input parameters...
c
1001  sig=sig+0.3/51.
c
c     reset variables for new solution search...
c
      itotal=-itotal
      istep=0.1d-6
      k=0
      olddiffer=0.
      start=.true.
      going=.false.
c
c     continue looping until the desired range of input
c     parameters is covered...
```

```
c
1000  continue
c
c     stop and end program...
c
      stop
      end
c
c
c     subroutine coef finds the terms in the boundary layer
c     growth equation...
c
      Subroutine coef(r,sig,phistar,phislop,e0,
     *                  a,e,f,itotal,ephi,phic)
c
      double precision r,sig,phistar,phislop,
     *e0,e,f,phic,pi,tau,itotal,
     *a,ephi,isur,capa,capb,capc,
     *capd,b1,b2,b3,b4,b5,b6,b7,b8,
     *b9,b10,b11,b12,b13,b14,b15,b16,
     *b17,b18,a1,a2,a3,a4,a5,a6,
     *a7,a8,a9,a10,a11,a12
c
      real mu
c
      common t,rho,mu,rjet,efield,alpha
c
      pi=3.141592654
c
      isur=itotal/(1.+sig*r*(1.-
     *      dcos(phic))*a/(e0**2.*ephi**2.*
     *      dsin(phic)*(e/(e0*ephi*f)+
     *      r*(phic-phistar)/(2.*mu)
     *      )))
      tau=isur/(2.*pi*e0*ephi*r
     *  *dsin(phic)*(e/(e0*ephi*f)
```

```
     *  +r*(phic-phistar)/(2.*mu)))
c
333   b1=e0*ephi*f*itotal*mu
      b2=pi*r**2.
      b3=2.*a*f*mu*r*sig
      b4=-2.*a*f*mu*r*sig*dcos(phic)
      b5=2.*e*e0*ephi*mu*dsin(phic)
      b6=e0**2.*ephi**2.*f*phic*r*dsin(phic)
      b7=-e0**2.*ephi**2.*f*r*dsin(phic)*phistar
      b8=e0*ephi*f*itotal*mu
      b9=2.*a*f*mu*sig
      b10=-2.*a*f*mu*sig*dcos(phic)
      b11=e0**2.*ephi**2.*f*phic*dsin(phic)
      b12=-e0**2.*ephi**2.*f*dsin(phic)*phistar
      b13=-e0**2.*ephi**2.*f*r*dsin(phic)
      b14=2.*a*f*mu*r*sig
      b15=-2.*a*f*mu*r*sig*dcos(phic)
      b16=2.*e*e0*ephi*mu*dsin(phic)
      b17=e0**2.*ephi**2.*f*phic*r*dsin(phic)
      b18=-e0**2.*ephi**2.*f*r*dsin(phic)*phistar
c
      a1=-10.*mu**2.*phic*t
      a2=10.*mu**2.*t*phistar
      a3=-10.*mu**2.*r*dtan(phic)*tau
      a4=2.*phic**3.*r**3.*rho*dtan(phic)*tau**2.
      a5=-6.*phic**2.*r**3.*rho*dtan(phic)*phistar*tau**2.
      a6=6.*phic*r**3.*rho*dtan(phic)*phistar**2.*tau**2.
      a7=-2.*r**3.*rho*dtan(phic)*phistar**3.*tau**2.
      a8=phic**3.*r**4.*rho*dtan(phic)*tau
      a9=-3.*phic**2.*r**4.*rho*dtan(phic)*phistar*tau
      a10=3.*phic*r**4.*rho*dtan(phic)*phistar**2.*tau
      a11=-r**4.*rho*dtan(phic)*phistar**3.*tau
      a12=3.*r**4.*rho*dtan(phic)*(phic-phistar)**2.*tau**2.
      capa=-((b1)/(b2*(b3+b4+b5+b6+b7)))
     *      -(b8*(b9+b10+b11+b12))/
     *     (pi*r*(b14+b15+b16+b17+b18)**2.)
```

```
capb=-b8*b13/(pi*r*(b14+b15+b16+b17+b18)**2.)
capc=2.*(a1+a2+a3+a4+a5+a6+a7)/a12
capd=2.*(a8+a9+a10+a11)/a12
phislop=(capc+capa*capd)/(1.-capb*capd)
end
```

Appendix C: Program Listing–EHDA2.F

```
c     EHDA2.F
c
c     Written by Aaron J. Rulison, 3/8/91.
c
c     EHDA2.F is a subroutine called by EHDA1.F.
c     It solves the
c     jet acceleration portion of the boundary layer model.
c
      Subroutine ehda2(vel0,sig,e0,e,f,itotal,
     *                 b,a3,vdot,ephi,
     *                    outfile,phic,ishould,vel,rdrop
     *                 ,z,zdrop,spacing,cap,ephifac,a2)
c
c     variable declarations...
c
      double precision sig,itotal,ephifac,
     *cap,e0,phic,vel0,a2,
     *vel,deltat,tauold,
     *e,f,pi,tau,isur
     *,vdot,ep,rdrop,vdrop,
     *fdrop,ishould,vslop,veldz,
     *dz,z,rjet0,zdrop
     *,ephi,rold,interp1,v0,
     *a3,k,ephidrop,spacing,imax
c
      real efield,mu
c
      character*8 outfile
c
      common t,rho,mu,rjet,efield,alpha
c
c     define constants...
c
      pi=3.141592654
```

```
      e0=8.85e-12
      e=1.6e-19
c
c     find initial jet radius and speed...
c
      rjet0=(vdot/(pi*vel0))**.5
      rjet=rjet0
      vel=vdot/(pi*rjet**2.)
c
c     find normal electric field at the jet surface...
c
408   ephidrop=ephi*cap*dlog(4.*spacing
     *    /cap)/(rjet*dlog(4.*spacing
     *    /rjet))*a2
      ep=ephidrop
c
c     find surface current...
c
      isur=(itotal+f*pi*rjet**2.*sig*b*vel/e)/
     *       (1.+rjet*sig*b*f/(2.*e*e0*ep))
c
c     find ion speed...
c
      uc=isur/(2.*pi*rjet*e0*ep)
c
c     find surface stress...
c
      tau=e0*ep*f*(uc-vel)/e
c
c     if the surface stress is
c     less than zero then the jet
c     has reached terminal speed...
c
      if(tau.lt.0.) then
c
c       go to the current calculation...
```

```
c
         goto 4444
       end if
c
c      find change in jet speed...
c
       vslop=2.*pi*rjet*tau/vdot
c
c      find z increment...
c
       if(vslop.eq.0.) then
          veldz=rjet
       else
          veldz=dabs(vel/1000./vslop)
       end if
c
c      update jet speed and z...
c
       dz=veldz
       vel=vel+vslop*dz
       z=z+dz
c
c      increment time...
c
       deltat=dz/vel
       time=time+deltat
c
c      update jet radius...
c
       rjet=(vdot/(pi*vel))**.5
c
c      if the surface shear stress is
c      less than zero then the
c      jet is at terminal speed...
c
4444   if(tau.lt.0.) then
```

```
          interp1=(0.-tauold)/(tau-tauold)
          rjet=rold+(rjet-rold)*interp1
          goto 401
c
c     else is has not, so continue integrating...
c
      else
          rold=rjet
          tauold=tau
          goto 408
      end if
c
c     calculate final properties...
c
c     normal component of the
c     electric field at the jet surface
c
401   efield=ep
c
c     droplet radius...
c
      rdrop=2.*rjet
c
c     droplet volume...
c
      vdrop=4.*pi*rdrop**3./3.
c
c     droplet formation frequency...
c
      fdrop=vdot/vdrop
c
c     normal component of the electric
c     field at the droplet surface
c     including the RC curcuit time scale factor...
c
      ephidrop=ephi*a2*cap*dlog(4.*spacing/cap)
```

```
     */(rjet*dlog(4.*spacing
     *    /rjet))*(1.-dexp(-1.*a3/(fdrop*e0/sig)))
c
c     total electrical current...
c
      ishould=fdrop*9.*2.**.5*pi*e0*rdrop**2.*ephidrop
c
c     maximum possible current according to the
c     Rayleigh charge limit...
c
      imax=fdrop*(64.*pi**2.*e0*t*(rdrop)**3.)**.5
c
c     Rayleigh charge limit fraction...
c
      zdrop=ishould/imax
c
c     end program
c
      end
```

Appendix D: Program Listing–DISRUPT.F

```
c     DISRUPT.F models the disruption of a
c     droplet charged to the Rayleigh
c     limit.  Uses a Monte Carlo
c     method and the disruption model
c     by Roth and Kelly
c     (Roth, D. G. and A. J. Kelly 1983,
c     Trans. on Ind. Appl. IA-19(5), 771-775.)
c
c     Written by Aaron Rulison 9/25/91...
c
c     declare variables...
c
      double precision dp0,c0,rhosolute,
     *   rhosolvent,cmax,charge0,
     *   rhosol,pi,e0,dp,c,charge,r,
     *   mass,msolute,msolvent,mc1,mc2,
     *   deltam1,deltam2,nsibs,t,
     *   dist(1:10000),ran,n,zfrac,dpmax,
     *   rd,dellog
c
      integer i,j,iseed,numreal
c
      character*8 outfile
c
      logical outrange
c
c     open set-up file...
c
      open(1,file="disrupt.inp")
c
c     read and open output file name...
c
      read(1,10) outfile
10    format(A8)
```

```
      open(2,file=outfile)
c
c     read run-specific variables...
c
c     read initial diameter...
c
      read(1,15) dp0
c
c     read intitial concentration...
c
      read(1,15) c0
c
c     read solute density...
c
      read(1,15) rhosolute
c
c     read solvent density...
c
      read(1,15) rhosolvent
c
c     read saturation solution concentration...
c
      read(1,15) cmax
c
c     read surface tension...
c
      read(1,15) t
c
c     read number of realizations in
c     the Monte Carlo simulation...
c
      read(1,16) numreal
c
c     read righthand side of rightmost diameter bin in the
c     histogram...
c
```

```
      read(1,15) dpmax
c
c     read initial fraction of the Rayleigh charge limit--
c     it must be less than 1...
c
      read(1,15) zfrac
15    format(d10.4)
16    format(i6)
c
      if(zfrac.ge.1.) then
         write(6,888)
888      format('zfrac is greater than one.')
         stop
      end if
c
c     set the solution density equal
c     to the solvent density...
c
      rhosol=rhosolvent
c
c     define constants...
c
      pi=3.141592654
c
c     iseed and useed are used in the random
c     number generator...
c
      iseed=985
      useed=ustart(iseed)
      e0=8.85d-12
      outrange=.false.
      rd=dp0/2.
c
c     find initial charge...
c
      charge0=zfrac*(64.*pi**2.*e0*t*(dp0/2.)**3.)**.5
```

```
c
c     begin Monte Carlo...
c
      do 100 i=1,numreal
c        write(6,31)
31       format(' ')
         dp=dp0
         c=c0
         charge=charge0
         r=dp/2.
c
c        find droplet mass...
c
         mass=4.*pi*r**3.*rhosol/3.
c
c        find solute and solvent masses...
c
         msolute=mass*c
         msolvent=mass-msolute
c
c        find mass of droplet that would
c        result in a droplet charged
c        to the Rayleigh limit...
c
30       mc1=charge**2./(48.*pi*e0*t/rhosol)
c
c        find mass of droplet that would
c        result in a droplet saturated
c        with solute...
c
         mc2=msolute/cmax
c
c        update total mass...
c
         mass=msolute+msolvent
c
```

```
c        find increments in mass which
c        would result in mc1 and
c        mc2 above...
c
         deltam1=mass-mc1
         deltam2=mass-mc2
c
c        if deltam1 is greater than deltam2 then
c        the solute precipitates before the Rayleigh
c        charge limit is reached...
c
         if(deltam1.gt.deltam2) then
c
c           update solvent mass...
c
            msolvent=msolvent-deltam2
c
c           only one droplet results from the precipitation...
c
            nsibs=1.
c
c           tell the user that a droplet has precipitated...
c
c           write(6,11123)
11123       format(' precipitating')
c
c           call bin to count this droplet
c           for the size distribution...
c
            call bin(msolute,rhosolute,
c           nsibs,dist,outrange,dpmax)
c
c           goto the loop continuation line...
c
            goto 100
c        else if the droplet reaches the
```

```
c        Rayleigh charge limit
c        before the solute precipitates then...
c
         else
c
c           update the solvent mass...
c
            msolvent=msolvent-deltam1
c
c           find the number of sibling droplets resulting
c           from the explosion...
c
            ran=uni()
            l=dint(6.*ran+2.)
            n=l
c
c           tell the user that a droplet disrupted...
c
c           write(6,1122)
1122        format(' disrupting')
c
c           update number of siblings formed...
c
            rrrr=rrrr+n
c
c           call the disruption subroutine...
c
            call disrup(charge,t,msolute,msolvent,dist,
     *        rhosol,n,rhosolute,dpmax)
c
c        end if
c
         end if
c
c        the mother droplet continues
c        to evaporate after disrupting...
```

```
c
         goto 30
c
c     continue Monte Carlos simulations...
c
100   continue
c
c     if some droplets were outside the specified histogram
c     boundaries, then alert the user...
c
      if(outrange.eq..true.) then
         write(6,203)
203      format(' some values out of range')
      end if
c
c     normalize and write size distribution to the screen
c     and to the output file...
c
      do 202 j=1,10000
         dp=dpmax*j/1.d4
         totnum=totnum+dist(j)/1.e4
         if(dist(j).ne.0.) then
            write(2,212) dp-dpmax/2.e4,0.
            dellog=dlog10(dp)-dlog10(dp-(dpmax/1.e4))
            write(2,212) dp,dist(j)/(numreal*dellog)
212         format(1x,e15.9,1x,e10.4)
            write(6,211) dp,dist(j)/(numreal*dellog)
            write(2,212) dp+dpmax/2.e4,0.
211         format(2(1x,e10.4))
         end if
202   continue
c
c     write the total number of droplets
c     and siblings formed after
c     all solvent has evaporated...
c
```

```
      write(6,3030) totnum,rrrr/1.e4
3030  format(e10.4,1x,e10.4)
c
c     stop and end program...
c
      stop
      end
c
c     subroutine bin puts an evaporated droplet into the
c     size distribution histogram...
c
      Subroutine bin(msolute,rhosolute,
c     nsibs,dist,outrange,dpmax)
c
c     declare variables...
c
      double precision msolute,rhosolute,
c     diameter,nsibs,pi,dpmax
     * ,dist(1:10000)
c
      logical outrange
c
      integer j
c
c     define constants...
c
      pi=3.141592654
c
c     find diameter of dried particle...
c
      diameter=((msolute/nsibs)*6./(pi*rhosolute))**(1./3.)
c
c     find bin for dried particle and increments counts...
c
      j=dint(diameter*1.d4/dpmax)
      if(j.ge.1.and.j.le.10000) then
```

```
         dist(j)=dist(j)+nsibs
       else
         outrange=.true.
       end if
c
c      end program...
c
       end
c
c      subroutine disrup finds the sibling mass and charge
c      and mother size and charge
c      given the number of siblings,
c      and the initial droplet size and charge...
c
       Subroutine disrup(charge,t,msolute,msolvent,dist,
     *    rhosol,n,rhosolute,dpmax)
c
c      declare variables...
c
       double precision t,n,r0,dp,q0,charge,r1,
     * q1,q2,r2,arg,x1,x2,di,fn,ke,
     * check,differ,msolvent,
     * msolute,mass,nsibs,pi,e0,rhosol,
     * rhosolute,dist(1:10000),dpmax
c
       logical start
c
c      define constants...
c
       pi=3.141592654
       e0=8.85e-12
       dp=(6.*(msolute+msolvent)/(pi*rhosol))**(1./3.)
       r0=dp/2.
       q0=charge
       start=.true.
c
```

```
c     guess and solve for the mother radius...
c
      r1=r0*.5
2     q1=q0/(1.+n**(1./3.)*(r0**2./r1**2)
     **(1.-r1**3./r0**3.)**(1./3.))
      q2=q0*(1.-q1/q0)/n
      r2=r0*((1.-r1**3./r0**3.)/n)**(1./3.)
      arg=(1.+(1.+4.*r1/r2)**.5)/2.
      x1=r2*log(arg+(arg**2.-1.)**.5)
      x2=r2*1.061275062
      di=r2*dsinh(x1/r2)*(dcosh(x1/r2)-1)+x1
     *   +r2*dsinh(x2/r2)*(dcosh(x2/r2)-1.)+x2
      fn=-0.28290+0.35415*n-0.04385*n*n
      ke=n*n*q2*q2*fn/(8.*pi*e0*di)+n*q1*q2/(4.*pi*e0*di)
      check=2.*r0*(q1/q0)**2./r1+(r1/r0)**2.
     *      +2.*n*r0*(q2/q0)**2./r2+
     *      n*(r2/r0)**2.+ke/(4.*pi*t*r0*r0)-3.
      differ=check
c
c     if solution has been found then...
c
      if(dabs(differ/1.d8).lt.1d-08) then
         msolvent=msolvent*(r1/r0)**3.
         msolute=msolute*(r1/r0)**3.
         mass=msolvent+msolute
         charge=charge*q1/q0
         nsibs=n
c
c        call the bin subroutine update size distribution...
c
         call bin(msolute,rhosolute,
     *             nsibs,dist,outrange,dpmax)
c
c     else if the solution has not been found then
c     continue iterating...
c
```

```
      else
         r1=r1-differ/1.d8
         goto 2
      end if
c
c     end program
c
      end
c
c     the following function is
c     the random number generator...
c
      REAL FUNCTION UNI()
C***BEGIN PROLOGUE  UNI
C***DATE WRITTEN   810915 (YYMMDD)
C***REVISION DATE  871210 (YYMMDD)
C***CATEGORY NO.  L6A21
C***KEYWORDS  RANDOM NUMBERS, UNIFORM RANDOM NUMBERS
C***AUTHOR    KAHANER, DAVID, SCIENTIFIC COMPUTING
C             DIVISION, NBS
C             MARSAGLIA, GEORGE,
C             SUPERCOMPUTER RES. INST., FLORIDA ST. U.
C
C***PURPOSE  THIS ROUTINE GENERATES REAL
C             (SINGLE PRECISION) UNIFORM
C             RANDOM NUMBERS ON [0,1)
C***DESCRIPTION
C        Computes real (single precision) uniform
C           numbers on [0,1).
C           From the book, "Numerical Methods and Software" by
C                D. Kahaner, C. Moler, S. Nash
C                Prentice Hall, 1988
C
C       USAGE:
C              To initialize the generator
C                   USEED = USTART(ISEED)
```

```
C               where: ISEED is any NONZERO integer
C                  will return floating point value of ISEED.
C
C               Subsequently
C                       U = UNI()
C                  will return a real uniform on [0,1)
C
C                One initialization is necessary, but
C                  any number of evaluations
C                  of  UNI in any order, are allowed.
C
C            Note: Depending upon the value
C                        of K (see below), the output
C                        of UNI may differ from one
C                         machine to another.
C
C            Typical usage:
C
C                REAL U,UNI,USTART,USEED
C                INTEGER ISEED
CC                  Set seed
C                ISEED = 305
C                USEED = USTART(ISEED)
C                DO 1 I = 1,1000
C                    U = UNI()
C              1 CONTINUE
CC                  NOTE: If K=24 (the default,
CC                            see below) the output value of
CC                            U will be 0.1570390462475...
C                WRITE(*,*) U
C                END
C
C           NOTE ON PORTABILITY: Users can choose
C                to run UNI in its default
C                mode (requiring NO user action)
C                which will generate the same
```

```
C               sequence of numbers on any computer
C               supporting floating point
C               numbers with at least 24 bit mantissas,
C               or in a mode that
C               will generate numbers with a longer
C               period on computers with
C               larger mantissas.
C          TO EXERCISE THIS OPTION:  B E F O R E
C               invoking USTART insert
C               the instruction        UBITS = UNIB(K)
C                                                 K >= 24
C               where K is the number of bits in
C               the mantissa of your floating
C               point word (K=48 for Cray, Cyber 205).
C               UNIB returns the
C               floating point value of
C               K that it actually used.
C                    K input as .LE. 24, then UBITS=24.
C                    K input as .GT. 24, then UBITS=FLOAT(K)
C               If K>24 the sequence of numbers
C               generated by UNI may differ
C               from one computer to another.
C
C
C
C***REFERENCES  MARSAGLIA G., "COMMENTS ON THE
C                 PERFECT UNIFORM RANDOM
C                 NUMBER GENERATOR",
C                 UNPUBLISHED NOTES, WASH S. U.
C***ROUTINES CALLED  (NONE)
C***END PROLOGUE UNI
      PARAMETER(
     *    CSAVE=362436./16777216.  ,
     *    CD=7654321./16777216.,
     *    CM=16777213./16777216.  )
C                           2**24=16777216
```

```
      REAL U(17),S,T,USTART,C,UNIB
      INTEGER I,J,II,JJ,K,KK,I1,J1,K1,L1,M1,ISEED
C
      SAVE U,I,J,K,C
C      Load data array in case user forgets to initialize.
C      This array is the result of calling UNI 100000 times
C         with ISEED=305 and K=64.
      DATA U/
     *0.8668672834288,  0.3697986366357,  0.8008968294805,
     *0.4173889774680,  0.8254561579836,  0.9640965269077,
     *0.4508667414265,  0.6451309529668,  0.1645456024730,
     *0.2787901807898,  0.06761531340295, 0.9663226330820,
     *0.01963343943798, 0.02947398211399, 0.1636231515294,
     *0.3976343250467,  0.2631008574685/
      DATA I,J,K,C/17,5,24,CSAVE/
C
C   Basic generator is Fibonacci
C
      UNI = U(I)-U(J)
      IF(UNI.LT.0.0)UNI = UNI+1.0
      U(I) = UNI
      I = I-1
      IF(I.EQ.0)I = 17
      J = J-1
      IF(J.EQ.0)J = 17
C
C   Second generator is congruential
C
      C = C-CD
      IF(C.LT.0.0) C=C+CM
C
C   Combination generator
C
      UNI = UNI-C
      IF(UNI.LT.0.0)UNI = UNI+1.0
      RETURN
```

```
C
      ENTRY USTART(ISEED)
C
C          Set up ...
C          Convert ISEED to four smallish positive integers.
C
        I1 = MOD(ABS(ISEED),177)+1
        J1 = MOD(ABS(ISEED),167)+1
        K1 = MOD(ABS(ISEED),157)+1
        L1 = MOD(ABS(ISEED),147)+1
C
C               Generate random bit pattern
C               in array based on given seed.
C
        DO 2 II = 1,17
          S = 0.0
          T = 0.5
C             Do for each of the bits of mantissa of word
C             Loop  over K bits, where K
C              is defaulted to 24 but can
C               be changed by user call to UNIB(K)
          DO 3 JJ = 1,K
                M1 = MOD(MOD(I1*J1,179)*K1,179)
                I1 = J1
                J1 = K1
                K1 = M1
                L1 = MOD(53*L1+1,169)
                IF(MOD(L1*M1,64).GE.32)S=S+T
    3           T = .5*T
    2   U(II) = S
        USTART = FLOAT(ISEED)
        RETURN
C
      ENTRY UNIB(KK)
        IF(KK.LE.24)THEN
             K=24
```

```
        ELSE
             K=KK
        ENDIF
        UNIB=FLOAT(K)
c
c     end function...
c
      END
```

Appendix E: Program Listing–BIN1.F

```
c     BIN1.F
c
c     Written by Aaron J. Rulison 8/17/91.
c
c     BIN1.F takes SEMS data and
c     combines several up and down scans
c     into size distributions based
c     on diameter, area, and
c     volume.  The number of bins and
c     lower and upper diameter bounds
c     are user-specified in the input file "bin1.inp."
c
c     Last modification 2/22/92.
c
c     declare variables...
c
      double precision lowdp,midd1,highd1,counter,dellog1
     *   ,dp(0:1000),dellog2,
     *   time,dpr,raw,inve,frac,olddp,frac2,
     *   count(0:1000),area(0:1000),
     *   volume(0:1000),pi,scount,acount,
     *   vcount,dndlogdp,dadlogdp,
     *   dvdlogdp,rnumbins,dpr,dlogdp,
     *   eu,place,diam,pi
c
      integer index,i,numbins,numpts
c
      character*10 infile,outfile,dummy
c
      logical start
c
c     define constants...
c
      pi=3.141592654
```

```
      eu=2.7182818
      start=.true.
c
c     open set-up file...
c
      open(1,file="bin1.inp")
      read(1,10) infile
10    format(a10)
c
c     open input file...The input file
c     is the output file from programs
c     such as "scanone3" which run the
c     SEMS instrument.  No modification
c     is necessary.
c
      open(2,file=infile)
c
c     read and open the output file...
c
      read(1,10) outfile
      open(3,file=outfile)
c
c     read numpts, the total number of
c     lines in the input file...
c
      read(1,25) numpts
20    format(d10.4)
c
c     read midd1, the right hand boundary
c     of the rightmost bin...
c
      read(1,20) midd1
c
c     read highd1, the left hand
c     boundary of the rightmost bin...
c
```

```
      read(1,20) highd1
c
c     read numbins, the of bins in the histogram...
c
      read(1,25) numbins
      rnumbins=real(numbins)
25    format(i6)
c
c     set left hand boundary of the leftmost bin...
c
      lowdp=13.
c
c     fill the "dp" array with bin boundaries...
c
      dp(numbins)=midd1
      dp(numbins-1)=highd1
      dellog2=dlog10(dp(numbins))-dlog10(dp(numbins-1))
      dellog1=(dlog10(highd1)-dlog10(lowdp))/(rnumbins-1)
      do 40 i=0,numbins-1
         counter=counter+1.
         dp(i)=10.**((counter-1.)*dellog1+dlog10(lowdp))
40    continue
c
c     read un-used lines from input file...
c
      do 46 i=1,18
         read(2,10) dummy
46    continue
c
c     read in data from input file...
c
70    do 50 i=1,numpts
         read(2,60) time,dpr,raw,inve
60       format(3x,f8.2,1x,f9.2,1x,f9.2,f10.2)
         if(start.eq..true.) then
            start=.false.
```

```
            olddp=dpr
            goto 50
         end if
c
c        find width of bin...
c
         dlogdp=dabs(dlog10(dpr)-dlog10(olddp))
c
c        if the inputted diameter
c        is less than the old diameter
c        then set working diameter
c        to the old diameter...
c
         if(dpr.lt.olddp) then
            diam=olddp
c
c        else set the working diameter
c        to the inputted diameter...
c
         else
            diam=dpr
         end if
c
c        if working diameter falls
c        below the rightmost bin then...
c
         if(diam.ge.lowdp.and.diam.lt.highd1) then
c
c           find location of working diameter...
c
            frac=(dlog10(diam)-dlog10(lowdp))/
     *           (dlog10(highd1)-dlog10(lowdp))
            index=idint(frac*(rnumbins-1.))+1
c
c           if the width of the inputted
c           bin is greater than the
```

```
c           width of the specified bin,
c           then indicate an error...
c
            if(dlogdp.gt.dellog1) then
               write(6,59)
59          format('dellog1 error')
            end if
c
c           find location of working diameter...
c
            place=frac*(rnumbins-1.)+1.
c
c           find fraction of inputted bin that lies in
c           the set-up bin...
c
            frac2=(place-dint(place))*dellog1/dlogdp
c
c        else if the working diameter
c        falls in the rightmost bin then...
c
         else  if(diam.ge.highd1) then
c
c           find location of working diameter...
c
            frac=(dlog10(diam)-dlog10(dp(numbins-1)))/
     *          (dlog10(dp(numbins))-dlog10(dp(numbins-1)))
            index=numbins+idint(frac)
            place=frac+1.
c
c           find fraction of inputted bin that lies in
c           the set-up bin...
c
            frac2=(place-dint(place))*dellog2/dlogdp
c
c           if the width of the
c           inputted bin is greater than the
```

```
c           width of the specified bin,
c           then indicate an error...
c
            if(dlogdp.ge.dellog2.or.dlogdp.ge.dellog1) then
               write(6,52)
52             format('dellog2 error')
            end if
c
c         else if the working diameter falls below
c         the leftmost bin then go back to beginning to read a
c         new input line after updating olddp...
c
          else  if(diam.lt.dplow) then
             olddp=dpr
             goto 50
          end if
c
c         if the inputted bin lies
c         entirely in the set-up bin then
c         set fraction to 1...
c
          if(frac2.gt.1.) then
             frac2=1.
          end if
c
c         if the diameter falls
c         below the leftmost bin then
c         go back and read a new input line...
c
          if(index.lt.2) then
              goto 50
          end if
c
c         increment count of particles in the set-up bin--
c         Part of the inputted bin lies in one set-up bin
c         and the rest lies in the adjacent bin...
```

```
c
          count(index)=count(index)+inve*dlogdp*frac2
          count(index-1)=count(index-1)+inve*dlogdp*(1.-frac2)
c
c         update old diameter...
c
          olddp=dpr
c
c     continue...
c
50    continue
c
c     find area and volume from number...
c
      do 80 i=1,numbins
         area(i)=count(i)*((dp(i)+dp(i-1))/2.)**2.*pi
         volume(i)=count(i)*((dp(i)+dp(i-1))/2.)**3.*pi/6.
80    continue
c
c     find total number, area, and volume...
c
      do 90 i=1,numbins
         scount=scount+count(i)
         acount=acount+area(i)
         vcount=vcount+volume(i)
90    continue
c
c     write total number, area, volume,
c     and volume-mean diameter
c     to the screen...
c
      write(6,2002) scount,acount,vcount
2002  format(3(1x,e10.4))
      write(6,2002) vcount/scount,((6./pi)*vcount/scount)
     *      **(1./3.)
c
```

```
c     find and write (1/N)dn/dlog(dp), (1/A)da/dlog(dp),
c     and (1/V)dv/dlog(dp)...all logarithms are base 10...
c
      do 100 i=1,numbins-1
         dndlogdp=count(i)/dellog1
         dadlogdp=area(i)/dellog1
         dvdlogdp=volume(i)/dellog1
         write(3,110) dp(i-1),dndlogdp/scount,dadlogdp/acount,
     *          dvdlogdp/vcount
         write(3,110) dp(i),dndlogdp/scount,dadlogdp/acount,
     *          dvdlogdp/vcount
100   continue
      i=numbins
      dndlogdp=count(i)/dellog2
      dadlogdp=area(i)/dellog2
      dvdlogdp=volume(i)/dellog2
      write(3,110) dp(i-1),dndlogdp/scount,dadlogdp/acount,
     *       dvdlogdp/vcount
      write(3,110) dp(i),dndlogdp/scount,dadlogdp/acount,
     *       dvdlogdp/vcount
110   format(1x,d10.4,6(1x,d10.4))
118   format(i6,1x,i6)
c
c     end of program...
c
      end
```

Appendix F: Program Listing–BIN2.F

```
c     BIN2.F
c
c     BIN2.F takes hand-measured diameter data and combines
c     into size distributions, based on diameter, area, and
c     volume.
c
c     Written by Aaron J. Rulison 12/31/91.
c
c     declare variable...
c
      double precision lowd2,highdp,
     *   counter,dellog(0:100),dp(0:1000),
     *   dp,
     *   count(0:1000),area(0:1000),
     *   volume(0:1000),pi,scount,acount,
     *   vcount,dndlogdp,dadlogdp,dvdlogdp,rnumbins,dpr,
     *   eu,midd2
c
      integer index,i,numbins,numpts
c
      character*10 infile,outfile
c
      logical start
c
c     define constants...
c
      pi=3.141592654
      eu=2.7182818
      start=.true.
c
c     open set-up file...
c
      open(1,file="bin3.inp")
c
```

```
c     read input file name and open it.  The input file is
c     a list of diameters...
c
      read(1,10) infile
10    format(a10)
      open(2,file=infile)
c
c     read output file name and open it.
      read(1,10) outfile
      open(3,file=outfile)
c
c     read number of line in the input file...
c
      read(1,25) numpts
20    format(d10.4)
c
c     read lefthand boundary of the leftmost bin...
c
      read(1,20) lowd2
c
c     read lefthand boundary of the rightmost bin...
c
      read(1,20) midd2
c
c     set number of bins...
c
      numbins=5
      rnumbins=real(numbins)
25    format(i6)
c
c     set righthand boundary of the rightmost bin...
c
      highdp=1200.
c
c     set up the bin boundaries...
c
```

```
      dp(0)=midd2
      dp(1)=lowd2
      dellog(1)=dlog10(dp(1))-dlog10(dp(0))
      do 40 i=1,numbins
         counter=counter+1.
         dellog(i+1)=(dlog10(highdp)
     *   -dlog10(lowd2))/(rnumbins-1.)
         dp(i)=10.**((counter-1.)*
     *   dellog(i)+dlog10(lowd2))
40    continue
c
c     read data...
c
      do 50 i=1,numpts
70       read(2,60) dpr
60       format(e10.4)
c
c        find the appropriate bin for dpr...
c
         if(dpr.ge.midd2.and.dpr.lt.lowd2) then
            index=1
            mrc=mrc+1
         else if(dpr.ge.lowd2.and.dpr.lt.dp(2)) then
            index=2
         else if(dpr.ge.dp(2).and.dpr.lt.dp(3)) then
            index=3
         else if(dpr.ge.dp(3).and.dpr.lt.dp(4)) then
            index=4
         else if(dpr.ge.dp(4).and.dpr.lt.dp(5)) then
            index=5
         else
            goto 50
         end if
c
c        increment counts...
c
```

```
          count(index)=count(index)+1.
c
c     continue
c
50    continue
c
c     find area and volume from number...
c
      do 80 i=1,numbins
         area(i)=count(i)*((dp(i-1)+dp(i))/2.)**2.*pi
         volume(i)=count(i)*((dp(i-1)+dp(i))/2.)**3.*pi/6.
80    continue
c
c     find total number, area, and volume...
c
      do 90 i=1,numbins
         scount=scount+count(i)
         acount=acount+area(i)
         vcount=vcount+volume(i)
90    continue
c
c     find (1/N)dn/dlog(dp), (1/A)da/dlog(dp),
c     and (1/V)dv/dlog(dp) and write them to the screen...
c
      do 100 i=1,numbins
         dndlogdp=count(i)/dellog(i)
         dadlogdp=area(i)/dellog(i)
         dvdlogdp=volume(i)/dellog(i)
         write(3,110) dp(i-1),dndlogdp/scount,
     *          dadlogdp/acount,
     *          dvdlogdp/vcount
         write(3,110) dp(i),dndlogdp/scount,
     *          dadlogdp/acount,
     *          dvdlogdp/vcount
100   continue
      write(3,110) dp(numbins),0.,0.,0.
```

```
      write(6,111) scount,acount,vcount
111   format(3(1x,e10.4))
110   format(1x,d10.4,6(1x,d10.4))
118   format(i6,1x,i6)
c
c     end program
c
      end
```

Appendix G: Program Listing–DEV.F

```
c     DEV.F
c
c     Written 4/8/92 by Aaron J. Rulison
c
c     DEV.F  calculates the geometric
c     standard deviation from normalized
c     particle size distributions.
c     The input file should consist of
c     rows of data as follows:
c
c     dp (1/N)dn/dlog(dp) (1/A)da/dlog(dp) (1/V)dv/dlog(dp)
c
c     The input file is assumed to be set
c     up for plotting a histogram.
c     Therefore, the first and seconds
c     rows are read, followed by the fourth,
c     sixth, etc. to the end of the input
c     file.  The total number of
c     bins in the input file is (numbins-1),
c     the boundaries of which
c     are specified by (numbins) diameters.
c
c     variable definitions...
c
      real dp(1:35),dndp(1:35),dadp(1:35),
     *     dvdp(1:35),sigg,siggv,dpg,dpgv,
     *     n(1:35),v(1:35),a(1:35),logdpmid
c
      character*10 input
c
      integer numbins
c
c     open set-up file...
c
      open(1,file="dev.inp")
```

```
c
c     read and open the input file...
c
      read(1,20) input
20    format(a10)
      open(2,file=input)
c
c     read the first line of data
c     from the input file...
c
      read(2,*) dp(1),dndp(1),dadp(1),dvdp(1)
30    format(4(1x,e10.4))
c
c     read the remaining lines of
c     data from the input file...
c
1     do 40 i=2,numbins-1
         read(2,*) dp(i),dndp(i),dadp(i),dvdp(i)
         read(2,*) d,d,d,d
40    continue
      read(2,*) dp(numbins),dndp(numbins),
     *              dadp(numbins),
     *              dvdp(numbins)
c
c     process data...
c
      do 50 i=1,numbins-1
c
c        find numbers, volume, and area in each bin...
c
         n(i)=(log10(dp(i+1))-log10(dp(i)))*dndp(i+1)
         v(i)=(log10(dp(i+1))-log10(dp(i)))*dvdp(i+1)
         a(i)=(log10(dp(i+1))-log10(dp(i)))*dadp(i+1)
c
c        find midpoint of each bin...
c
```

```
          logdpmid=0.5*(log10(dp(i+1))+log10(dp(i)))
c
c         find sums used below...
c
          sum1=sum1+n(i)*logdpmid
          suma=suma+a(i)*logdpmid
          sum2=sum2+v(i)*logdpmid
c
50     continue
c
c      find diameter-based, area-based,
c      and volume-based geometric mean
c      diameters...
c
       dpg=10.**sum1
       dpga=10.**suma
       dpgv=10.**sum2
c
c      find sums used below...
c
       do 60 i=1,23
          logdpmid=0.5*(log10(dp(i+1))+log10(dp(i)))
          sum3=sum3+n(i)*(logdpmid-log10(dpg))**2.
          sumaa=sumaa+a(i)*(logdpmid-log10(dpga))**2.
          sum4=sum4+v(i)*(logdpmid-log10(dpgv))**2.
60     continue
c
c      find diameter-based, area-based,
c      and volume-based geometric
c      standard deviations...
c
       sigg=10.**(sum3**.5)
       sigga=10.**(sumaa**.5)
       siggv=10.**(sum4**.5)
c
c      write results to the screen...
```

```
c
      write(6,31)
31    format('dpg,  dpga, dpgv, sigg, sigga, siggv')
      write(6,32) dpg,dpga,dpgv,sigg,sigga,siggv
32    format(6(1x,e10.4))
c
c     end program
c
      end
```

Bibliography

[1] Taylor, G. I. 1964, Proc. Royal Soc. of London A, 280, 383

[2] Bailey, A. G. 1974, Sci. Prog. Oxf., 61, 555

[3] Slamovich, E. B., and Lange, F. F. 1990, J. Am. Ceram. Soc., 73(110), 3368

[4] Fenn, J. B., Mann, M., Meng, C. K., Wong, S. K., Whitehouse, C. 1989, Science, 246, 64

[5] Mahoney, J. F., Yahiku, A. Y., Daley, H. L., Moore, R. D., and Perel, J. 1969, J. Appl. Phys., 40, 5101

[6] Melcher, J. R., and Smith, C. V. Jr. 1969. The Physics of Fluids, 12(4), 778

[7] Smith, D.P.H. 1986, IEEE Trans. on Ind. Appl., IA-22(3), 527

[8] Fernandez de la Mora, J., Navascues, J., Fernandez, F. and Rosell-Llompart, J. 1990, J. Aero. Sci. 21, suppl 1, s673

[9] Kelly, A. J. 1978, J. Appl. Phys., 49(5), 2621

[10] Fernandez de la Mora, J. 1991, private communication.

[11] Landau, L. D. and Lifshitz, E. M. 1960, Electrodynamics of Continuous Media (Oxford:Pergamon Press)

[12] Probstein, R. F. 1989, Physicochemical Hydrodynamics (Boston:Butterworths)

[13] Weast, R. C., Astle, M. J., and Beyer, W. H. 1990, Handbook of Chemistry and Physics, 71st edition (Boca Raton:CRC Press)

[14] Bird, B. B., Stewart, W. E., and Lightfoot, E. N. 1960, Transport Phenomena, (New York:John Wiley and Sons)

[15] Hayati, I., Bailey, A., and Tadros, Th. F. 1987, J. Coll. and Interface Sci., 117(1), 222

[16] Jones, A. R., and Thong K. C. 1971, J. Phys. D.: Appl. Phys., 4, 1159

[17] Saville, D. A. 1971, The Physics of Fluids, 14(6), 1095

[18] Peters, J. M. H. 1980, Eur. J. Phys., 1, 143

[19] Press, W. H., Flannery, B. P., Teukolsky, S. A., and Vetterling W. T. 1990, Numerical Recipes(Cambridge:Cambride University Press)

[20] Schlamp, A. 1894, Ztschr. Phys. Chem., 14, 272

[21] Gomez, A. 1991, private communication.

[22] Meesters, G. M. H., Vercoulen, P. H. W., Marijnissen, J. C. M., and Scarlett, B. 1992, J. Aero. Sci., 23(1), 37

[23] TSI, Inc. 1992, Private Communication.

[24] Wang, S. C., and Flagan, R. C. 1990, Aerosol Science and Technology, 13, 230

[25] Weast, R. C., Astle, M. J., and Beyer, W. H. 1983, Handbook of Chemistry and Physics, 64th edition, (Boca Raton:CRC Press)

[26] Nebergall, W.H., Holtzclaw, H. R. Jr., and Robinson, W. R. 1980 General Chemistry, (Lexington:D.C. Heath and Company)

[27] Cussler, E. L. 1984, Diffusion Mass Tranfer in Fluid Systems (New York:Cambridge University Press)

[28] Bankston, C. D., Back, L. H., Kwack, E. Y. and Kelly A. J. 1988, J. of Engineering for Gas Turbines and Power, 110, 361

[29] Blades, A. T., Ikonomou, M. G., and Kebarle, P. 1991, Anal. Chem., 63, 2109

[30] Roth, D.G., and Kelly, A. J. 1983, IEEE Trans. on Ind. Appl., IA-19(5), 771

[31] Pfeifer, R.J., and Hendricks, C. D. 1967, Physics of Fluids, 10(10), 2149

[32] Elghazaly, H.M.A., and Castle, G. S. P. 1986, IEEE Trans. on Ind . Appl., IA-22(5), 892

[33] Elghazaly, H.M.A., and Castle, G. S. P. 1986, Conf. Record of IEEE Ind. Appl.Soc. Annual Meeting, 2, 1429

[34] Rice, R. W. 1990, AIChE Journal, 36(4), 481

[35] Lange, F. F. 1989, J. Amer. Ceram. Soc., 72(1), 3

[36] Wu, J. J., Nguyen, H. V., and Flagan, R. C. 1987, Langmuir, 3, 266

[37] Kodas, T. T., Engler, E. M., Lee, V. Y., Jacowitz, R., Baum, T. H., Roche, K., Parkin, S. S. P., Young, W. S., Hughes, S., Kleder, J., Auser, W. 1988, Appl. Phys. Letters, 52(19), 1622

[38] Roy, D. M., Neurgaonkar, R. R., O'Holleran, T. P., and Roy R., 1977, Ceramic Bulletin, 56(11), 1023

[39] Ruthner, M. J. 1983, Ceramic Powders, P. Vincenzini ed., (Amsterdam:Elsevier Scientific Pulishing Co.) p. 515

[40] Ishizawa, H., Sakurai, O., Mizutani, N., and Kato, M. 1986, Am. Ceram. Soc. Bull., 65(10), 1399

[41] Michelson, D. 1990 Electrostatic Atomization, (New York:Adam Hilger)

[42] Gomez, A. 1991, Private communication

[43] Charlesworth, D. H., and W. R. Marshall, Jr. 1960, A.I.Ch.E. Journal, 6(1), 9

[44] Leong, K. H. 1981, J. Aero. Sci. 12(5), 417

[45] Leong, K. H. 1987, J. Aero. Sci. 18(5), 511

[46] Leong, K. H. 1987, J. Aero. Sci. 18(5), 525

[47] Zhang, S. C., Messing, G. L., and Bordon, M. 1990, J. Am. Cer am. Soc., 73(1), 61

[48] Rhodes, W. H. 1981, J. Am. Ceram. Soc. 64(1), 13

[49] Warren, B. E. 1990, X-ray Diffraction (New York:Dover)

[50] Slamovich, E. B., and Lange, F. F. 1988, Mat. Res. Soc. Symp. Proc., 121, 257

[51] Seaver, A. E., and Eckhardt, C. J. 1988, United States Patent #4,748,043

[52] Morton, N. 1982, Crop Protection, 1(1), 27

[53] Bartoli, C., von Rohden, H., Thompson, S. P., and Blommers, J. 1984, J. Phys. D: Appl. Phys., 17, 2473

[54] Fenn, J. B.,Mann, M., Meng, C. K., Wong, S. K., and Whitehouse, C. 1989, Science, 246, 64

[55] Becker, D. G., and Friichtenicht, J. F. 1971, The Astrophysica l Journal, 166, 699

[56] Becker, D. G., and Slattery, J. C. 1973, The Astrophysical Journal, 186, 1127

[57] Friichtenicht, J. F., and Becker, D. G. 1971, The Astrophysica l Journal, 166, 717

[58] Friichtenicht, J. F., Slattery, J. C., and Tagliaferri, E. 1968, The Astrophysical Journal, 151, 747

[59] Slattery, J. C.,and Friichtenicht, J. F. 1967, The Astrophysical Journal, 147, 235

[60] Bronshten, V. A. 1983, Physics of Meteoric Phenomena (Boston : D. Reidel Publishing Co.)

[61] Forney, L. J., Walker, A. E., and McGregor, W. K. 1987, Aero. Sci. and Tech., 6, 143

[62] Crowe, C. T. 1967, AIAA Journal, 5, 1021

[63] Eckert, E. R. G., and Drake, R. M. 1972, Analysis of Heat and Mass Transfer (Washington:McGraw Hill)

[64] Hirschfelder, J., Curtiss, C., and Bird, R. 1964, Molecular Theory of Gases and Liquids (New York:Wiley)

[65] Liepmann, H. W., and Roshko, A. 1957, Elements of Gasdynamics (New York: Wiley)

[66] Bansal, N. P., and Doremus, R. H. 1986, Handbook of Glass Properties (New York: Academic Press)

[67] Chen, E. C. M., and Wentworth, W. E. 1975, J. of Chem. Educ, 52(8), 486

[68] Flagan, R. C., and Seinfeld, J. H. 1988, Fundamentals of Air Pollution Engineering (Englewood Cliffs:Prentice Hall)

[69] Anderson, D. A., Tannehill, J. C., and Pletcher, R. H. 1984, Computational Fluid Mechanics and Heat Transfer (Washington:McGraw Hill)

[70] Hayes, B. S., and Wagner, H. G. 1981, Prog. Energy Combust. Sci., 7, 229